UNIVERSITAT DE BARCELONA

Designing Advanced Nanocatalysts: Synthesis of complex CeO_2-based Nanostructures

Carmen Hervés Carrete

DESIGNING ADVANCED NANOMATERIALS:

SYNTHESIS OF COMPLEX CeO_2-BASED NANOSTRUCTURES

Memòria presentada per optar al grau de doctor per la

UNIVERSITAT DE BARCELONA

Doctorat en Nanociències

CARMEN HERVÉS CARRETE

Supervisores

Prof. Víctor F. Puntes

Dra. Neus G. Bastús

Tutor

Dr. Albert Figuerola Silvestre

Barcelona, Febrer 2023

UNIVERSITAT DE BARCELONA

ICN2 Institut Català de Nanociència i Nanotecnologia

EXCELENCIA SEVERO OCHOA

A mi madre,
Mª del Carmen Carrete Ortiz

ACKNOWLEDGEMENTS

The road of any PhD candidate towards their title is never free of curves and obstacles. Completing a project as demanding as a several years-long research plan takes a lot of focus, effort, and, to a certain degree, a great deal of luck. I hope that this text reflects properly my dedication to the first two, serving as a suitable credential for my abilities and expertise. The luck component, however, relies on too many factors and can never be accurately measured. I'm taking this space to thank and acknowledge all the people who, directly or not, had a significant contribution to all the luck that makes this text possible.

First, I want to thank my supervisors, Prof. Víctor F. Puntes and Neus G. Bastús for the topic of my research, for allowing me a place in the *Inorganic Nanoparticles Group* at ICN2 to develop it, and for the guidance and support for almost four years. To my tutor at Universitat de Barcelona, Dr. Albert Figuerola, I want to thank the patience and help at every personal and bureaucratic turbulence experienced. To the Spanish Ministry of Education for the financial support through a FPU grant, and to the Inorganic Chemistry Department at UB for allowing me to take a part in the department's curriculum for my teaching practices.

XAS measurements of Chapter VI were performed at beamline ID26 of the European Synchrotron Radiation Facility (ESRF) in Grenoble. I would like to express my deepest gratitude to Dr. Vinod Paidi and Prof. Pieter Glatzel for hosting me and introducing me to the technique, for their time and patience and for every scientific discussion.

I want to express appreciation to the people that directly contributed to the elaboration of this text. Thanks to the research support division at ICN2: Dr. Jessica Padilla from XRD facilities, Dr. Guillaume Sauthier from the XPS facilities and to Dr. Belén Ballesteros and the rest of the Electron Microscopy facilities for their guidance, patience, and help with the different techniques which have allowed me to provide an accurate characterization to the synthesized materials. Also, thanks to Elizaveta Demakova, Javier Fonseca, Dr. Jana Oliveras, Dr. Chiara Spadaro and Dr. Oscar Moriones for their contribution to Chapter IV. On the same note, Chapter V

would not be possible without the different collaborations that allowed me to learn beyond my field: Thanks to Dr. A. J. Moral-Vico and Dr. A. Markeb from the Department of Chemical, Biological and Environmental Engineering at Universitat Autònoma de Barcelona, for the heterogeneous catalysis tests; and thanks to my colleagues at VHIR's Pharmacokinetic Nanoparticles Group: Lena, Muriel, Vivian and Ramon for your expertise and help with everything bio-related. Thanks also to those who provided me advice during the writing process: Muriel (again), David, Sara, Glòria, Anaís.

I'm also thankful for all the people who have worked alongside me during this period. Your input may not be directly reflected here but I know it is undeniably valuable. To all the people from my group, present and past, especially: Francesco, Óscar and Karen. To Liza. To the rest of the ICN2 community: Despoina, Noelia Enric, Massimo and all the PUMEKO group. To the VHIR community, who took me in as if I was always there, specially Elba (always in first place), Marta and Estela. To my friends Ana and María whose patience with my antics never finds an end.

Finally, none of this would have been possible without the inconditional support from my partner, Anaís, and from my family. Gracias a mis padres Javier y Carmen y a mi hermano Carlos por ser mi punto de partida.

"Our willingness to accept scientific claims that are against common sense is the key to an understanding of the real struggle between science and the supernatural.

We take the side of science *in spite* of the patent absurdity of some of its constructs, *in spite* of its failure to fulfill many of its extravagant promises, *in spite* of the tolerance of the scientific community for unsubstantiated just-so stories, because we have a prior commitment, a commitment to materialism. […] We cannot allow a Divine Foot in the door."

Richard Lewontin, *Billions and Billions of demons*, 1997

INDEX

LIST OF ABBREVIATIONS

ABS	Absorption
AFM	atomic force micrposcopy
BSA	Bovine Serum Albumin
CCD	Charge-Coupled Device
Cit	Citrate
cw	continuous wave
DCA	dicarboxyacetone
DLS	Dynamic Light Scattering
DMEM	Dulbecco's Modified Eagle Medium
DMSO	Dimethylsulfoxide
DPD	Dissipative Particle Dynamics
DSC	Differential Scanning Calorimetry
DVLO	Derjaguin-Landau-Verwey-Overbeek
E	Energy
EDL	Electrical Double Layer
EDTA	Ethylenediaminetetraacetic acid
EDX	Energy Dispersive X-ray Spectroscopy
EELS	Electron Energy Loss Spectroscopy
ELISA	Enzyme-Linked Immunosorbent Assay
EtOH	Ethanol
EXAFS	Extended X-Ray Absorption Fine Structure
FBS	Foetal Bovine Serum
fcc	Face Centered Cubic
FFT	Fast Fourier Transform
FWMH	Full Width at Medium Height
HAADF	High Angle Angular Dark Field
HEK	Human Embryonic Kidney
HMTA	Hexamethylenetetramine

HRTEM	High Resolution Transmission Electron Microscopy
HWMH	Half Width at Medium Height
ICP-OES	Inductively Coupled Plasma - Optical Emission Spectroscopy
LFIA	Lateral Flow ImmunoAssay
LSPR	Localized Surface plasmon resonance
MeOH	Methanol
MOF	Metal Organic Framework
MUA	Mercaptoundecanoic Acid
NA	Numerical Aperture
NC	Nanocrystal
NIR	Near Infrared
NP	Nanoparticle
OSC	Oxygen Storage Capacity
PAA	PolyAcrylic Acid
PB	Phosphate Buffer
PEG	Polyetilene Glycol
PVP	Polyvynilpirrolidone
RNS	Reactive Nitrogen Species
ROS	Reactive Oxygen Species
SA	Specific Activity
SC	Sodium Citrate
SOD	Superoxide Dismutase
STD	Standard Deviation
STEM	Scanning Transimssion Electron Microscopy
STY	Space-Time Yield
Syngas	Synthesis gas
TA	Tannic Acid
TEM	Transmission Electron Microscopy
TGA	Thermogravimetric Analysis
TMAOH	Tetramethylammonium hydroxide
TMB	3,3',5,5'-Tetramethylbenzidine

TWC	Three-Way Catalytic converter
UV	Ultraviolet
UV-vis	Ultraviolet-visible
VdW	Van der Waals
WGSR	Water-Gas Shift Reaction
XANES	X-Ray Absorption Near-Edge Structure
XAS	X-Ray Absorption Spectroscopy
XPS	X-Ray Photoelectron Spectroscopy
XRD	X-Ray Diffraction

SYMBOLS

ΔG	Gibbs free energy
D	Diffusion coefficient
E_g	Bandgap energy
E_u	Urbach Energy
I	Ionic Strength
r	Radius
S	Supersaturation
t	Time
α	Absorption coefficient
γ	Surface tension
ε_λ	Extinction Coefficient
κ^{-1}	Debye Length
λ	Wavelength
μ	Mobility
ν	Frequency
σ	Conductivity
Ψ	Wavefunction

MOTIVATION AND OVERVIEW

Progress in society, the final aim of any scientific effort, comes from the coordinated action of the scientific community, whose role is to provide the necessary tools for a correct pathway to be collectively taken. The role of the individual scientist, however, falls far from that significance. In order to take part in progress, a scientist must find their place in the scientific conversation through deep specialisation on a research topic.

The scope of this thesis work is aimed at understanding the catalytical properties of CeO_2 nanocrystals and the applications arising from them, constructing a bridge between material science and its fields of application. In order to tackle it, the chemist labour consists in providing a cutting-edge nanosynthesis technology able to improve efficiencies of the chemical processes, reduce energy consumption and minimise the environmental impact of both activity and waste products. Research on nanomaterial synthesis involves the design of nanomaterials optimised in terms of their physicochemical, morphological, and colloidal properties towards their final application. While for bulk materials properties are independent from size and shape, at the nanoscale the structure and morphology of a nanomaterial, which are consequence of the characteristics of its synthesis, determine its functionality. Coupled with the appropriate description of the structure-activity relations, the current aim of nanosynthesis is a quality-oriented design strategy towards programmable properties of the products.

Within this framework, this thesis work is divided into two parts. The first part revolves around nanomaterial synthesis, pursuing the optimised formulation of nanostructured CeO_2, a semiconductor material that holds a strong set of redox catalytic properties (**Chapter II**), and the extension of the nanomaterial's functionality through different derivation strategies such as doping with different trivalent lanthanide ions (**Chapter III**) and coupling to plasmonic metal domains (**Chapter IV**). The second part of this work involves the characterisation of structure-activity relations of the CeO_2-based nanomaterials synthesised in the first part. These are evaluated through the catalytic performance of each nanomaterial for

different processes, oriented mainly to the chemical industry and biomedical fields (**Chapter V**) and the characterisation of the material's singular electronic structure, in order to further understand the origin and mechanics of the redox catalytic properties of CeO_2 (**Chapter VI**). Each chapter introduces State-of-the-art of the addressed topic. The general conclusions of each chapter are detailed in **Chapter VIII** The basic theoretical background in which the experimental work is sustained, is compiled in **Chapter I**, the general introduction, and will be referred to at any point of the text where a theoretic explanation would be necessary. Lastly, materials, methods, and other experimental details of each chapter are described in the corresponding section of **Chapter VII**, and other supplementary information can be found in the **Annexes**, to which the reader is referred from the main text when necessary**.**

CHAPTER I

GENERAL INTRODUCTION

CHAPTER I

GENERAL INTRODUCTION

1.1 INTRODUCTION TO NANOMATERIALS

Over the history of science, the classification of knowledge into different disciplines has been subject to change matching the human trends of thought. From the platonic *episteme* or the medieval *quadrivium* to today's branches of natural sciences, there lies a long road of growth and specialisation of expertise in different fields. It is but a step on this road that within the late XX century the field of nanoscience was born. Nanoscience originally appeared as a branch of solid-state physics. However, it quickly became a crossroad between empirical and formal sciences. It finds applications in almost every natural science, turning into a transversal field to the modern classification of knowledge.

The object of study of nanoscience is the nanoscale properties (often defined as the range between 1 and 100 nm), the interphase between the atomic realm, where quantum physics apply, and the macroscale, where classical mechanics take place. The first mention of the field is generally attributed to Feynman in 1959, due to his famous talk "*There's Plenty of Room in the Bottom*".[1] It is impossible to talk about nanoscience without mentioning the concept of nanotechnology. It emerges as the practical application of nanoscience: the ability to manipulate the nanoscale. Definitions of both concepts are a subject of discussion within the community, as the frontiers between them are diffuse.[2] The first mention of the term nanotechnology in the literature dates back to 1974 by Taniguchi, who defined it as "*the process of separation, consolidation, and deformation of materials by one atom or one molecule*". [3]

While Feynman and Taniguchi are considered pioneers of the field, the first examples of nanotechnology that we know of are dated centuries before them: The Lycurgus Cup, a Roman piece of art made of dichroic glass, whose optical properties are known to be a consequence of the presence of a colloidal alloy of gold and silver particles within the glass, is estimated to date around 300 A.C. Similar cases can be found through history of the use of nanoparticles embedded in glass, ceramics and other materials: stained glasses on medieval cathedrals, Islamic pottery, within paints and other artefacts during Italian Renaissance, and several other examples where, without a clear understanding on the cause, nanotechnology was intentionally employed for the properties it held. [4,5]

In 1827, Brown observed for the first time the random motion of suspended particles under the microscope while looking at pollen grains and mistook it for proof of life. After observing the same motion on clay particles, he discarded his own hypothesis.[6] It was not until 1905 that Einstein and Smoluchowski provided with an explanation: this random motion, now known as Brownian motion, is the result of the collisions of the observed particles against the surrounding solvent molecules.[7]

Within the matter of gold colloids, in 1857 Michael Faraday[8] attributed the differences in the optical behaviour of a reduced gold salt precursor solution compared to the bulk metal to the size of the precipitated product, and even described the phenomenon of particle aggregation[a]. His findings were supported and further explained by Maxwell-Garnett in his paper "Colours in Metal Glasses and in Metallic films" (1904)[9] and Mie, "Contributions in the optics of turbid media, particularly colloidal metal solutions" (1908),[10] who proved how the observed optical properties deviated from those of the bulk material due to their small size.

[a] "[…] part of the gold is reduced in exceedingly fine particles, which becoming diffused, produce a beautiful ruby fluid. […] The particles in these fluids are remarkable for a set of physical alterations occasioned by bodies in small quantities which do not act chemically on the gold, or change its intrinsic nature; for through all of them it seems to remain gold in a fine state of division. […] it will be found that the changed gold tends to deposit far more readily than when in the ruby state. […] there is probably some physical change in the condition of the particles, caused by the presence of the salt and such affecting media, which is […] a change of the relation of the surface of the particles to the surrounding medium […]" See reference 8

Also, from today's perspective, one of the main contributions of nanoscience to the modern world is superparamagnetism, described by Louis Néel in 1949. For ferro- and ferrimagnetic materials, when size is reduced enough for the material to be single-domain, a magnetic behaviour similar to paramagnetism arises in which magnetisation appears to be zero in the absence of a magnetic field. Still, upon the effect of an external magnetic field, its magnetic susceptibility takes much higher values.[11] This phenomenon occurs exclusively in the nanoscale: magnetism is a consequence of order in the solid state and, therefore, it is not an intrinsic property of atoms, and the size limitations of the single-domain crystal make it impossible to attain in the bulk of the macroscale.

Finally, it was even a few years before Feynman's lecture that in 1951 Turkevich reported a synthetic method for the production of colloidal Au nanoparticles that is still used in the present day[12]. These are just a sprinkle of examples to illustrate how, while the language to articulate this field is relatively new, nanoscience is not an emerging field as much as a long-unknown part of our academic know-how. The fast development of the field from the second half of the XX Century has brought us nowadays with a deep understanding of the nanoscale phenomena, providing us with a great variety of nanomaterials applicable in practically every research field within life and technological sciences.

1.2 SYNTHESIS OF NANOMATERIALS

1.2.1 Basic principles of nanomaterials synthesis

From the first reports of nanomaterial synthesis until now there has been an enormous amount of research directed towards the control of synthetic processes producing nanomaterials. Many methods have been developed and studied over the past decades. Typically, they have been classified into two main categories according to the approach to reach the nanoscale from a macroscale perspective: "Top-down" (reducing a bulk material to nanoscale sizes) or "Bottom-up" (constructing from zero to the nanoscale).[13]

As previously described, in opposition to typical molecular products of a chemical reaction, the properties of nanomaterials are strongly dependent not only on chemical composition but also on size, shape, and structure. It arises new reproducibility issues for nanomaterial synthesis. Many factors intervene, both for obtaining the desired product and uniformity in its size distribution and shape, and for adequacy in its presentation to be application-disposed. There is no point in the ability to manipulate single atoms if the same product cannot be obtained twice or the assembler cannot separate from the assembly. For that, nano-assembly processes are very sensitive to experimental conditions.[14]

The ideal synthetic route needs to control all parameters mentioned (size, shape and composition uniformity), present a stable, optimised and available product and do so meeting the principles of *green chemistry*:[15] The process of manufacture should be inexpensive and environmentally friendly, meaning that sustainable chemicals should be employed and extreme synthesis conditions or the generation of hazardous waste should be avoided.[16] The branch of the synthetic chemistry field that can potentially meet all the mentioned conditions is a "Bottom-up" approach originating from colloidal science: Colloidal self-assembly or "wet-chemistry" methods.[17]

1.2.1.1 Nanocrystal synthesis: LaMer-Dinegar Model

The principles of crystal formation by which the synthesis mechanisms are explained nowadays come from a 70-year-old qualitative explanation of the nucleation and growth processes, the so-called LaMer-Dinegar model.[18] This model describes the

crystal formation as a sequence of a process of "burst nucleation" and subsequent "diffusion-controlled growth" and provides with an explanation of synthetic conditions considered necessary for achieving monodisperse size distribution for the colloidal synthesis of crystals.

According to this model, nanoparticle formation starts with the precipitation of a solid from a solution. It consists of three differentiated stages (as shown in **Figure 1.1**) that ideally take part in turns: (i) Crystal "monomer" concentration increases until reaching supersaturation levels in solution (C_{min}), then (ii) spontaneous nucleation considered "instantaneous" that lowers the concentration of solute below supersaturation levels and (iii) seed diffusion-controlled growth of the previously formed nuclei within the saturation range of concentration of "monomer", a process that stops once the saturation concentration (C_s, solubility of the monomer) is reached.

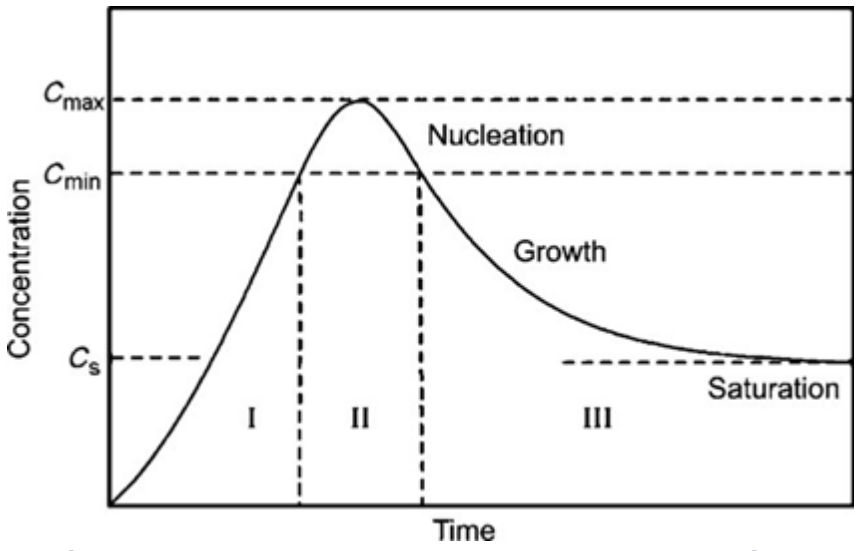

Figure 1.1: *Qualitative curve representing monomer concentration in solution as function of time. Areas I, II and III represent the three stages of crystal formation.*

The model validity for quantitative prediction of the process' kinetics has been thoroughly called into question[19], and since its publication, it has been revised and corrected for several inaccuracies. However, as a pioneer work in the field it stood as the only proposed mechanism of crystal formation for a long time and it has provided space for today's basic concepts of nanocrystal formation mechanisms: Nucleation and growth, and size control mechanisms such as size focusing and Ostwald ripening.[20]

1.2.1.2 Nanocrystal synthesis: Nucleation

As previously defined, nucleation is the process by which the primal crystal particle is formed under supersaturation conditions. To understand its mechanics, a molecular approach introducing the concept of monomer is required: The monomer of a crystal formation reaction is the minimal building unit of the crystal, a "molecule" of a crystal substance. Upon supersaturation levels of this monomer in solution, the chemical process involving collisions between molecules starts. It generates clusters containing a different number of monomers: nuclei, which can either remain solid as a proto-crystal or redissolve.[21]

Thermodynamics determine the stability of the formed nuclei through the total free energy, the summatory of a surface term and a volume term, expressed as equation 1.1. Total free energy can be expressed as a function of the nuclei radius. The surface term is proportional to the surface free energy per area unit (γ) and the volume term to the free energy per volume unit (eq. 1.2), in which V_m is the monomer molar volume and S the supersaturation level (fraction of the monomer concentration with respect of the supersaturation concentration). This equation 1.1 is proved to accurately predict stability data within nuclei sized 10-100 monomers.[22]

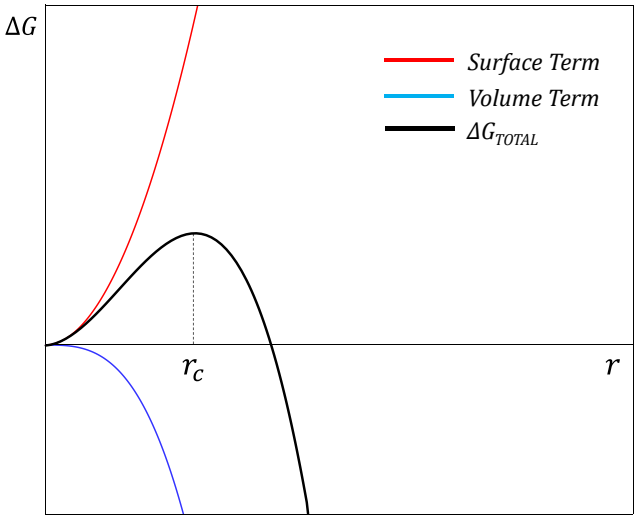

$$\Delta G(r) = 4\pi r^2\gamma + \frac{4}{3}r^3\Delta G_V \quad (1.1)$$

$$\Delta G_V = -\frac{RT\ln S}{V_m} \quad (1.2)$$

***Figure 1.2**: Total free energy of a nucleus as a function of its radius. Plotted from equation 1.1.*

As long as the system is in supersaturation conditions (S > 1), the volume term (ΔG_V) takes negative values, favouring crystal formation, and nucleation happens. The surface term, however, is always positive, so in order for the total free energy to favour the crystal formation, the second condition to be met is that the absolute value

of the volume term has to be greater than the surface one. As a result (**Figure 1.2**), only nuclei bigger than a critical radius r_C are stable to remain in solution and grow to continue decreasing their free energy. Those smaller than r_c can only redissolve. Critical radius is easily calculated by finding where $\partial\Delta G/\partial r = 0$ at $r = r_c$, proving how it is a parameter directly proportional to the surface energy and inversely proportional to supersaturation and temperature.[23]

While the main director of size distribution control is the growth stage, to avoid polydispersity, the nucleation stage should be the shortest possible, as it can heavily influence the posterior process. In principle, there is no time separation between the nucleation and growth stages in the solution. When a stable nuclei forms, it starts to grow, so both processes take place simultaneously until monomer depletion forces nucleation to stop. Nuclei formed at different times will have different sizes after the synthesis is terminated. So, ideally, for a perfectly monodisperse sample, all particles must nucleate simultaneously and grow the same amount of time, as the growth rate is size dependent. It must be noted that in experimental conditions, S is in constant decrease, so r_C is in constant increase. As so, it is experimentally impossible to meet the simultaneity condition. Fast monomer consumption ("burst nucleation") ensures the shortest nucleation period possible and avoids secondary nucleation during the rest of the reaction. In burst nucleation conditions, the number of particles rapidly increases, which is maximum at the end of the nucleation regime. During the growth period, the number of particles remains constant while size distribution evolves.[24]

1.2.1.3 Nanocrystal Synthesis: Growth

Particle growth rate is dependent on size, monomer consumption (reaction rate) and diffusion rate. As previously stated in section 1.2.1.2, during the particle formation process, *S* is constantly decreasing, and so the critical radius for nucleation increases. Consequently, the particle growth rate decreases with a larger particle radius. At the same time, at the nanoscale, precipitation processes are reversible, and the solubility of a particle is heavily affected by its radius: Due to chemical potential differences, smaller nanoparticles are more soluble (Gibbs-Thompson effect).[25] For that reason, an equilibrium between precipitation and dissolution is established.

The growth of crystalline particles in solution is a two-step process: diffusion of the monomers from the solution to the surface and the chemical reaction of incorporation

to the surface. Due to the monomer consumption in the surface reaction, the concentration of monomer on the surface is always lower than in the bulk solution. Thanks to this concentration gradient, the flux of the diffusion, governed by Fick's law,[26] is always happening towards the surface. Two growth regimes are then differentiated depending on whether the growth process is dominated by diffusion rate or reaction rate. To distinguish between them, the effect of chemical potential variation with size, the diffusion rate and the reaction rate are weighted through a parameter called the Damköhler number. [24,27]

If the reaction rate is significantly higher than the diffusion rate, the growth regime is a diffusion-controlled one. Monomer precipitates immediately once it reaches the surface, and the particle growth rate is equal to the diffusion rate, which is inversely proportional to particle radius. It translates into a "size focusing" effect, as the larger the size of the particle the slower its growth, so the size difference between smaller and bigger particles is constantly decreasing. This effect of size focusing narrows size dispersion as mean size increases.

In opposition, if the diffusion rate is significantly higher than the reaction rate, particle growth falls in a reaction-controlled regime, in which the particle growth rate is proportional to the monomer concentration. Within this regime, once the monomer concentration is close to the solubility concentration, the Gibbs-Thompson effect kicks off and smaller particles dissolve back into solution. Larger ones not affected by it keep growing from the redissolved monomers. This is the Ostwald ripening process, by which, at a very slow rate, larger particles grow faster than smaller ones, increasing size dispersion as particles grow and "defocusing" the total size distribution.[28]

1.2.2 Synthesis methods

In order to achieve as ideal as possible nucleation and growth processes for monodisperse nanocrystal production, the wet-chemical methods' approach consists of the tuning of synthetic parameters affecting nucleation kinetics and growth regimes. It can be attained through a wide variety of techniques and setups that, in their majority, can be grouped into hot-injection and heat-up methods.

The hot injection approach consists of the rapid addition of the precursor's solution to a previously heated solvent at a high temperature, so supersaturation is reached in a very short period. When the time for the monomer accumulation stage is reduced, nucleation occurs at a very fast rate, and monomer depletion quickly brings it to an end, favouring size focusing. Heat-up approaches consist of the mixing of all reagents at low temperatures and posterior heating at a controlled rate to induce the initiation of the chemical reaction. Temperature, reaction time, precursor concentrations, pH, ionic force and presence of surfactants or shape-directing agents are the key synthetic parameters at play in both cases. Once the process is over, the nanocrystal solution is quickly cooled down, preventing further evolution of the system.[29]

Both the hot injection and heat-up synthetic approaches allow for the formation of monodisperse nanocrystals of diverse compositions with size deviations smaller than 5%. There are several strategies described in the literature in which these two methods take form. Some of them are (i) the suspension methods, involving a precursor and a precipitation agent like a base for the synthesis of metal sulfide or oxide nanocrystals[30] (ii) chemical reduction, by which a metallic salt is reduced to the zerovalent species, is an easy, effective, one-pot strategy for the synthesis of metallic nanostructures[12,31] (iii) seeded-growth, a very handy strategy for particle size and shape control using small pre-made seeds allowing monomers of the same or other material to grow in their surface,[16] (iv) biogenic synthesis approaches, that introduce the use of enzymes, algae, bacteria and other biological entities to carry the chemical reactions artificially performed by other synthetic routes for an environmentally-friendly process[32,33] (v) hydro- and solvothermal methods, which use high temperatures and pressures of water or non-polar solvents to exploit the solubility and other properties of inorganic precursors and achieve formation of high crystallinity products,[34] (vi) microemulsion methods, where the chemical reactions occur in the interface of two immiscible solvents forming a stable dispersion, typically assisted by surfactants, and combinations between them.[35]

1.3 GENERAL PROPERTIES

The primary condition for something to be considered a "nanomaterial" is that its size falls, in at least one dimension, into the nanoscale (1-100 nm). As previously mentioned, special properties of nanomaterials come from two main features: First, if the size is closer to De Broglie's wavelength of a material, it may exhibit confined wave-like behaviour, which is a phenomenon dictated by quantum mechanics. As so, the nanoscale is the meeting point of quantum and classical mechanics. Second, the surface-to-volume ratio increases to values high enough for surface phenomena to be the primary factor determining the system's characteristics. Depending on the number of nanosized dimensions of a material, we will talk of nanofilms (2D materials), nanowires (1D materials) or nanoparticles (0D nanomaterials). It is worth discussing the general properties of the most common form of the latter: Inorganic nanocrystals. Since this work is based on nanocrystals made of semiconductor and plasmonic metal materials, this section will focus mainly in these two categories.

1.3.1 Morphology

When a nanocrystal is formed, it takes the most energetically favourable morphology according to its crystalline structure and surface energy. For amorphous materials or liquids, in which all surface atoms have the same energy, the less energetic morphology is the one that minimises the number of surface atoms for a constant volume, that is, spherical shape. For crystalline materials, once a size is reached in which crystal facets can be defined, the environment of surface atoms is also affected by the facet in which they are located. For that, energy minimisation gets more complex, becoming a problem of stability of facets. Factors affecting this stability are the density of surface atoms, charge, and intermolecular interactions with ligands and solvent.[36] For example, the surface energy for *fcc* crystals typically is γ_{111} (octahedron) < γ_{100} (cubic) < γ_{110} (dodecahedron), so an octahedral shape should be expected for *fcc* nanocrystals, but for ionic crystals, where charge balance is the most important factor, (111) facets contain ions of the same charge, so facets containing both types of charges are favoured, like (100). Also, surface ligands play a very important role in colloidal crystal growth, as they can stabilise specific nanocrystal facets.[37,38]

The final surface energy is the sum of the surface energy of each facet weighted by their respective surface area. When the less energetic facets of a crystalline structure include different families of facets, all of them will appear in the final morphology of the nanocrystal, truncating edges and corners and making the nanocrystal look rounder with each extra facet appearing.

Hybrid nanostructures

The applicability of nanocrystals relies on the properties exhibited as a result of control of size, morphology and structure. With increasing demands for finer nanostructures of specific properties not achievable under the single-component nanocrystal technology, the urge for synthetic control over advanced complex nanocrystals, hybrid nanostructures containing two domains of different compositions, arises. It is important to acknowledge how combining two or more domains into a single structure can lead to a synergetic combination of the properties of the separated components (semiconductors, plasmonics, magnetic materials, etc.), leading to increased functionality products. The simpler hybrid nanoarchitecture is the core-shell hybrid in which one domain is encapsulated by the other, insulating it from the hybrid surroundings. From the core-shell architecture and by refining morphological control, many different architectures can be obtained, like heterodimers, dumbbell-like hybrids by selective nanocrystal growth on the tips of nanorods, and other branched structures for specific, complex applications.[39]

For prediction of the shape that nanohybrids containing two domains of different composition will take, the relations between surface tensions of all interfaces involved need to be taken into account. The equilibrium shape from a thermodynamic point of view is determined by the balance of forces acting on the three possible interfaces (each component with the solvent and the interface between both components). It can be predicted through the spreading coefficient of the interfaces, Γ_i (equation 1.3), as if one component "wetted" the surface of the other. Where γ is the surface tension of the interface between each phase *i*, *j* or *k*. If this coefficient is negative ($\Gamma_i < 0$) for *i*, interface formation between the other two phases, *j* and *k*, is expected.[40] While interfacial energies on the surface of nanoparticles cannot be measured, the general trend can be observed.

$$\Gamma_i = \gamma_{jk} - \gamma_{ij} - \gamma_{ik} \quad (1.3)$$

In order to step-up morphological control and achieve core-shell derived architectures, synthetic mechanisms require to acknowledge the importance of kinetic control to achieve shapes beyond thermodynamic equilibrium and the role of nanocrystals as reagents rather than just products. Nucleation and growth processes can be harnessed by kinetic control of the nanocrystal's morphology. Controlled dosing of reagents, rather than the total amount reacting, can trap nanocrystals into metastable states or modify the secondary product formation affecting the final product (e.x. hollow nanoparticles). However, despite the potential morphological versatility that kinetic control can offer, yields may be compromised, and a general preparation method is yet lacking. Another viable strategy for complex nanocrystal production is the self-assembly of different domains linked to each other into a single nanostructure through organic molecules attached by both ends.[39] This strategy, however, loses the synergistic properties of hybrid materials that emerge from intimate contact between components.

1.3.2 Mechanical and thermal properties

Another known effect of surface gaining weight against bulk atoms in inorganic materials is the change in mechanical properties (hardness, elasticity, interfacial adhesion and friction, etc.). Variations in mechanical properties in bulk materials come from grain structure, defects, and lattice diffusion. Typically, when talking about the mechanical properties of nanomaterials, the topic discussed is how nanomaterials modify the mechanical properties of bulk bodies as they are introduced to control grain size, boundaries and several other parameters affecting these properties.[41] Nowadays, there exist a few methods for their determination in the nanoscale: AFM techniques for measuring nanoindentation[42], *in-situ* TEM for measuring the evolution of a nanomaterial structure in response to external stimuli[43], or computational simulation methods are among the most important ones. However, mechanical properties are explained through classical theory, and its applicability within the nanoscale, where quantum effects may play a major role, is not yet clear. As so, the reliability of the aforementioned techniques is still under discussion. [44–46]

In order to avoid weighting in such discussion from an external perspective, we can talk of mechanical properties through the example of the melting point. Surface atoms and bulk ones in crystalline solids are differentiated by the coordination

number: First ones do not reach saturation, giving rise to surface tension. This surface tension is higher in the solid phase than in the liquid phase. In the case of liquids, fluidity of atoms mitigates surface tension, as surface atoms can diffuse towards the bulk. The rigid geometry of the solid phase does not allow it, as diffusion coefficients are several orders of magnitude lower. The melting process stabilises the liquid phase and reduces the total surface energy, but it presents a temperature barrier due to the lattice energy of the crystalline structure. In bulk materials, when surface contribution is at its minimum, the temperature at which the melting is spontaneous is the highest. Within the nanoscale, as the surface-to-volume ratio grows, the contribution of surface energy to the total system energy increases gradually while the contribution of lattice energy decreases, diminishing the energy barrier for the melting process. As a result, the smaller the nanoparticle, the lower its melting point (or any other phase transition temperature).[47]

Surface tension is the motor of atomic diffusion from surface towards bulk. Again, since surface contribution in a nanomaterial is so high, atomic diffusion in nanocrystalline solids is higher than in bulk ones. It is translated as variations in mechanical properties and other phenomena related to the material's crystalline structure. As a consequence, the plasticity of nanocrystals is much higher than bulk counterparts.[48]

1.3.3 Optical properties of Semiconductor materials

In a bulk semiconductor, the large number of molecular orbitals of similar energies within the crystalline structure leads to the formation of two broad energy bands: the lower energy band, valence band, filled with electrons at 0 K, and the higher energy band, conduction band, empty at 0 K. Both bands are separated by an energy gap, known as band gap, characteristic of each material. Above 0 K, electrons in the valence band can be promoted to the conduction band thanks to thermal energy, and together with the resulting hole each electron leaves when excited to the conduction band form "electron-hole pairs" (charge carriers). The conductivity (σ) of the material is determined by the concentration of these charge carriers (equation 1.4). Where q is the charge of the carrier, n the charge carrier concentration (in number of particles per volume) and μ their mobility.

$$\sigma = qn_e\mu_e + qn_h\mu_h \qquad (1.4)$$

For nanocrystalline semiconductors (or quantum dots), it occurs a phenomenon known as the quantum confinement effect. The valence and conduction bands are discrete sets of electronic levels, so the continuous optical transitions of the bulk material become quantised when entering the nanoscale, and optical properties arise now from the discrete quantum-size levels rather than chemical composition and structure.[49] When nanocrystal size decreases, the energy of electronic excitations between levels increases. Quantum confinement size dependence comes from the relationship between the nanocrystal radius and the Bohr radius of the bulk exciton of the material. Quantum confinement is weak when the nanocrystal radius is bigger than the Bohr radius, intermediate when they are of similar values, and the difference in mobility between electrons and holes is notorious, and strong when the nanocrystal radius is much smaller than the Bohr radius of the bulk exciton. In the latter case, Coulomb interaction between electrons and holes lowers the energy of the transitions, affecting the optical spectra.[23]

There exist two different types of transitions from semiconductor nanocrystals that can be reflected on their spectra: Optical transitions from intrinsic states, the energy levels for electrons and holes; and optical transitions from surface states, the origin of luminescence. Electron-hole pairs formed by electron promotion in the material are not permanent, they hold limited lifetimes before recombination. When they recombine, a photon is emitted as a consequence of the shift to lower energy electronic states. The energy of the photon emitted is lower than the one from the photon absorbed due to the Stokes shift arising from surface traps.[50] For fluorescent emission, the lifetime of the electron-hole pair is minimal, and the recombination process happens immediately after the excitation. Luminescent emission, on the other hand, is a case of delayed recombination, thanks to entrapment of the electron-hole pairs in metastable states (coming from the surface structure defects) separately. They need an energy intake to be released from the traps, making lifetimes longer.

Band gap determination is the most important parameter required for characterising semiconductors. Absorption spectroscopy and related techniques are the most commonly employed for this. Given that electronic transitions are quantised, it could be expected, in theory, that the absorption spectra of semiconductor nanomaterials presented narrow lines as the absorption peaks. However, due to intrinsic or extrinsic broadenings, the spectra present broad peaks of Lorentzian or Gaussian shape. Band

gap can be extrapolated from the absorption spectra of the material through Tauc's Plot,[51] a method proposed in 1966 for amorphous semiconductors. Tauc's approach relates the light absorption data to energy through the following expression (eq. 1.5):

$$(\alpha h\nu)^{1/\gamma} = m(h\nu - E_g) \tag{1.5}$$

Where h is Plank's constant, ν is the photon's frequency, m is a proportionality constant, α is the absorption coefficient, that defines the capacity of penetration of light on a material before being absorbed (eq. 1.6), E_g is the bandgap energy in eV and γ a factor denoting the nature of the electronic transition. For allowed direct and indirect transitions, the values are γ=1/2 or γ=2, respectively. For prohibited transitions, it takes the values γ=3/2 for direct ones and γ=3 in the case of indirect ones. The absorption coefficient can be determined through the absorbance data and the optical path length l (eq. 1.7). Taking into account Plank's relation (eq. 1.8) and Tauc's expression (eq. 1.5), the absorption data can be plotted against energy, obtaining a characteristic curve that shows a linear increase of absorption with photon energy. The value of E_g is extrapolated from the slope of the linear regression and the x-intercept. This method is applicable to any semiconductor material that shows negligible absorbance in the sub-band energy region.

$$I = I_0 e^{-\alpha l} \tag{1.6}$$

$$A = \log\frac{I}{I_0} = -\alpha l \log e \; ; \; \alpha = \frac{2.303A}{l} \tag{1.7}$$

$$E = h\nu = \frac{hc}{\lambda} \tag{1.8}$$

Another feature extrapolated from this plot is the "degree of order" of the crystalline structure of the semiconductor. The presence of defects or modifications of the structure (dopants, surface adsorption, etc.) may cause the formation of intra-band gap states. These intermediate energy levels do not only manifest through a decrease of total band gap energy but also as a broadening of the low-energy region of the absorption band called Urbach Tail.[52] The width of the Urbach Tail is measured through a parameter called Urbach Energy. This parameter is linked to the variation of the absorption coefficient α with photon energy according to Urbach's empirical relation (eq. 1.9) and can be calculated as the reciprocal value of the slope resultant from the linear regression of the plot ln(α) against photon energy ($h\nu$).

$$\alpha = \alpha_0 e^{\frac{h\nu - E_g}{E_U}} \quad (1.9)$$

This feature needs to be taken into account in order to correctly determine the band gap energy. It has been pointed out in the literature how many authors misinterpret the shift in the plot to an apparent decrease of the E_g value.[53,54] Indeed, if the Urbach Energy of a system is low, the Tauc plot method would be rendered inapplicable to that case.

1.3.4 Optical Properties of Metals: Localized Surface Plasmon Resonance

Quantum size effects give rise to very different effects depending on the type of material treated. One may think that the case of conductor materials as metallic nanoparticles would not differ too much from the quantum size effect in semiconductor nanocrystals. However, the optical properties presented by each type of material are unique. Colloidal solutions of nanoparticles of metals exhibit interesting optical behaviour due to interaction with incident light. The propagation of the electromagnetic wave along the surface excites electrons in the conduction band. For nanoparticles smaller than the incident wavelength ($r < \lambda/10$), the oscillation of the electromagnetic field combines with a Coulombic restoring force of opposite direction. Frequencies of both electromagnetic field and electron oscillation align, resulting in the coherent oscillation of the excited electrons and surface charge polarisation. This phenomenon is known as Localized Surface Plasmon Resonance (LSPR, **Figure 1.3**).

For some metals like Au, Ag, or Cu, the frequency of the LSPR falls within the visible range. Coherent oscillation of electrons on the surface leads to a distinct absorption phenomenon from the metal nanoparticles, experimentally observable through spectroscopy characterisation techniques. LSPR's associated frequency depends strongly on composition, morphology, and size of the nanoparticle and on other characteristics of the system, such as medium refractive index and dielectric constant, surface modification and separation between particles.[55]It is possible to empirically observe the dependence of plasmon absorbance to these parameters, the most typical example being spherical Au nanoparticle colloids presenting colour variation with size, since the LSPR absorption occurs within the visible range of the spectrum.

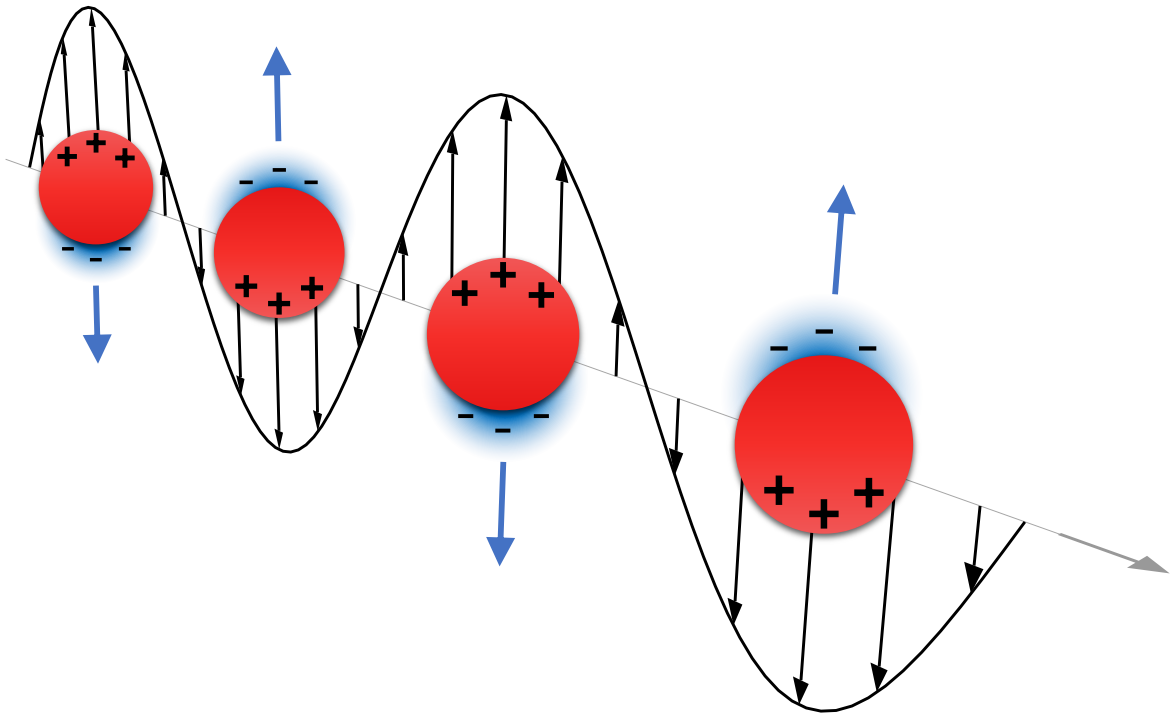

***Figure 1.3**: Scheme of the Localized Surface Plasmon Resonance (LSPR) as consequence of electron cloud oscillation in the presence of an electromagnetic field.*

The spectroscopic appearance of the LSPR can be predicted thanks to Mie's theory. The term extinction refers to the loss of intensity of a transmitted beam due to absorption and scattering when interacting with a medium. Its magnitude is described by the cross-section, the parameter that provides the total flux of electromagnetic waves retained by said medium. Mie's resolution of Maxwell equations for small spherical particles interacting with an electromagnetic field provides with a description of the contribution of size, shape, and each of the previously mentioned parameters to the final extinction cross-section of the system. If the coherent oscillation of electrons within particles meets the size condition ($r < \lambda/10$), the only contribution to the extinction cross-section is the absorption one, resulting in the dipolar oscillation of the electron cloud. For larger particles, light scattering contributes to total extinction along with absorption, and homogeneity of the field polarisation is lost, provoking phase retardations dependent on the size. As a consequence, modes of higher multipoles may appear, such as a quadrupole oscillation where half the electron cloud moves parallel and the other half antiparallel to the electrical field. Symmetry and surface curvature changes also play a role on phase retardation and split of the LSPR into different modes. Ellipsoidal shapes exhibit strong dependency on the polarisation spectra, increasing its effect on the extinction cross-section with increasing aspect ratio. Mie's theory can take each parameter into account to predict the final extinction coefficient for each case.[56,57]

1.4 COLLOIDAL PROPERTIES

The principles of colloid science indicate that in a heterogeneous system formed by a mixture of dispersed particles and dispersant, particles large enough (around 1 μm or above) will slowly sediment out of the suspension, and smaller particles will remain dispersed, forming a colloid. Then, by definition, nanoparticles are colloidal systems when dispersed in a continuous medium. Now, nanomaterials bear very high surface energies due to their characteristic surface-to-volume ratio. In all systems where surface tension is high, the tendency to stability goes through the minimisation of the surface contribution. For nanoparticles, the pathway towards decreasing surface-to-volume ratio is aggregation, the process by which particles irreversibly attach to each other when they enter into contact. This phenomenon makes every colloid an out-of-equilibrium state, unstable by definition: dispersed particles would continuously grow in size by aggregation until surpassing the critical size that makes the colloid collapse and sediment. The understanding of aggregation processes and all the driving forces acting on colloidal nanoparticle systems is a key aspect to correctly describing the general properties of nanomaterials.[58]

1.4.1 Aggregation

Aggregation is the result of a series of physical processes of diffusion and collision, and chemical processes, that lead to irreversible attachment once two surfaces enter into contact. Long-range interactions between particles that lead to collisions are controlled by Brownian diffusion. When contact happens, either repulsion or attachment happen as a result of a series of short-range thermodynamic interactions understood in the context of the DVLO and derived theories.[58]

Aggregation processes are of fractal nature, unpredictable at single nanoparticle level. To describe the structure of an aggregate, the sticking coefficient α (that is, the attachment efficiency or fraction of collisions that lead to attachment) is employed.[59] If every collision leads to attachment, $\alpha=1$ and the aggregation kinetics are fast (diffusion-limited regime of aggregation). If $\alpha<1$, more than one collision is required for attachment and the kinetics of the process are slower (reaction-limited regime of aggregation). Higher values of α lead to dendritic aggregates, whereas slower processes involving several collisions lead to denser, more compact structures, as particles have the chance to arrange into more stable configurations. The final

structure and dimension may affect the surface area, reactivity, bioavailability and toxicity of the aggregate. All these properties are predictable through the understanding of the aggregation process.[60]

1.4.2 Derjaguin-Landau-Verwey-Overbeek (DLVO) theory

The DLVO theory, constructed by the merging of the works of the different scientists naming it[61,62], is used to describe the short-range (0.1-10 nm) interactions that lead to either repulsion or aggregation upon particle collision in a dispersion, predicting the stability of the colloid. It takes into account the attractive (Van der Waals) and repulsive (electrostatic) forces acting in the system.[63,64]

Van der Waals forces (VdW) are the weak interactions consequence of oscillatory asymmetries in the charge distribution that translate into the presence of dipolar moments in particles or molecules dispersed in a medium. It includes the orientation force (Keesom force), resultant of the interaction of permanent dipolar moments;[65] the induction force (Debye force) from the interaction between a permanent dipolar moment and an induced one;[66] and the dispersion forces (London forces) that include interactions between instantaneous induced dipoles.[67] As mentioned, these forces are always attractive, so they are attributed a negative sign in the global summation of forces acting on the system, and they are stronger at shorter distances, so the closer the particles are between each other the more intense is their contribution.

When particles are suspended in a medium of high dielectric constant like water, the presence of charges in the interface between solid and liquid originates repulsive forces that prevent particles from coalescing. The surface charge has its origin in the ionisation of surface groups and the presence of charged species in solution. Balance between the two comes with their distribution: An ion layer of the opposite sign of the surface charge, forming an Electrical Double Layer (EDL). The EDL model was first proposed by Helmholtz,[68] and later improved by Gouy and Chapman.[69,70] Their contribution to the model is the introduction of the effect of ion mobility due to thermal effects, disordering the ionic layer. They describe it as a “diffuse” double layer where ions’ concentration is a gradient following a Boltzmann distribution. The final modifications of the model were proposed by Stern. On one side, his proposal takes into account that ions are not point charges, and at close distances their size plays a role in the distance between the surface and the position of the diffuse double

layer. On the other hand, Stern assumed that the part of the diffuse ionic layer closer to the surface would be adsorbed to it, forming the "Stern layer". At very short distances, electrostatic interaction is stronger than thermal effects and hinders mobility of the ions. The boundary between the Stern layer and the diffuse layer is known as "slipping plane", and it separates the particle and attached molecules from the dispersion medium and ions solubilised there.[71] The schematic model of the EDL is represented in **Figure 1.4**.

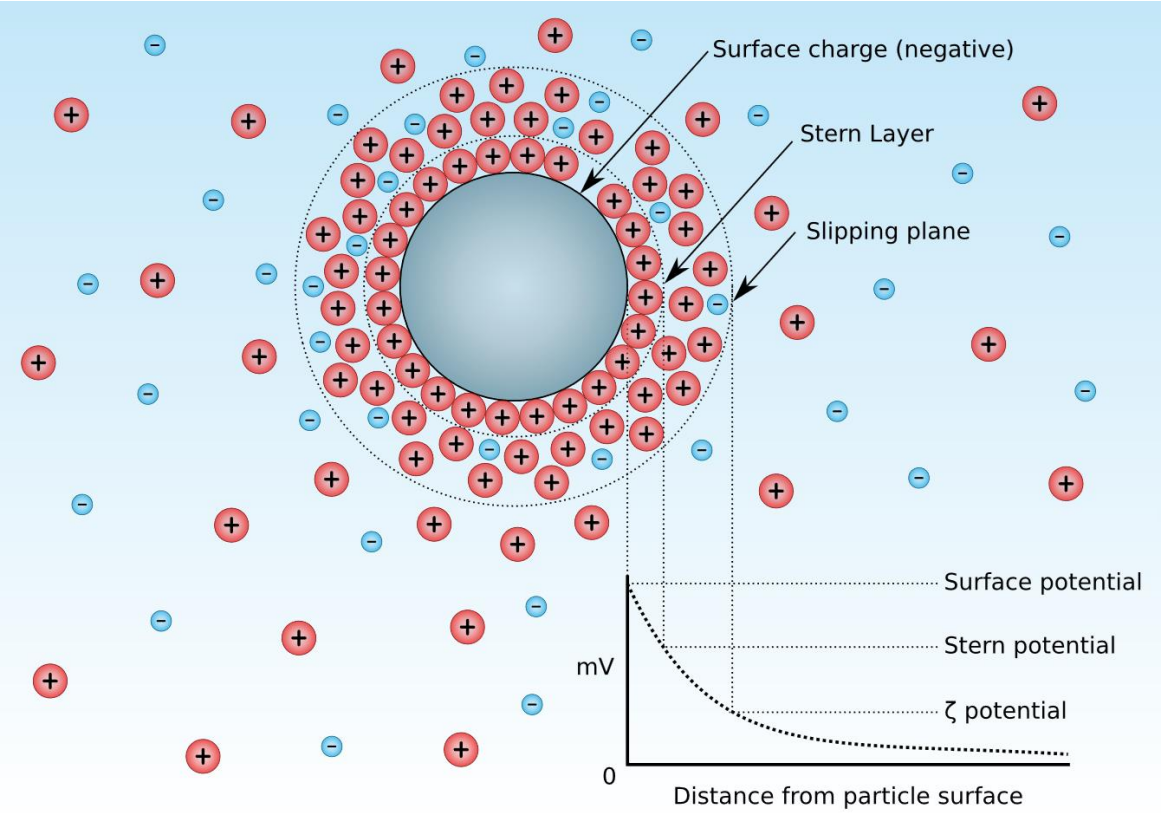

***Figure 1.4**: Schematic representation of the electrical double layer (EDL) around the negatively charged surface of a particle.*

The presence of the EDL neutralising surface charge generates, in turn, an electrokinetic potential between the surface and any point in distance within the dispersant liquid. The voltage difference is called surface potential. Its magnitude is in the order of millivolts and is affected by surface charge and the "thickness" of the EDL: the Debye length κ^{-1} (eq. 1.10). The value of the surface potential is maximum closer to the surface and then falls exponentially through the diffuse layer, reaching zero at its limit. The magnitude employed to measure it is the ζ-potential, which corresponds to the potential at the slipping plane. The value of the debye length is determined by the ionic force, I (eq. 1.11).[72] Where ε is the absolute permittivity value, k_B is the Boltzmann constant, T the absolute temperature, and e elementary charge. Ionic strength I is a function of the concentration c of each ion present in

solution, and *z* is the charge number of each ion. Low ionic strength leads to a higher Debye length of the particles and, consequently, a thicker EDL, while strong ionic strength translates to a lower value of the Debye length: a narrower, stronger EDL.

$$\kappa^{-1} = \sqrt{\frac{\varepsilon k_B T}{2e^2 I}} \tag{1.10}$$

$$I = \frac{1}{2}\sum_{i=1}^{n} c_i z_i^2 \tag{1.11}$$

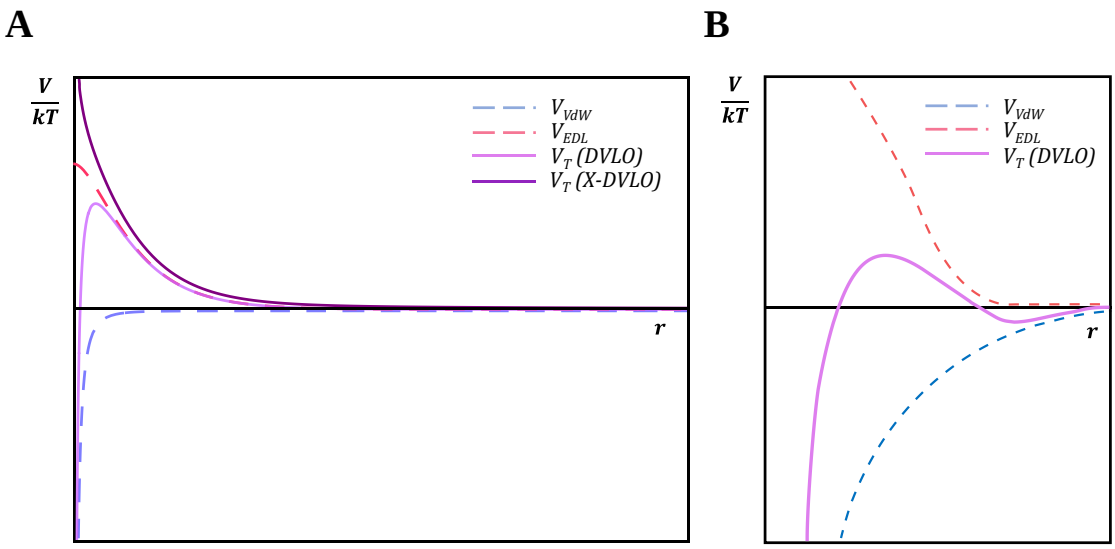

Figure 1.5 *(A) Interaction between to particles as function of the distance between them according to the DLVO and X-DLVO model. (B) The special case of a secondary potential well formation upon reduced EDL thickness.*

The DLVO model simplifies all forces acting between two particles in suspension through the net interaction energy. The net interaction energy is the result of the sum of the Van der Waals attractive and electrostatic repulsive forces (eq. 1.12). A positive net interaction is repulsive, and a negative one is attractive.

$$V_T = \sum V_R + \sum V_A = V_{EDL} + V_{VdW} \tag{1.12}$$

Figure 1.5.A, where net interaction is plotted against particle distance in a model system, illustrates how the DVLO theory predicts the behaviour of aggregation. At long distances, the net interaction value is negligible, and particles do not interact. At short distances, net interaction shows peaks, if repulsion forces are dominant, and wells, in the case of attractive regimes. The peaks act as energy barriers, as for two particles to effectively attach in these conditions they'll need to be provided with enough energy to overcome the barrier. If this barrier is surpassed, the particles will access an attractive potential well where they will enter into contact and irreversibly

aggregate. In the special case of reduced surface charge and strong ionic force reducing the thickness of the EDL, the net interaction function may show a secondary attractive well of less depth and an almost non-existent energy barrier that may be overcome by weak thermal fluctuations (**Figure 1.5.B**). Particles "trapped" in this secondary well are reversibly aggregated.[44,58,60]

1.4.3 Extended Derjaguin-Landau-Verwey-Overbeek (X-DLVO) theory

While DLVO theory is a good description of the phenomena that lead to aggregation, it fails to qualitatively predict aggregation behaviour for colloidal systems deviating from the simple case of the model, like biological systems. Within the short range that DLVO interactions operate, there exist additional forces of similar magnitude that come into play and should be taken into account, and these interactions are not completely independent of each other.[73]

The addition of other attractive and repulsive forces of different natures to the DVLO theory (eq. 1.12) is known as extended DVLO (X-DVLO). The main force included in this extension is the steric repulsion, originated by the resistance to entropy loss due to the compaction of big molecules (such as polymers, organic materials or surfactants) adsorbed onto the surface. In this way, as shown in **Figure 1.5.A**, coated particles may not show attractive net attraction. Other forces included in the extended theory are the magnetic attraction, acid-base interactions, osmotic repulsion, or bridging attraction.[74]

Other factors influencing the net interaction between dispersed particles are the size of the nanoparticles (below a certain size, surface reactivity and charge may vary, and also curvature of the surface cannot be assumed to be negligible), the chemical composition of the surface (reflected on the Hamaker constant), the crystal structure (presence of defects can alter surface charge distribution and Hamaker constant of the material), shape (both EDL and VdW interactions are calculated assuming spherical shape, shape differences can give rise to deviations; oriented attachment and other specific aggregation mechanisms may originate from energetic differences in the exposed crystal facets of anisotropic particles).[60]

1.5 CATALYTIC PROPERTIES AND APPLICATIONS

Catalysis is the phenomenon of increasing the rate of a chemical reaction by mechanistically lowering the process' activation energies but without participating in the chemical transformation. The catalyst, a substance performing the catalytic activity, alters the mechanism of a chemical reaction but is neither a reagent nor a product. Catalysis processes are typically classified into heterogeneous or homogeneous according to whether the catalyst exists in the same phase as the reactants or as a second phase in the reaction mixture.[75] In the first case, the catalyst acts as support for the adsorption of the substrate, in the second case, the catalyst operates forming intermediate compounds with the substrate. Both categories however are not immovable, as the bounds between them are often hazy.[76] Such is the case of enzymatic catalysis, often defined as a special kind of homogeneous process[77] in which the binding of the catalyst, an enzyme, and the substrate shares similarities with the adsorption process of a heterogeneous catalysis.

Another example of the blurred frontiers between homogeneous and heterogeneous catalysis are nanocrystals, often referred as "semi-heterogeneous" catalysts[78] due to their high catalytic activities, consequence of their large surface-to-volume ratio (compared to their bulk counterparts)[79] A heterogeneously catalyzed reaction happens in the interface between the reaction media and the catalyst. The general mechanism of this catalysis involves the diffusion and adsorption of reagents to the "active sites" of the surface of the crystalline structure, the reaction, and posterior desorption and diffusion away from products.[80] Ergo, the catalytically active part of a heterogeneous catalyst is its surface. Catalytic behaviour is strongly dependent on the material's chemical composition, crystalline structure, surface chemistry and size. The nanoscale regime is dominated by quantum confinement and surface phenomena, and the density of active sites is proportional to the surface-to-volume ratio. Heterogeneous catalysis is governed then by nanoscale phenomena and part of the nanoscience umbrella.[81,82]

When there is a chemical transformation involved within the practical application of a nanomaterial, even if it is not the primary objective of said nanomaterial, it happens almost all the time due to a catalytic process. For that, chemically speaking, most applications of nanomaterials emerge from their nanocatalytic properties. Some

examples would be the transformations involved in sensing applications,[83] light harvesting for energy production and storage,[84] degradation of contaminants for environmental remediation or enzyme-mimetic activity,[85] imaging applications or therapeutic applications[86] for biomedical purposes.

Light harvesting for different catalytic processes is a phenomenon known as photocatalysis, where energy from absorbed photons translates into a chemical transformation. While it falls within the scope of this work, it has not been explored experimentally. For that reason, no further description of this phenomenon is provided. However, it is worth mentioning how the different strategies employed to increase functionality of pure CeO_2 NCs synthesized in Chapter II, doping and coupling to plasmonic metals in a hybrid structure (described in Chapter III and Chapter IV) are known strategies for the sensitization of semiconductor materials, with the objective of enhancing their photocatalytic performance. On the other hand, the vast world of biomedical applications of nanocrystals is a core matter of this text, both theoretically and experimentally, and is addressed in the following section.

1.5.1 Biomedical applications

The use of nanomaterials is an expanding tool in the field of human health. Materials smaller than 100 nm can enter inside cells by diverse mechanisms, and those below 10 nm easily diffuse out of blood vessels while circulating the body.[87] This accessibility, provided by size coupled with their intrinsic properties, arises new functionalities that nanomaterials can bring to medicine. The application of nanomaterials for the prevention and treatment of several diseases is called nanomedicine.[88]

For inorganic nanocrystals to be employed in nanomedicine, their biocompatibility is crucial: They need to be dispersed in an aqueous phase with no traces of organic non-biocompatible solvents and be chemically and colloidally stable. Changes in its composition or aggregation may lead to toxic features, and so both must be avoided.[60] Surface modification of the inorganic nanocrystals with proteins and other biomolecules not only improves their biocompatibility and cellular uptake but also prevents aggregation by providing steric impediment effects to their surface.[89]

Some examples of the use of nanomaterials for nanomedicine are the improvement of diagnostic tools: gold nanostructures and magnetic nanocrystals are among the most used biosensors for biomolecule detection and for imaging and contrast enhancement.[90] Other important applications are within the therapy scope, as is their use as drug delivery systems, designed to improve pharmacokinetic and biodistribution of the loaded drug[91]. Delivery of a drug close to its specific target can maximise its primary effect and minimise off-target side effects, allowing a lower dosage than traditional uptake, which is particularly significant in chemotherapy treatments. Their applications in tissue engineering are also remarkable; the ability to mimic the composition of several tissues and improve their mechanical properties has promising prospects for physical therapy. Beyond that, hyperthermia, the localised thermal ablation of tumour cells, is induced by the use of magnetic or gold-based nanocrystals. Inorganic nanocrystals acting as photosensitisers that produce reactive oxygen species (ROS) when receiving photons of the adequate wavelength are used to induce cell apoptosis in a tumour treatment strategy called photodynamic therapy.[92]

1.5.1.1 Enzyme-Mimetic Activity of Inorganic Nanocrystals

Enzymes are biological catalysts that regulate metabolic processes in biological environments. Since the last century there have been many attempts to artificially imitate enzymatic activity to improve stability and reusability for both *in vitro* and *in vivo* applications. One of the first strategies to synthesise artificial enzymes were the so-called "metalloenzymes"[93], which incorporate a metallic cofactor to a protein scaffold to control the catalytic active site. While the metalloenzyme pathway was rendered impractical, the research towards artificially made enzymes was not abandoned. On the contrary, with the popularisation of nanoscience, a new trend emerged as inorganic nanomaterials proved to have intrinsic enzyme-mimicking activity. The first time the term "nanozyme" or "nanoenzyme" was coined was to describe the activity of ligand-functionalized gold as a transphosphorylation catalyst.[94] Since then, it has been updated to describe nanomaterials for which their intrinsic catalytic properties mimic any enzyme-like activity. The pioneering example is the peroxidase-like activity of Fe_3O_4 nanocrystals. Fe^{2+} and Fe^{3+} ions in solution were known for causing the Fenton reaction, similar catalytic process to the one from peroxidase enzyme; however, it was not expected that the nanocrystals

would show that activity without being dissolved first.[95] There are several examples in the literature of metallic, transition metal oxide and carbon-based nanocatalysts able to catalyse enzyme-substrate reactions under physiological conditions. These enzyme-mimicking nanocrystals show similar efficiencies and kinetics as natural enzymes such as peroxidase, oxidase, catalase, and superoxide dismutase, among other redox metabolic processes.[96]

Inorganic nanocrystals performing biomimetic activity show promising results for several applications such as *in vitro* biomolecule detection, replacing natural enzymes in assays such as ELISA (Enzyme-Linked Immunosorbent Assay)[97] or LFIA (Lateral Flow Immunoassay)[98] and in *in vivo* applications as oxidative stress modulators, like Radical Oxygen Species (ROS) scavenging or generation.[99] They also prove to have applications in biofuel generation, environmental remediation, and other non-nanomedicine-related applications.[100]

1.5.1.2 Radical Scavenging Activity

Reactive Oxygen Species (ROS) and Reactive Nitrogen Species (RNS) are molecules containing oxygen (or nitrogen) atoms with an unpaired electron, also known as free radicals. Some examples are ·OH, $O_2{\cdot}^-$ or ·NO. They are very unstable and possess high reactivity towards oxidation reactions due to their uneven number of electrons.

ROS/RNS are naturally produced in the body both as metabolites of some cellular processes, such as mitochondrial respiration and by exogenous causes, such as UV radiation or the metabolism of certain drugs. They serve several cell-signalling purposes and act as regulators for no few metabolic processes, but they are also linked to cell ageing, cancer, and many cardiovascular, inflammatory, and degenerative diseases due to excess concentrations. To avoid the oxidative stress that causes these pathologies, there exist several metabolic and non-metabolic routes regulating the ROS/RNS concentration. The substances that mediate these routes, either natural or artificially made, are typically referred as radical scavengers or antioxidants (as in sacrificial biomolecules and other substances in biological environments that undergo oxidation in the presence of strong oxidizers, preventing

the oxidation of other biologically-relevant species).[99] This terminology should not be mistaken with "antioxidant" as in the opposite of an oxidant (that would be a reducer). By definition, then, antioxidants are weak reducers.

There are several endogenous biomolecules (vitamins, cysteine, glutathione, etc.) and macromolecules (bilirubin, albumin, ferritin…) that show antioxidant properties by acting as sacrificial reagents to consume the excess of radical species.[100] However, from the catalytic point of view, the molecules of interest are the enzymes regulating the radicals' metabolism. Superoxide dismutase (SOD), catalase and peroxidase are the most important among them. The substrate of SOD is $O_2\cdot^-$, that is transformed into O_2 and H_2O_2 upon its activity. The H_2O_2, which is also a free radical precursor, is decomposed to water and O_2 upon the presence of the catalase enzyme. In parallel, peroxidases are a family of enzymes responsible for the oxidation of other biomolecules acting as substrate using H_2O_2. The main difference between catalase and peroxidase is the final electron donor. In the case of catalase, the same molecule is both an acceptor and electron donor in its dismutation to water and molecular oxygen. The relation between all these processes is better illustrated in equations 1.13 and 1.14.[101]

$$O_2^{\cdot -} + H^+ \overset{SOD}{\Longrightarrow} O_2 + H_2O_2 \overset{catalase}{\Longrightarrow} H_2O + O_2 \qquad (1.13)$$

$$H_2O_2 + electron\ donor \overset{peroxidase}{\Longrightarrow} oxydized\ donor + H_2O \qquad (1.14)$$

The presence of this enzymatic set in the organism regulates the endogenous generation of ROS. However, it presents certain limitations in the case of certain diseases or exogenous radical generation causes. The normal concentrations are not adequate for the regulation of sudden ROS bursts, and the antioxidant activity is susceptible to being dysregulated by pH changes. Also, their high selectivity for the substrate leaves secondary ROS species such as OH· without specific enzyme and susceptible to regulation only through antioxidant species such as ascorbic acid.[102]

The use of nanomaterials both as drug delivery systems for antioxidant molecules and as "nanozymes" has been popularised within biomedical research. The improved pharmacokinetics, tolerance to changes in the environment, and lack of substrate specificity of inorganic nanocrystals mimicking SOD, catalase and peroxidase

activities bring good prospects for their application in oxidative stress treatment. Some examples often mentioned in literature are CeO_2, which works as a universal ROS/RNS scavenger;[83,103,104] Fe_3O_4 and MnO_2, which perform both catalase and peroxidase activities;[105] noble metals (Au, Pt, Pd…) for peroxidase, catalase or oxidase mimicking activities;[106–108] or carbon-based nanostructures such as fullerenes or carbon nanotubes that perform ·OH and $O_2\cdot^-$ scavenging.[109]

1.6 OBJECTIVES

The intention of this thesis work is, using the knowledge and concepts described in this chapter, to develop a "tool-box" of CeO_2-based nanomaterials functional for a wide range of applications in several research and industrial fields. Within this framework, the following objectives are set:

- To develop a synthetic protocol for the production of colloidal CeO_2 nanocrystals of the minimal size possible using a water-based precipitation method.
- To increase functionality of CeO_2 Nanocrystals by increasing the complexity of the nanomaterial's structure. Specifically, carrying out two derivation strategies:
  - Lanthanide doping to provide the material with Photon Upconversion and photocatalytic properties.
  - The introduction of a secondary metallic domain to obtain synergistic effects between the metal's LSPR and CeO_2's improving the nanostructure's optical and catalytic properties.
- To attain the complete characterisation from a physicochemical point of view of all the synthesised nanomaterials.
- To define the possible applicability of each nanomaterial synthesized through the description of their structure-activity relations, determining the surface reactivity of each for various model reactions, such as fuel production or radical scavenging, to characterize them.
- To describe the origin of the catalytic behaviour of nanostructured CeO_2-based materials through the characterization of their electronic structure using core-level spectroscopic techniques to determine chemical states, local geometries and nature of the chemical bond.

1.7 REFERENCES

1. Feynman, R. P. There's Plenty of Room at the Bottom. *Engineering and Science Magazine* **23**, 22–36 (1960).
2. Mulvaney, P. Nanoscience vs Nanotechnology—Defining the Field. *ACS Nano* **9**, 2215–2217 (2015).
3. Taniguchi, N. On the Basic concept of Nanotechnology. *Proceeding of the ICPE* (1974).
4. Sciau, P. Nanoparticles in Ancient Materials: The Metallic Lustre Decorations of Medieval Ceramics. in *The Delivery of Nanoparticles* (ed. Hashim, A. A.) (IntechOpen, 2012). doi:10.5772/34080.
5. Pradell, T. *et al.* Metallic and nonmetallic shine in luster: An elastic ion backscattering study. *J Appl Phys* **101**, 103518 (2007).
6. Brown, R. XXVII. A brief account of microscopical observations made in the months of June, July and August 1827, on the particles contained in the pollen of plants; and on the general existence of active molecules in organic and inorganic bodies . *The Philosophical Magazine* **4**, (1828).
7. Haw, M. D. Colloidal suspensions, Brownian motion, molecular reality: a short history. *Journal of Physics: Condensed Matter* **14**, 315 (2002).
8. Faraday, M. X. The Bakerian Lecture. —Experimental relations of gold (and other metals) to light. *Philos Trans R Soc Lond* **147**, 145–181 (1857).
9. Maxwell-Garnett, J. C. & Larmor, J. XII. Colours in metal glasses and in metallic films. *Philosophical Transactions of the Royal Society of London. Series A, Containing Papers of a Mathematical or Physical Character* **203**, 385–420 (1904).
10. Mie, G. Beiträge zur Optik trüber Medien, speziell kolloidaler Metallösungen. *Ann Phys* **330**, 377–445 (1908).
11. Coey, J. M. D. Louis Néel: Retrospective (invited). in *Journal of Applied Physics* vol. 93 (2003).
12. Turkevich, J., Stevenson, P. C. & Hillier, J. A study of the nucleation and growth processes in the synthesis of colloidal gold. *Discuss Faraday Soc* **11**, 55–75 (1951).
13. Abid, N. *et al.* Synthesis of nanomaterials using various top-down and bottom-up approaches, influencing factors, advantages, and disadvantages: A review. *Adv Colloid Interface Sci* **300**, 102597 (2022).
14. Smalley, R. E. Of chemistry, love and nanobots. *Sci Am* **285**, 68 (2001).
15. T. Anastas, P. & M. Kirchhoff, M. Origins, Current Status, and Future Challenges of Green Chemistry. *Acc Chem Res* **35**, 686–694 (2002).

16. A. Dahl, J., L. S. Maddux, B. & E. Hutchison, J. Toward Greener Nanosynthesis. *Chem Rev* **107**, 2228–2269 (2007).

17. Parak, W. J. Complex colloidal assembly. *Science (1979)* **334**, 1359–1360 (2011).

18. K. LaMer, V. & H. Dinegar, R. Theory, Production and Mechanism of Formation of Monodispersed Hydrosols. *J Am Chem Soc* **72**, 4847–4854 (2002).

19. Whitehead, C. B., Özkar, S. & G. Finke, R. LaMer's 1950 Model for Particle Formation of Instantaneous Nucleation and Diffusion-Controlled Growth: A Historical Look at the Model's Origins, Assumptions, Equations, and Underlying Sulfur Sol Formation Kinetics Data. *Chemistry of Materials* **31**, 7116–7132 (2019).

20. Ostwald, W. Über die vermeintliche Isomerie des roten und gelben Quecksilberoxyds und die Oberflächenspannung fester Körper. *Zeitschrift für Physikalische Chemie* **34U**, 495–503 (1900).

21. van Embden, J., E. Sader, J., Davidson, M. & Mulvaney, P. Evolution of Colloidal Nanocrystals: Theory and Modeling of their Nucleation and Growth. *The Journal of Physical Chemistry C* **113**, 16342–16355 (2009).

22. Strey, R., E. Wagner, P. & Viisanen, Y. The Problem of Measuring Homogeneous Nucleation Rates and the Molecular Contents of Nuclei: Progress in the Form of Nucleation Pulse Measurements. *J Phys Chem* **98**, 7748–7758 (2002).

23. Burda, C., Chen, X., Narayanan, R. & A. El-Sayed, M. Chemistry and Properties of Nanocrystals of Different Shapes. *Chem Rev* **105**, 1025–1102 (2005).

24. Kwon, S. G. & Hyeon, T. Formation Mechanisms of Uniform Nanocrystals via Hot-Injection and Heat-Up Methods. *Small* **7**, 2685–2702 (2011).

25. Sarkar, S., Bansal, C. & Chatterjee, A. Gibbs-Thomson effect in nanocrystalline Fe-Ge. *Phys Rev B* **62**, 3218 (2000).

26. Fick, A. V. On liquid diffusion. *The London, Edinburgh, and Dublin Philosophical Magazine and Journal of Science* **10**, 30–39 (1855).

27. v. Talapin, D., L. Rogach, A., Haase, M. & Weller, H. Evolution of an Ensemble of Nanoparticles in a Colloidal Solution: Theoretical Study. *J Phys Chem B* **105**, 12278–12285 (2001).

28. Voorhees, P. W. The theory of Ostwald ripening. *J Stat Phys* **38**, 231–252 (1985).

29. Timonen, J. V. I., Seppälä, E. T., Ikkala, O. & Ras, R. H. A. From Hot-Injection Synthesis to Heating-Up Synthesis of Cobalt Nanoparticles: Observation of Kinetically Controllable Nucleation. *Angewandte Chemie International Edition* **50**, 2080–2084 (2011).

30. Schüth, F. Nucleation and crystallization of solids from solution. *Curr Opin Solid State Mater Sci* **5**, 389–395 (2001).

31. Tan, K. S. & Cheong, K. Y. Advances of Ag, Cu, and Ag-Cu alloy nanoparticles synthesized via chemical reduction route. *Journal of Nanoparticle Research* vol. 15 Preprint at https://doi.org/10.1007/s11051-013-1537-1 (2013).

32. Faramarzi, M. A. & Sadighi, A. Insights into biogenic and chemical production of inorganic nanomaterials and nanostructures. *Advances in Colloid and Interface Science* vols 189–190 1–20 Preprint at https://doi.org/10.1016/j.cis.2012.12.001 (2013).

33. Narayanan, K. B. & Sakthivel, N. Biological synthesis of metal nanoparticles by microbes. *Advances in Colloid and Interface Science* vol. 156 1–13 Preprint at https://doi.org/10.1016/j.cis.2010.02.001 (2010).

34. Li, J., Wu, Q. & Wu, J. Synthesis of nanoparticles via solvothermal and hydrothermal methods. *Handbook of Nanoparticles* 295–328 (2015) doi:10.1007/978-3-319-15338-4_17/COVER.

35. Diodati, S., Dolcet, P., Casarin, M. & Gross, S. Pursuing the Crystallization of Mono- and Polymetallic Nanosized Crystalline Inorganic Compounds by Low-Temperature Wet-Chemistry and Colloidal Routes. *Chem Rev* **115**, 11449–11502 (2015).

36. Wang, Y., He, J., Liu, C., Chong, W. H. & Chen, H. Thermodynamics versus Kinetics in Nanosynthesis. *Angewandte Chemie International Edition* **54**, 2022–2051 (2015).

37. R. Bealing, C., J. Baumgardner, W., J. Choi, J., Hanrath, T. & G. Hennig, R. Predicting Nanocrystal Shape through Consideration of Surface-Ligand Interactions. *ACS Nano* **6**, 2118–2127 (2012).

38. Pan, A. *et al.* Insight into the Ligand-Mediated Synthesis of Colloidal CsPbBr3 Perovskite Nanocrystals: The Role of Organic Acid, Base, and Cesium Precursors. *ACS Nano* **10**, 7943–7954 (2016).

39. Bastús, N. G. *et al.* Exploring New Synthetic Strategies for the Production of Advanced Complex Inorganic Nanocrystals. **229**, 65–83 (2015).

40. Guzowski, J., Korczyk, P. M., Jakiela, S. & Garstecki, P. The structure and stability of multiple micro-droplets. *Soft Matter* **8**, 7269–7278 (2012).

41. Wu, Q., Miao, W. S., Zhang, Y. du, Gao, H. J. & Hui, D. Mechanical properties of nanomaterials: A review. *Nanotechnol Rev* **9**, 259–273 (2020).

42. Giessibl, F. J. Advances in atomic force microscopy. *Rev Mod Phys* **75**, 949–983 (2003).

43. Yu, Q., Legros, M. & Minor, A. M. In situ TEM nanomechanics. *MRS Bulletin* vol. 40 62–68 Preprint at https://doi.org/10.1557/mrs.2014.306 (2015).

44. Guo, D., Xie, G. & Luo, J. Mechanical properties of nanoparticles: Basics and applications. *Journal of Physics D: Applied Physics* vol. 47 Preprint at https://doi.org/10.1088/0022-3727/47/1/013001 (2014).

45. Tranchida, D., Piccarolo, S. & Soliman, M. Nanoscale mechanical characterization of polymers by AFM nanoindentations: Criticalr approach to the elastic characterization. *Macromolecules* **39**, 4547–4556 (2006).

46. Ritter, C., Heyde, M., Schwarz, U. D. & Rademann, K. Controlled translational manipulation of small latex spheres by dynamic force microscopy. *Langmuir* **18**, 7798–7803 (2002).

47. Roduner, E. Size matters: Why nanomaterials are different. *Chem Soc Rev* **35**, 583–592 (2006).

48. Kizuka, T. Atomic configuration and mechanical and electrical properties of stable gold wires of single-atom width. *Phys Rev B Condens Matter Mater Phys* **77**, (2008).

49. Trindade, T., O'Brien, P. & L. Pickett, N. Nanocrystalline Semiconductors: Synthesis, Properties, and Perspectives. *Chemistry of Materials* **13**, 3843–3858 (2001).

50. Yang, F., Wilkinson, M., Austin, E. J. & O'Donnell, K. P. Origin of the Stokes shift: A geometrical model of exciton spectra in 2D semiconductors. *Phys Rev Lett* **70**, 323–326 (1993).

51. Tauc, J., Grigorovici, R. & Vancu, A. Optical Properties and Electronic Structure of Amorphous Germanium. *physica status solidi (b)* **15**, 627–637 (1966).

52. Urbach, F. The Long-Wavelength Edge of Photographic Sensitivity and of the Electronic Absorption of Solids. *Physical Review* **92**, 1324 (1953).

53. Makuła, P., Pacia, M. & Macyk, W. How To Correctly Determine the Band Gap Energy of Modified Semiconductor Photocatalysts Based on UV-Vis Spectra. *Journal of Physical Chemistry Letters* vol. 9 6814–6817 Preprint at https://doi.org/10.1021/acs.jpclett.8b02892 (2018).

54. Feng, Y., Lin, S., Huang, S., Shrestha, S. & Conibeer, G. Can Tauc plot extrapolation be used for direct-band-gap semiconductor nanocrystals? *J Appl Phys* **117**, (2015).

55. Pelton, M., Aizpurua, J. & Bryant, G. Metal-nanoparticle plasmonics. *Laser Photon Rev* **2**, 136–159 (2008).

56. M. Liz-Marzán, L. Tailoring Surface Plasmons through the Morphology and Assembly of Metal Nanoparticles. *Langmuir* **22**, 32–41 (2005).

57. Petryayeva, E. & Krull, U. J. Localized surface plasmon resonance: Nanostructures, bioassays and biosensing—A review. *Anal Chim Acta* **706**, 8–24 (2011).

58. Zhang, W. Nanoparticle Aggregation: Principles and Modeling. in *Nanomaterial: Impacts on Cell Biology and Medicine* (eds. Capco, D. G. & Chen, Y.) 19–43 (Springer Netherlands, 2014). doi:10.1007/978-94-017-8739-0_2.

59. Smoluchowski, M. v. Drei vortrage uber diffusion, brownsche bewegung und koagulation von kolloidteilchen. *Physik. Zeit* **17**, 557–585 (1916).

60. Hotze, E. M., Phenrat, T. & Lowry, G. v. Nanoparticle Aggregation: Challenges to Understanding Transport and Reactivity in the Environment. *J Environ Qual* **39**, 1909–1924 (2010).

61. Derjaguin, B. & Landau, L. Theory of the stability of strongly charged lyophobic sols and of the adhesion of strongly charged particles in solutions of electrolytes. *Prog Surf Sci* **43**, 30–59 (1993).

62. Verwey, E. J. W. & Overbeek, J. T. G. Theory of the stability of lyophobic colloids. *Journal of Physical and Colloid Chemistry* **51**, 631–636 (1947).

63. Derjaguin, B. v, Churaev, N. v & Muller, V. M. The Derjaguin—Landau—Verwey—Overbeek (DLVO) Theory of Stability of Lyophobic Colloids. in *Surface Forces* (eds. Derjaguin, B. v, Churaev, N. v & Muller, V. M.) 293–310 (Springer US, 1987). doi:10.1007/978-1-4757-6639-4_8.

64. Bhattacharjee, S., Ko, C.-H. & Elimelech, M. DLVO Interaction between Rough Surfaces. *Langmuir* **14**, 3365–3375 (1998).

65. Keesom, W. H. On the deduction of the equation of state from Boltzmann's entropy principle'. *KNAW Proc* **15**, 240–256 (1912).

66. Debye, P. Molecular forces and their electrical interpretation. *Physikalische Zeitschrift* **22**, 302–308 (1921).

67. London, F. The general theory of molecular forces. *Transactions of the Faraday Society* **33**, 8b–26 (1937).

68. Helmholtz, H. Ueber einige Gesetze der Vertheilung elektrischer Ströme in körperlichen Leitern mit Anwendung auf die thierisch-elektrischen Versuche. *Ann Phys* **165**, 211–233 (1853).

69. Gouy, M. Sur la constitution de la charge électrique à la surface d'un électrolyte. *J. Phys. Theor. Appl.* **9**, 457–468 (1910).

70. Chapman, D. L. LI. A contribution to the theory of electrocapillarity. *The London, Edinburgh, and Dublin Philosophical Magazine and Journal of Science* **25**, 475–481 (1913).

71. Stern, O. ZUR THEORIE DER ELEKTROLYTISCHEN DOPPELSCHICHT. *Zeitschrift für Elektrochemie und angewandte physikalische Chemie* **30**, 508–516 (1924).

72. IUPAC. ionic strength, I. in *The IUPAC Compendium of Chemical Terminology* (International Union of Pure and Applied Chemistry (IUPAC), 2014). doi:10.1351/goldbook.I03180.

73. Boström, M., Williams, D. R. M. & Ninham, B. W. Specific Ion Effects: Why DLVO Theory Fails for Biology and Colloid Systems. *Phys. Rev. Lett.* **87**, 168103–168107 (2001).

74. Butt, H.-J., Jaschke, M. & Ducker, W. Measuring surface forces in aqueous electrolyte solution with the atomic force microscope. *Bioelectrochemistry and Bioenergetics* **38**, 191–201 (1995).

75. Ted Oyama, S. & Somorjai, G. A. Homogeneous, heterogeneous, and enzymatic catalysis. *J Chem Educ* **65**, 765–769 (1988).

76. Bailar, J. C. "HETEROGENIZING" HOMOGENEOUS CATALYSTS. *http://dx.doi.org/10.1080/01614947408079625* **10**, 17–36 (2006).

77. Cole-Hamilton, D. J. & Tooze, R. P. Homogeneous Catalysis — Advantages and Problems. 1–8 (2006) doi:10.1007/1-4020-4087-3_1.

78. Schatz, A., Reiser, O. & Stark, W. J. Nanoparticles as Semi-Heterogeneous Catalyst Supports. *Chemistry – A European Journal* **16**, 8950–8967 (2010).

79. Astruc, D., Lu, F. & Aranzaes, J. R. Nanoparticles as Recyclable Catalysts: The Frontier between Homogeneous and Heterogeneous Catalysis. *Angewandte Chemie International Edition* **44**, 7852–7872 (2005).

80. Bond, G. C. The Use of Kinetics in Evaluating Mechanisms in Heterogeneous Catalysis. *http://dx.doi.org/10.1080/01614940802480338* **50**, 532–567 (2009).

81. Schlögl, R. & Abd Hamid, S. B. Nanocatalysis: Mature science revisited of something really new? *Angewandte Chemie - International Edition* vol. 43 1628–1637 Preprint at https://doi.org/10.1002/anie.200301684 (2004).

82. Kalidindi, S. B. & Jagirdar, B. R. Nanocatalysis and Prospects of Green Chemistry. *ChemSusChem* **5**, 65–75 (2012).

83. Bai, J. & Zhou, B. Titanium Dioxide Nanomaterials for Sensor Applications. *Chem Rev* **114**, 10131–10176 (2014).

84. Mohamed, R. M., McKinney, D. L. & Sigmund, W. M. Enhanced nanocatalysts. *Materials Science and Engineering: R: Reports* **73**, 1–13 (2012).

85. Mishra, P. *et al.* Engineered Nanoenzymes with Multifunctional Properties for Next-Generation Biological and Environmental Applications. *Adv Funct Mater* **32**, 2108650 (2022).

86. Taylor-Pashow, K. M. L., della Rocca, J., Huxford, R. C. & Lin, W. Hybrid nanomaterials for biomedical applications. *Chemical Communications* **46**, 5832–5849 (2010).

87. Casals, E., Vázquez-Campos, S., Bastús, N. G. & Puntes, V. Distribution and potential toxicity of engineered inorganic nanoparticles and carbon nanostructures in biological systems. *TrAC Trends in Analytical Chemistry* **27**, 672–683 (2008).

88. Park, W. *et al.* Advanced hybrid nanomaterials for biomedical applications. *Progress in Materials Science* vol. 114 Preprint at https://doi.org/10.1016/j.pmatsci.2020.100686 (2020).

89. Barbero, F. *et al.* Formation of the Protein Corona: The Interface between Nanoparticles and the Immune System. *Semin Immunol* **34**, 52–60 (2017).

90. Pankhurst, Q. A., Connolly, J., Jones, S. K. & Dobson, J. *Applications of magnetic nanoparticles in biomedicine*. *J. Phys. D: Appl. Phys* vol. 36 (2003).

91. Liang, R., Wei, M., Evans, D. G. & Duan, X. Inorganic nanomaterials for bioimaging, targeted drug delivery and therapeutics. *Chemical Communications* **50**, 14071–14081 (2014).

92. Das, S., Mitra, S., Khurana, S. M. P. & Debnath, N. Nanomaterials for biomedical applications. *http://dx.doi.org/10.1080/21553769.2013.869510* **7**, 90–98 (2014).

93. Rosati, F. & Roelfes, G. Artificial Metalloenzymes. *ChemCatChem* **2**, 916–927 (2010).

94. Manea, F., Houillon, F. B., Pasquato, L. & Scrimin, P. Nanozymes: Gold-Nanoparticle-Based Transphosphorylation Catalysts. *Angewandte Chemie International Edition* **43**, 6165–6169 (2004).

95. Cleland, W. W. *Derivation of Rate Equations for Multisite Ping-Pong Mechanisms with Ping-Pong Reactions at One or More Sites*. THE: JOURNAL cm BIOLOGICAL CHEMI~TRP* vol. 248 http://www.jbc.org/ (1973).

96. Wu, J. *et al.* Nanomaterials with enzyme-like characteristics (nanozymes): next-generation artificial enzymes (II). *Chem Soc Rev* **48**, 1004–1076 (2019).

97. Asati, A., Santra, S., Kaittanis, C., Nath, S. & Perez, J. M. Oxidase-Like Activity of Polymer-Coated Cerium Oxide Nanoparticles. *Angewandte Chemie International Edition* **48**, 2308–2312 (2009).

98. Duan, D. *et al.* Nanozyme-strip for rapid local diagnosis of Ebola. *Biosens Bioelectron* **74**, 134–141 (2015).

99. Karakoti, A., Singh, S., Dowding, J. M., Seal, S. & Self, W. T. Redox-active radical scavenging nanomaterials. *Chem Soc Rev* **39**, 4422–4432 (2010).

100. Singh, L., Rana, S., Thakur, S. & Pant, D. Bioelectrofuel Synthesis by Nanoenzymes: Novel Alternatives to Conventional Enzymes. *Trends Biotechnol* **38**, 469–473 (2020).

101. Winterbourn, C. C. Reconciling the chemistry and biology of reactive oxygen species. *Nature Chemical Biology 2008 4:5* **4**, 278–286 (2008).

102. Frijhoff, J. *et al.* Clinical Relevance of Biomarkers of Oxidative Stress. *Antioxid Redox Signal* **23**, 1144–1170 (2015).

103. Matés, J. M., Pérez-Gómez, C. & de Castro, I. N. Antioxidant enzymes and human diseases. *Clin Biochem* **32**, 595–603 (1999).

104. Liu, Y. & Shi, J. Antioxidative nanomaterials and biomedical applications. *Nano Today* **27**, 146–177 (2019).

105. Banavar, S., Deshpande, A., Sur, S. & Andreescu, S. Ceria nanoparticle theranostics: harnessing antioxidant properties in biomedicine and beyond. *Journal of Physics: Materials* **4**, 042003 (2021).

106. Ernst, L. M. & Puntes, V. How Does Immunomodulatory Nanoceria Work? ROS and Immunometabolism. *Front Immunol* **13**, 974 (2022).

107. Huang, Y. *et al.* Self-Assembly of Multi-nanozymes to Mimic an Intracellular Antioxidant Defense System. *Angewandte Chemie International Edition* **55**, 6646–6650 (2016).

108. Kim, M.-C., Lee, D., Hoon Jeong, S., Lee, S.-Y. & Kang, E. Nanodiamond–Gold Nanocomposites with the Peroxidase-Like Oxidative Catalytic Activity. *ACS Applied Materials & Interfaces* **8**, 34317–34326 (2016).

109. Jawaid, P. *et al.* Effects of SOD/catalase mimetic platinum nanoparticles on radiation-induced apoptosis in human lymphoma U937 cells. *Apoptosis* **19**, 1006–1016 (2014).

110. Long, R., Huang, H., Li, Y., Song, L. & Xiong, Y. Palladium-Based Nanomaterials: A Platform to Produce Reactive Oxygen Species for Catalyzing Oxidation Reactions. *Advanced Materials* **27**, 7025–7042 (2015).

111. Ding, H. *et al.* Carbon-based nanozymes for biomedical applications. *Nano Research 2020 14:3* **14**, 570–583 (2020).

CHAPTER II

CeO_2 NANOCRYSTAL SYNTHESIS

CHAPTER II

CeO_2 NANOCRYSTAL SYNTHESIS

2.1 INTRODUCTION

Nanostructured metal oxides, the crystalline solid materials of cationic metal atoms compensated by oxide anions, hold a comprehensive set of catalytic, optical, and electronic properties that make these materials appealing for applications in many fields. The properties of these materials in the nanoscale strongly depend on their size, morphology, and surface chemistry, which are determined during their synthesis. Consequently, there is an interest in developing synthetic processes and understanding the mechanisms governing the synthetic routes of these materials.

The model for a generic crystal formation mechanism has been previously described in chapter I section 1.2.1. The case of oxides, however, deserves a couple of extra lines for its description. Generally, in the case of metals, their behaviour in solution depends on the nature of the complexation sphere around the atom. For the basic precipitation of metal oxides, substituting water molecules with hydroxyl anions upon pH rise leads to insolubility in basic media, the motor for crystal formation. The accumulation of monomers occurs through the hydroxylation and posterior hydrolysis of the zero-charge complex resultant. Usually, a diffusion-limited growth of oxide crystal nuclei leads to very small-sized monocrystalline particles. In order to grow beyond this focused size, it is primarily necessary for an ageing or coarsening stage posterior to crystal formation in which they aggregate and define their shape as polycrystalline particles.[1] The final shape, density and porosity of the oxide particles then depend on the nature of the aggregation process.[2]

Cerium is the most abundant rare-earth metal on the periodic table. It exists in its native form under the earth's crust but oxidises in contact with the atmosphere.

Cerium (IV) Oxide (ceria, CeO_2), its most stable form, is at present one of the most interesting rare-earth material compounds for nanotechnology. The interest in the production of this material comes from its unique nanocatalytic properties.

Nanoceria's characteristic redox behaviour originates in the relationship between its crystal and electronic structure. The famous spectroscopist Kotani mentioned once that it does not exist a pure sample of cerium (IV).[3] CeO_2 crystallises in a fluorite structure, an *fcc* unit cell containing four atoms of Ce (distributed along the eight corners and six facets) and eight oxygen atoms occupying all the tetrahedral sites inside (**Figure 2.1.a**).[4] While oxygen vacancy defects are found in different facets of the structure, exposed (111) facets of CeO_2 prove to be intrinsically unstable, as they expose an uneven amount of Ce and O atoms (illustrated by **Figure 2.1.b**). As a result, it gives rise to charge separation and, subsequentially, surface polarisation. The path towards charge balance within these facets goes through the partial elimination of the surface oxygen.[5] The degree to which the reversible removal of oxygen atoms along the (111) surfaces happens depends on the temperature and partial O_2 pressure of the atmosphere. The constant presence of oxygen vacancies makes it a *non-stoichiometric* oxide of the chemical formula CeO_{2-x}.

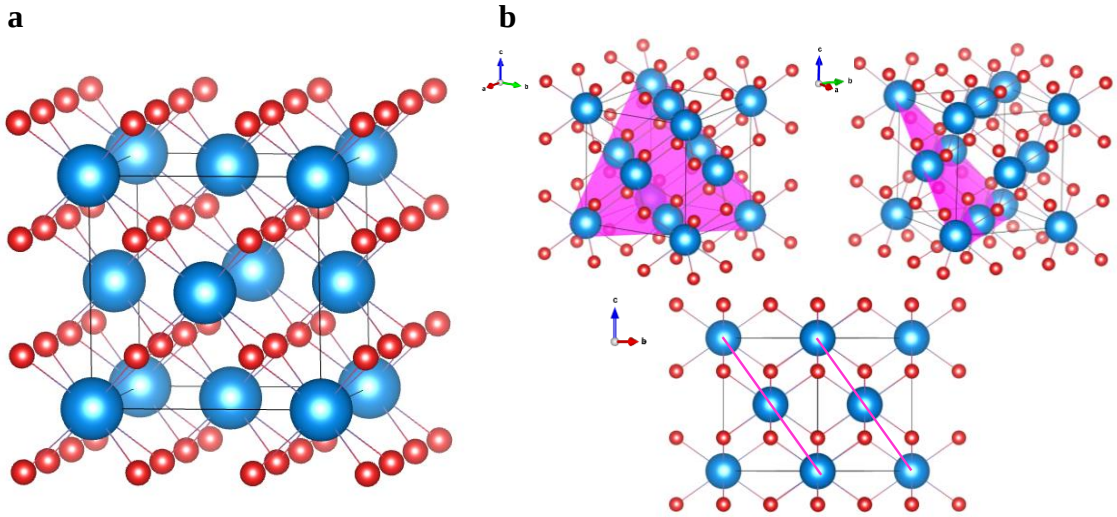

***Figure 2.1**: CeO_2 (a) fcc Unit Cell and (b) (111) plane intersect with the unit cell from different angles. Ce atoms in blue, O atoms in red. Crystallographic structure extracted from Artini et al. Illustrated using VESTA software.*[4,41]

The increase in surface area that comes with the nanometric regime generates a high density of oxygen defects in the crystal structure. The crystal, however, can hold them without being altered, thanks to the particularities of the compound's electronic structure. The cerium atom's electronic structure contains 58e^-, [Xe] $4f^1$ $5d^1$ $6s^2$. For the +4 valency, it loses the four outer electrons. The empty *f* states, being shielded

from the core's charge by three internal shells of electrons, serve as an "electron sponge". They hold the electron charge excess left behind by the presence of oxygen vacancies within the crystal structure, blocking the alteration of the material's crystal structure at its surface. The literature describes this phenomenon as the interconversion between III and IV oxidation states ($4f^1$ and $4f^0$ configurations). This item will be further developed in oncoming chapters.

The flexibility of the oxide towards defects on its structure allows the material to work as an "oxygen buffer" and electron scavenger in several environments and conditions, making it an ideal nanocatalyst for many fields.[6] In energy research, CeO_2 works as a photocatalyst for oxidation semirreaction in water splitting.[7] As a wide-band semiconductor (3.2 eV), charge carrier generation occurs under the illumination of UV light. Oxygen vacancies play a role in tuning the observed bandgap, work as electron traps preventing charge recombination, and serve as active sites for adsorbate molecules to react. Transition metal doping of CeO_2 has proven a good strategy towards visible absorption enhancement,[8] making it possible to design a CeO_2-based nanocatalyst containing a controlled amount of oxygen vacancies capable of performing water oxidation under photosynthesis conditions.[9] In industry, CeO_2 is widely applied for many redox processes, mainly oxidations. The representative example of this role of CeO_2 would be as part of the Three-Way Catalytic Converters (TWCs), in combination with precious metals such as Rh, Pt or Pd and other metal oxides, in combustion exhaust streams (oxidising carbon monoxide and unburnt hydrocarbons to water and carbon dioxide). When the oxygen concentration of the exhaust stream is insufficient to convert toxic gases efficiently, CeO_2 releases surface oxygen to compensate for the shortage and regenerates once the partial O_2 pressure returns to normal. Besides oxidations, CeO_2 has shown catalytic properties towards hydrogenation reactions, such as the CO/H_2 reaction.[10] In biomedicine, CeO_2 redox properties manifest in its activity as a ROS scavenger: it is mainly used as an antioxidant-like substance capable of modulating oxidative stress in living organisms and, in general, for all inflammation-related processes.[11] CeO_2 NCs have also been reported to have potential applications in different medical fields such as ophthalmology[12], cardiology[13], oncology[14], neurology[15], etc... Other health-related uses are as UV absorbent or as treatment of burns and other skin injuries.

Also, the characteristic electronic properties of this material reflect in the increase of unit cell parameters when size is heavily decreased and in the bandgap narrowing in the nanoscale. Both phenomena are caused due to a higher percentage of oxygen vacancies.[16,17]

2.1.1 State of the Art

CeO_2 nanocrystal (NC) synthesis has been performed and reported for a long time. Current necessities for CeO_2 NCs production, considering the global necessities for sustainable and cheap technologies, are aqueous-based synthetic routes of mild pressure and temperature conditions. Most methods involve either the use of toxic solvents, high temperatures and pressures or other conditions which limit not only the surface chemistry of nanostructured CeO_2 but also the sustainability and biocompatibility of the product. However, aqueous media raises some challenges: The solvent also plays a role as a reagent in the reaction; thus, controlling the reagent concentration during the process is more complex than in organic media. Another critical aspect to also bear in mind for designing materials aimed at biomedical and catalytic fields is that the optimised formulation should provide an available surface. Thus, surfactants must be avoided as much as possible, even if biocompatible. Conversely, a big issue for both biocompatibility and catalytic performance is aggregation: it not only reduces the availability of surface and hinders catalysis, but it is also considered one the main causes of nanomaterials toxicity. Size is a determinant parameter in bioaccumulation, cellular uptake mechanism and reactivity.[18]

Among all the possible synthesis methods for CeO_2 NCs, those of biological interest are based on the precipitation method: The aqueous precipitation of Ce (IV) due to its insolubility in basic media. The most common precursors are Ce (III) salts, as, according to the Pourbaix diagram of cerium (**Figure 2.2**), the Ce (III) transformation to Ce (IV) is spontaneous in water at basic pH. The overall process involves the following steps: hydroxylation, oxidation, precipitation (which in turn consists of the stages of crystal formation) and ageing.[19] The final CeO_2 NCs produced should ideally be the smallest monocrystalline size possible, both chemically and colloidally stable. Variations of synthetic parameters within this method, such as the precursor to precipitating agent ratio, reagent counter ions or temperature, will lead to different

colloidal formulations of the same material, distinguishable mainly in the aggregation state and final particle size. While chemically identical, different formulations will hold differences affecting their performance both catalytically and in terms of biocompatibility.

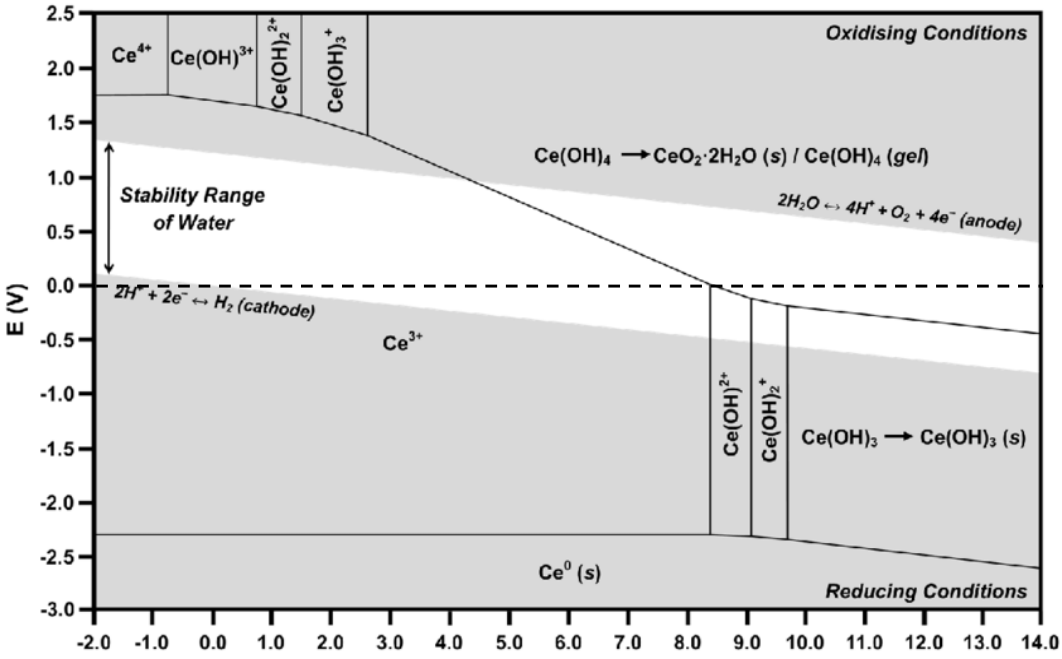

***Figure 2.2**: Pourbaix diagram for Ce in water(E vs pH). Modified from Channei et al.*[42]

Some of the most remarkable protocols for CeO_2 NCs reported in the literature are those in which citrate salts are used as a stabilising agent, among other common stabilisers such as Polyetilene Glycol (PEG) or Polyvynilpirrolidone (PVP). Citrate, an organic molecule containing three negative charges and limited mobility compared to smaller ions, is a very common peptisation agent for achieving colloidal stability in nanoparticle dispersions. Heckman et al.[20] reported the successful synthesis of monocrystalline CeO_2 NCs of 2.9 nm in size by injecting a $Ce(NO_3)_3$ salt into a solution of ammonia 30% and hydrogen peroxide at 70ºC containing sodium citrate and ethylenediaminetetraacetic acid (EDTA) in different proportions as stabilisers. The use of EDTA proved problematic, as it is an adsorbed surfactant and cannot be washed off, blocking the availability of the surface. As a result, the catalytic activity of the NCs sees itself restrained. Performing the protocol using just citrate as a stabiliser, in the absence of EDTA, resulted in the discrete aggregation of monocrystals onto 7.8 nm polycrystalline nanoparticles.[21] Reed, one of the authors behind this CeO_2 NC formulation, proposed that the optimal size for a nanoceria colloid maximising reactivity while remaining thermodynamically stable is around

2-3 nm.[22] It is also worth mentioning the works of Yokel et al., in which discretely aggregated 5 nm CeO_2 NCs were obtained.[23–26] Their method consists of the preincubation of $Ce(NO_3)_3$ as a precursor and an equimolar amount of citric acid in solution before adding NH_3 as a base in a 1:6 molar ratio at 50ºC for the precipitation and 80ºC for their ageing. This synthetic protocol is a variation of the method proposed by Masui in 2002,[27] that also reports crystal sizes around 4 nm and mentions partial aggregation. This method uses a preincubation step of citric acid and the salt precursor to which the ammonia in a 1:3 molar ratio is injected at 50ºC. Notably, for these two reported synthetic approaches, the acid form of the citrate ion is employed instead of the trisodium salt, leading to a partial neutralisation of the base immediately when injected and milder pH conditions. The final ratio of Ce precursor to base would, as consequence, be lower than 1:3. Masui mentions how citric acid plays a role in the final size of the particles while acting as a stabiliser due to its adsorption to the crystal surface. The concentration of citrate as a stabiliser is essential in terms of a strong EDL formation and for attaining the optimal size of the product.

Other authors, such as Ivanov or Malyukin, also reported the influence on stabiliser concentration and particle size. Ivanov et al. published the patented method for synthesising particles between 1 and 2 nm in size due to PolyAcrylic Acid (PAA) stabilisation at highly basic pH levels.[28] In the case of Malyukin et al., the preincubated stabiliser chosen is Hexamethylenetetramine (HMTA), which works as a surfactant prevents the particles' aggregation in a high excess of ammonia and hydrogen peroxide in the solution.[29] These methods have the same drawbacks as the previously mentioned EDTA method. Other synthetic methods reported for the synthesis of CeO2 spherical NPs are summarised in **Table 9.1** (surfactant-free methods) and **Table 9.2** (surfactant assisted methods) at Annex B. Different shapes of the CeO_2 NCs, such as stamps, nanocubes, nanorods, or nanowires have also been thoroughly reported, some examples can be found in **Table 9.3** (Annex B).

Finally, using a Ce (IV) precursor is also possible for synthesising CeO_2 NCs, leading to the formation of NCs of very small sizes. However, due to Ce^{4+} low water solubility, high temperatures are typically required, making these precursors less desirable. **Table 9.4** at Annex B lists several synthesis methods using Ce(IV) salts.

2.2 RESULTS AND DISCUSSION

2.2.1 Synthesis of CeO_2 Nanocrystals

Experimentally, the synthesis protocol developed for CeO_2 NCs consists of two stages: The precipitation stage, at room temperature, where NCs highly rich in oxygen vacancies and other defects are slowly forming in solution, and the ageing stage, where the crystallinity is improved until reaching the minimum stable amount of oxygen vacancies for the NC size.

The precipitation stage consists of several steps: hydroxylation, consisting of forming a wide range of mostly soluble $[Ce(OH)_x]^{3-x}$ species, occurring spontaneously and at basic pH, as Ce^{+3} ions have a high affinity for hydroxyl groups. Next, the progressive oxidation of Ce (III) to Ce (IV) occurs within the hydroxide species in the solution and under the presence of solubilised oxygen from the air. The oxidation provides the "monomer" for crystal formation, as the immense polarisation power of Ce^{4+}, containing such a high charge in a significantly reduced volume, makes it unstable in solution. After the accumulation of enough Ce^{4+} in the solution, nucleation and growth of the NCs start.

For the precipitation stage, the first step is the slow addition of the Cerium (III) salt precursor solution onto the sodium citrate (Cit) one in a 1:2.2 molar ratio while stirring at room temperature. It allows for the $[Ce(Cit)_2]^{3-}$ complex formation and avoids the precipitation of the insoluble Cerium (III) citrate salt occurring when there is an stoichometrical excess of Ce^{3+} with respect to the citrate. No difference was observed in the resultant particles when changing the salt precursor between $Ce(NO_3)_3$, $CeCl_3$ or Cerium (III) acetylacetonate. However, chloride salt was preferred for its transparency within the UV region (See Inset at **Figure 2.5.a**) and its biocompatibility. At this point, the pH of the solution is between 7.7 and 8.2, depending on the citrate excess.

To this solution, a sub-stoichiometric amount of base is added, raising pH to 10.5-11. The final molar ratio of precursor to the base is 1:2.7 to avoid precipitation of bulk $Ce(OH)_3$. The chosen alkaline solution is tetramethylammonium hydroxide (TMAOH), a known biocompatible additive commonly used to synthesise several metal oxide NCs.[30,31] Alternative compounds tested as a base were NaOH, which

provided 8-10 nm sightly aggregated NCs but otherwise proved effective, and NH_4OH, which proved inefficient due to its weak base behaviour, as it does not allow for precisely controlling the precursor-to-base ratio. Either the reaction was not completely carried out due to low pH, or the hydroxide precipitation occurred due to base excess. Once the salt precursor and the base have been mixed, the solution is left stirring for 8 hours at least, allowing the Ce^{3+} ions to slowly oxidise and precipitate. As this sequence takes place, the pH of the solution slowly goes down to approximately 9.

After the CeO_2 NCs precipitation, the ageing stage takes place. It consists of a series of changes that reflect on the absorption spectra of the NCs, changing the colloid's appearance: The slope of the peak increases, diminishing absorption on the visible range and affecting the bandgap of the material. The changes suffered by the solids during this stage are estimated to be surface transformations: Dehydration of surface hydroxyl groups, diminishing the amorphous character of the surface, and the partial filling of oxygen vacancies until reaching the minimum stable amount for the surface-to-volume ratio at this size. The effect of ageing on the crystalline solids will be further developed in section 2.2.3 of this Chapter. Ageing can be performed at room temperature by leaving the solution closed and stirring for at least two months or boiling it under reflux conditions for four hours. It is also achievable chemically by introducing an oxidising agent such as H_2O_2. The resultant NCs from this stage are highly stable both chemically and colloidally. In the right conditions, they can be stored for up to 3 years before use without significant changes. Since there is no complete annealing step, there is expected to be a certain amount of water within the structure, also playing a role in the colloidal stability of this formulation.

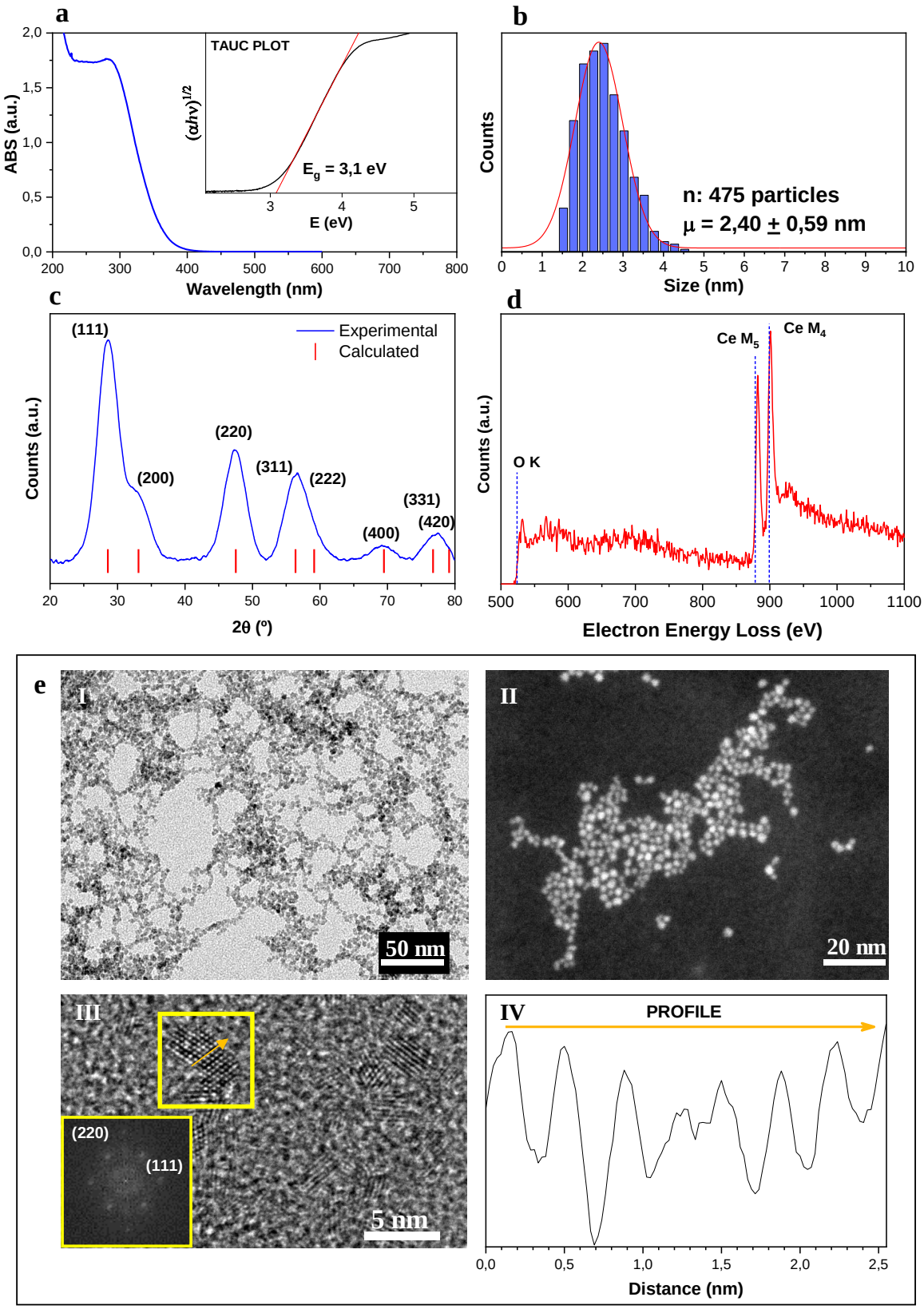

***Figure 2.3**: (a) UV-vis Absorption spectrum and calculated bandgap (inset), (b) Calculated size distribution from STEM image analysis, (c) XRD pattern, (d) Recorded EELS, (e) I. HRTEM image II. STEM image, III. HRTEM image and FFT of selected area, and IV. Profile graph of a CeO_2 NC (extracted from the marked arrow on the selected area).*

The UV-vis absorption spectra (**Figure 2.3.a**) of the synthesised CeO_2 NCs show the characteristic broad band between 200-300 nm corresponding to a $O_{2p} \rightarrow Ce_{4f}$ charge transfer, and 100% transmittance in the rest of the visible spectra, indicating the absence of scattering coming from big aggregates in solution. DLS of the sample shows a unique peak at 3.5 nm when quantifying by number, which indicates that the particles remain monocrystalline with no degree of aggregation whatsoever. The observed bandgap of the NCs was calculated to be 3.1 eV using Tauc's plot method (**Figure 2.3.a**, inset). The final size distribution (**Figure 2.3.b**) was calculated by STEM image analysis ((**Figure 2.3.e, II)** to be 2.4 ± 0.6 nm. XRD pattern (**Figure 2.3.c**) matches the $Fm\bar{3}m$ spatial group permitted reflections for the fluorite structure. The lattice parameter is calculated as 0.542 nm, concordant with the theoretical value (0.541 nm)[4]. The mean crystallite size is calculated to be 2.5 nm through Scherrer's law. The broadness of the peaks is not a bad feature of the XRD pattern but an expected characteristic for small NCs. A crystallite size bigger than 20 nm is typically expected for a defined peak, so they contain enough planes stacked for a good diffraction quality.[32] The EELS spectrum (**Figure 2.3.d**) of the same sample confirms the sample atomic composition. HRTEM imaging (**Figure 2.3.e, I**) shows spherical crystalline particles. Under enough magnification, the electron diffraction can be distinguished (**Figure 2.3.e, III**). Inverse lattice obtained through the FFT (Fast Fourier Transform) of the same (inset) is used to measure interplanar distances: 0.31 nm, identifying the (111) plane and 0.2 nm, corresponding to the (220) plane of the structure. Roughly, each particle stacks around eight layers of the (111) plane, as the grayscale profile of the selected area confirms (**Figure 2.3.e, IV**).

The reaction yield was calculated to be 99,9% by determining Ce concentration by ICP-OES in the purified sample and the supernatant. The purification process consisted of using a centrifugal concentrator device with a 3 kDa Ultracel® cellulose membrane to separate NCs from solubilised species, as the particles are colloidally stable and cannot be separated by a standard centrifugation procedure.

2.2.2 Role of Citrate in the reaction

While it is not a direct participant in the chemical reaction, sodium citrate plays several roles in the crystal formation process: Chelator, buffer, and stabiliser. This section describes the critical aspects of the citrate activity within these roles. When

the reaction is performed without using sodium citrate, the kinetics of the oxidation is faster, and the oxidation is terminated in about one hour after the base addition. However, in the absence of a strong EDL, the synthesised particles irreversibly aggregate onto ~50 nm particles that, when left stored after resuspending in a 10 mM TMAOH solution, coalesce reversibly in bigger nuclei and precipitate. This second aggregation can be reversed by strong stirring or ultrasound treatment, proving that it is caused by a secondary potential well.[33]

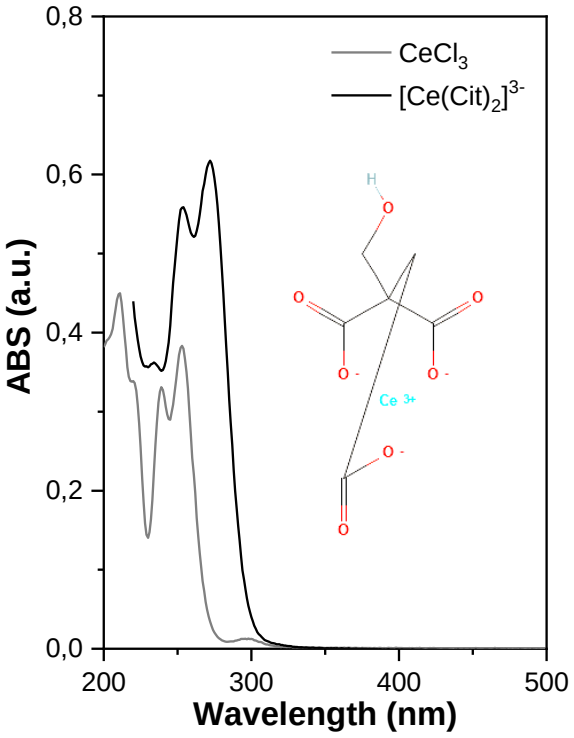

***Figure 2.4**: UV-vis absorption spectra of Ce^{3+} ions in solution before and after citrate complexation.*

The first role of citrate, as a chelator, manifests in the change of the oxidation kinetics. Cerium (III) cations in solution, if not surrounded by any ligands beside water molecules (Hexa-aqueous complex, $[Ce(H_2O)_6]^{3+}$), are susceptible to immediate hydroxylation in the presence of strong bases. However, Ce^{3+} cations form a highly stable complex in the presence of sodium citrate. Acting as a polydentate ligand, sodium citrate "traps" the Ce^{3+} cations present in solution: $[Ce(Cit)_2]^{3-}$. The formation of the coordination complex can be followed through UV-vis spectroscopy, as the position of *d-f* transition peaks in metals is altered by the ligand field's effect (**Figure 2.4**).[34] The kinetics of the ligand exchange between the citrate and the hydroxyl groups at basic pH are slower than the exchange involving the water ligands. Consequently, oxidation is hindered and takes for the same reagent concentrations, up to 8h. This has consequences in the process of "burst nucleation", which will be addressed in the following sections.[35] The formation of this complex before the addition of the base to the reaction mixture is revealed as necessary when changing the order of addition of reagent since variations in the final product size were observed: When adding the Ce (III) salt precursor to a solution containing the corresponding amount of citrate and base, the pH levels varied, and the size dispersion was slightly wider than the typical procedure

(2.8 nm ± 0.8 nm). It indicates that kinetically, citrate complexation is favoured, but thermodynamically, the oxidation to CeO_2 is the most stable product. On the other hand, if the citrate is the last of the three reagents added, even if the addition interval is too short for the crystals to have appeared in solution, the resultant particles are colloidally stable but discretely aggregated crystals of 10 nm in size, measured by DLS.

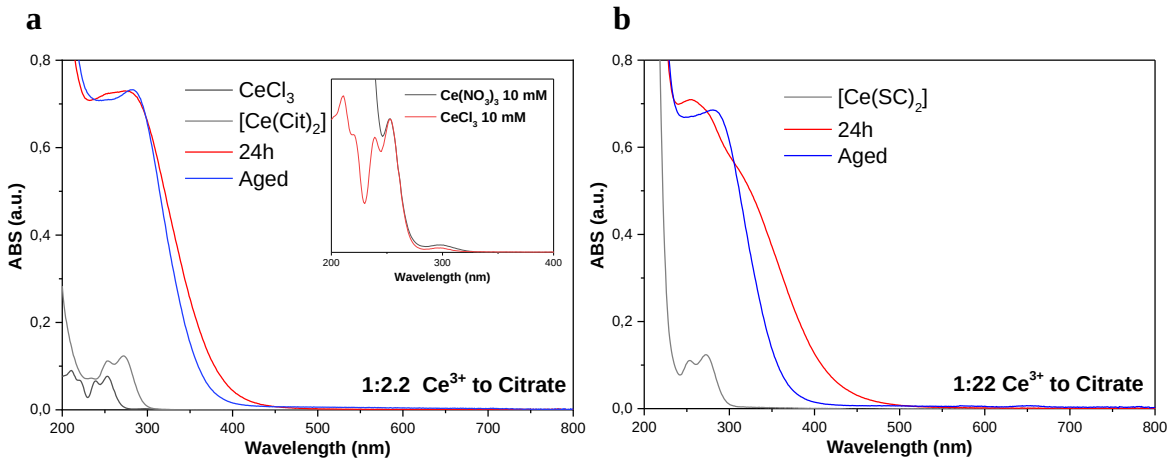

Figure 2.5: *UV-vis absorption spectra of (a) Time evolution at standard reagent concentration. Final DLS size 3.5 nm. Inset: Comparation between different precursors. (b) Time evolution and final DLS size at ten times more concentration of citrate. Final DLS size 2.9 nm.*

As the conjugate base of a weak acid, citrate also acts as a buffer, preventing the pH of the colloid from falling below 7 during synthesis, and it indirectly provides the necessary hydroxyl groups that, due to the sub-stoichiometric amount of base injected, are not directly supplied to the reaction mixture. Citrate is also a well-known antioxidant that may play a role in hindering the redox processes around the cerium cations. If the typical CeO_2 NC synthesis is performed in a sealed beaker containing an almost non-existing amount of air in the head space, the oxidation process gets hindered, and a pale violet or pinkish colour appears in the solution. This colour is attributed to a very high density of oxygen vacancies within the CeO_2 solids, and it disappears in a matter of seconds when the beaker is opened to air and the solution is oxygenised back. The concentration of solubilised oxygen in water is proportional to atmospheric O_2 partial pressure, taking values around the 10^{-3} M range, in the same order of magnitude as our synthetic concentrations. Enough oxygen should be present to carry out the oxidation, therefore. Under these circumstances, it is then assumed that an excess of oxygen of several orders of magnitude is required for the reaction to occur, overcoming the antioxidant properties of citrate. In a different experiment it was also observed that upon a

significant excess of sodium citrate (1:22), ten times more than in the standard process, oxidation kinetics are even slower, and particle size measured by DLS is slightly smaller, in agreement with the findings of Masui et al. about the role of stabiliser in particle size (**Figure 2.5**).[27] When performing the synthesis in anaerobic conditions using $Ce(NO_3)_3$ as a precursor, the oxidation is expected to go, to some extent, through the nitrate counterions of the precursor under reflux conditions. It was observed, however, that no change could be observed during the first two hours of the process. After that time, the presence of white solids observable to the naked eye denoted the precipitation of $Ce(OH)_3$. Upon air exposure, the solution attains the characteristic yellowish colour of the CeO_2 colloids. The presence of citrate in anaerobic conditions may have prevented the nitrate from acting as an oxidiser with the Ce^{3+} and, instead, getting itself oxidated to dicarboxyacetone (DCA). However, no other experiments to confirm this hypothesis were performed.

Last, the reason behind the high colloidal stability of the CeO_2 NCs is the colloid's EDL, which avoids even the smallest percentage of aggregation. The well-known mechanism of the double electrical layer formed by the bulky cation and anion species TMA^+ and Cit^{3-} around the surface gives rise to a strong electrostatic barrier preventing close interaction between particles. It can be explained through the Einstein-Smoluchowski equation for the diffusion of charged particles (eq. 2.1) and the previously mentioned Debye's length (eq. 1.8 in Chapter I). Equation 2.2 shows the relationship between the thickness of the EDL and the charge diffusion coefficient.[36]

$$D = \frac{\mu_q k_B T}{q} \tag{2.1}$$

$$\kappa^{-1} \approx \sqrt{\frac{\varepsilon D}{K_m}} \tag{2.2}$$

In which D is the diffusion coefficient, q is the electrical charge of the particle, K_m is the medium's conductivity, and μ_q is the electrical mobility of the charged species, which is inversely proportional to its mass. Higher ion mass implies lower mobility, resulting in slower diffusions and narrower EDLs.

2.2.3 Apparent deviations from LaMer-Dinegar model

From the perspective of a particle, NC synthesis in solution consists of three stages: crystal monomer accumulation, nucleation and growth. For adequate size dispersion, it is necessary that i) monomer accumulation is terminated when the nucleation stage starts and ii) the duration of the nucleation process should be as short as possible for all the nuclei to enter the growth regime as close to simultaneously as possible. These quality requirements for the crystal formation processes are typically addressed as "Burst nucleation". For further details on the theory of crystal formation (model, mechanisms, and techniques), see Chapter I, section 1.2.1.

However, from the description provided in this Chapter, the synthesis of CeO_2 NCs apparently stems a set of severe deviations to this theory. The experimental parameter often employed to govern nucleation is temperature, as generally it is thermodynamically a high energy-demanding process, and growth does not pertain to such energetic barriers. The *hot injection* or *heating-up* synthetic strategies exploit temperature to enhance fast nucleation and prevent secondary nucleation after the growth stage has started. Our case, however, consists of a prolonged process at room temperature, motivated by the chemical potential, in which no thermal treatment is employed until crystal formation is finished. In fact, it was previously pointed out how chelation of the Ce^{3+} cations in solutions with citrate as polydentate ligand is a necessary step of the synthesis and how it retards the kinetics of oxidation. Consequently, nucleation and growth of the NCs coexist with the reaction of oxidation that generates the crystal monomer. When the process is terminated, it would then be expected to have a very polydisperse set of NCs in the solution. Even so, the employed synthetic protocol proves to be very robust in terms of mean size and monodispersity. Sequential addition of any metal precursor or the precipitating agent does not lead to a seeded-growth process but to new nucleation of NCs, increasing the number of NPs per volume but maintaining size distribution constant. Far from a model deviation, this is a common behaviour for oxide crystal formation, as indicated in this chapter's introduction. The diffusion-limited growth stage is dominated by a powerful size-focusing effect, where the growth rate falls exponentially with particle size.[1] Growth of oxide particles beyond the "focused" size is expected to happen through aggregation into polycrystalline particles during an ageing stage. However, the strong effect of EDL prevents it from happening.

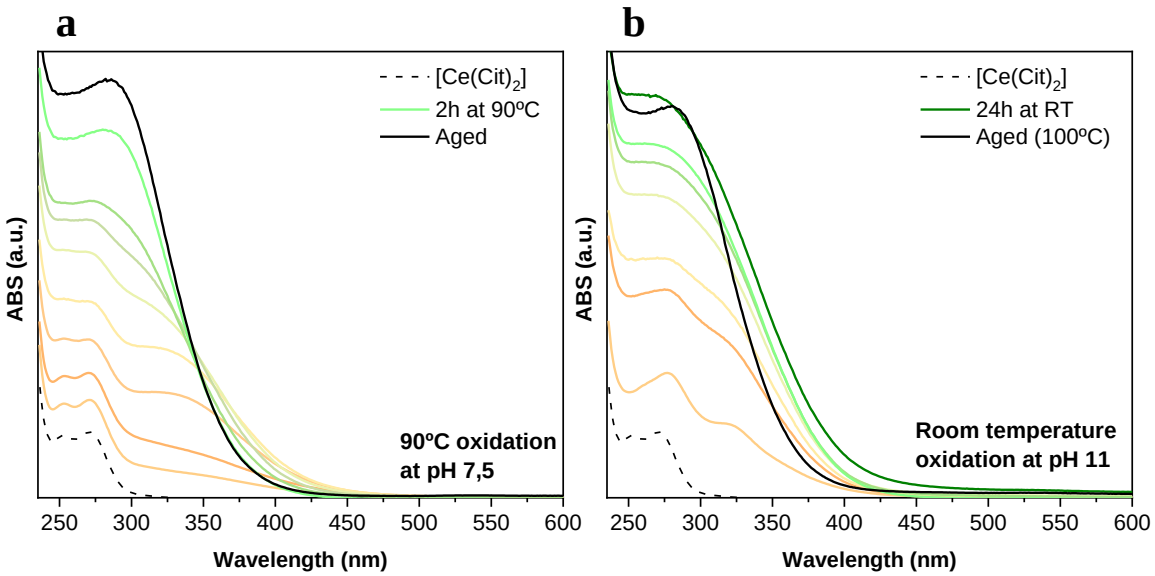

***Figure 2.6**: Time evolution of the UV-vis absorption spectra of oxidation of Ce^{3+} in a citrate solution (a) in absence of basic reagent at 90ºC and (b) at room temperature in standard synthesis conditions.*

Thermal treatments during the oxidation and precipitation stage of the CeO_2 NC synthesis have been tested for improving the kinetics of the procedure: Both *heating-up* (mixing of all the reagents at room temperature and then heating the mixture to 100ºC into reflux conditions) and *hot injection* (Heat the $[Ce(Cit)_2]^{3-}$ complex until reflux conditions and then inject the base concentrated in a small volume) approaches. During the *hot injection* test a particularity was observed: at high temperatures (90ºC), hydrolysis of the water molecules at the buffered pH of a sodium citrate solution provides enough hydroxyl groups for the reaction to be carried out in similar conditions as the room temperature process when the base is injected (see **Figure 2.6**). However, every synthesis carried out under temperatures higher than 90ºC led to a faster reaction but resulted in the partial aggregation of the nuclei into 10-20 nm polycrystalline particles.

2.2.4 Nanocrystal curing: Ageing stage

The changes CeO_2 NCs undergo during the ageing stage are thermodynamically spontaneous and lead to the chemically stable formulation of the material. Its primary manifestation is the narrowing of the charge transfer peak in the near UV range, that also reflects in the Tauc plot. At standard pressure and temperature conditions, the crystals take up to two months to finish this process. It can be accelerated by physical methods (i.e., rising temperature to reflux conditions for a certain amount of time) or chemical ones (adding an oxidiser such as H_2O_2 to the mixture after the precipitation

stage). To provide some insights into the nature of the transformations occurring at this stage, deep characterisation of the NCs in the earliest stage possible of the process and after its termination is conducted. Highlights of this characterization are summarised in **Figure 2.7**.

The UV-vis spectra before and after the ageing (**Figure 2.7a**) show how during this stage, the main peak shifted its position to higher wavelengths and narrowed its width, changing the slope of the curve. The peak is positioned at higher energies than the commercial CeO_2 powder's peak, which also matches the position of the commercial hydroxide. This peak displacement may have an origin in the oxygen defects and, therefore, the size of the crystals: Bigger particles peak closer to the reference than the as-synthesized NCs. As the Tauc plot for the allowed indirect transition (**Figure 2.7b**) confirms, results indicate an apparent change in the material bandgap from 2.91 to 3.15 eV. However, the difference between both plots (dotted line on the same graph) evidences a heavy asymmetry in the distribution of said changes. Urbach's parameter calculation (1.15 eV and 1.00 eV before and after the ageing stage, respectively) indicates changes in the "degree of order" of the structure due to the density of defects (i.e. oxygen vacancies, majorly). As mentioned in section 1.3.3 (Chapter I), the value of Urbach's parameter may impact on the linear range of Tauc's plot. Tauc's plot works under the assumption that the absorption coefficient α is independent of the incident photon's energy. For this condition to be met, variation of α with photon energy must be negligible. It happens only if the exponential term Urbach relation is close to 0. Higher values of the Urbach energy parameter ensure that this condition is met. For lower parameter values, α's variation with incident photon energy may vary with bandgap calculations, and obtained values are not to be trusted.[37] Even so, the dimension of the parameter for the case of CeO_2 NCs is not enough to considerably impact the absorption coefficient.

HRTEM image analysis shows no difference between the NCs before and after ageing. The DLS size determination, however, shows a slight increase (from 2.9 to 3.5 nm) in the mean size of the particles but no changes in the number of NPs per volume. Since the difference between both characterization techniques is the definition of the limit of the particle, we assume that observed changes come from the region of the hydrodynamic radius of the particle not observable by TEM: the layer of water molecules bonded to the particle by electrostatic interactions.

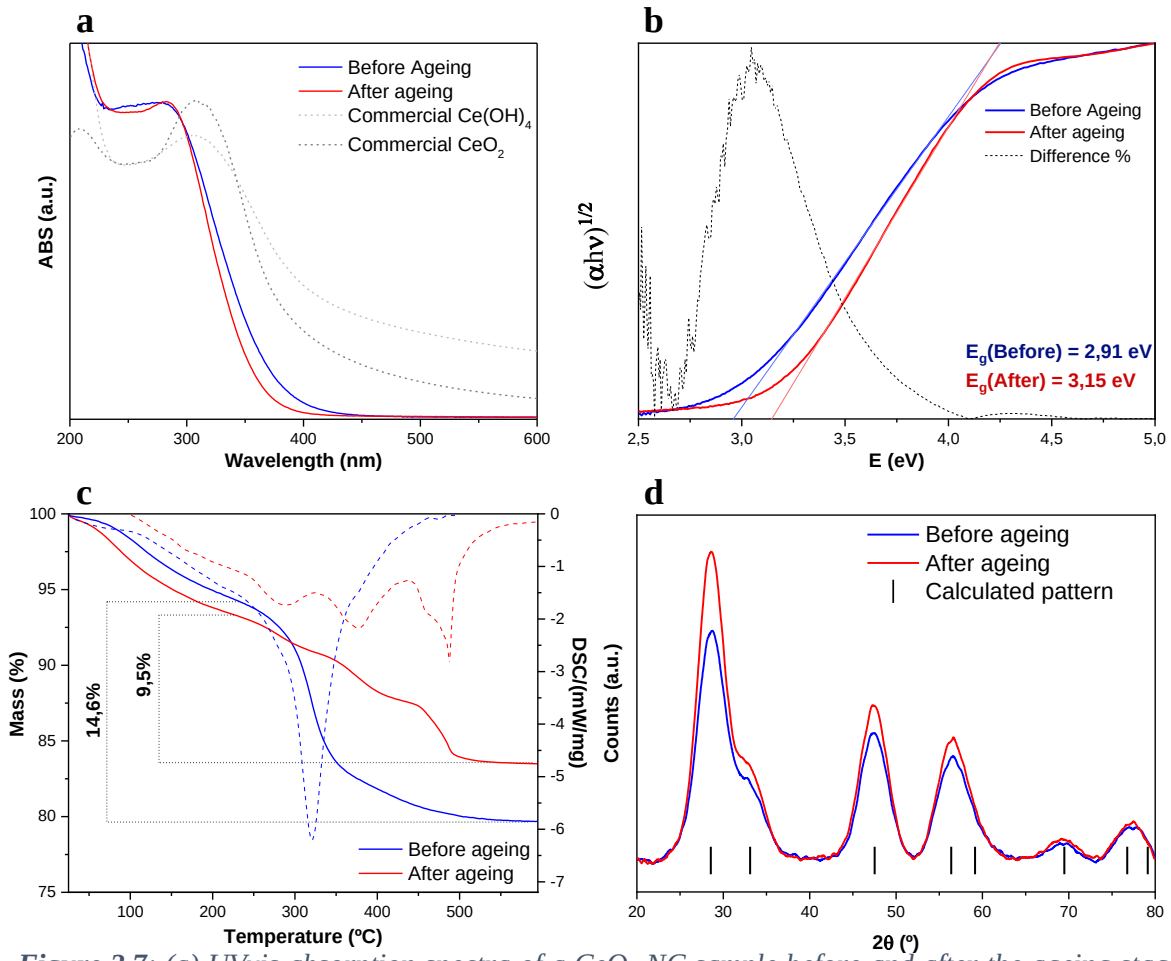

***Figure 2.7**: (a) UVvis absorption spectra of a CeO_2 NC sample before and after the ageing stage compared to the ones from commercial samples. (b) Tauc plot and calculated indirect bandgap from the absorption data. (c) Thermogravimetric analysis before and after the ageing stage. Dotted lines: Differential Scanning calorimetry (DSC). (d) comparison between XRD pattern before and after ageing stage.*

Thermogravimetric Analysis (TGA) coupled with Differential Scanning Calorimetry (DSC) (**Figure 2.7c**) of particles before their ageing shows a major loss of structural water (14.6% in total sample weight) at 322ºC. For already aged CeO_2 NCs, the weight of structural water was 9.5%, and it is lost sequentially in three steps at 287ºC, 378ºC and 487ºC. It indicates not only a lower content of structural water in the NCs after the ageing stage but also a higher energy barrier for its release, probably emerging from a more compact crystal structure.

XRD of the crystalline structure before and after this stage (**Figure 2.7d**) do not show significant differences: Same peak position and similar relative intensities between peaks. The mean crystallite size calculated for the NCs before ageing is 2.44 nm and after ageing, 2.50 nm, and the lattice parameter for both cases is 0.542 nm. It could be expected that interstitial water molecules would broaden the peaks. Nonetheless,

it is not noticeable, implying water content is not affecting the crystalline structure, and it could be mostly understood as a high density of surface hydroxyl terminal groups within the structure.

It can be concluded that the as-precipitated particles, before enduring the ageing stage, resemble the structure of an oxygen vacancy-rich cerium (IV) oxide of a highly hydroxylated surface. During this stage, they slowly dehydrate and partially fill these defects until reaching the CeO_{2-x} structure holding the stable oxygen vacancies for the atmospheric conditions of the laboratory.

2.3 PERSPECTIVES

Maximising the surface-to-volume ratio maximises the density of active sites per mass of CeO_2. However, the typical challenge of nanomaterial synthesis runs in the opposite direction: Achieving the controlled growth of nanocrystals to a desired size. For metals such as gold or silver, the pathway towards controlled growth goes by the sequential injection of precursor over previously synthesised nanocrystals under mild conditions to prevent new nucleation in a seeded-growth fashion.[38,39] For oxides such as CeO_2, growth besides the thermodynamically stable size "focused" by the monocrystal growth mechanism comes in the form of aggregation.[1] A very interesting path to follow would involve developing strategies towards the use of the described 2.5 nm CeO_2 NCs as building blocks for more complex structures, which in the end translates to the use of synthesised NCs as reagents themselves, a known goal for the field of nanomaterials.

As an example of the possibility of engineering complex structures using the synthesised NCs as building blocks, a few strategies for producing different kinds of aggregate structures are described. A few synthetic conditions leading to the obtention of stable aggregates of less than 100 nm in size have been mentioned in this chapter, and more examples can be found in **Table 9.1** at Annex B. Another exciting possibility for aggregation is the self-assembly into anisotropic shapes. Favouring the expression of some facets over others through shape anisotropy can have a heavy impact on the catalytic performance of a nanomaterial. For example, the redox processes carried out by CeO_2 are favoured in the (111) facet, as it is where the most oxygen vacancies are held.[5] Some examples of anisotropic self-assembly of CeO_2 NCs into nanorods, nanowires, nanocubes and other shapes can be found in **Table 9.3** at Annex B.

As a synthetic exercise, it has been proved the capacity of this CeO_2 system to self-assemble into different shapes under suitable conditions. The aggregate structure is dependent on the probability of collision between particles, which is dominated by Brownian motion on the long-range, and the sticking coefficient, the probability that the collision results in aggregation. A strategy to promote aggregation, therefore, is increasing temperature to promote Brownian motion and lower EDL energetic barriers.

Under reflux conditions, keeping the pH close to neutral will neutralise the ionisation of surface groups, lowering the value of the surface charge. It will lead to a lower sticking coefficient, as the mean number of collisions required for aggregation is higher. In these conditions, aggregation through some facets will be favoured over others due to chemical differences between them that, in different pH conditions, are negligible. Similar to the results of Yu Taekyung et al.,[40] 2D nanosheets of CeO_2 can be obtained by heating to reflux a solution of $CeCl_3$ and sodium citrate in a 1:2 molar ratio avoiding the addition of any strong base that may raise the pH over 8 for enough time for the nanocrystals to precipitate and recrystallise into the 2D shape (**Figure 2.8**).

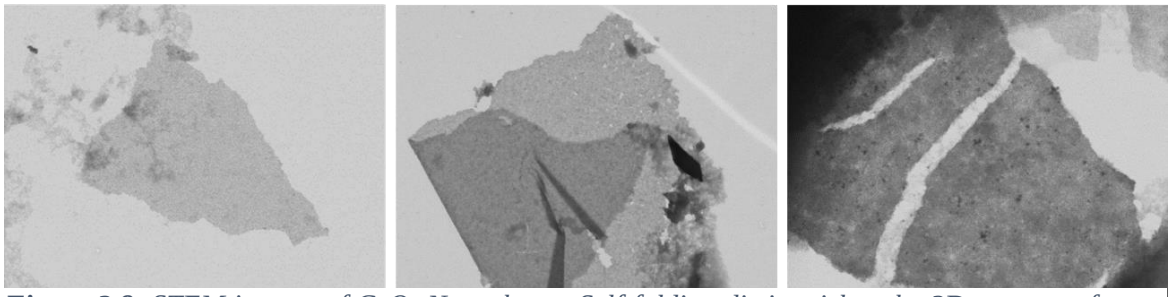

Figure 2.8: *STEM images of CeO_2 Nanosheets. Self-folding distinguishes the 2D structure from a particle monolayer.*

On the other hand, by enhancing aggregation with the temperature at a high pH, a mixture of $Ce(OH)_3$ and CeO_2 will precipitate and quickly aggregate in a condensed spherical fashion where the internal part of the aggregate is composed of $Ce(OH)_3$ hydroxide and CeO_2 rich in defects, of higher solubility than the outer part of the aggregate, that will contain a higher proportion of curated CeO_2. Supposing that the mixture is left under reflux temperature conditions long enough, dissolution and recrystallisation processes may lead to the formation of template-free hollow CeO_2 spheres, such as the ones pictured in **Figure 2.9**.

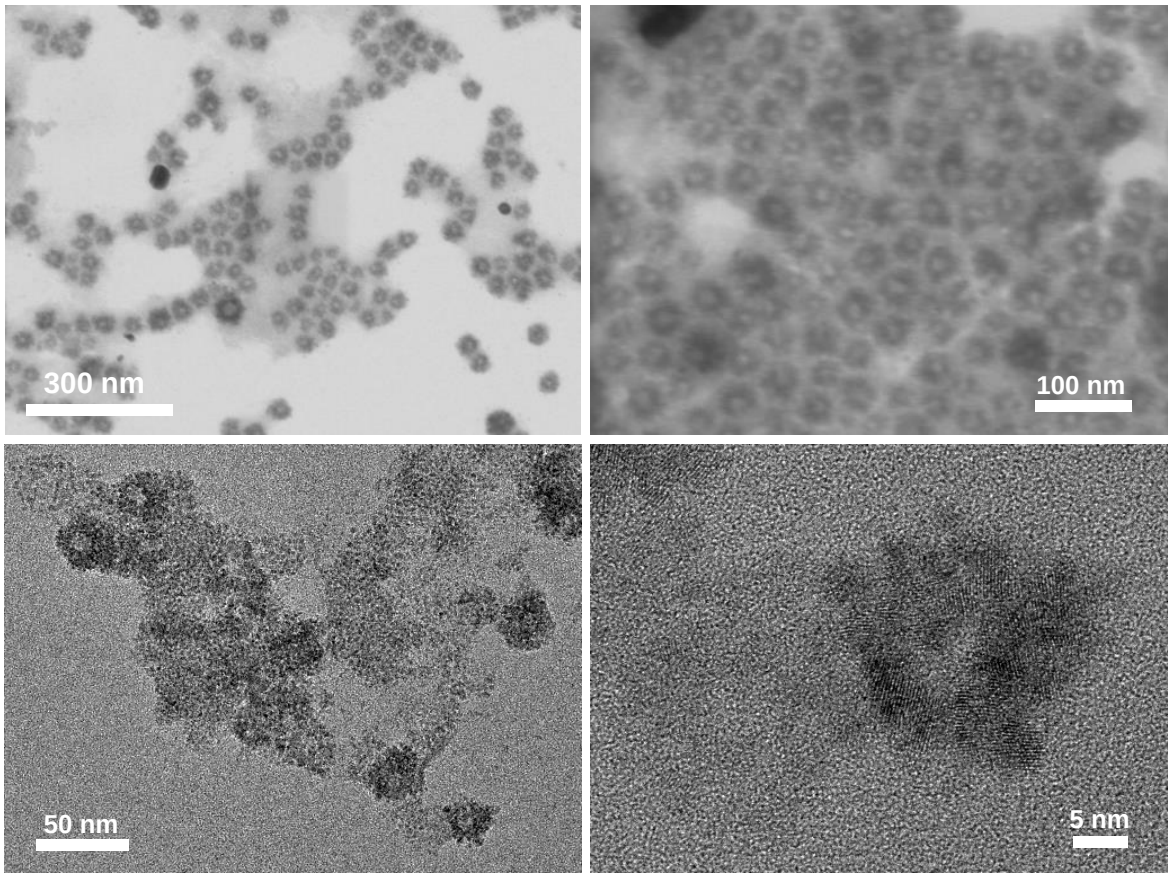

Figure 2.9: *STEM (top) and HRTEM (bottom) images of hollow CeO_2 nanospheres.*

2.4 REFERENCES

1. Oskam, G. Metal oxide nanoparticles: synthesis, characterization and application. *J Sol-Gel Sci Techn* 37, 161–164 (2006).

2. Zhang, W. Nanoparticle Aggregation: Principles and Modeling. in *Nanomaterial: Impacts on Cell Biology and Medicine* (eds. Capco, D. G. & Chen, Y.) 19–43 (Springer Netherlands, 2014). doi:10.1007/978-94-017-8739-0_2.

3. Kotani, A., Jo, T. & Parlebas, J. C. Many-body effects in core-level spectroscopy of rare-earth compounds. *http://dx.doi.org/10.1080/00018738800101359* 37, 37–85 (2006).

4. Artini, C. *et al.* Structural Features of Sm- and Gd-Doped Ceria Studied by Synchrotron X-ray Diffraction and μ-Raman Spectroscopy. *Inorg Chem* 54, 4126–4137 (2015).

5. Capdevila-Cortada, M. & López, N. Entropic contributions enhance polarity compensation for CeO_2 (100) surfaces. *Nat Mater* 16, 328–334 (2017).

6. Schelter, E. J. Cerium under the lens. *Nature Chemistry 2013 5:4* 5, 348–348 (2013).

7. Primo, A., Marino, T., Corma, A., Molinari, R. & García, H. Efficient Visible-Light Photocatalytic Water Splitting by Minute Amounts of Gold Supported on Nanoparticulate CeO_2 Obtained by a Biopolymer Templating Method. *J Am Chem Soc* 133, 6930–6933 (2011).

8. Yue, L. & Zhang, X. M. Structural characterization and photocatalytic behaviors of doped CeO_2 nanoparticles. *J Alloys Compd* 475, 702–705 (2009).

9. Montini, T., Melchionna, M., Monai, M. & Fornasiero, P. Fundamentals and Catalytic Applications of CeO_2-Based Materials. *Chem Rev* 116, 5987–6041 (2016).

10. Trovarelli, A. Catalytic properties of ceria and CeO_2-Containing materials. *Catal Rev Sci Eng* 38, 439–520 (1996).

11. Banavar, S., Deshpande, A., Sur, S. & Andreescu, S. Ceria nanoparticle theranostics: harnessing antioxidant properties in biomedicine and beyond. *Journal of Physics: Materials* 4, 042003 (2021).

12. Chen, J., Patil, S., Seal, S. & McGinnis, J. F. Rare earth nanoparticles prevent retinal degeneration induced by intracellular peroxides. *Nature Nanotechnology 2006 1:2* 1, 142–150 (2006).

13. Niu, J., Azfer, A., Rogers, L. M., Wang, X. & Kolattukudy, P. E. Cardioprotective effects of cerium oxide nanoparticles in a transgenic murine model of cardiomyopathy. *Cardiovasc Res* 73, 549–559 (2007).

14. Shcherbakov, A. B., Zholobak, N. M., Spivak, N. Y. & Ivanov, V. K. Advances and prospects of using nanocrystalline ceria in cancer theranostics. *Russian Journal of Inorganic Chemistry 2014 59:13* 59, 1556–1575 (2014).

15. Jin Kwon, H. *et al.* Mitochondria-Targeting Ceria Nanoparticles as Antioxidants for Alzheimer's Disease. *ACS Nano* 10, 2860–2870 (2016).

16. Tsunekawa, S., Sivamohan, R., Ito, S., Kasuya, A. & Fukuda, T. Structural study on monosize CeO_{2-x} nano-particles. *Nanostructured Materials* 11, 141–147 (1999).

17. Khan, M. M. *et al.* Defect-induced band gap narrowed CeO_2 nanostructures for visible light activities. *Ind Eng Chem Res* 53, 9754–9763 (2014).

18. Sharifi, S. *et al.* Toxicity of nanomaterials. *Chem Soc Rev* 41, 2323–2343 (2012).

19. Chang, H. Y. & Chen, H. I. Morphological evolution for CeO_2 nanoparticles synthesized by precipitation technique. *J Cryst Growth* 283, 457–468 (2005).

20. L. Heckman, K. *et al.* Custom Cerium Oxide Nanoparticles Protect against a Free Radical Mediated Autoimmune Degenerative Disease in the Brain. *ACS Nano* 7, 10582–10596 (2013).

21. Estevez, A. Y. *et al.* Antioxidant Enzyme-Mimetic Activity and Neuroprotective Effects of Cerium Oxide Nanoparticles Stabilized with Various Ratios of Citric Acid and EDTA. *Biomolecules 2019, Vol. 9, Page 562* 9, 562 (2019).

22. Reed, K. *et al.* Exploring the properties and applications of nanoceria: is there still plenty of room at the bottom? *Environ Sci Nano* 1, 390–405 (2014).

23. Yokel, R. A. *et al.* The yin: an adverse health perspective of nanoceria: uptake, distribution, accumulation, and mechanisms of its toxicity. *Environ Sci Nano* 1, 406–428 (2014).

24. Yokel, R. A. *et al.* Biodistribution and biopersistence of ceria engineered nanomaterials: size dependence. *Nanomedicine* 9, 398–407 (2013).

25. Yokel, R. A. *et al.* The preparation temperature influences the physicochemical nature and activity of nanoceria. *Beilstein Journal of Nanotechnology 12:43* 12, 525–540 (2021).

26. Hancock, M. L. *et al.* The characterization of purified citrate-coated cerium oxide nanoparticles prepared via hydrothermal synthesis. *Appl Surf Sci* 535, 147681 (2021).

27. Masui, T. *et al.* Synthesis of cerium oxide nanoparticles by hydrothermal crystallization with citric acid. *Journal of Materials Science Letters 2002 21:6* 21, 489–491 (2002).

28. Ivanov, V. K., Usatenko, A. v. & Shcherbakov, A. B. Antioxidant activity of nanocrystalline ceria to anthocyanins. *Russian Journal of Inorganic Chemistry 2009 54:10* 54, 1522–1527 (2009).

29. Malyukin, Y. *et al.* Hydrogen peroxide sensing using Ce^{3+} luminescence of cerium oxide (CeO_{2-x}) nanoparticles. *Opt Mater (Amst)* 85, 303–307 (2018).

30. Pfaller, T., Puntes, V., Casals, E., Duschl, A. & Oostingh, G. J. In vitro investigation of immunomodulatory effects caused by engineered inorganic nanoparticles – the impact of experimental design and cell choice. *http://dx.doi.org/10.1080/17435390802546071* 3, 46–59 (2009).

31. Oostingh, G. J. *et al.* Problems and challenges in the development and validation of human cell-based assays to determine nanoparticle-induced immunomodulatory effects. *Part Fibre Toxicol* 8, 1–21 (2011).

32. Holder, C. F. & E. Schaak, R. Tutorial on Powder X-ray Diffraction for Characterizing Nanoscale Materials. *ACS Nano* 13, 7359–7365 (2019).

33. Espada-Santacreu, A. Optimization of a Synthetic Route for CeO_2 Nanoparticles. (Universitat Autònoma de Barcelona, 2022).

34. Miessler, G. L. & Tarr, D. A. Coordination Chemistry III: Electronic Spectra. in *Inorganic Chemistry* 379–411 (Upper Saddle River, N.J.: Pearson Education, 2004).

35. Leffler, V., Ehlert, S., Förster, B., Dulle, M. & Förster, S. Nanoparticle Heat-Up Synthesis: In Situ X-ray Diffraction and Extension from Classical to Nonclassical Nucleation and Growth Theory. *ACS Nano* 15, 840–856 (2021).

36. Dukhin, A. S. & Goetz, P. J. Fundamentals of Interface and Colloid Science. *Characterization of Liquids, Dispersions, Emulsions, and Porous Materials Using Ultrasound* 19–83 (2017) doi:10.1016/B978-0-444-63908-0.00002-8.

37. Feng, Y., Lin, S., Huang, S., Shrestha, S. & Conibeer, G. Can Tauc plot extrapolation be used for direct-band-gap semiconductor nanocrystals? *J Appl Phys* 117, (2015).

38. G. Bastús, N., Comenge, J. & Puntes, V. Kinetically Controlled Seeded Growth Synthesis of Citrate-Stabilized Gold Nanoparticles of up to 200 nm: Size Focusing versus Ostwald Ripening. *Langmuir* 27, 11098–11105 (2011).

39. G. Bastús, N., Merkoçi, F., Piella, J. & Puntes, V. Synthesis of Highly Monodisperse Citrate-Stabilized Silver Nanoparticles of up to 200 nm: Kinetic Control and Catalytic Properties. *Chemistry of Materials* 26, 2836–2846 (2014).

40. Yu, T., Lim, B. & Xia, Y. Aqueous-Phase Synthesis of Single-Crystal Ceria Nanosheets. *Angewandte Chemie International Edition* 49, 4484–4487 (2010).

41. Momma, K. & Izumi, F. VESTA 3 for three-dimensional visualization of crystal, volumetric and morphology data. *urn:issn:0021-8898* 44, 1272–1276 (2011).

42. Channei, D. *et al.* Aqueous and surface chemistries of photocatalytic Fe-doped CeO_2 nanoparticles. *Catalysts* 7, (2017).

CHAPTER III

LANTHANIDE-DOPED CeO_2 NANOCRYSTALS

CHAPTER III

LANTHANIDE-DOPED CeO_2 NANOCRYSTALS

3.1 INTRODUCTION

It is mentioned in section 1.5 of Chapter I that doping is one of the strategies employed to improve the catalytic and photocatalytic activity of a pure inorganic compound. Doping semiconductor materials with the appropriate substance can enhance their performance in different ways. Using metal ions as dopants can extend charge-carrier lifetimes, trapping electrons or holes and preventing recombination. It has also been reported that transition metal and non-metal doping can sensitise the semiconductor absorption spectrum, expanding it to the visible light region, as the electronic structure is altered by the presence of atoms of different nature due to the appearance of intermediate electronic levels, which narrow the bandgap.[1]

3.1.1 State of the Art

The main objective of this strategy is to improve the catalytic efficiencies of CeO_2 catalysts. Non-metal dopants (Nitrogen, phosphate, sulfur, etc.) cause a broadening of the absorption band that extends its reach to the visible light range, consequently reducing the bandgap.[2] Metal doping plays a role in introducing oxygen vacancies within the oxide structure, narrowing the bandgap and increasing the reducibility of the material towards redox reactions. It has been proved how the induction of oxygen vacancy defects into nanometric CeO_2 sensitises the material towards visible light photocatalysis.[3] In addition, the CeO_2 structure has been able to support high concentrations of metal doping (up to 30% even).[4] Some examples of metal doping include noble metal inclusion (Au, Ag) or divalent noble metal ions (Cu^{2+}, Pt^{2+}, Pd^{2+}, etc.)[5] for increasing oxygen vacancy density.[6] Another exciting feature of transition metal doping is the reduced charge recombination processes in contrast with the

undoped material.[7] Lanthanide doping has also been extensively reported. Trivalent cations such as Eu^{3+}, Sm^{3+} or Tb^{3+} induced structural defects that caused a shift to higher wavelengths of the emission band of the material according to Wang et al.[8] Gupta et al.,[9] however, reported how lanthanide doping in CeO_2 (La^{3+} cations) had little to none effect in the improvement of the oxygen storage capacity of undoped CeO_2, as the metal-oxygen bond distance is almost unaltered by the presence of a lanthanide, in contrast with the higher distances in the case of transition metals. Lanthanide doping, however, remains relevant not for its performance in comparison with transition metal doping but for the exciting properties that arise from it, such as photon upconversion.

Photon upconversion is the principle behind the design of nanocrystalline domains able to generate visible or UV light from NIR absorption. It is the anti-Stokes emission of high energy luminescence through the sequential absorption of low energy photons. Inorganic materials displaying this property are usually composed of a crystalline matrix doped with trivalent lanthanide cations. Low phonon energy and short interdopant distances are required for inorganic nanocrystals to act as host matrix efficiently. Several oxides and fluorides of different crystalline structures are reported to work as an upconversion matrix, the most relevant being $NaYF_4$ on its hexagonal phase.[10] It is still a synthetic problem, however, to obtain nanosized crystals of hexagonal $NaYF_4$ as, due to surface tension, stability shifts towards the cubic phase at the nanoscale.

For the multiple-step excitation to happen, it is required the existence of intermediate electronic states within the material structure. The $4f^n$ electronic configuration of trivalent lanthanide ions is split by electronic repulsion and spin-orbit coupling, supplying the material with a rich energy-level pattern. The most common upconversion mechanism reported is the combination of the activity of two species that, by energy transfer, carry the sequential absorption and posterior emission. Yb^{3+} is the most common sensitiser species employed, absorbing in the NIR region and providing low energy excitations. The activator species (Er^{3+}, Tm^{3+} or Gd^{3+} are the most common) receive excited electrons and emit higher energy photons for their relaxation.[11,12]

3.1.2 Motivation

The possibility to harvest NIR photons into visible or even UV ones makes upconversion a promising future for several fields, both in photocatalysis[13] and biomedicine in particular, since the composition of our organism is transparent to NIR radiation but not to UV one.[12,14] With the current technology of nanomaterial synthesis, it is expected to control and tune the wavelength of emission of nanocrystals to achieve broad NIR-to-UV upconversion. Regardless, synthesising small nanosized crystals showing strong upconversion luminescence has been challenging. Despite the scarcity of literature on this topic, there can be found reported cases of upconverting nanocrystals conformed by a CeO_2 matrix doped with Yb^{3+} and Er^{3+}.[15,16] Reproducing these properties within the CeO_2 nanocrystals formulated in this work brings the possibility of enhanced catalytic activity and expanded functionality of the material.

3.2 RESULTS

To test the loading capacity of CeO_2, five samples containing different dopant concentrations (nominally, from 5% to 25%) were synthesised and characterised: 5% Er^{3+}, 10% Yb^{3+}, 20% Yb^{3+} and combinations between Er^{3+} and the two loads of Yb^{3+}.

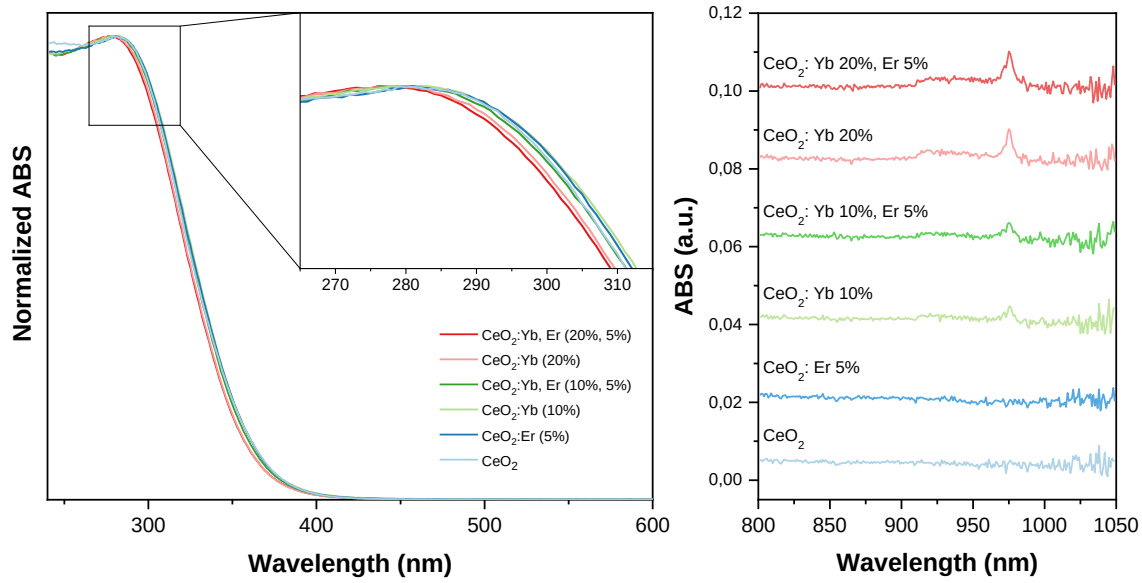

***Figure 3.1**: UV-vis absorption spectra (left) and NIR absorption spectra (right) of CeO_2 doped samples. Undoped CeO_2 included as a reference.*

The UV-vis spectra of the samples, **Figure 3.1 (left)**, show the characteristic CeO_2 band around 280 nm for all the samples. Minor differences in peak position and bandwidth are summarised in **Table 3.1**, along with the doping quantification calculated by EDX and ICP-OES. It should be taken into account that EDX quantification pertains higher degree of uncertainties due to sample preparation and instrumental artifacts, and the most robust quantification comes from the ICP-OES determination. The NIR absorbance of the same samples, **Figure 3.1 (right)**, reveals the small band of Er^{3+} and Yb^{3+} at 980 nm, identified by comparison with the precursor's spectra (**Figure 9.1** at Annex C).

HAADF-STEM imaging, calculated size distribution and Tauc's plot for bandgap calculation of each sample can be found in **Figure 9.2** at Annex C. EDX spectra of each sample in **Figure 9.3** at Annex C. The effective loading of lanthanide ions as dopants within the CeO_2 structure has been achieved, holding yields around 95%-100% concerning the expected values. However, the band structure of the material does not show significant changes even to larger amounts of doping, as UV spectra and bandgap values illustrate.

Sample	UV peak	Bandgap	Doping % (EDX)	Doping % (ICP-OES)
CeO_2	279 nm	3,10 eV	-	-
CeO_2:Er (5%)	281 nm	3,10 eV	6% Er^{3+}	4.87% Er^{3+}
CeO_2:Yb (10%)	281,5 nm	3,12 eV	11% Yb^{3+}	9,77% Yb^{3+}
CeO_2:Yb, Er (10%, 5%)	279 nm	3,12 eV	7.8% Yb^{3+} 2.2% Er^{3+}	9.56% Yb^{3+} 4.74% Er^{3+}
CeO_2:Yb (20%)	278 nm	3,14 eV	21.2% Yb^{3+}	19.47% Yb^{3+}
CeO_2:Yb, Er (20%, 5%)	277 nm	3,12 eV	21.1% Yb^{3+} 3.6% Er^{3+}	19.68% Yb^{3+} 4.68% Er^{3+}

***Table 3.1**: UV peak position, bandgap, and doping quantification both by EDX and ICP-OES (uncertainty <0.01%) for the CeO_2 and doped CeO_2 samples.*

The XRD of the samples (**Figure 3.2**) is analysed to determine the impact of doping in the crystalline structure. Results are summarised in **Table 3.2**. Doping does not visibly alter peak position. Since Er and Yb atoms are smaller than Ce ones due to the lanthanide contraction effect, a distortion of unit cell parameters is expected. Mean Scherrer's size and STEM measured size are very similar to the undoped particles. Still, the lattice parameter seems to be reduced compared to the value of the undoped particles (0.542 nm) and the literature's value (0.5410 nm).[17] This contraction of the lattice parameter is most notable in the (111) and (220) planes, in opposition to the (200) plane that remains unaltered. This feature could mean that lanthanide ions occupy positions within these planes.

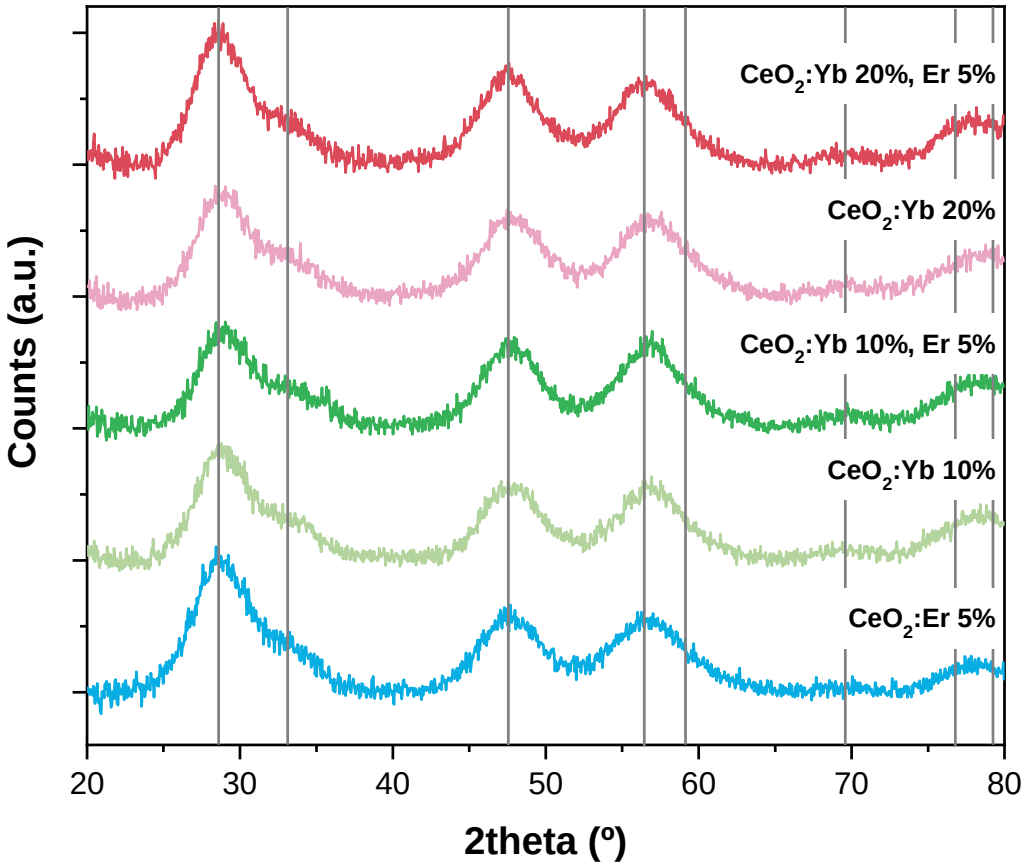

***Figure 3.2**: XRD patterns of doped CeO_2 NCs. Gray lines: CeO_2 peak positions.*

To determine photon upconversion capacity of the doped NCs, a setup for recording the emission spectra of the particles at 90º position from the incident beam using a CCD camera was prepared. Sample preparation included the concentration of the colloidal solution and the deposition of dried material onto a glass substrate. NCs were excited with a cw NIR laser (excitation wavelength of 980 nm, power 120 mW) focused onto the sample with a 10x objective (NA=0.25). No spectra could be recorded for any doped samples in both colloidal and dried form, as no emission was observed. Therefore, it was concluded that absorbed 980 nm photons are dissipated through other mechanisms as the NCs hold no Upconversion properties.

Sample	STEM size	Scherrer's size	hkl	Lattice parameter	Mean Value
CeO_2:Er (5%)	2.47 nm	2.38 nm	111	0.5413 nm	0.5429 nm
			200	0.5474 nm	
			220	0.5400 nm	
CeO_2:Yb (10%)	2.51 nm	2.46 nm	111	0.5374 nm	0.5388 nm
			200	0.5413 nm	
			220	0.5375 nm	
CeO_2:Yb, Er (10%, 5%)	2.61 nm	2.51 nm	111	0.5380 nm	0.5391 nm
			200	0.5410 nm	
			220	0.5384 nm	
CeO_2:Yb (20%)	2.63 nm	2.54 nm	111	0.5359 nm	0.5381 nm
			200	0.5402 nm	
			220	0.5381 nm	
CeO_2:Yb, Er (20%, 5%)	2.36 nm	2.31 nm	111	0.5383 nm	0.5399 nm
			200	0.5442 nm	
			220	0.5372 nm	

***Table 3.2**: Summarised parameters from XRD data analysis of doped CeO_2 NCs*

3.3 PERSPECTIVES

Even if no Photon Upconversion was observed during the tests, the absorbance spectra of the doped samples show the characteristic 980 nm band of Yb^{3+}. It means an energy uptake excites electrons within the sample if illuminated from a source of the adequate wavelength, and charge carriers are generated. If the mechanism of dissipation for that energy uptake is not spontaneous emission, then electron-phonon coupling could cause the temperature to rise locally. Doped CeO_2 nanocrystals may be an interesting asset for either photocatalysis or light-to-heat conversion.

3.4 REFERENCES

1. Mohamed, R. M., McKinney, D. L. & Sigmund, W. M. Enhanced nanocatalysts. *Materials Science and Engineering: R: Reports* 73, 1–13 (2012).

2. Tran, D. P. H., Pham, M. T., Bui, X. T., Wang, Y. F. & You, S. J. CeO_2 as a photocatalytic material for CO_2 conversion: A review. *Solar Energy* 240, 443–466 (2022).

3. Mansoob Khan, M. *et al.* Defect-Induced Band Gap Narrowed CeO_2 Nanostructures for Visible Light Activities. *Industrial & Engineering Chemistry Research* 53, 9754–9763 (2014).

4. Montini, T., Melchionna, M., Monai, M. & Fornasiero, P. Fundamentals and Catalytic Applications of CeO_2-Based Materials. *Chem Rev* 116, 5987–6041 (2016).

5. B. Kehoe, A., O. Scanlon, D. & W. Watson, G. Role of Lattice Distortions in the Oxygen Storage Capacity of Divalently Doped CeO_2. *Chemistry of Materials* 23, 4464–4468 (2011).

6. Mittal, M., Gupta, A. & Pandey, O. P. Role of oxygen vacancies in Ag/Au doped CeO_2 nanoparticles for fast photocatalysis. *Solar Energy* 165, 206–216 (2018).

7. Qi, Y. *et al.* Controllable synthesis of transition metal ion-doped CeO_2 micro/nanostructures for improving photocatalytic performance. *J Alloys Compd* 782, 780–788 (2019).

8. Wang, Z., Quan, Z. & Lin, J. Remarkable changes in the optical properties of CeO_2 nanocrystals induced by lanthanide ions doping. *Inorg Chem* 46, 5237–5242 (2007).

9. Gupta, A., v. Waghmare, U. & S. Hegde, M. Correlation of Oxygen Storage Capacity and Structural Distortion in Transition-Metal-, Noble-Metal-, and Rare-Earth-Ion-Substituted CeO_2 from First Principles Calculation. *Chemistry of Materials* 22, 5184–5198 (2010).

10. Wang, F. *et al.* Simultaneous phase and size control of upconversion nanocrystals through lanthanide doping. *Nature 2010 463:7284* 463, 1061–1065 (2010).

11. Zhou, B., Shi, B., Jin, D. & Liu, X. Controlling upconversion nanocrystals for emerging applications. *Nature Nanotechnology 2015 10:11* 10, 924–936 (2015).

12. Chen, G., Qiu, H., Prasad, P. N. & Chen, X. Upconversion nanoparticles: Design, nanochemistry, and applications in Theranostics. *Chem Rev* 114, 5161–5214 (2014).

13. Xu, Z. *et al.* Harvesting Lost Photons: Plasmon and Upconversion Enhanced Broadband Photocatalytic Activity in Core@Shell Microspheres Based on Lanthanide-Doped $NaYF_4$, TiO_2, and Au. *Adv Funct Mater* 25, 2950–2960 (2015).

14. Fischer, L. H., Harms, G. S. & Wolfbeis, O. S. Upconverting nanoparticles for nanoscale thermometry. *Angewandte Chemie - International Edition* vol. 50 4546–4551 Preprint at https://doi.org/10.1002/anie.201006835 (2011).

15. Cheng, Y. *et al.* Color tunable upconversion emission in CeO_2:Yb,Er three-dimensional ordered macroporous materials. *Journal of Rare Earths* 33, 599–603 (2015).

16. Zhao, R. *et al.* Double-shell CeO2:Yb, Er@SiO2@Ag upconversion composite nanofibers as an assistant layer enhanced near-infrared harvesting for dye-sensitized solar cells. *J Alloys Compd* 769, 92–95 (2018).

17. Artini, C. *et al.* Structural Features of Sm- and Gd-Doped Ceria Studied by Synchrotron X-ray Diffraction and μ-Raman Spectroscopy. *Inorg Chem* 54, 4126–4137 (2015).

CHAPTER IV

MULTIDOMAIN Au/Ag-CeO_2 HYBRID NANOSTRUCTURES

CHAPTER IV

MULTIDOMAIN Au/Ag-CeO_2 HYBRID NANOSTRUCTURES

4.1 INTRODUCTION

The second strategy towards improving the catalytic activity of a pure inorganic compound is designing hybrid nanocrystals, combining domains of different compositions into a single nanomaterial: nanocomposites. Section 1.5 of Chapter I of this text mentions this strategy, which serves as introduction for the concepts behind catalytic performance and enhancement strategies.[1,2] The interest in hybrid nanomaterials arises from the synergistic properties they hold, which the sum of those of their individual components cannot match .[3] A brief comment on plasmonic sensitisation and how hybridization affects the properties of metal-semiconductor nanomaterials, as they are the object of study in this section, is required.

Hybridization synergistic effects on metal-semiconductor nanocomposites manifest in their optical properties, electronic structure, and charge separation phenomena. For example, the metal's characteristic LSPR is affected by the close contact with the semiconductor in both absorption cross-section and position. The observed red-shift can be explained as the change in the surrounding medium's refractive index due to the semiconductor-metal interface's creation. This effect is maximised in core-shell structures as the thickness of the semiconductor shell grows. Another feature of the coupling is the near-field effect caused by the metal onto the semiconductor, which affects scattering within the semiconductor's surface.[4]

The most representative characteristic of the metal-semiconductor synergy is the promoted charge separation phenomena occurring within the semiconductor-metal interface: Schottky barriers facilitate the transference of electrons between the conduction band of the semiconductor and the metal's surface plasmon. At the same

time, the holes remain localised to the surface defects in the structure of the semiconductor, increasing charge carrier lifetimes by preventing recombination. Furthermore, excited electrons generated by the LSPR can be transferred to active sites within the semiconductor's structure, sensitising the material to lower energy photons received under visible/NIR illumination, which is beneficial during a catalytic process. The charge transfer phenomenon holds an interest in the fields of photovoltaics and photocatalysis, and the possibility of tuning the structure to optimise the photoinduced processes is key for the application of the materials for solar energy harvesting and other photochemical processes. [5–7]

4.1.1 State of the Art

Combining two components onto a unique nanostructure in a controlled manner is a synthetic challenge. For the synergistic properties to manifest in a nanocomposite, intimate contact between components is required. The most important structural parameters affecting the epitaxial growth of two components are lattice constant mismatch and respective crystalline structures, charge distribution along the surfaces, interfacial energy, miscibility, and the presence of defects. Synthetic approaches that provide a high degree of control over the final nanomaterial's size, composition and architecture are fundamental for exploiting these features.

Wet-chemistry techniques to produce hybrid nanocrystals are usually based on either the simultaneous co-precipitation of the components in a one-pot approach or following a sequential process where a second component is grown onto preformed NCs in a different stage (heterogeneous nucleation). This synthetic strategy, known as the seeded-growth approach, represents the most common method. One-pot methods are characterised by their simplicity and robustness. However, these benefits make the implementation of directed growth strategies difficult, as the common grounds for the growth of more than one component limit the degrees of the synthetic control of the system and, with it, the freedom of controlling their functionality. Different structures of metal-metal oxide and other hybrid materials with different architectures, such as nanostars[8], core-shell and heterodimers[9,] synthesised through this approach can be found in the literature.

Heterogeneous nucleation presents lower energy barriers than homogeneous nucleation. Thus, if the structural conditions are met, growth on top of a previously formed crystal is more favourable than separate precipitation in the presence of the seeds. Seeded-growth methods allow for a great degree of control of all the parameters mentioned above: the seeds' size, composition and shape are determined before adding the second component. In turn, the growth of this second component can also be directed by different strategies to tune reactivity, controlling the final architecture of the hybrid. Several examples of metal-metal oxide hybrid nanocrystals, such as Au-Fe_3O_4,[10] Au-ZnO[11] or Au@$MgFe_2O_4$[12] synthesised by seeded-growth methods, are reported in the literature. Moreover, the morphology and crystalline structure of the seeds may lead to selective growth over some facets, leading to the formation of anisotropic structures.[13,14] Other structures that have attracted attention recently for their catalytical potential and plasmonic resonance modulation are hollow nanostructures. They are also produced by a sequential synthesis method, where the seeds act as a sacrificial template for depositing a second component that conforms to the cage material. The main mechanisms to create voids are Kirkendall effect[15,16] and galvanic replacement.[17]

Hybridization to plasmonic metals appears as an exciting strategy towards increasing nanostructured CeO_2 functionality. On the matter of CeO_2 coupled to plasmonic metals, there exist already reported examples of the enhancement of its catalytic properties in comparison to the simple combination of individual components.[18] Said hybrids are prepared by a wide range of methods, one-pot[19,20] and seeded growth[21] strategies. However, following the tendency towards increasing the complexity of the resultant architectures, synthetic protocols have become considerably more complicated themselves. The aim of this section is to achieve the heterogeneous nucleation of CeO_2 on top of plasmonic metals and to extend the control of the morphology of the products to higher degrees of complexity only by simple tuning of reaction parameters.

4.2 RESULTS

This section's objective, as previously mentioned, is the derivation of previously designed CeO_2 NCs through their hybridization to a metal domain, achieving plasmonic sensitisation and extending the control of the morphology of the products to higher degrees of complexity only by simply tuning reaction parameters. Commencing from previously developed works from the group for the synthesis of $AuCeO_2$ nanocrystals by both one-pot[22] and seeded-growth[23] approaches, the production of $AuCeO_2$ and $AgCeO_2$ hybrids of several architectures was studied to define the systems' properties and applicability.

4.2.1 One pot method

For the one-pot approach, all precursors are mixed together in the reaction media to form a uniform dispersion of $AgCeO_2$ or $AuCeO_2$ hybrids. Morphological characteristics such as surface coverage and shell thickness of the product are adjusted by tuning parameters like precursors ratio, pH or reaction time. Surface coverage is an important parameter to control, as it determines the extent of the metal-oxide interface and the existence or not of a metal-solvent interface. As previously stated, exposed facets are key for the catalytic properties of the material and consequently, they'll be defined by this parameter. The simplicity of the one-pot method allows good reproducibility; however, it does not allow for a versatile size control of the product, as the size of the core crystal cannot be adjusted.

4.2.1.1 $AuCeO_2$

For the $AuCeO_2$ case, the typical reaction involves the subsequential injection of first, 1 mL of Au precursor solution ($HAuCl_4$, 25 mM) and then 1 mL of CeO_2 precursor ($CeCl_3$, 25 mM) onto a refluxing solution of sodium citrate 10 mM to a final volume of 100 mL. Afterwards, the mixture is left reacting for 2h. HRTEM and HAADF-STEM images of the final product reveal the formation of core-shell $Au@CeO_2$ NCs consisting of ~7 nm Au cores surrounded by a CeO_2 shell composed by several 2.5 nm CeO_2 crystalline domains. It is important to note how the Au core size in the hybrids (~7 nm) is smaller than the equivalent Au NPs synthesised in the absence of CeO_2 (~11 nm). The porosity and lack of uniformity of the CeO_2 layer indicate a Volmer-Weber growth mode[24] for the material, expected for the high

lattice mismatch between the two components (0.4065 nm and 0.5412 nm, respectively). Interestingly, no free Au NPs can be found in the solution.

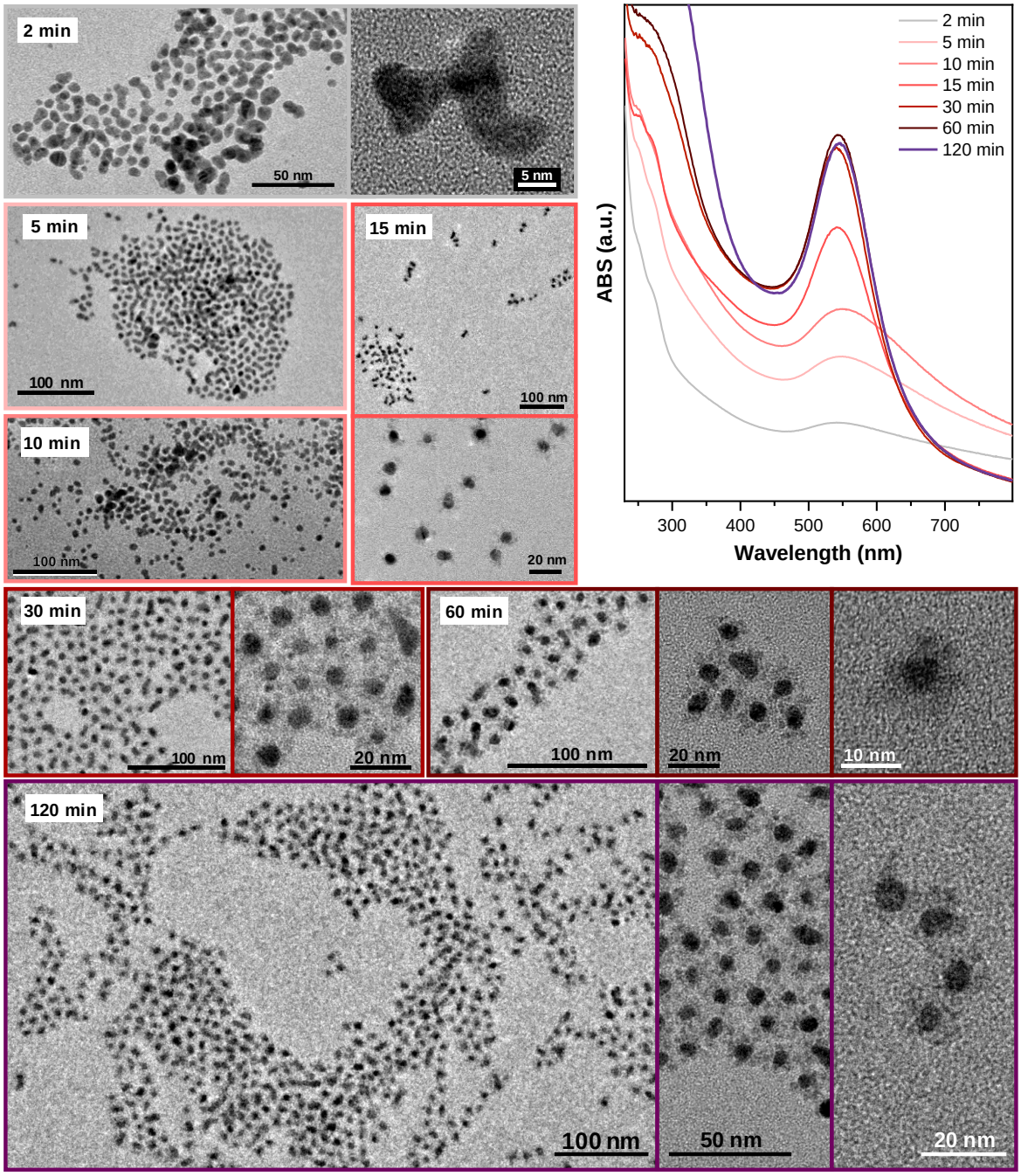

***Figure 4.1**: Time evolution of the $AuCeO_2$ hybrids synthesis by the one-pot method, followed both by UV-vis spectroscopy and HRTEM imaging.*

While the process apparently consists of a reaction involving Au^{3+} to Au^0 reduction and Ce^{3+} to Ce^{4+} oxidation processes, the chemical process is a little bit more complicated. Sodium citrate was previously stated to hold several key roles in CeO_2 NC synthesis (see section 2.2.2 in Chapter II), as it does for Au.[25] It does not only act as a colloid stabiliser. Firstly, in the absence of citrate, no Au reduction is observed in the reaction media, which is to be expected as both cationic species lead

to slightly acidic pH levels. Second, the Au reactivity is maximised at slightly acidic pH levels of around 6.5,[26] while CeO_2 oxidation occurs at basic pH levels. Therefore, the role of citrate as a buffer provides adequate pH levels (between 7-8) for both species to react at the same time that Au^{3+} is reduced by sodium citrate itself. It adds another known item to citrate's list of tasks to perform. Ce^{3+} is oxidised by the solubilised oxygen present.

During this process, Au cores are formed and crystalised within the first 10-15 min of the reaction. In these pH conditions, CeO_2 reaction is slower. Progressive nucleation on top of the Au surface can be observed between 15-120 mins after the injection, as the HRTEM imaging (**Figure 4.1**) shows. The size of Au cores does not change over time after the CeO_2 starts to deposit, as the rigidness of the oxide shell impedes reconfiguration of the feebler metal trapped inside.

Several features can be observed through UV-vis spectroscopy analysis of the samples (**Figure 4.1**, top left). Besides de CeO_2 characteristic band between 200 and 300 nm that illustrates the degree of CeO_2 coating over the Au cores as the reaction proceeds, the LSPR peak position at around 538 nm (the typical position for 10 nm Au seeds is 518 nm) emerges 5 minutes after the precursors' injection. It was previously mentioned how the close contact between metal and the semiconductor counterparts alters the LSPR extinction cross-section and position due to the higher refractive index of the environment surrounding the metal. The refractive index of CeO_2 ($n = 2.2$) is significantly higher than the one of water ($n = 1.33$). As so, in the case of an open CeO_2 shell, where a fraction of the Au surface is exposed to water, the red-shift experienced by the LSPR is smaller than in the case of a completely closed CeO_2 shell where the refractive index is at its maximum. Interestingly, the extent of red-shift saturates once a certain shell width is reached. From this point on, even if the shell keeps growing, the peak remains constant. It is a signature of the maximum distance at which near-field enhancement extends.[27,28] Intensity changes in the LSPR peak also respond to this change in refractive index. Lastly, shape changes of the peak (width and baseline height) correspond to changes in the Au core shape. At short reaction times (up to 10 minutes), the sample is composed of elongated Au NPs of low crystallinity, which has been reported in the literature as an Au reaction intermediate of mixed valences.[26,29] LSPR absorption peak in these gel-like Au structures presents higher FWMH values as there is a large size and shape

variability within the sample. Once the Au formation is completed and CeO_2 starts its nucleation, the LSPR peak undergoes a narrowing process as the shape variability of the Au cores decays. After the reaction is over, reflux conditions favour recrystallisation of the shell towards a more uniform configuration under a small risk of aggregation of the colloidal system.

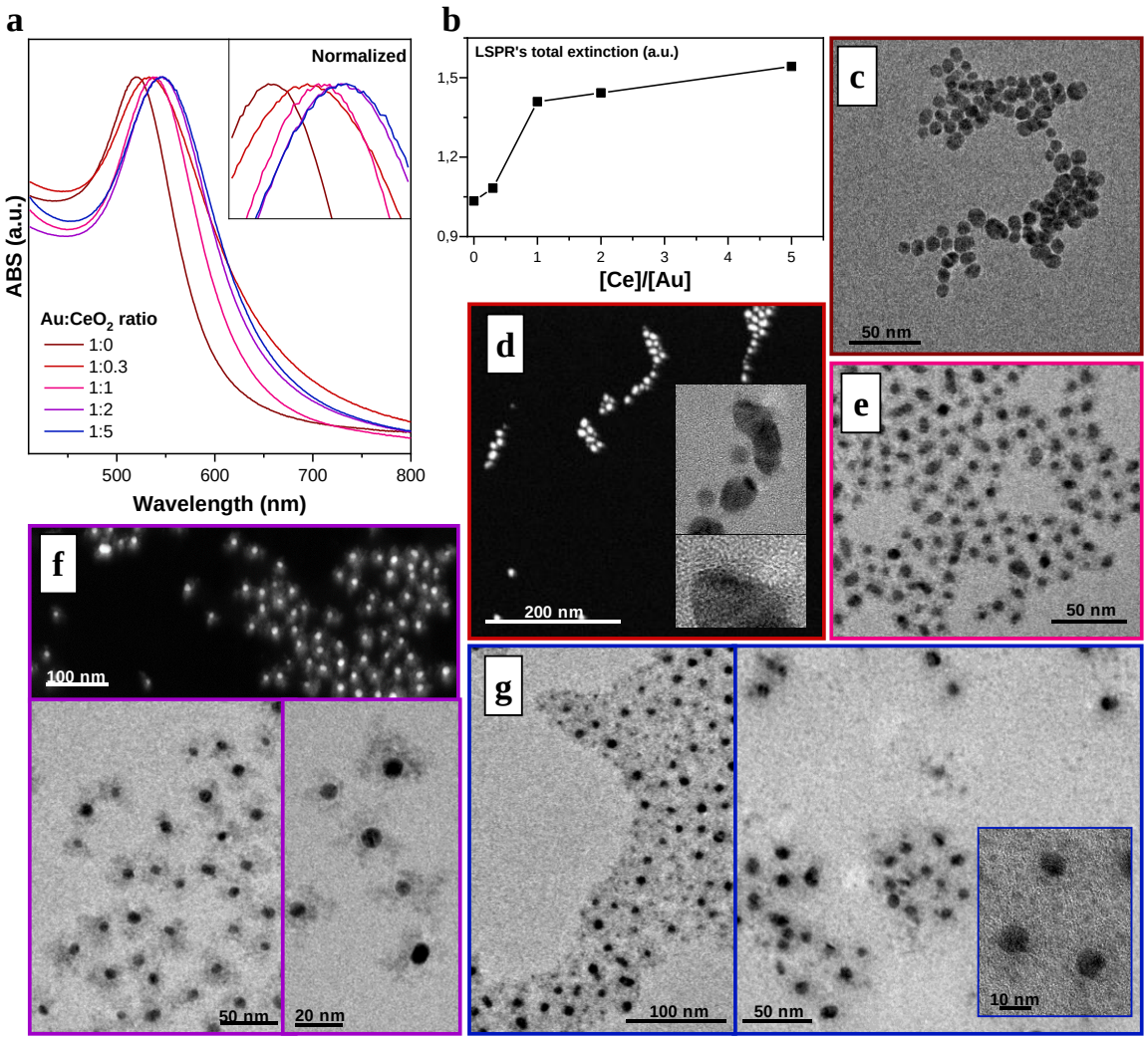

***Figure 4.2**: (a) Normalized peak and (b) Peak intensity comparison of UV-vis spectra and HR(S)TEM imaging of resultant $AuCeO_2$ hybrids containing (c) 0:1, (d) 0.3:1, (e) 1:1, (f) 2:1 and (g) 5:1 CeO_2 to Au molar ratio.*

Morphological control is achieved through variations in the amount of CeO_2 precursor. The structural evolution with increasing Ce: Au ratios is followed by UV-vis absorption spectroscopy (**Figure 4.2 a,b**) and HRTEM/HAADF-STEM imaging (**Figure 4.2 c-g**). Lower Ce: Au ratios lead to incomplete Au surface coverage and thinner shells. The 2.5 nm CeO_2 nanocrystals nucleate on top of the Au core. The only Au surface sacrificed is the fraction destined for the CeO_2-Au interface, but it remains accessible due to the porosity caused by the CeO_2 growth mode (**Figure 4.2 d, e**). Increasing the CeO_2 precursor leads to thicker and more compact shells (**Figure 4.2 f, g**). The acidic nature of the metal cations leads to a pH decrease that could stop the reaction from happening, and thus a pH control is a necessary step for higher Au: Ce ratios. Adjusting the reaction media to pH 8 using a few drops of NaOH 0.1 M may be required. Higher pH levels than standard protocol conditions (pH 9) lead to faster precipitation of the CeO_2 on the gold surface, leading to a more compact coverage of the Au surface and free nucleation of CeO_2 due to this excess. It, however, can be removed easily through centrifugation. Notably, when the amount of CeO_2 precursor is one order of magnitude larger than the amount of Au precursor, the pH of the solution drops significantly. At pH 6, the surface charge of CeO_2 nanocrystals is low due to the closeness to the point of electrostatic instability (ζ-potential in the range of ±20 mV).[30,31] In this environment, nucleating particles tend to aggregate following an oriented attachment self-assembly mechanism, forming 2D planar structures defined as "nanosheets" of Au-embedded CeO_2.

4.2.1.2 $AgCeO_2$

Ag is a noble metal very similar to Au. Belonging to the 11th group of the periodic table, they share many characteristics: both present an LSPR within the visible range, an *fcc* crystalline structure of similar lattice parameters (0.4065 nm for Au and 0.4079 nm for Ag), similar reactivity and atomic radius, etc… It would be expected that it behaves similarly than Au for its hybridization with CeO_2. The same way as in the Au case, when injecting the correspondent volume of Ag precursor ($AgNO_3$ 25 mM, 1 mL) and CeO_2 precursor (between 0.5 and mL) to a refluxing 10 mM sodium citrate solution, Ag nucleates first and then CeO_2 nucleates heterogeneously on top of the Ag surface, forming $AgCeO_2$ hybrid NCs. The larger the amount of CeO_2 precursor, the thicker the CeO_2 layer.

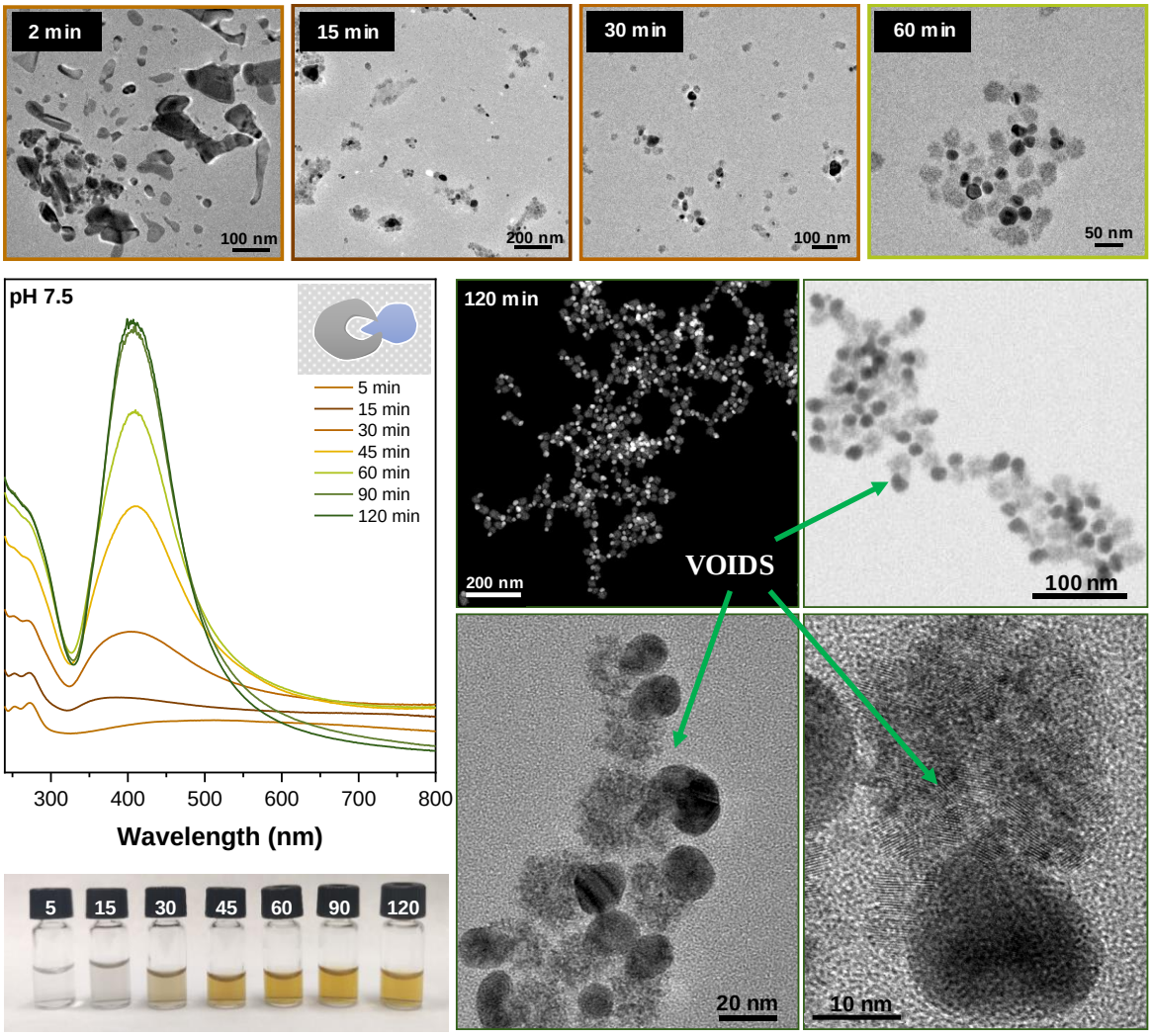

***Figure 4.3**: Time evolution of the process and final characterization of $AgCeO_2$ hybrid nanocrystals produced by the One-pot method at pH 7.5 by UVvis spectroscopy and HR(S)TEM imaging. Picture below: appearance of the colloid solution at each of the measured steps.*

However, some differences concerning $AuCeO_2$ hybrid NCs arise from the few dissimilarities between both metals. Ag reduction kinetics are faster in basic environments, and its dissolution in the form of Ag^+ takes place in acid media.[32] This reactivity affects its miscibility with CeO_2, altering the final architecture of the hybrids. Performing the reaction at neutral pH leads to forming of $AgCeO_2$ heterodimers, a Janus-like structure where Ag and CeO_2 share a single interface, but the rest of their surfaces are available to the solvent. This configuration originates from the low miscibility between Ag and CeO_2. This effect has a chemical explanation: the precipitation of the CeO_2 causes the depletion of OH^- groups from the solution. It does not alter the reaction conditions in a basic media where hydroxyl groups find themselves in excess. In neutral media, water molecules take the role of the base, and the liberation of H^+ involved in the CeO_2 precipitation causes an abrupt

decrease of pH locally in the surroundings of the nucleated particle. The local acidic conditions can cause the dissolution of the Ag into Ag^+ ions. The most stable configuration for CeO_2 once both Ag and CeO_2 surfaces coexist in the hybrid is to nucleate in the CeO_2 surface rather than extend the coverage of the Ag, which is slowly dissolving and growing away from the nucleated CeO_2, originating a semi-hollow structure. The resultant hybrids take the morphology of "hollow" heterodimers, as shown in **Figure 4.3**. The hollowing process resembles a galvanic replacement reaction. However, it should not be mistaken for one since CeO_2 precipitation causes the environment for Ag dissolution sequentially, rather than a simultaneous reaction in which CeO_2 requires the Ag dissolution to precipitate.

A notable feature of the $AgCeO_2$ system that differs from the $AuCeO_2$ one is the influence of the reaction time. For the core-shell case, it was stated that CeO_2 caging prevents core size to be altered. Nonetheless, for the heterodimer morphology, if the reaction conditions are kept after the hybrid formation, the system will keep evolving thanks to the reactivity of Ag around CeO_2. Once the hybrids are formed after 2h of reaction, continuous liberation of Ag^+ prevents monomer depletion from the solution. It gives rise to a continuous Ostwald ripening regime, making bigger Ag cores grow while smaller one's collapse, a consequence of the *pseudo*-galvanic replacement. The final size of the hybrids is then time-dependent. After enough reaction time, voids are formed in the interior of the CeO_2 aggregate, giving rise to a new morphology of the hybrid: Empty CeO_2 cages capped by the Ag core (**Figure 4.4**, after 6h). To stop this process, the mixture must be cooled down and cleaned from unreacted precursors to avoid further evolution. These hybrids are much bigger than the heterodimers or core-shell nanoflowers, and the solution appears turbid suspension.

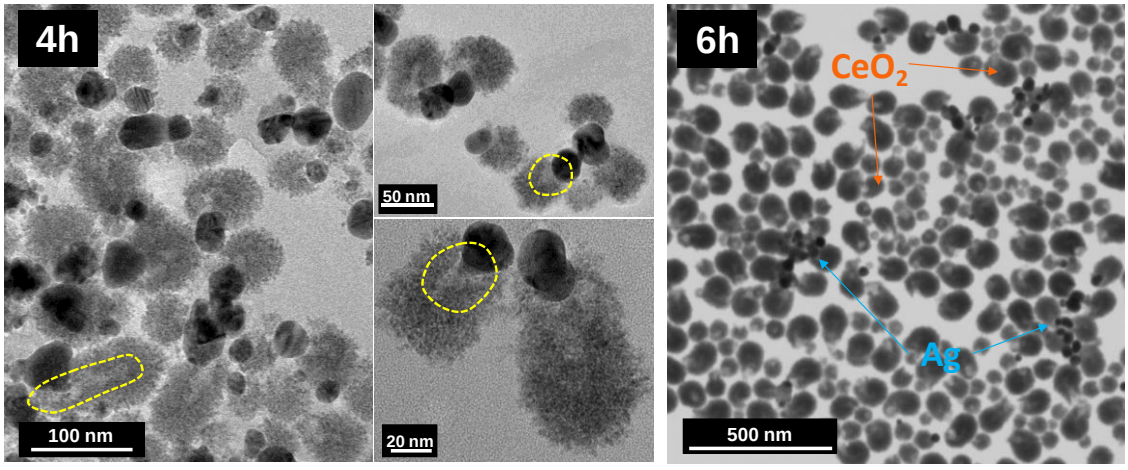

***Figure 4.4**: HRTEM image of a $AgCeO_2$ nanocrystal sample left boiling for 4h and 6h, respectively. Marked in yellow: Voids inside the CeO_2 domain.*

4.2.1.3 $AuAgCeO_2$

In the case of injection of both Ag and Au precursors into the reaction mixture, the metals come together in an AuAg alloy that forms the core of the hybrid core-shell nanoflowers. In **Figure 4.5 (a)**, the absorbance spectra following the time evolution of the $AgAuCeO_2$ system and its comparison to $AgCeO_2$ and $AuCeO_2$ hybrids are presented. The alloying of both metals is proven by the joint LSPR peak, which positions itself between the $AgCeO_2$ and $AuCeO_2$ ones. **Figure 4.5 (b)** and **(c)** show HAADF-STEM and HRTEM images of the resultant particles conformed by 2.5 nm CeO_2 nanocrystals on top of a 5-7 nm AuAg alloy.

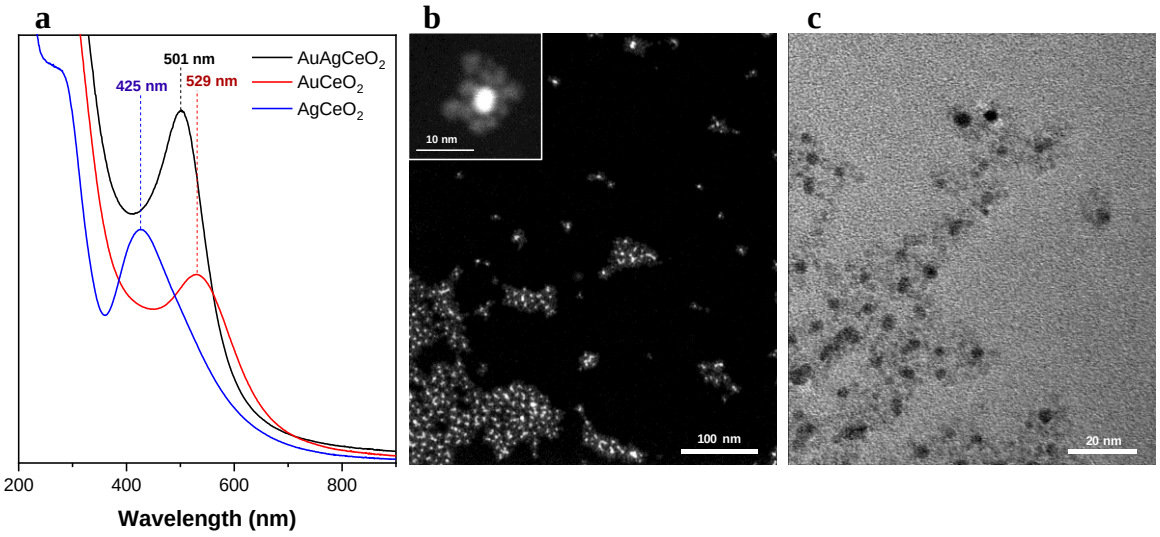

***Figure 4.5**: (a) UV-vis spectroscopy of $AgAuCeO_2$ hybrids synthesized by the one.pot method. Dotted lines: time evolution of the synthesis. Red: Equivalent syntesis of $AuCeO_2$. Bue: Equivalent synthesis of $AgCeO_2$. (b) HAADF-STEM imaging of the sample. (c) HRTEM imaging of the sample.*

4.2.2 Seeded Growth Approach

The seeded-growth approach consists of the sequential synthesis of the metal core first and its posterior coating with the CeO_2 layer. While it increments the complexity of the overall procedure, it allows for the decoupling of both redox processes, which translates into an independent control of the size and thickness of the core-shell hybrid nanocrystal, eventually opening the possibility of different engineering morphologies. It doesn't come without drawbacks, however. Attaining a controlled deposition of the CeO_2 onto the metal surface and avoiding its homonucleation is one of the main challenges of this approach. To tackle this problem, a strategy to promote heteronucleation is hampering the hydrolysis rate. Sodium citrate, acting as a chelate agent for Ce^{3+} ions in solution, slows down the reaction kinetics, playing,

yet again, a vital role in the synthetic process. By maintaining a high enough (20-40 times the concentration of precursor) amount of citrate on the reaction media, complex formation constantly occurs, preventing the supersaturation of Ce^{4+}.

4.2.2.1 Synthesis of metal seeds

Monodisperse Au NPs and Ag NPs of different sizes ranging from 10 to 100 nm stabilised in sodium citrate were produced by synthetic methods previously developed by the group.[25,33] These methods are based on reducing the metal precursor in a boiling citrate solution (for the Ag case, tannic acid is also employed as a co-reducer). Size control is achieved by sequentially injecting small amounts of the precursor at a lower temperature, following a seeded-growth strategy. For each NP "generation" (growth step), a vial of the as-synthesised particles is stored, so at the end of the process, vials of monodisperse NP of different sizes between a few nanometres and the final size are obtained. For a more detailed characterisation of the produced nanoparticles, see sections 9.3.1 and 9.3.2 (Annex D). For the second stage of the process, the CeO_2 shell deposition, metal nanoparticles as synthesised are employed without further purification.

4.2.2.2 Seeded-growth synthesis of Ag/Au-CeO_2 hybrid nanostructures

For the CeO_2 layer deposition onto the metal surface, a specific volume of the previously made seeds is poured into a preconditioned reaction media (5 mM sodium citrate), and the pH is adjusted to 8-9. Afterwards, this solution is heated to reflux. When the temperature reaches 60ºC, the Ce precursor is injected, and the mixture is left under reflux conditions for 2h. For the detailed process, see experimental section.

When Ce^{3+} is injected into the solution, Ce-citrate complexes are immediately formed. Upon boiling, the ions slowly oxidise through O_2 present in the solution and hydrolyse, nucleating onto the metal surface. While at high temperatures, the dissolved O_2 in water is lower than at room temperature, performing the reaction in an open flask allows the reaction to be carried out. As the reaction proceeds, the appearance of the solution changes both in colour and intensity as a consequence of the refractive index affectations to the LSPR absorption. For the case of Au cores, the colour shift is from wine red to bright purple. For Ag cores, it goes from yellow to a reddish-orange solution. These changes are easily monitored through the

respective UV-vis absorption spectra, represented alongside the STEM images of the manufactured metal@CeO_2 core-shell hybrid nanocrystals in **Figure 4.6** and **Table 4.1**.

The seeded-growth approach allows for precise and independent tailoring of both sizes of the core and the thickness of the CeO_2 layer. The aspect ratio of the LSPR absorption peak (calculated as extinction intensity/HWMH of the peak) remains constant as the reaction moves forward, indicating that no change in seed size, morphology or aggregation state occurs during the process. For different Metal@CeO_2 core sizes, different generations of seeds are employed. In detail, hybrids containing 35 nm (**Figure 4.6.a**) and 25 nm (**Figure 4.6.b**) Au seeds and 50 nm Ag seeds (**Figure 4.6.c**) were obtained. Increased thickness of the CeO_2 shell was attained by raising the amount of Ce^{3+} injected per amount of metal seeds (**Figure 4.6.a III-V**). However, exceedingly high Ce^{3+} amounts may increase concentration levels enough for homonucleation, leading to single CeO_2 NCs rather than thicker shells. Sequential injections of small amounts of precursor or lower temperatures are strategies to incorporate to reach thicker shells without self-nucleation of CeO_2 NCs but a certain limit to the maximum thickness still applies. Similarly to the one-pot case, a low Ce-to-metal ratio results in incomplete clover-like shells, which present a fraction of accessible metal surface (**Figure 4.6.a II**).

Seed (size)	LSPR peak	Shell size	Peak displacement
Au (30 nm)	526 nm	~5 nm	19 nm
		8 nm	31 nm
		11 nm	39 nm
		12,5 nm	44 nm
Au (25 nm)	524 nm	8 nm	25 nm
Ag (50 nm)	431 nm	13 nm	56 nm

***Table 4.1**: Shell thicknes and LSPR position and displacement for the $AuCeO_2$ and $AgCeO_2$ samples depicted in **Figure 4.6**.*

Interestingly, the red shift of the LSPR position after the coating is proportional to the Ce^{3+}:Metal ratio until saturation is reached, as the UV-vis spectra prove (**Fig 4.6 A**, right). Precise control of the shell thickness is key for the hybrid design, as it affects the material's applicability. Thinner and less compact shells maximise surface

towards enhanced catalytic applications, but thicker ones provide protection against chemical transformations such as dissolution and aggregation, ensuring long-term stability of the material.[34]

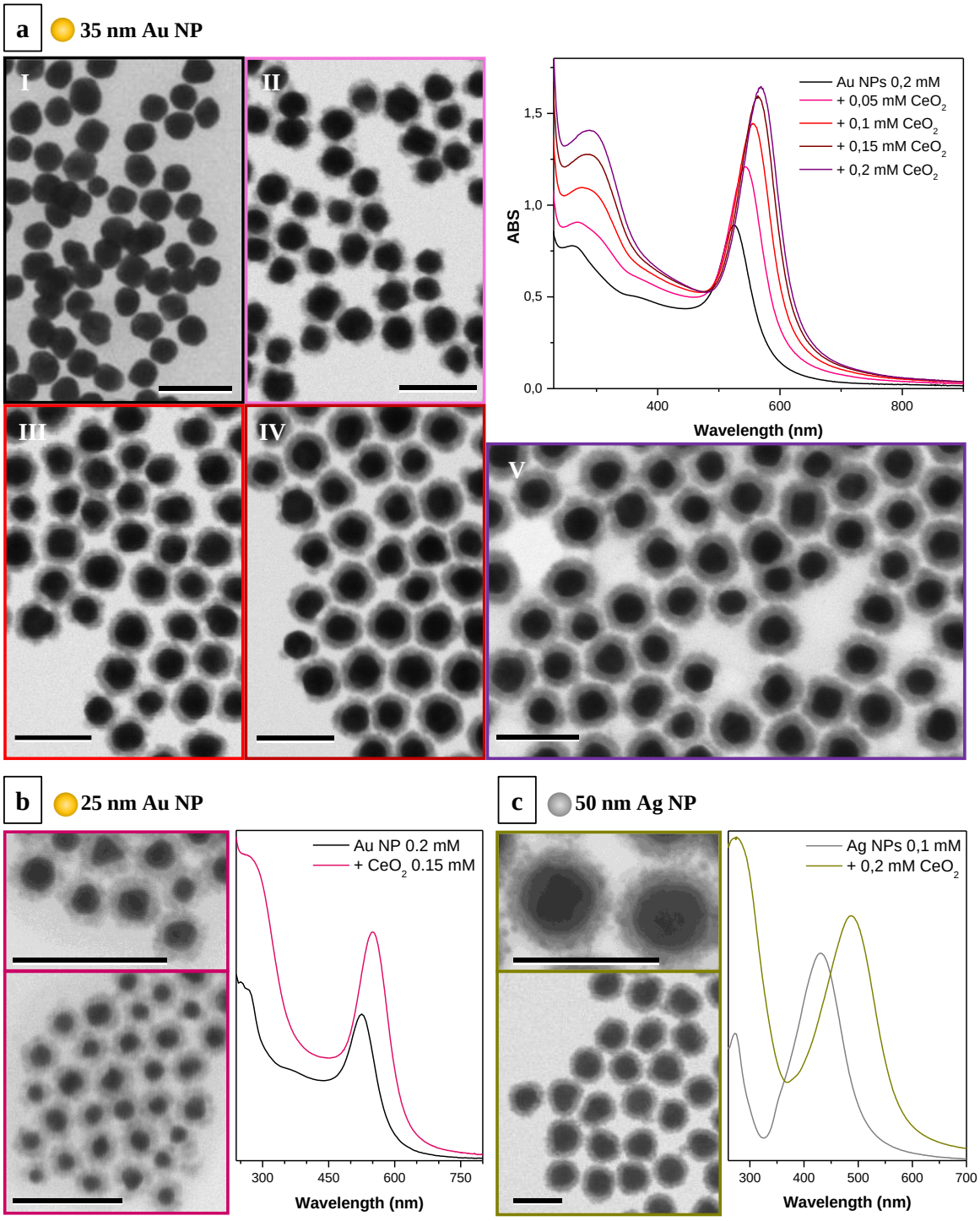

Figure 4.6: *(a) Characterization by UV-vis spectroscopy and STEM imaging of 35 nm Au seeds and four corresponding samples of $AuCeO_2$ hybrids of different shell thickness. Colour of the line in the UV-vis spectra matches the colour of the border for the microscopy image of the sample. (b) Characterization by UV-vis spectroscopy and STEM imaging of 25 nm core $AuCeO_2$ hybrids. (c) Characterization by U-Vvis spectroscopy and STEM imaging of 50 nm core $AgCeO_2$ hybrids. Scale bars: 100 nm*

A thorough look at the metal-CeO_2 interface (**Figure 4.7**) evidences again a Volmer-Weber growth mode that lead to high compressive and tensile stress of the material due to the formation and coalescence of "islands" of the CeO_2 on top of the metal. Nevertheless, the lower curvature of the surface in bigger seeds leads to forming a more compact layer than in the one-pot case.

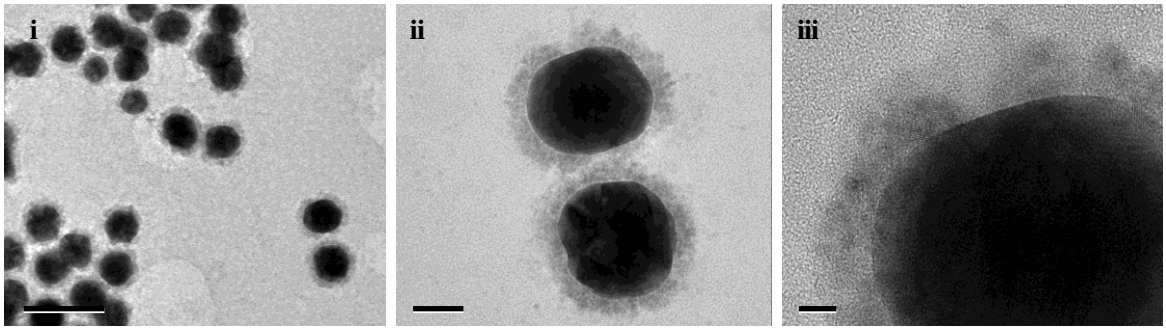

***Figure 4.7**: HRTEM microscopy of 45 nm core $AuCeO_2$ hybrids. Scale bars (i) 100 nm, (ii) 20 nm, and (iii) 5 nm*

4.2.2.3 Effect of reaction parameters over the CeO_2 growth

To attain a heteronucleation regime free of self-nucleated CeO_2, the restraining of reaction kinetics is necessary to favour only the less energetic reaction pathway. For the CeO_2 NC synthesis, oxidation kinetics are controlled by citrate chelation of Ce^{3+} ions and a sub-stoichiometric amount of base at room temperature. Likewise, for the hybrid system, the effect of citrate concentration, pH and temperature and precursors concentration has been evaluated.

Role of citrate as a reducer, pH buffer, stabiliser and, in this context, chelate has been thoroughly described through the text. Its hold over the reaction kinetics gives the precursor's reactivity a strong dependence on pH and temperature, which allows for finer tuning of the $AuCeO_2$ hybrids' morphology. It is worth mentioning how, for the proper development of the reaction, the concentration of citrate in solution needs to be carefully chosen. Citrate-stabilised metallic NPs used as seeds are very susceptible to aggregation when subjected to changes in the electrolyte concentration. Consequently, in both its defect (less than 2 mM) and excess (more than 10 mM), the seeds will be at risk of aggregation, causing the collapse of the system and the isolated precipitation of aggregated Au and CeO_2 NCs.

It has been brought up several times both within this section and previous ones that the Ce^{3+} oxidation and hydrolysis is favoured at pH higher than 7.[35] It could be expected that the presence of the metal seeds allows for hydrolysis at lower basicity conditions due to their catalytic properties. Nonetheless, adjusting the reaction media to slightly acidic conditions (pH 6) by adding a few drops of HCl, no precipitation whatsoever of CeO_2 occurred, neither on the top of the metal seeds nor independently, and under boiling conditions after some time the metal seeds aggregate and collapse. Performing the reaction at the pH levels provided by the citrate-buffered media (pH 7-8) leads to a slow hydrolysis (up to 4h-5h) and a non-continuous coverage of the metal surface. Saturation of nucleated oxide particles around the metal seed surface is not attained, and the characteristic "islands" of the system's growth mode do not coalesce. As pH was adjusted to the initially proposed ideal levels (pH 9), the reaction proceeded faster (1h) and colloidally stable metal@CeO_2 core-shell hybrid nanocrystals were obtained. Further increase of pH (pH > 11) leads to very fast and uncontrolled precipitation of CeO_2, both self-nucleated and on top of the metal surface.

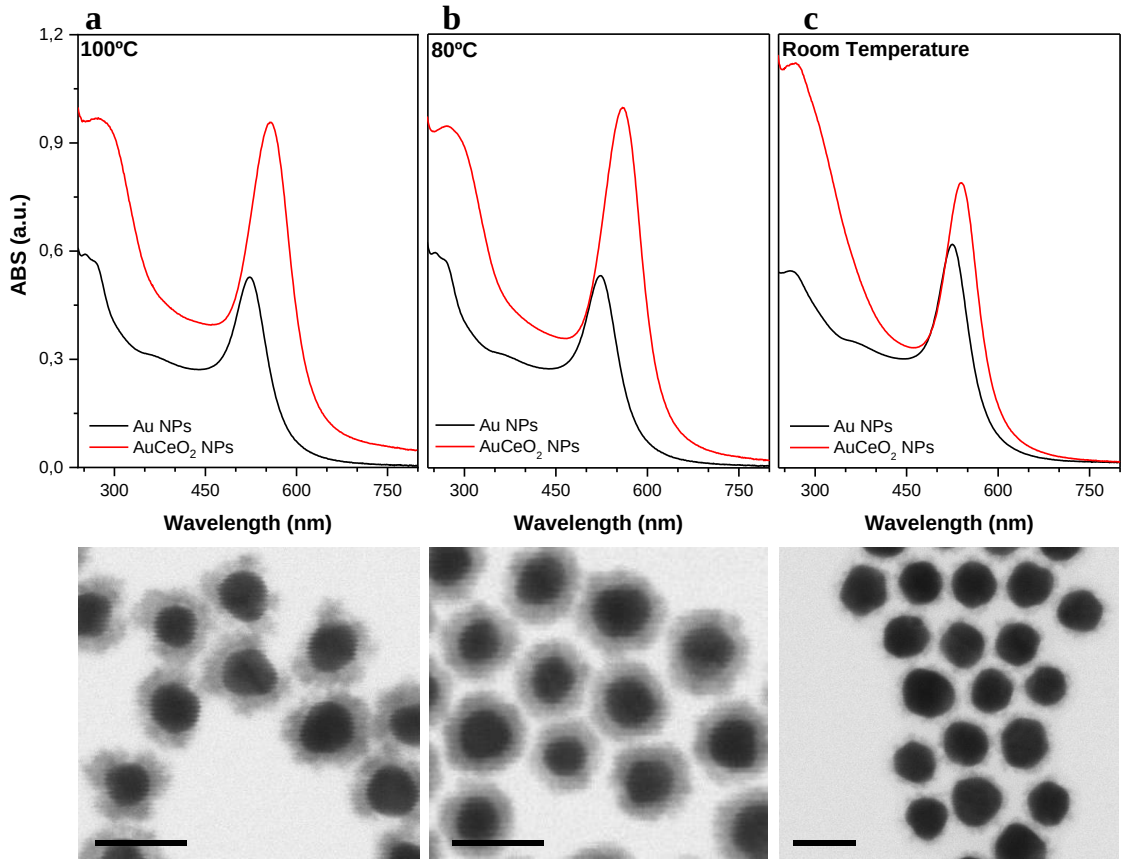

***Figure 4.8**: UV-vis spectroscopy (top) and STEM imaging (bottom) of $AuCeO_2$ hybrids prepared by the seeded-growth approach at (a) 100ºC, (b) 80ºC and (c) room temperature. Scale bars: 50 nm*

For the evaluation of the effect of temperature in CeO_2 growth, the synthesis of $AuCeO_2$ hybrids is carried out at different temperatures and the differences in the produced CeO_2 layer are evaluated (**Figure 4.8**). Besides the expected dependence of the overall reaction kinetics to temperature, this parameter proves to play a key role in both thermodynamic barriers of nucleation and structure of CeO_2 domain. At 100ºC (**Figure 4.8.a**), standard reaction conditions, a fast reaction produces a non-compact shell of high surface exposed per mol of material. At 80ºC and mild basicity conditions (**Figure 4.8.b**), all the Ce^{3+} takes more time to deposit, but highly uniform and dense CeO_2 domains are produced. When performing the reaction at room temperature and under a slight excess of base (**Figure 4.8.c**), a thin (2-3 nm), non-continuous CeO_2 monolayer deposits over the Au surface, but neither the growth of this layer nor the self-nucleation of the remanent Ce^{3+} in solution is observed after 24h. The explanation of these changes is easily described: Once temperature allows overcoming the energy barrier for nucleation, the CeO_2 layer grows by the aggregation of the heteronucleated CeO_2 particles on top of the previously formed CeO_2 surface. As with any other aggregation process, CeO_2 grows following widely known aggregation mechanics (see section 1.4.1, from Chapter I). Temperature promotes faster aggregation kinetics, resulting in higher sticking coefficients that produce more porous, dendritic structures in comparison to the dense, compact ones produced by slower aggregation rates.

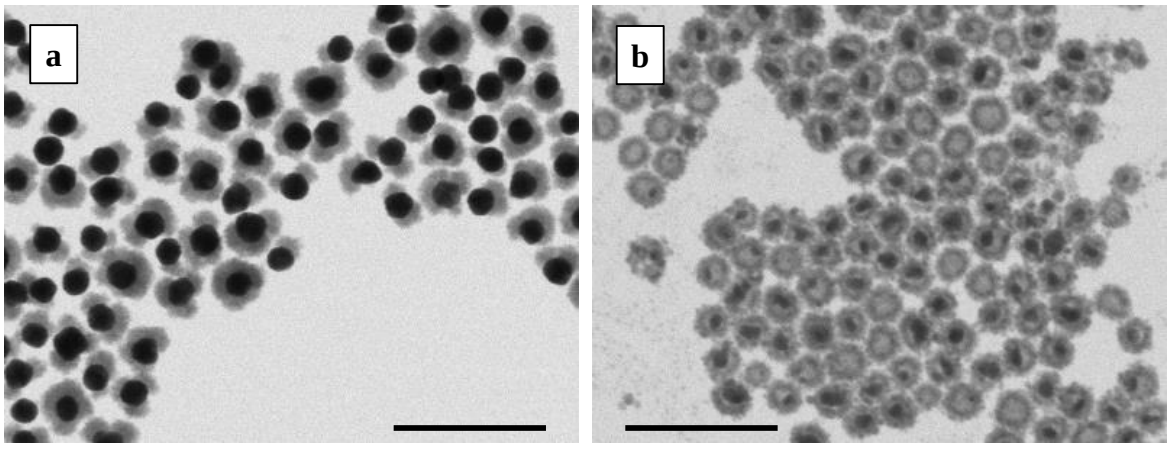

***Figure 4.9**: STEM imaging of (a) $AuCeO_2$ heterodimers and (b) CeO_2 cages synthesized by Ag sacrificial templating. Scale bars: 200 nm*

Morphology of the final hybrid can be tuned exploiting the reactivity dependence on these parameters: mildly basic pH conditions (pH 7-9) favour the heteronucleation of CeO_2 on top of the metal or previously nucleated CeO_2. Within this range, a higher basicity (pH 9) leads to faster production of core-shell morphologies for both Au and

Ag seeds (**Figure 4.9**). Milder conditions (pH 7 and lower temperatures) open the possibility of tuning coverage fraction of the metal surface by favouring the definition of the CeO_2 domains over their extension along the metal surface. It translates into different morphologies for the hybrid nanocrystals: For the Au seeds, allows to the production of heterodimers, where the CeO_2 domains grow as "petals" or “clovers” within the structure (**Figure 4.9.a**). For the Ag seeds, reactivity of this metal allows for its use as sacrificial template, as the local acidic conditions originated by the CeO_2 nucleation at neutral pH cause the Ag to dissolve as Ag^+, creating voids inside the CeO_2 layer (**Figure 4.9.b**).

4.2.2.4 Surfactant-mediated synthesis

The use of surfactants is very popular among the nanosynthesis field as colloid stabilisers, the purpose initially intended for them to fulfil, and as mediators of nucleation and growth processes since it has been proved that their presence affects the reaction [36,37] This kind of molecules hold the capacity to tune surface reactivity and, therefore, every surface-mediated phenomenon, such as catalytic activity. When in contact with a colloidal nanocrystal system, surfactants interact by forming a corona around the solid surface. The density and extension of this corona, for a given surfactant species, is dependent on its concentration. Moreover, chemical nature of the surfactant species also determines the hardness of the corona formed.

The way this corona interacts with the growth of a CeO_2 layer on top of an Au surface may provide insights into its own structure. Accessibility of the reaction precursor to the Au surface and growth direction of the CeO_2 domain will vary whether it forms a uniformly distributed layer around the surface, growing in density as concentration increases or if, on the contrary, its formation is more of a packed molecular domain growing in extension around the particle surface. The final growth mode will be evidenced in the layer's morphology after synthesis.

In order to test CeO_2 capacity to efficiently work as a "negative" for the surfactant corona around Au NPs, the growth reaction was performed over 50 nm Au seeds previously conjugated to increasing amounts of irreversibly bonded surfactant. The model surfactant chosen was mercaptoundecanoic acid (MUA) for its long chain length and high affinity of thiol groups to Au surfaces.[38] The ratio of surfactant-to-surface was calculated assuming a packing area of 0.22 nm^2/molecule for the MUA

and calculating the available Au surface according to the size and concentration of the Au NPs.[39] The experiment was performed for 1:1, 100:1 and 1000:1 surfactant-to-surface ratios. It is not expected for the surfactant to exclusively deposit on top of the particle surface, so the first sample, 1:1 surfactant-to-surface ratio is considered in defect conditions. As expected, while in the absence of MUA a homogeneous CeO_2 layer is grown, the formation of separated domains in the form of clover-like or heterodimer-like structures is observed as MUA concentration is increased (**Figure 4.10**, left). The selective deposition of CeO_2 can be explained by the formation of MUA domains which protect certain areas of the NP surface. As a result, the surface available exposed is reduced, thereby generating binary Au-CeO_2 structures (**Figure 4.10**, middle). Note that if, in subsaturation conditions, MUA was evenly distributed on the surface, the reaction would take longer and would result in less dense coronas, but isotropic still. Finally, when the concentration of MUA is the highest tested, the growth of CeO_2 is almost suppressed, proving that in saturation conditions there is no available surface (**Figure 4.10**, right).

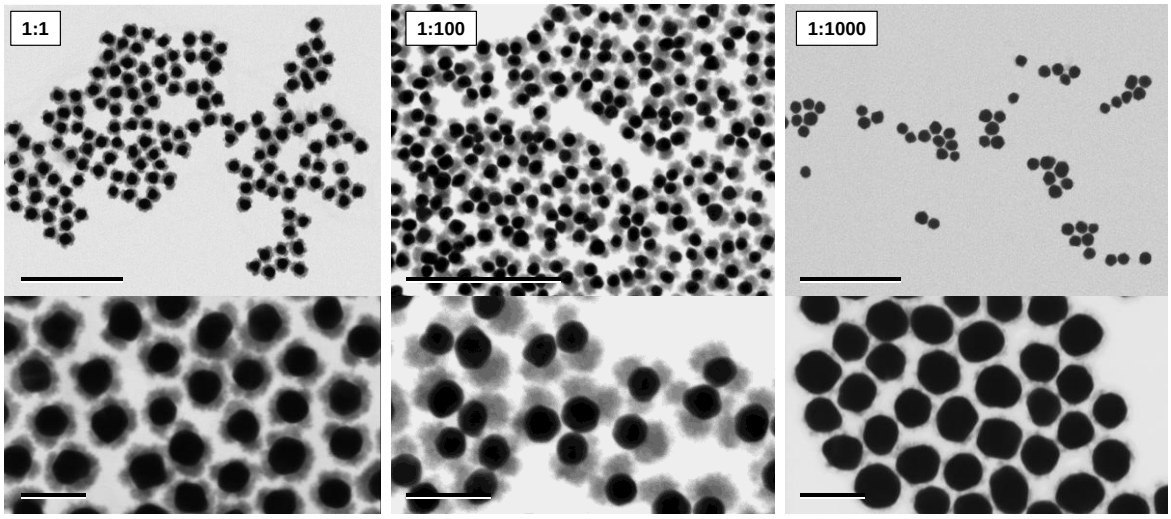

***Figure 4.10**: STEM imaging of $AuCeO_2$ hybrids synthesized by growing the CeO_2 layer onto Au NPs previously conjugated with different amounts of MUA. Surfactant-to-surface ratio from left to right: 1:1, 100:1 and 1000:1. Scale bars: 500 nm (top) and 100 nm (bottom).*

A deeper analysis of the surfactant interaction with the Au surface and its influence can be found in the publication that, following the theoretical Dissipative Particle Dynamics (DPD) simulations performed by Suárez-Lopez, arises from this work. In this paper, where the MUA domain formation is followed, its presence on the Au surface denies the process of full coating of the Au NP.[40]

4.2.3 Combination of one-pot and seeded-growth approaches: Synthesis of hybrid trimers

The versatility of both one-pot and seeded growth strategies described here allow to extensively manipulate the hybrids architecture towards more complex structures by simple variations of the synthetic procedures. Following the scientific spirit of stretching as far as possible the possibilities of structural control over a given system, a last approach is proposed to achieve further levels of complexity on the hybrid's morphology. The combination of one-pot and seeded-growth strategies is carried out by introducing metal seeds to the one-pot setup and performing the co-precipitation of CeO_2 and the metal in presence of said seeds. The resultant metal-oxide-metal structures, herein denoted as hybrid trimers, account for a great variety of complex, colloidally stable structures that are also easily tuned by synthetic parameters such as pH.

For chemical stability issues with Ag NPs (known templates for Au-Ag galvanic replacement[41], and, as demonstrated previously in this text, reactive in CeO_2 environments), in this section Au NPs are chosen as seeds and the co-injection of both Au and CeO_2 precursors and Ag and CeO_2 precursors.

4.2.3.1 Au and CeO_2 precursor co-injection over Au seeds

At the simultaneous addition of equimolar amounts of $HAuCl_4$ and $CeCl_3$ onto a pH-adjusted citrate solution containing also previously synthesised 50 mM Au NPs, both precursors heteronucleate on top of the Au seed surface, forming secondary domains. The kinetics of both reactions is tuned by the solution pH levels. Mild basic conditions (pH 7.5-8) lead to faster precipitation of the Au, while at more basic conditions (pH 9), CeO_2 is the faster to precipitate. It traduces in different morphologies of the resultant trimers: slower CeO_2 precipitation at neutral or mildly basic pH results in thin, elongated semicrystalline Au tails emerging from the Au NPs and surrounded by the CeO_2 shell (**Figure 4.11.a**), structurally similar to a tadpole, while a faster CeO_2 precipitation leads to "*nanostars*" of thick, short Au extrusions over the CeO_2 shell (**Figure 4.11.b**), as the presence of the shell blocks the growth of the Au domain. All these structures are susceptible to forming plasmonic hot-spots due to the spatial confinement of the plasmonic metals.

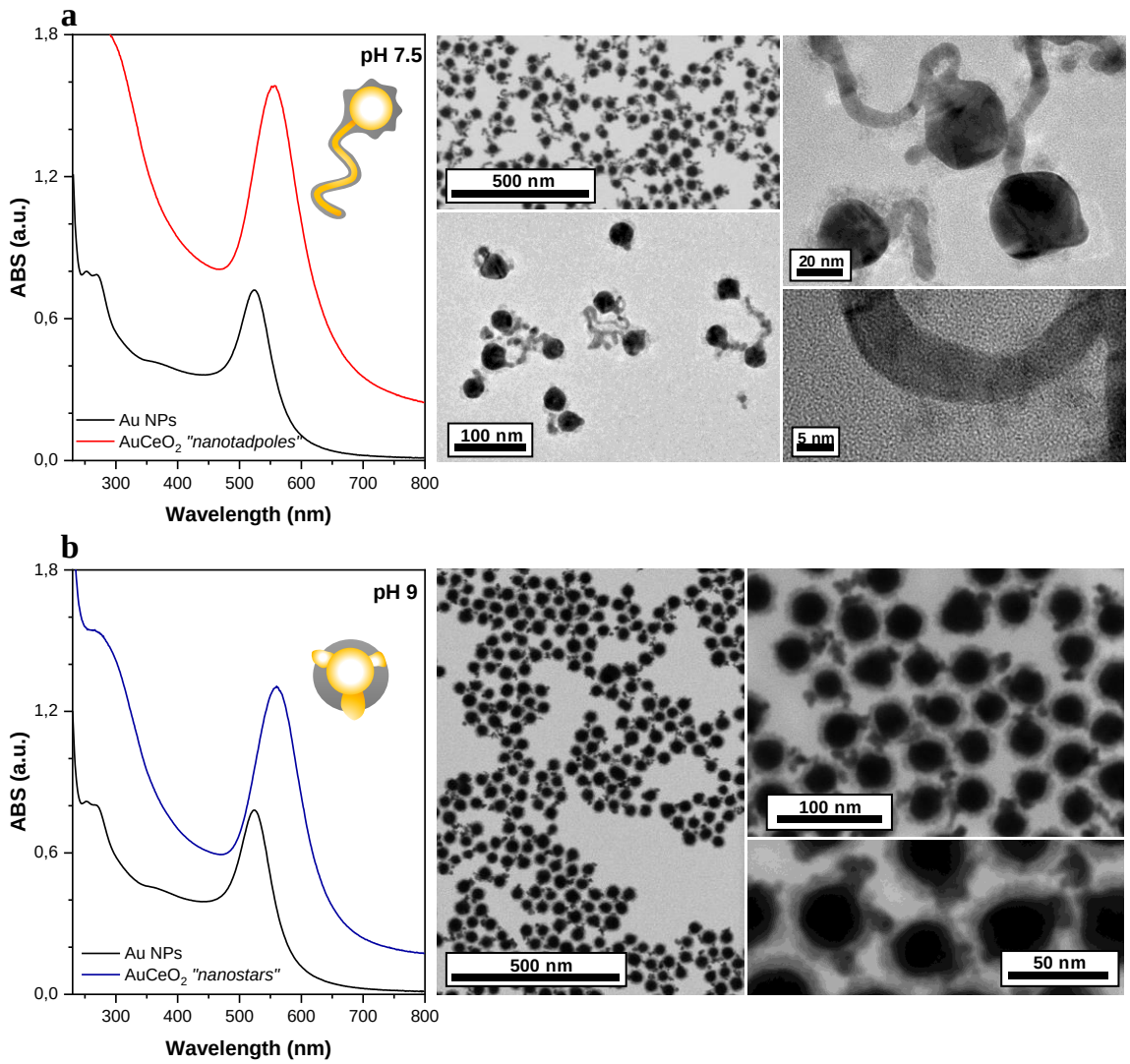

***Figure 4.11**: AuAuCeO₂ hybrid "trimers" synthesized at (a) pH 7.5 and (b) pH 9. Both characterized by UV-Vis spectroscopy (left) and HR(S)TEM (right).*

4.2.3.2 Ag and CeO₂ precursor co-injection over Au seeds

The case of $AgNO_3$ and $CeCl_3$ co-precipitation on top of 30 nm Au seeds is very similar to the previous case. Reactivity is highly dependent on pH, and the final morphology of the hybrid trimer will depend on this parameter. At pH levels below 7.5 the reaction does not take place, and at pH over 10, kinetics both processes are completely disconnected from each other: CeO_2 grows first on top of the Au surface, and later Ag nucleates independently.

At slightly basic conditions (pH 7.5-8), the same way as the $AuCeO_2$ "*nanostars*" from the previous section, Ag is the faster to nucleate in the Au surface, and CeO_2 forms the shell afterwards. However, the nucleation of CeO_2 around the particle causes the dissolution of the just-nucleated Ag due to its reactivity in this almost

neutral environment. As result, the morphologies adopted by the trimers are hollow CeO_2 tubes between an Au and Ag domain (**Figure 4.12.a**). Interplanar distances measured over the marked sections at the bottom of the figure match the (111) distances of CeO_2 (0.31 nm) and Ag (0.24 nm), respectively. If the temperature is maintained at boiling conditions for too long, Ag and CeO_2 will continue to evolve until the Ag completely dissolves and nucleates independently. It is proof of how this product is not a thermodynamically stable one but rather a consequence of kinetic control over the process. Higher basicity (pH 9) translates as faster CeO_2 precipitation kinetics, that results in the formation of a closed CeO_2 shell where Ag heteronucleates (**Figure 4.12.b**) without entering into contact with the Au surface.

An interesting feature of these structures, where both Ag and Au coexist, is that the LSPR of both species remains independent, resulting in very broad band absorbing in almost all the visible range (from 200 to 600 nm), as appears at the UV-vis absorption spectra of the samples. Due to the surface alloying of Au and Ag, the original red-shift of the Au LSPR gets hindered, similarly to the $AgAuCeO_2$ structures of **Figure 4.5**. However, as the CeO_2 shell grows, the surface of the original seeds is no longer available, and the nucleating Ag does not enter into direct contact with it. As a consequence, the LSPR of the Ag particles remains independent.

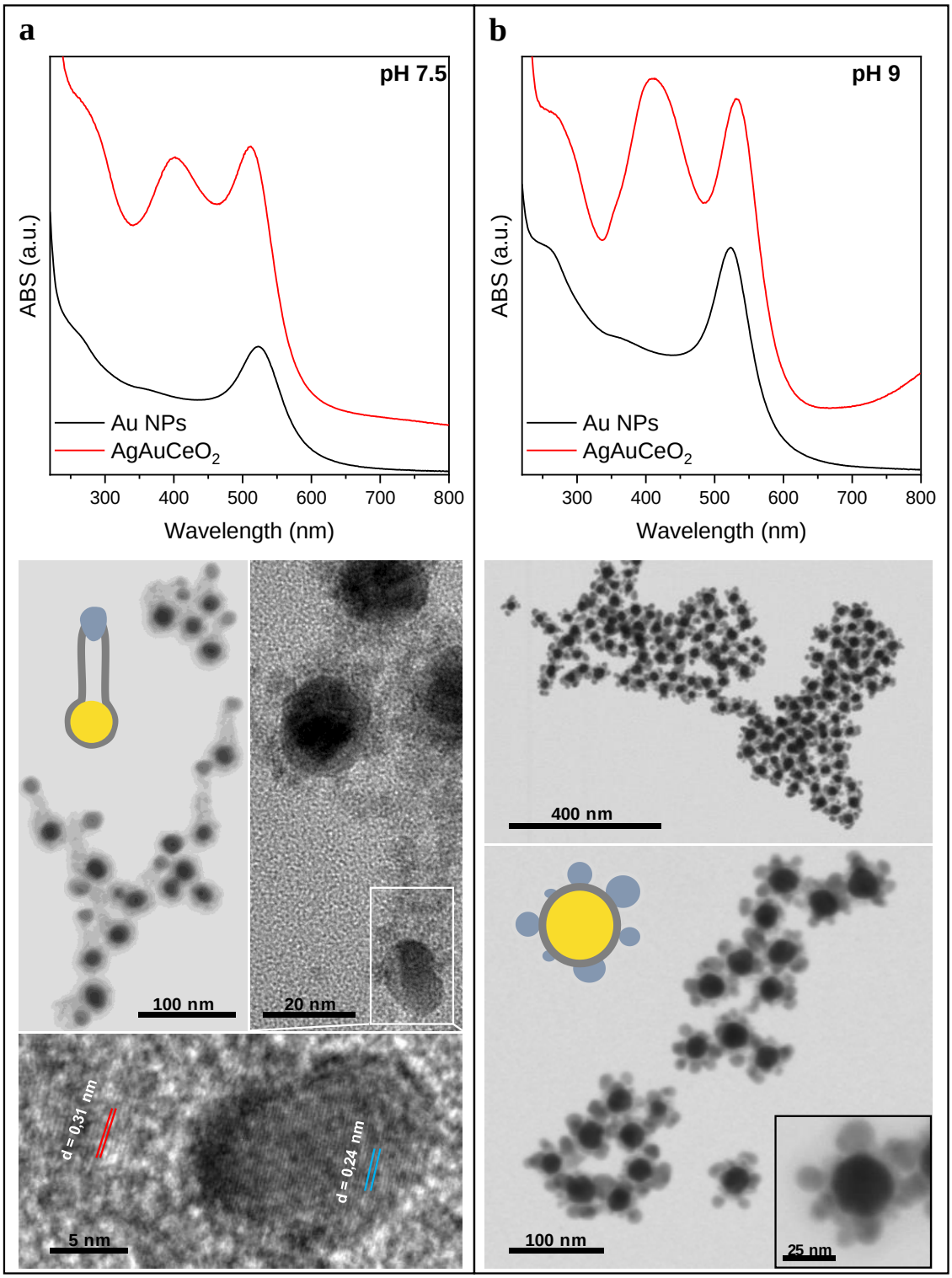

***Figure 4.12**: UV-vis (top) and HR(S)TEM (bottom) characterization of $AgAuCeO_2$ hybrid trimers synthesized at (a) pH 7.5 and (b) pH 9. Diagrams of the trimers are color-coded according to the domain composition: Yellow for Au, blue for Ag and gray for CeO_2.*

4.3 PERSPECTIVES

Besides the possibility of deepening morphology control of the shown hybrids by themselves, several possible pathways exist to increment the complexity and functionality of the Metal@CeO_2 hybrid nanostructures presented in this chapter. A promising strategy would be to increase the number of components of the construction, incorporating structural domains providing support and physicochemical protection for their application in real-life environments.

As a proof-of-concept, $AuCeO_2$ hybrids have been synthesised by both strategies described in this text and then left to be incorporated into different support materials by other PhD students and other personnel from both our group and adjacent groups. Below, a small characterisation of the different materials obtained is provided. Special mention to J. Fonseca for their incorporation onto an UiO-66 MOF structure (**Figure 4.13**), J. Oliveras and M. C. Spadaro for the graphene functionalisation and high-resolution microscopy of $AuCeO_2$-decorated graphene samples (**Figure 4.14**) and to O. H. Moriones for the SiO_2 and polystyrene coating of the material (**Figure 4.15**).

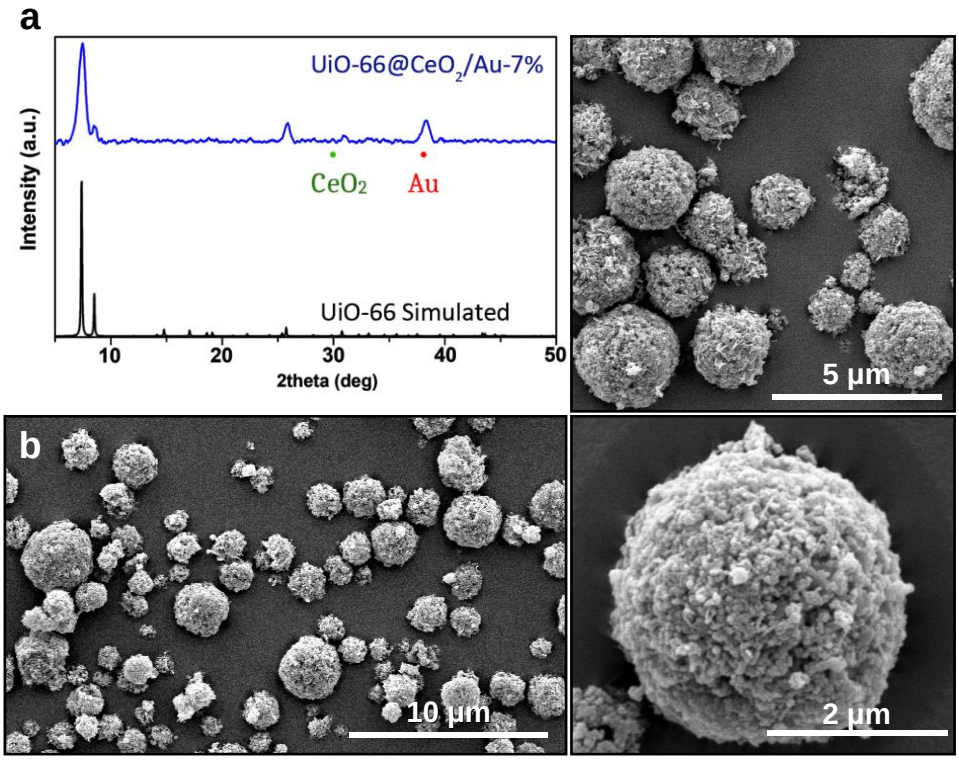

***Figure 4.13**: Representative (a) XRD pattern and (b) FE-SEM images at different magnifications of UiO-66@$AuCeO_2$ (7%)*

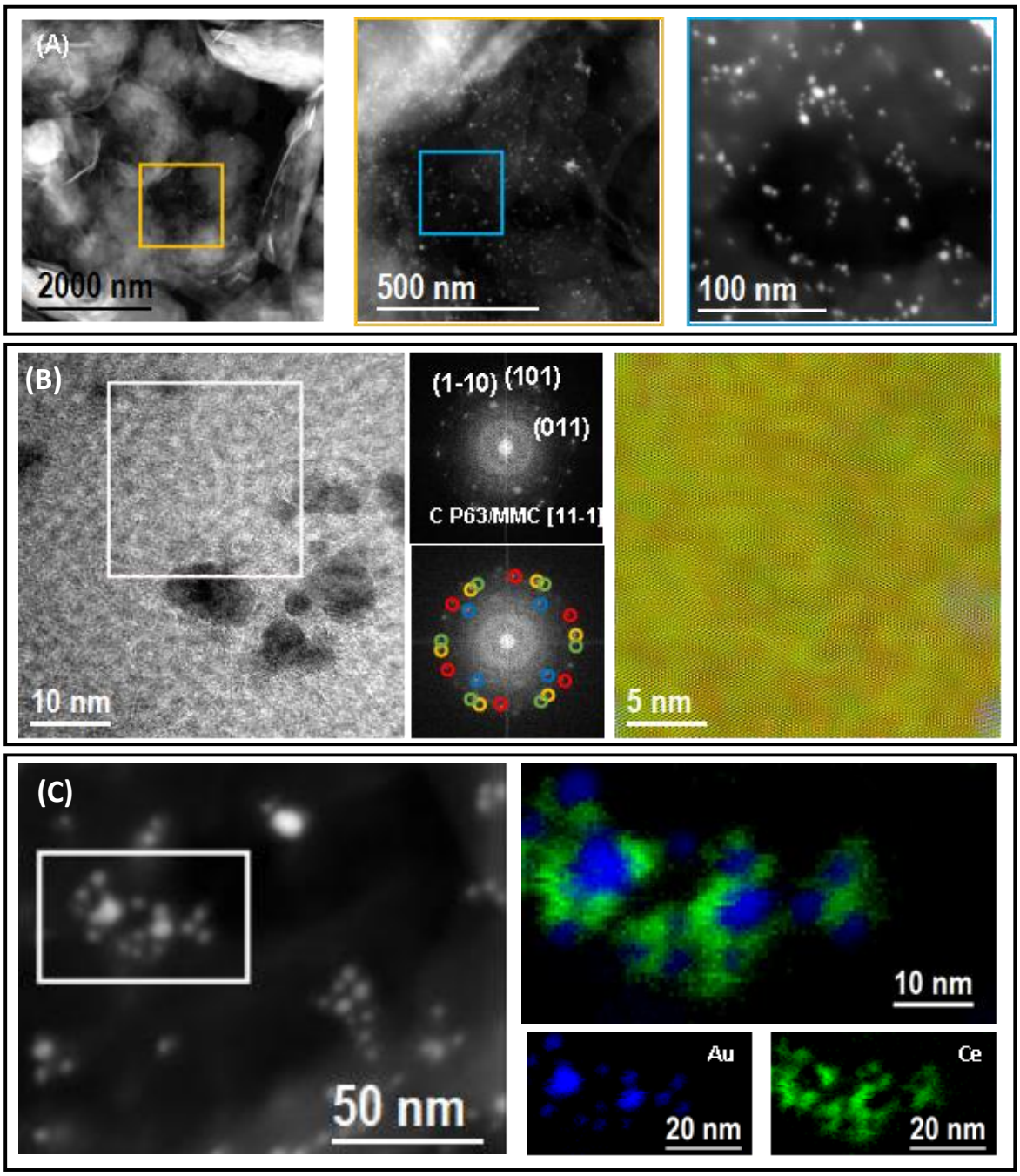

***Figure 4.14**: (A) HAADF-STEM images of the Graphene-AuCeO₂ sample at different magnifications. (B) HRTEM image of the sample, FFT and frequency filtered structural map of the white-marked area. The power spectrum of the white box evidence the graphene flake orientation, highlighted in the coloured frequency filtered structural map. Different orientations are reported in different colour (yellow, green and red). Blue areas on the bottom part corresponds to CeO₂ frequencies. (C) HAADF-STEM image of the sample and STEM-EELS elemental maps obtained on the selected area as indicated in the white box. The maps shown in the Spectrum Images have been obtained by using Au M-edge at 2206 eV (blue) and Ce M-edge at 883 eV (green), as well as composites of Au-Ce.*

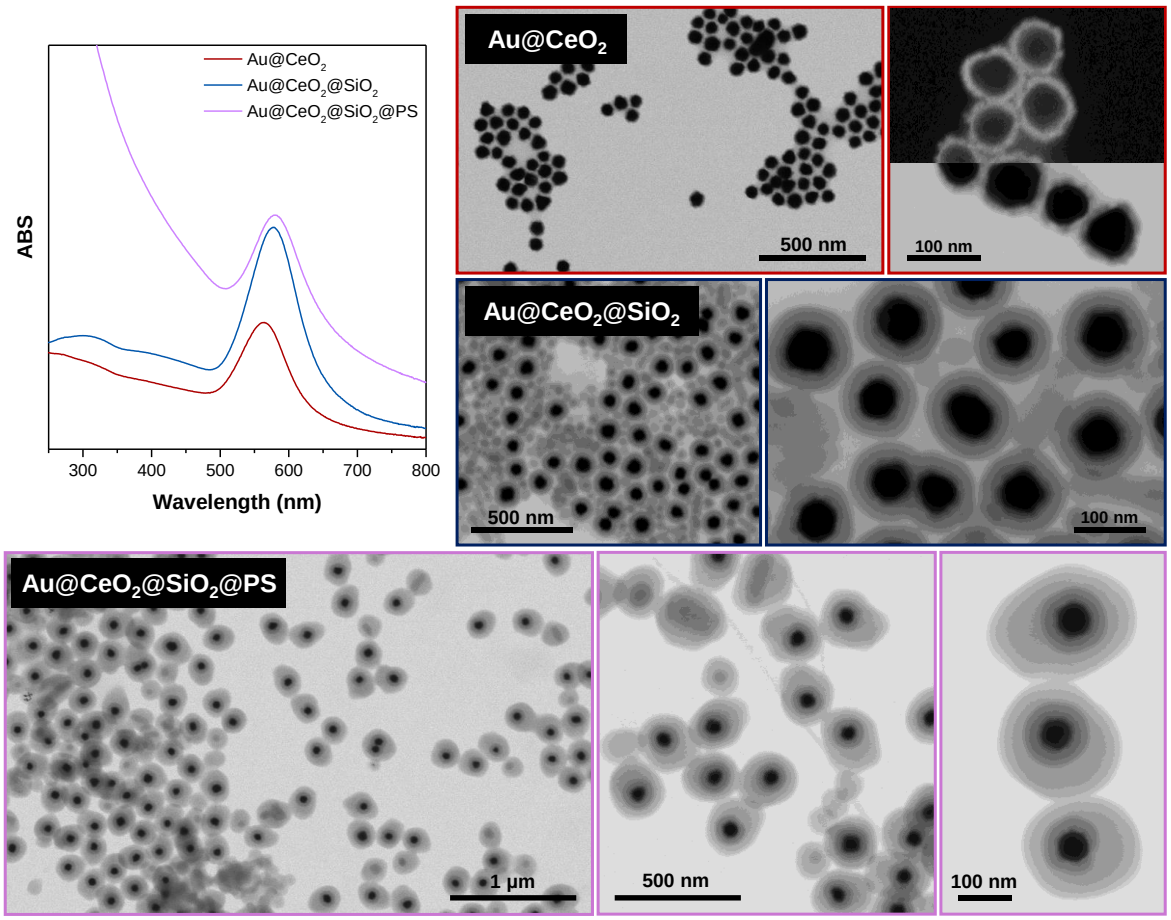

***Figure 4.15**: Characterization of the sequential coating of $Au@CeO_2$ hybrids with SiO_2 and polystyrene (PS) via UV-vis spectroscopy and STEM.*

4.4 REFERENCES

1. Sakthivel, S. *et al.* Enhancement of photocatalytic activity by metal deposition: characterisation and photonic efficiency of Pt, Au and Pd deposited on TiO_2 catalyst. *Water Res* 38, 3001–3008 (2004).

2. Bai, S., Yin, W., Wang, L., Li, Z. & Xiong, Y. Surface and interface design in cocatalysts for photocatalytic water splitting and CO_2 reduction. *RSC Adv* 6, 57446–57463 (2016).

3. Li, J. & Zhang, J. Z. Optical properties and applications of hybrid semiconductor nanomaterials. *Coord Chem Rev* 253, 3015–3041 (2009).

4. Agrawal, A. *et al.* Localized Surface Plasmon Resonance in Semiconductor Nanocrystals. *Chem Rev* 118, 3121–3207 (2018).

5. Banin, U., Ben-Shahar, Y. & Vinokurov, K. Hybrid Semiconductor–Metal Nanoparticles: From Architecture to Function. *Chemistry of Materials* 26, 97–110 (2013).

6. Zhang, C., Zhang, Y. & Xie, W. Plasmonic metal/semiconductor hybrid nanomaterials for solar to chemical energy conversion. *Journal of Energy Chemistry* 63, 40–53 (2021).

7. Zhang, P., Wang, T. & Gong, J. Mechanistic Understanding of the Plasmonic Enhancement for Solar Water Splitting. *Advanced Materials* 27, 5328–5342 (2015).

8. Cho, S., Yim, G., Park, J. T. & Jang, H. Surfactant-free one-pot synthesis of Au-TiO_2 core-shell nanostars by inter-cation redox reaction for photoelectrochemical water splitting. *Energy Convers Manag* 252, 115038 (2022).

9. Chen, Y., Gao, N. & Jiang, J. Surface Matters: Enhanced Bactericidal Property of Core–Shell Ag–Fe_2O_3 Nanostructures to Their Heteromer Counterparts from One-Pot Synthesis. *Small* 9, 3242–3246 (2013).

10. Fantechi, E. *et al.* Seeded Growth Synthesis of Au–Fe_3O_4 Heterostructured Nanocrystals: Rational Design and Mechanistic Insights. *Chemistry of Materials* 29, 4022–4035 (2017).

11. Liu, L. *et al.* Au–ZnO hybrid nanoparticles exhibiting strong charge-transfer-induced SERS for recyclable SERS-active substrates. *Nanoscale* 7, 5147–5151 (2015).

12. Qiu, E. *et al.* Fabricating Dual-Functional Plasmonic-Magnetic Au@$MgFe_2O_4$ Nanohybrids for Photothermal Therapy and Magnetic Resonance Imaging. *ACS Omega* 7, 2031–2040 (2022).

13. Wu, B. *et al.* Anisotropic Growth of TiO_2 onto Gold Nanorods for Plasmon-Enhanced Hydrogen Production from Water Reduction. *J Am Chem Soc* 138, 1114–1117 (2016).

14. Wang, Y. *et al.* Length-Dependent Photocatalytic Activity of Hybrid Ag-CdS Nanorods. *The Journal of Physical Chemistry C* 126, 15685–15693 (2022).

15. el Mel, A. A., Nakamura, R. & Bittencourt, C. The Kirkendall effect and nanoscience: hollow nanospheres and nanotubes. *Beilstein Journal of Nanotechnology 6:139* 6, 1348–1361 (2015).

16. Tu, K. N. & Gösele, U. Hollow nanostructures based on the Kirkendall effect: Design and stability considerations. *Appl Phys Lett* 86, 093111 (2005).

17. Merkoçi, F. *et al.* Understanding galvanic replacement reactions: the case of Pt and Ag. *Mater Today Adv* 5, 100037 (2020).

18. Qi, J. *et al.* Facile synthesis of core–shell Au@CeO_2 nanocomposites with remarkably enhanced catalytic activity for CO oxidation. *Energy Environ Sci* 5, 8937–8941 (2012).

19. Mitsudome, T. *et al.* One-step Synthesis of Core-Gold/Shell-Ceria Nanomaterial and Its Catalysis for Highly Selective Semihydrogenation of Alkynes. *J Am Chem Soc* 137, 13452–13455 (2015).

20. Mitsudome, T. *et al.* Design of a Silver–Cerium Dioxide Core–Shell Nanocomposite Catalyst for Chemoselective Reduction Reactions. *Angewandte Chemie International Edition* 51, 136–139 (2012).

21. Li, B. *et al.* (Gold Core)@(Ceria Shell) Nanostructures for Plasmon-Enhanced Catalytic Reactions under Visible Light. *ACS Nano* 8, 8152–8162 (2014).

22. Bastús, N. G. *et al.* Robust one-pot synthesis of citrate-stabilised Au@CeO_2 hybrid nanocrystals with different thickness and dimensionality. *Appl Mater Today* 15, 445–452 (2019).

23. Piella, J. *et al.* Seeded-Growth Aqueous Synthesis of Colloidal-Stable Citrate-Stabilized Au/CeO_2 Hybrid Nanocrystals: Heterodimers, Core@Shell, and Clover- and Star-Like Structures. *Chemistry of Materials* 31, 7922–7932 (2019).

24. Floro, J. A., Chason, E., Cammarata, R. C. & Srolovitz, D. J. Physical Origins of Intrinsic Stresses in Volmer–Weber Thin Films. *undefined* 27, (2002).

25. G. Bastús, N., Comenge, J. & Puntes, V. Kinetically Controlled Seeded Growth Synthesis of Citrate-Stabilized Gold Nanoparticles of up to 200 nm: Size Focusing versus Ostwald Ripening. *Langmuir* 27, 11098–11105 (2011).

26. Ji, X. *et al.* Size Control of Gold Nanocrystals in Citrate Reduction: The Third Role of Citrate. *J Am Chem Soc* 129, 13939–13948 (2007).

27. G. Bastús, N., Piella, J. & Puntes, V. Quantifying the Sensitivity of Multipolar (Dipolar, Quadrupolar, and Octapolar) Surface Plasmon Resonances in Silver Nanoparticles: The Effect of Size, Composition, and Surface Coating. *Langmuir* 32, 290–300 (2016).

28. Luis Montaño-Priede, J., Peña-Rodríguez, O. & Pal, U. Near-Electric-Field Tuned Plasmonic Au@SiO_2 and Ag@SiO_2 Nanoparticles for Efficient Utilisation in Luminescence

Enhancement and Surface-Enhanced Spectroscopy. *The Journal of Physical Chemistry C* 121, 23062–23071 (2017).

29. Schulz, F. *et al.* Little Adjustments Significantly Improve the Turkevich Synthesis of Gold Nanoparticles. *Langmuir* 30, 10779–10784 (2014).

30. Rodea-Palomares, I. *et al.* Physicochemical Characterization and Ecotoxicological Assessment of CeO_2 Nanoparticles Using Two Aquatic Microorganisms. *Toxicological Sciences* 119, 135–145 (2011).

31. Yu, T., Lim, B. & Xia, Y. Aqueous-Phase Synthesis of Single-Crystal Ceria Nanosheets. *Angewandte Chemie International Edition* 49, 4484–4487 (2010).

32. Dong, X. *et al.* Shape Control of Silver Nanoparticles by Stepwise Citrate Reduction. *The Journal of Physical Chemistry C* 113, 6573–6576 (2009).

33. G. Bastús, N., Merkoçi, F., Piella, J. & Puntes, V. Synthesis of Highly Monodisperse Citrate-Stabilized Silver Nanoparticles of up to 200 nm: Kinetic Control and Catalytic Properties. *Chemistry of Materials* 26, 2836–2846 (2014).

34. Zhang, Q., Zhang, T., Ge, J. & Yin, Y. Permeable silica shell through surface-protected etching. *Nano Lett* 8, 2867–2871 (2008).

35. Channei, D. *et al.* Aqueous and surface chemistries of photocatalytic Fe-doped CeO_2 nanoparticles. *Catalysts* 7, (2017).

36. Holmberg, K. Surfactant-templated nanomaterials synthesis. *J Colloid Interface Sci* 274, 355–364 (2004).

37. Sujana, M. G., Chattopadyay, K. K. & Anand, S. Characterization and optical properties of nano-ceria synthesised by surfactant-mediated precipitation technique in mixed solvent system. *Appl Surf Sci* 254, 7405–7409 (2008).

38. G. Pearson, R. Hard and Soft Acids and Bases. *J Am Chem Soc* 85, 3533–3539 (2002).

39. Hiramatsu, H. & E. Osterloh, F. pH-Controlled Assembly and Disassembly of Electrostatically Linked CdSe−SiO_2 and Au−SiO_2 Nanoparticle Clusters. *Langmuir* 19, 7003–7011 (2003).

40. Suárez-López, R., Puntes, V. F., Bastús, N. G., Hervés, C. & Jaime, C. Nucleation and growth of gold nanoparticles in the presence of different surfactants. A dissipative particle dynamics study. *Scientific Reports 2022 12:1* 12, 1–12 (2022).

41. Russo, L. *et al.* Time- and Size-Resolved Plasmonic Evolution with nm Resolution of Galvanic Replacement Reaction in AuAg Nanoshells Synthesis. *Chemistry of Materials* 30, 5098–5107 (2018).

CHAPTER V

CATALYTIC APPLICATIONS OF CeO_2-BASED NANOSTRUCTURES

CHAPTER V

CATALYTIC APPLICATIONS OF CeO_2-BASED NANOSTRUCTURES

5.1 INTRODUCTION

Practical applications are one of the pillars of material-related research for the generation of scientific advances. In this matter, the production of the minimal stable size for CeO_2 NCs and their derivation through doping and hybridization should be put to the test to consider which practical improvements the synthesised materials may bring. As described in section 1.5 (Chapter I), the applicability of nanomaterials revolves mainly around their catalytic properties. This aspect defines the final purpose of a nanomaterial in different fields such as industrial chemistry, energy production or biomedicine. Under this premise, this chapter addresses bibliographically the current state of catalytic applications of CeO_2-based materials and the perspectives brought by this approach towards the optimised formulation of CeO_2 nanomaterials. However, an experimental review of these aspects falls out of the expertise developed. Instead, a characterization of the developed materials in terms of reactivity towards different processes, as proof-of-concept of possible industrial applications that may be developed in further works, is presented.

In the last fifty years, many CeO_2-based materials have been developed and tested for their application in catalysis for different fields. The interest in this material emerges from its remarkable activity as a redox catalyst, which arises from the characteristic Oxygen Storage Capacity (OSC) of the material. OSC or "*electron sponge*" properties refer to the lability of near-surface lattice oxygen of CeO_2, which allows for the formation of oxygen vacancies within the structure and makes the material a non-stoichiometric compound (equation 5.1). Oxygen vacancies in the

surface are bosom for catalyzed redox processes, as they conform an active site where adsorption can take place, and the absence of oxygen leaves behind a charge excess (as equation 5.2 evidences) that promotes different reactions in order to regain charge balance. The location of the two electrons left behind by the formation of every oxygen vacancy is still a matter of discussion. It has been described in the literature as a valence switch between 3+/4+ oxidation states in neighbouring atoms in order to assimilate charge excess, which avoids altering the crystalline structure (meaning that no surface transformations towards Ce_2O_3 occur).[1,2] Computational studies, however, have pointed out how the nearest neighbour atoms to the oxygen vacancy in CeO_2 hold a 4+ oxidation state, localising the excess of charge away from the vacancy.[3,4] This matter is further developed in Chapter VI, where the electronic structure of the material is discussed. This section is focused on the consequences of this electronic structure over the surface reactivity of CeO_2 and its potential catalytic applications.

$$CeO_2 \rightarrow CeO_{2-x} + \frac{x}{2}\, O_2 \tag{5.1}$$

$$O^{2-}_{lattice} \rightarrow \frac{1}{2} O_2 + 2e^- \tag{5.2}$$

5.1.1 Nanostructured CeO_2 in Catalysis

On the matter of catalytic applications, many works review the current and future operation of CeO_2-based materials in different areas within industry and research.[5,6] While many other materials such as precious metal present stronger activities, the role of metal oxides as both structural and catalytic supports for metallic NPs continues to be a topic in the conversation as proves to be a key aspect for optimization and cost reduction in the field. The most widespread use of CeO_2 is in the automotive industry, as part of the TWCs (combined to other catalysts such as Rh, Pt and Pd) for the treatment of exhaust steams (CO/NO_x transformation to CO_2 and N_2, and the oxidation of unburnt hydrocarbons),[7] preventing pollutant liberation to the atmosphere, and as a catalyst for soot combustion in diesel engines. For this kind of application, the most common formulation is the solid solution of CeO_2-ZrO_2.

ZrO_2 enhances the OSC of the material and plays a role in the prevention of sintering at high temperatures. Another well-known application of the material is both as a structural component or catalyst in fuel cells for environmentally friendly energy generation.[8]

The current interest in nanocatalytic CeO_2 research lies mainly in two well-differentiated branches: processes related to clean energy generation and other industrial operations, and biological applications. Energy and industry include different reforming processes, Water-gas shift reaction and photocatalysis, among others, where nanoscale properties of materials are a feature rather than a characteristic condition to carefully engineer. For biological applications, on the other side, colloidal properties play a key role in the material's functionality and toxicity. The latter will be reviewed separately due to the vastness of the topic.

Steam reforming (involving the reaction of the chosen hydrocarbon with water) is the typical industrial route for hydrogen production. Methane, at 900ºC, is the most common hydrocarbon employed. Reforming processes refer to the synthesis gas (*syngas*) production from hydrocarbons (equation 5.3). *Syngas* is the mixture of CO and H_2 gases in an undetermined ratio. It is employed mainly for the production of fuels. Methanol and ethanol are also interesting alternatives to methane for reforming, as they are liquid reagents that are easier and cheaper to manipulate, allow for the reaction to be performed at lower temperatures (200-300ºC) and the still high hydrogen to carbon ratio ensures a higher energy density than other long-chain hydrocarbons that share the other two characteristics.[9] For that, CeO_2-ZrO_2 is again the most explored system among CeO_2-based materials acting as catalysts for these processes.[10] Au and other noble metals such as Pd in combination with CeO_2 are also emerging as promising catalysts for methanol and ethanol reforming respectively, mechanistically evidencing the importance of the role of oxygen vacancies on the overall catalytic process.[11,12]

$$C_nH_m + nH_2O \rightarrow nCO + \ (n + \frac{m}{2})H_2 \qquad (5.3)$$

The Water-Gas Shift Reaction (WGSR) between CO and water to produce CO_2 and H_2 (equation 5.4) is employed to adjust H_2/CO ratio on *syngas* before using it as a reactant for chemical processes requiring specific concentration conditions, and even

to purify the H_2 stream under the adequate setup. There exists a large trace of different CeO_2-based materials within the literature that prove to be active for the catalysis of the WGSR, especially metal-supported CeO_2, both pure, doped, or mixed with other oxides.[13]

$$CO + H_2O \rightarrow CO_2 + H_2 \quad (5.4)$$

CeO_2 has also brought attraction for photocatalytic processes such as the water splitting reaction as a potential alternative to TiO_2. It also is a wide bandgap semiconductor capable of generating charge carriers upon UV light illumination, and its characteristic oxygen vacancies have been shown to act as electron traps preventing recombination as well as adsorption sites for catalytic processes.[14,15] Nonetheless, global efficiencies of these applications are yet to demonstrate if CeO_2 can substitute TiO_2.

CeO_2 is also widely used as a UV blocker in glass and polymers. Transition metal doping is reported to be a working strategy towards the enhancement of carrier mobility,[16] and Yb^{3+}/Er^{3+} co-doped CeO_2 nanoparticles show NIR-to-visible upconversion properties, even if these were not possible to be reproduced within our CeO_2 NC formulation.[17,18] Other catalytic applications of CeO_2-based materials worth mentioning are the oxidation of organic pollutants[19] and dehalogenation (oxidation of HCl) from industrial wastewaters,[20] as a catalyst for organic chemistry reactions,[21] and to produce liquid hydrocarbons from *syngas* and other gas-phase reagents.[22]

5.1.2 ROS scavenging properties of CeO_2

The most remarkable applicability nanosized CeO_2 holds probably falls within the biomedical field, both for diagnosis and disease treatment. The OSC of the material allows it to work as a radical scavenger for biological systems, exhibiting antioxidant properties. Free radicals are naturally produced in the form of ROS and RNS molecules in aerobic metabolic processes. They hold key roles in several biological processes, but their excess induces oxidative stress, which causes damage to biomolecules such as DNA or phospholipids and is related to several other

alterations, including cell death. Among them, ROS are highly related to inflammation processes, which take part in the majority of pathologies and diseases affecting our organism.[23]

There exist several metabolic routes which regulate ROS/RNS concentrations, governed by different enzymes (SOD, Catalase, glutathione peroxidase, oxidase…) according to the substrate molecule they act on, as well as endogenous and exogenous antioxidant molecules that can suppress the free radical presence (see Chapter I section 1.5.1). In recent years, nanosized CeO_2 has been thoroughly reported as a buffer for ROS in the organism, active to excess concentrations but inactive at functional ROS levels. Another advantage of nanosized CeO_2 is that it is able to mimic several enzymatic processes thanks to its selectivity towards unpaired electrons rather than a specific molecule.[24] As with any other enzyme-mimicking nanomaterial, it is important to mention that CeO_2 NCs are not a mere provider of Ce^{4+} ions but an active principle whose properties are held by the solid-state nature of the material. The catalytic cycle at play, illustrated by equations 5.5 and 5.6, seems to enter action only under enough concentration of the radical molecule, allowing space for the biological functions of these species to be fulfilled and acting only in their excess.[25]

$$CeO_2 + xOH^{\cdot} \rightarrow CeO_{2-x} + \frac{x}{2}O_2 + H^+ \quad (5.5)$$

$$CeO_{2-x} + xOH^{\cdot} \rightarrow CeO_2 + OH^- \quad (5.6)$$

Upon its success as a radical scavenger, nano-formulated CeO_2 can be enabled as an antioxidant substance surpassing the limitations of previous antioxidant therapies, whose high uncontrolled reactivities and limited absorption profiles affect their final performance.[26] CeO_2 has been studied for its potential effect against oxidative stress on related pathologies such as chronic inflammation[27], ischemia,[28] neurodegenerative disorders (Parkinson's and Alzheimer's diseases or ageing, for example, are associated with a higher uptake of O_2 of the nervous system, which make it more susceptible to oxidative stress),[29] diabetes,[30] cancer (as evidenced by the Warburg effect),[31,32] etc... It also holds beneficial properties for regenerative medicine, as one of the biggest challenges nowadays on the field is to overcome inflammation.[33]

One of the main concerns about CeO_2 formulation towards the biomedical field is its biocompatibility. The low biodegradability causes it to accumulate in the liver and spleen on the organisms, and the long-term effects of the accumulation are not yet clear.[34] It has been tested both *in vitro* and *in vivo*, and while there are still gaps to fill on the topic of the safety of inorganic nanomaterials, CeO_2 does not seem to present high risks to the organism by itself. In fact, observed toxicity may arise from size, shape, excipients and other intermediate species present on the nanoparticle formulation, and aggregation profile of the nanocrystals, usually caused by the uncontrolled dispersion into highly saline biological media.[35,36] Therefore, well-described CeO_2 NCs of small and monodisperse size distribution dispersed in biological media should not raise concerns about its safety under the adequate dose and proper handling of the colloids.[37]

Radical scavenging properties also serve as tool for diagnosis through biosensing applications. CeO_2 acts as a free radical probe for colourimetric immunoassays by oxidising an organic reporter molecule in the presence of H_2O_2, replacing antibodies and natural enzymes in ELISAs.[38] For this application, the stability of the inorganic nanocrystal presents as an advantage, as enzymes may undergo denaturalisation and deactivation. It can also be used as the colourimetric reporter itself since the colour of the CeO_2 NC dispersion changes as catalytic activity increases the number of oxygen vacancies.[39] A CeO_2-based device has been reported to detect chronic inflammation, distinguishing between normal and altered physiological levels of ROS and pH, based on the enzyme-mimetic properties of CeO_2 and their pH dependence.[40]

Besides the radical scavenging, nanosized CeO_2 also shows other enzyme-mimetic catalytic properties,[41] like DNA photolyase-mimetic activity, which is not present on the human organism.[42] The ability to repair damage caused by UV radiation in DNA, coupled with the radical scavenging properties and the UV shielding properties from its extinction profile, may come as a significant advance in regenerative medicine, especially in dermatology, for preventing skin diseases associated to exposure to radiation.[43]

5.2 RESULTS

The proper evaluation of the catalytic properties of the synthesised materials would require a degree of dedication and expertise on the matter worth another completely different PhD dissertation. In order to take the characterization of the different CeO_2-based materials one step further, however, a series of tests to serve as proof-of-concept for surface reactivity in several model reactions have been performed. Within the group's expertise, the main function studied of CeO_2-based materials is ROS scavenging. However, through collaborations with experts from different research areas the study of applicability alternatives beyond the biomedical field has been assesed. These tests have served not only to stablish a comparison between the different synthesized materials but also to understand the perspective and necessities of the different fields of application of the materials, gaining valuable insight about the importance of taking into account the final target of a material at the design stage, as the material's formulation beyond its physicochemical characterization can render useless the most advanced material.

In the following, a brief description of the use of nanostructured CeO_2 for carbon reduction, and its application to buffer ROS in biological context is described.

5.2.1 CO_2 Reduction

The chosen reaction for the evaluation of the reactivity of the synthesised nanomaterials is the reduction of CO_2 to other molecules of interest such as methanol (MeOH, CH_3OH) (equation 5.7). Hydrogenation of CO_2 is an interesting approach for recycling a major air pollutant, and methanol is a common industrial substance employed both as fuel and in the production of other chemicals, which makes it a desirable product. The reaction, however, is described in the literature as a challenging process due to the difficulties for the activation of the CO_2 molecule and the possibility of side reactions lowering the reaction yield.[44]

$$CO_2 + 3H_2 \rightarrow CH_3OH + H_2O \qquad \Delta H^0_{298\,K} = -49.5\ kJ/mol \tag{5.7}$$

$$CO_2 + 3H_2 \rightarrow CH_4 + 2H_2O \qquad \Delta H^0_{298\,K} = -164.8\ kJ/mol \tag{5.8}$$

$$CO_2 + H_2 \rightarrow CO + H_2O \qquad \Delta H^0_{298\,K} = 42.1\ kJ/mol \tag{5.9}$$

Acording to the literature, reverse WGSR (eq. 5.9) can take place at high temperatures and produce CO and excess water that may tamper with the catalyst activity. To avoid it favouring methanol production (eq. 5.7), lower temperatures and higher pressures, according to Le Chatelier's principle, should displace the equilibrium between both chemical processes towards the production of methanol.[45] The main competition, however, is established between methanol production and methanation (eq. 5.8), as both are exothermic processes. In order to attain high selectivity, an adequate catalyst able to activate the CO_2 molecule at low temperature, breaking only one of the C-O bonds, should be employed. For that, conventional catalysts are dispersed metals in oxides, being the most commonly employed combinations of $Cu/ZnO/Al_2O_3$. Oxides prove to facilitate CO_2 activation, and the metal cores the H_2. It has been proposed that high defect density in oxides enhances the surface chemistry towards CO_2 activation, so CeO_2 is a potentially good candidate for the substitution of ZnO. Au-CeO_2 systems can be found in the literature, studied in the context of this reaction, proving how important is the presence of a metal-oxide interface for the CO_2 transformation into methanol.[46]

The proof-of-concept of the reactivity for the different CeO_2-based NC in this context was assessed for the described reaction, and the preliminary results obtained are summarised here. The synthesized nanomaterials were dryed and milled by hand to obtain fine powders which were exposed in a reaction chamber to a gas flow composed by the reactants of equations 5.7 to 5.9 at different temperatures. The output stream was collected and its composition analysed by gas chromatography in order to determine if any chemical transformation takes place in the presence of the tested CeO_2-based nanomaterial.

The flow rate was adjusted to a 10 mL/min flow rate at temperatures ranging from 180ºC to 300ºC. The tests have been performed at a moderate pressure of 10 bar and, for some cases, also at 15 bar in order to test the impact of the parameter. Samples tested came from colloidal NCs previously synthesised and dried at 60ºC overnight: CeO_2 NCs, Au NCs, $AuCeO_2$ NCs (synthesised by the One-pot method at a 1:3 precursors ratio) and CeO_2:Yb, Er of different doping concentrations. Further technical details may be checked in section 7.5.1 of chapter VII. Evaluated parameters to determine whether if a chemical reaction had taken place or not in the reactor were: space-time yield (STY), understood as the mass of MeOH produced

per mass of nanomaterialt and time (units mg/g·h), and selectivity (%) between the three possible products described in eqs. 5.7-5.9. While being a parameter of interest, experimental setup did not allow for the correct assessment of the reagent conversion as no *in situ* measurement of the composition of the entrance stream could be performed.

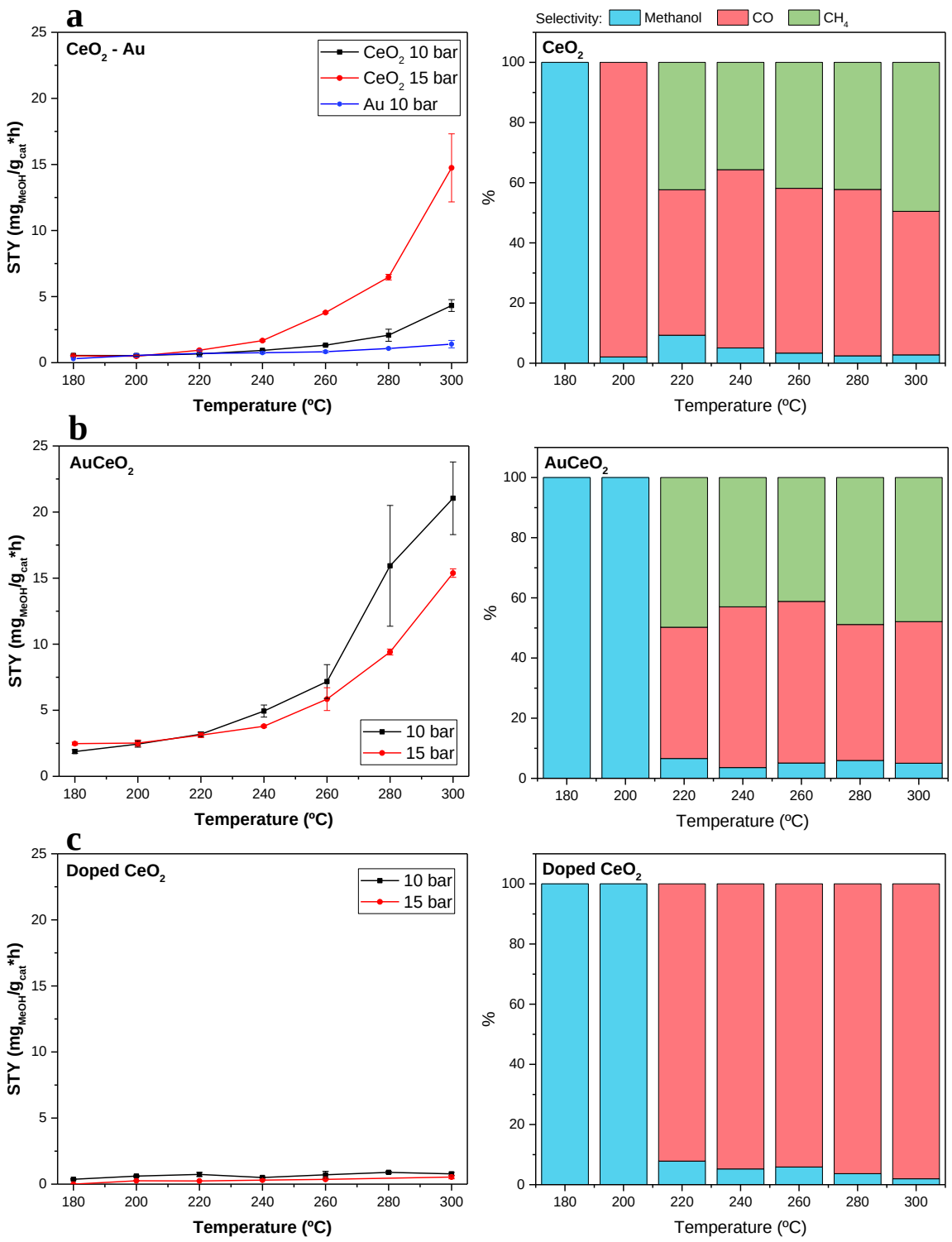

***Figure 5.1**: STY(left) and selectivity (right) values at different temperatures for the reactivity tests towards CO_2 hydrogenation in the presence of (a) CeO_2 NCs and Au NCs, (b) $AuCeO_2$ NCs and (c) CeO_2:Er (5%) NCs.*

Space-time yields at different temperatures for the tested nanomaterials are plotted in **Figure 5.1(left)**. Some kind of activity is recorded for the CeO_2 and the $AuCeO_2$ NC samples. In the presence of the doped CeO_2 NC samples and the Au NC control, on the other hand, does not seem to occur any chemical process, as the low and constant values of STY at different temperatures evidence. Interestingly, for the $AuCeO_2$ NCs, STY at 10 bar reaches a value of 21.6 $mg_{MeOH}.g_{cat}^{-1}.h^{-1}$ at 300ºC, while CeO_2 NCs reaches 4,3 $mg_{MeOH}.g_{cat}^{-1}.h^{-1}$ and Au NPs 1.4 $mg_{MeOH}.g_{cat}^{-1}.h^{-1}$ at the same temperature: further proof of the synergistic effects emerging from the integration of both components on a single structure, as the measured values surpass the ones resulting from the sum of the individual components. For CeO_2 NCs, STY increases with pressure, while for the rest of the materials works the other way around. At 15 bar, however, STY for CeO_2 and $AuCeO_2$ is very similar (14.8 and 15.8 $mg_{MeOH}.g_{cat}^{-1}.h^{-1}$, respectively). These results appear to be very promising when compared to STY of other nanomaterials made of Cu and ZnO, the typical composition of commercial catalysts for this reaction, which are reported to reach values around 50 $mg_{MeOH}.g_{cat}^{-1}.h^{-1}$ in the same conditions.[47] However, it is important to remark that these are preliminary tests and the obtained results come form an experimental design thought as proof-of-concept. There are still many variabilities to take into account in order to describe these materials as catalyst of any kind. Lanthanide-doped CeO_2 NCs did not generate STY of any significance no matter dopant concentration or temperature, evidencing a disruption of the intrinsic properties of pure CeO_2.

While values of STY seem to be somehow noteworthy, the composition of the output stream of the reactor evidences poor selectivity when STY increases (**Figure 5.1, right**). It should not be assumed however that no other species are formed: the formation of formic acid, formaldehyde and other intermediates has not been evaluated. Higher temperatures favour the production of carbon monoxide, as predicted through Le Chatelier's principle. It is, however, a drawback the high fraction of methane produced in the presence of both CeO_2 and $AuCeO_2$ NCs at temperatures over 220ºC. While it implies an evident deviation from the standard selectivity requirements, it leaves room for improvement upon the optimization of the formulation of the nanomaterials, as these are still preliminary results. The differences on the catalytic behaviour of the nanomaterials towards the same chemical process are consequence of their different structures. It is evidenced the

potential of hybrid nanostructures as catalytic tools in comparision to their pure counterparts, consequence of the intimate contact between both components.

It is worth noting that, for this kind of application, the nanomaterial needs to be formulated as a solid powder rather than a colloidal dispersion. In this regard, sample preparation requires purification and drying processes that may cause sintering and other phenomena that ultimately translate into the loss of active surface. In this case, we cannot ensure the degree of impact of this parameter in the final catalytic activity measured, as the catalysts design was originally optimised towards colloidal applications. Even so, in order to ensure maximum dispersion of the nanocrystals, a third, structural component, the MOF scaffold, is being introduced in the system: Following the fashion of a previous collaboration work from the group,[48] CeO_2 NCs, Au NCs, and $AuCeO_2$ NCs have been encapsulated into the Metal-Organic Framework (MOF) UiO-66 (See section 4.3 in chapter IV). They will be tested in the same conditions as the naked NCs, in order to assess the performance of the NCs in terms of yields and selectivity, attempting to optimize the material for the application at hand from the perspective of the interaction with the supporting component. As previously mentioned, the presented tests are preliminary results, part of a bigger experimental set aimed towards the design of advanced functional materials.

5.2.2 Radical scavenging activity

A common molecule employed as a ROS model is hydrogen peroxide (H_2O_2). The pathway towards its degradation goes by the split of the O-O bond, which generates the hydroxyl radical species $OH^{\cdot}$, and finally, molecular oxygen and protons, lowering the pH of the media (**Figure 5.2**, illustrated also by eqs. 5.5 and 5.6).[49] This reaction can be catalytically enhanced by heterogeneous catalysts such as CeO_2 or by trace metal ions in solution (Fenton-like reactions). Short lifetimes of free radicals make their detection difficult. For that reason, most quantification assays explored are indirect methods based on the chemical derivatisation using a probe molecule such as Amplex Red,[50] Terephthalic acid,[51] or 3,3',5,5'-Tetramethylbenzidine (TMB),[52] which are peroxidase substrates whose production can be followed by spectroscopic techniques. The risk that such strategies involve are that the system

may see itself perturbed by the chemical derivation, resulting in the alteration of kinetics of both production and degradation of free radicals.[53]

Three different sets of experiments have been performed to test the enzyme-mimetic

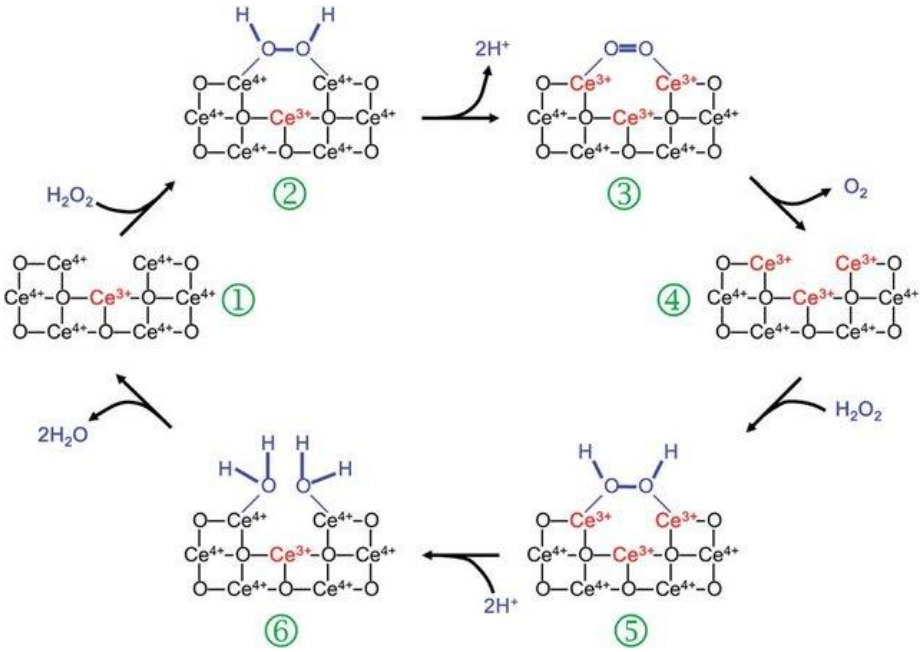

***Figure 5.2**: Model for the reaction mechanism of the catalytic oxidation of hydrogen peroxide on an oxygen vacancy-rich CeO_2 surface. Reproduced from ref. 49*

activity of the CeO_2-based nanomaterials synthesised in previous chapters. The first aims to study the effect of the catalytic activity from the catalyst perspective through the direct degradation of H_2O_2 in the presence of the nanocrystals, a case of catalase-mimetic activity that is complemented by the characterisation of the CeO_2 NCs from Chapter VI section 6.2.2.2. The second consisted in a standardized assay to determine the catalytic activity of the nanocrystals as peroxidase-like "nanozymes" (enzyme-mimicking nanocrystals) in order to easily compare catalytic properties between the different synthesised materials and relate them to other known enzyme-mimicking nanocrystals. Since CeO_2 is a semiconductor, it could be thought that it could act as photocatalyst for the peroxide degradation rather than having intrinsic enzyme-mimetic activity. Previous work from our group indicate that pure CeO_2 NCs efficiency as photocatalyst is quite poor,[54] however, to avoid any possible interference, the experiments corresponding to this section were carried out in the dark. Finally, for the third part, the *in-vitro* testing of nanomaterials toxicity and their radical scavenging properties has been assessed in cell cultures. Samples chosen were pure CeO_2 NCs of 2.5 nm, Yb- and Er-doped CeO_2 NCs of 2.5 nm (doping

concentration of 20% Yb^{3+} and 5% Er^{3+} respectively) and $AuCeO_2$ NCs of 12 nm synthesised by the One-Pot method of a 1:3 molar ratio of each component.

5.2.2.1 Effect of catalase-mimetic activity on CeO_2-based NCs

When injecting a certain amount of H_2O_2 solution onto the dispersed CeO_2 NCs, the colour of the solution visibly changes from pale yellow to intense orange and bubbling of O_2 can be observed. After enough time, the bubbling stops and the colour of the mixture slowly returns to its original state (**Figure 5.3**). Following eq. 5.5, the bubbling of O_2 is accompanied by a decrease in pH, and the regeneration of the catalyst is linked to the production of OH^-. The colour change indicates changes in the extinction of the material. These changes have been monitored by UV-vis spectroscopy and continuous pH measurements for a period of 4 days in equimolar mixtures of CeO_2 and H_2O_2 (0.5 mM) in a solution of 2.2 mM sodium citrate for the three CeO_2-based nanomaterials sampled.

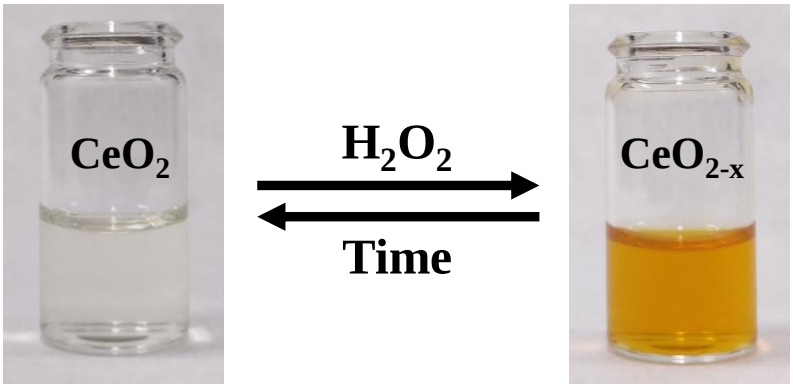

***Figure 5.3**: Pictographic description of the effect of H_2O_2 over CeO_2 NCs*

Changes in the extinction profile of the CeO_2-based nanomaterials and the consequent bandgap variation upon H_2O_2 exposure are plotted in **Figure 5.4**. It can be observed that the peak broadens, decreasing the slope of the peak and increasing the total area under the curve on the visible region (>400 nm). After reaching the maximum shift, at different rates depending on the sample, the spectrum comes back to the original state, as if it were a "swing". The solution's appearance to the eye changes in a similar fashion as CeO_2 NC samples before the ageing process shown in Chapter II section 2.2.4.

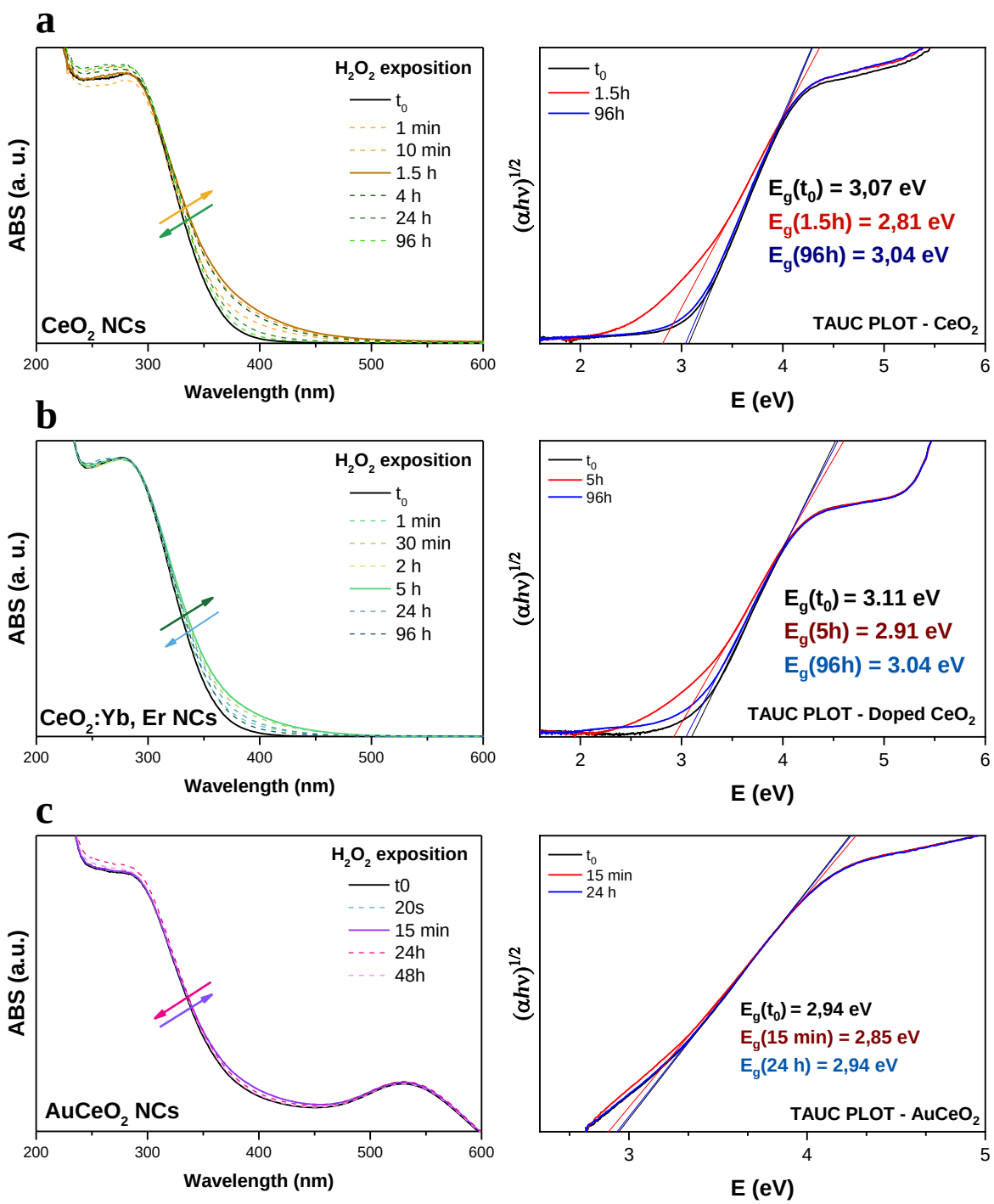

***Figure 5.4**: UVvis spectra (left) and respective Tauc plots for bandgap determination (right) of the monitorization of H_2O_2 exposition to (a) CeO_2 NCs, (b) CeO_2:Yb,Er (20%, 5%) NCs and (c) $AuCeO_2$ NCs.*

From the variations on Tauc plots (**Figure 5.4**, right column) and Urbach Energy calculated (Annex E, **Figure 9.8**), this effect is associated with a high increase in oxygen vacancy defects on the NC surface, which are believed to be active sites in the catalytic process. Now, from a comparative point of view, two main differences over the extinction changes can be pointed out among the different CeO_2-based nanomaterials tested: The intensity and kinetics of the process. For the CeO_2 NCs, it

can be observed that the maximum intensity of the "swing" (0.26 eV difference on the calculated bandgap by Tauc plot) is achieved in less than 10 minutes, lasts around 1.5h, and it is almost back to the original state after 24h. However, it takes five days for the complete restoration. For the doped CeO_2 NCs, the intensity of the swing at its maximum is not as pronounced (0.20 eV bandgap decrease), and it takes more than 30 mins to reach it, lasts around 5h after the exposition and after 5 days is not yet fully recovered to the original state.

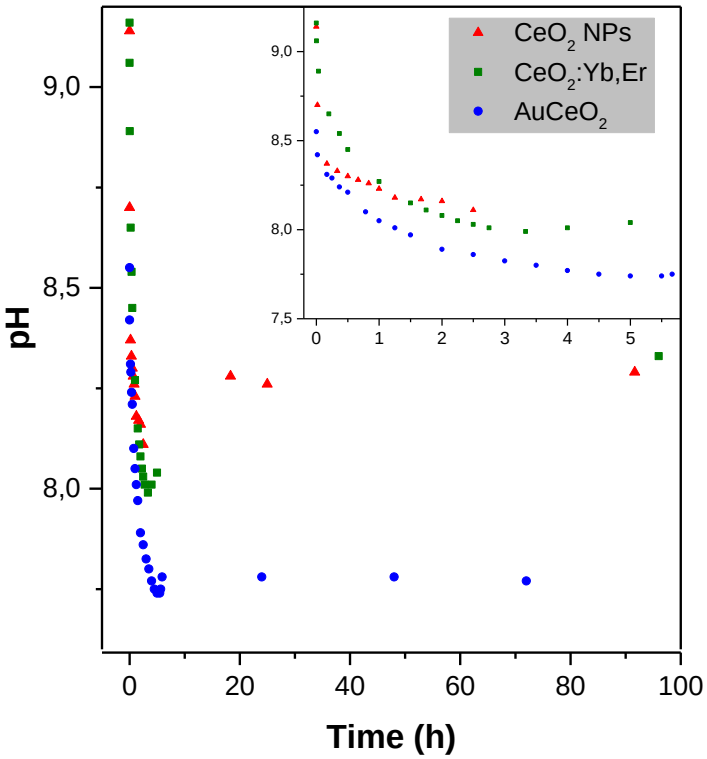

***Figure 5.5**: Recorded pH variation during the H_2O_2 exposure to different CeO_2-based NCs.*

Its easily deduced that lanthanide-doped CeO_2 NCs hold less OSC than pure CeO_2 NCs, so the swing is less intense and it takes more time to complete the catalytic cycle. For the case of $AuCeO_2$ NCs, the presence of the LSPR on the spectra partially masks the swing on the CeO_2 peak, but for comparison purposes, the Tauc plot has been calculated using only the region where Au absorption is constant. Absolute values, however, are not to be taken as a reference. While changes are almost imperceptible and observable "swing" is less than 0.1 eV, it takes only 20s to reach it and lasts only 15 minutes, completing the regeneration to the original state in less than 48h. The fast kinetics of the cycle indicate that the small swing intensity is not linked to a lower OSC of the material compared to the naked CeO_2 NCs, but to a higher catalytic capacity which has not been saturated by the chosen CeO_2-to-H_2O_2

ratio. For the three different CeO_2-based nanomaterials, the pH variation during the H_2O_2 exposure has also been monitored and plotted (**Figure 5.5**). **Table 5.1** summarises the main features recorded in both UV-vis spectra and pH monitorisation of the samples. Coherently, a decrease in pH is observed as the catalytic degradation of peroxide to O_2 takes place. Even though a small pH rise after reaching the minimum value is recorded, the return to the original pH level is not attained. It could most probably be explained by the partial neutralisation of the excess sodium citrate present in the solution acting as a buffer.

	CeO_2	**CeO_2:Yb, Er**	**$AuCeO_2$**
ΔpH	1,04	1,17	0,81
Time for ΔpH	2h	3-4h	4h-5h
ΔE_g	0,26 eV	0,20 eV	0,11 eV
Time for ΔE_g	1,5h	4h	15 min
Recovery time	4 days	>4 days	<48h

***Table 5.1**: Main features recorded of the effect of H_2O_2 exposure for CeO_2-based NCs.*

5.2.2.2 Determination of the Enzymatic Activity of CeO_2-based NCs

Many inorganic materials have been reported to hold enzyme-mimetic catalytic activity since the emerging of this research field.[55] Due to the versatility of their operation, which is presented as an advantage against their biological counterparts, the accurate description of their catalytic properties becomes a challenge. Their catalytic activity is highly dependent on the physicochemical properties of the material: size, morphology, composition, surface chemistry, aggregation state… In contrast, enzymes work on a very limited range and under very specific conditions. To avoid providing misleading information when describing the catalytic profile of a material, the complete physicochemical characterisation should always be detailed. Parameters employed to describe the catalytic properties of enzyme-mimicking nanocrystals are the specific activity and kinetics for a given enzyme-catalyzed reaction. The activity of a catalyst refers to the amount of substrate molecules transformed per unit of time, which is dependent on the catalyst concentration. Specific activity is a constant describing the activity per amount of catalyst for a given amount of substrate and temperature. The kinetics of the enzymatic process are typically described in terms of Michaelis-Menten curves. The catalytical

properties of the synthesised CeO_2-based materials in a biological context were characterised by the determination of their specific activity as peroxidase-like enzyme-mimicking nanocrystals. In the present study, a colourimetric assay for the determination of the peroxidase-mimetic activity through the oxidation of TMB, standardised by Jiang et al.,[56] was performed for the three nanomaterials also tested in the previous section (CeO_2 NCs, $AuCeO_2$ NCs and CeO_2:Yb, Er NCs) and Au NPs of 10 nm, as a control for the hybrids' activity.

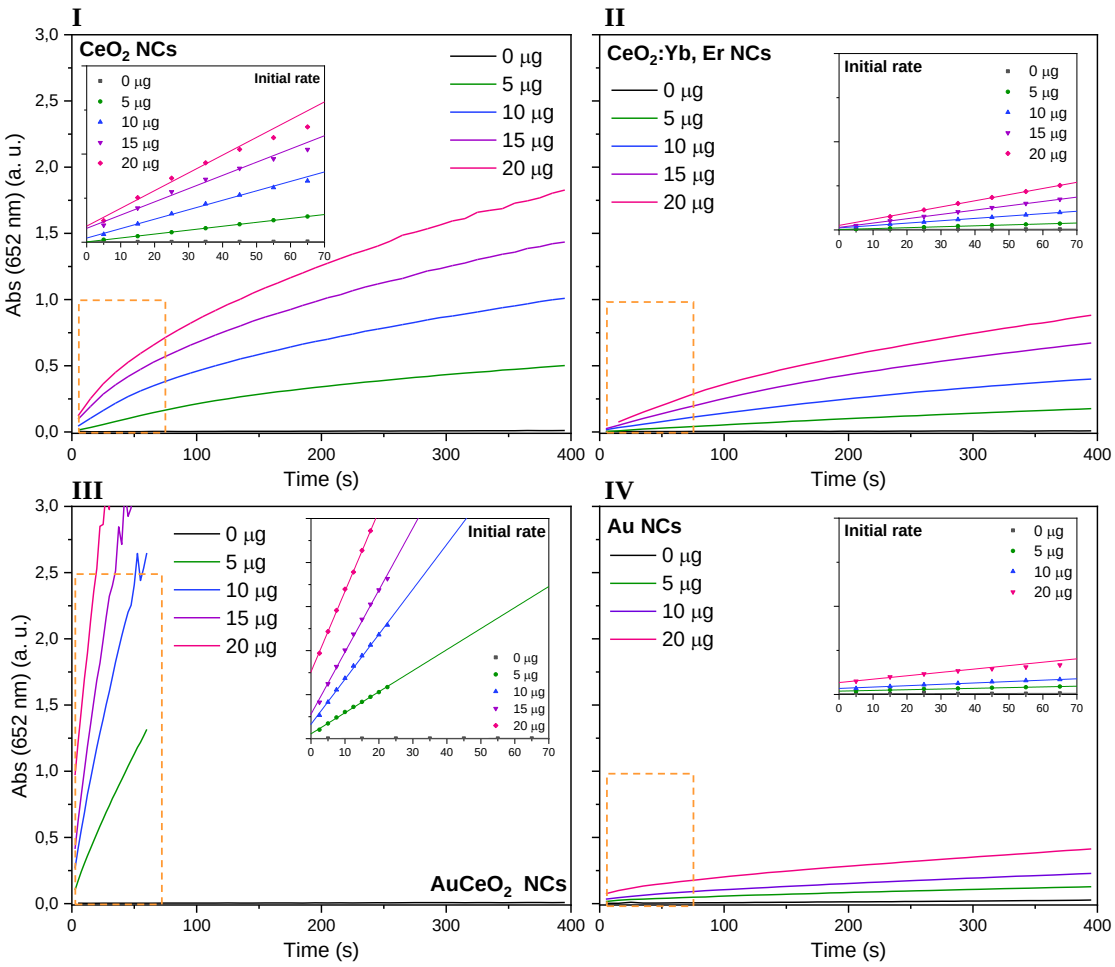

***Figure 5.6**: Reaction-time curves for the catalytic oxidation of TMB with H_2O_2 using increasing amounts of (I) CeO_2 NCs, (II) CeO_2:Yb,Er NCs, (III) $AuCeO_2$ NCs and (IV) Au NCs. Insets: Linear adjust for the initial rate of the reaction, zooming from the yellow area of each graph.*

The assay consists of the catalytic oxidation of a common peroxidase substrate, TMB, in the presence of H_2O_2. It leads to the degradation of the substrate into coloured species whose production can be easily followed through UV-vis spectroscopy. It is important to note that, in order to adapt the assay to measurable kinetics for the nanomaterial tested, several experimental conditions were modified from the standard protocol: it was carried out at room temperature rather than 37ºC, the employed substrate amount was 0.2 mg rather than 1 mg, and the concentration

of H_2O_2 was 0.15 M rather than 1 M. Consequentially, since catalytic activity is dependent on both substrate and nanocrystal concentration and temperature, final values of specific activity measured will be lower than those of the standard protocol. Also, since both H_2O_2 and TMB are susceptible of degradation under light exposure, the experiments were carried out in the dark to prevent any interference from external factors. The correspondent controls in the absence of nanocrystals and in the absence of H_2O_2 have been also carried out and can be found in section 9.4.2 (Annex E).

The time evolution of the UV-vis spectra for the catalytic degradation of 0.2 mg of TMB in 150 mM of H_2O_2 using from 0 to 20 mg of each nanocrystal mentioned above was recorded and plotted. It can be found in section 9.4.2 (Annex E). The reaction-time curves for each nanocrystal amount are plotted in **Figure 5.6**. Activity (A, measured in μmol of TMB reacted per minute) for each quantity of catalyst is calculated through equation 5.10, where V is the total reaction volume, ε_λ the extinction coefficient for TMB at the wavelength of interest, which in our case is ε_{652nm}= 39.10^3 $M^{-1}cm^{-1}$ and l path length of the cuvette. The term $\partial Abs/\partial t$ corresponds to the absorbance variation rate that, for simplification, is calculated as the slope of the linear region of the plot, the initial rate (**Figure 5.6 insets**).

$$A = \frac{V}{\varepsilon_\lambda . l}\left(\frac{\partial Abs}{\partial t}\right) \tag{5.10}$$

$$SA = \frac{A}{m} \tag{5.11}$$

Specific activity (SA, expressed in units, U, per mass of catalyst, eq. 5.11) is extracted as the slope of the linear regression of activity vs nanocrystal mass curve (**Figure 5.7**). The calculated specific activity at room temperature and for 0.2 mg of substrate for the CeO_2 NCs is 1.60 U/mg. Considering that, for assays at 37ºC, the literature values for other enzyme-mimicking nanocrystals are in the same order of magnitude, CeO_2 demonstrates great potential as radical scavenger.[56] For doped CeO_2:Yb, Er NCs the calculated specific activity was 0.56 U/mg and for Au NCs, 0.3 U/mg, which are very low values. For the case of the $AuCeO_2$ NCs, as can be observed on the Mass-Activity plot, the evolution is not linear, reaching an activity as high as 2.5 μmol/min at 20 μg of sample. This lack of linearity indicates that the kinetics of the catalysis are very fast and for the highest mass of catalyst used the amount of substrate is not enough to reach saturation. For comparative purposes, the

specific activity was calculated through a partial fit that did not take into account the highest point, obtaining a value of 59.5 U/mg for the $AuCeO_2$ NCs. While it is not a correct value, strictly speaking, it is already 40 times higher than plain CeO_2 alone, and, from the lack of saturation in the measured conditions, we can estimate it to be even higher.

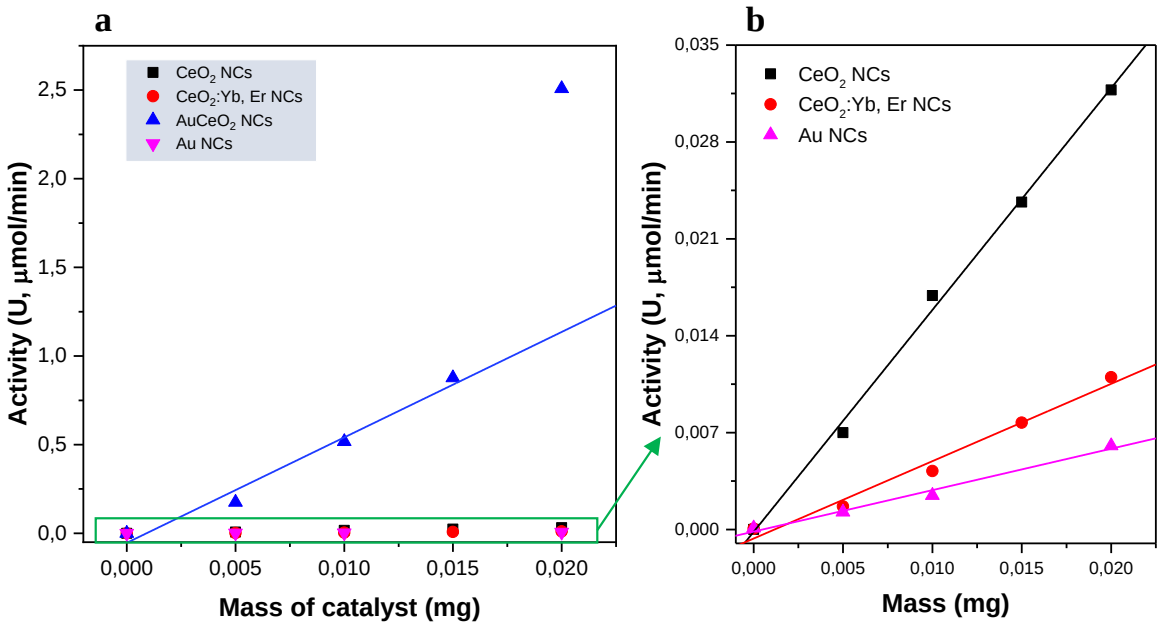

c

Sample	Spec. Activity
CeO_2	1.60 U/mg
CeO_2:Yb, Er	0.56 U/mg
$AuCeO_2$	59.5 U/mg*
Au	0,30 U/mg

***Figure 5.7**: (a) Activity vs mass plot for all nanocrystals tested and linear fit for specific activity determination. (b) Zoom of the green area marked on the Activity vs mass (c) Calculated values of specific activity for all the samples.*

5.2.2.3 In-vitro testing of ROS scavenging properties

The last part of the characterisation of the enzyme-mimetic activity of the different CeO_2-based nanocrystals consisted in determining the *in-vitro* toxicity of the nanomaterials and their prophylactic effect towards oxidative stress at a cell culture level. Three nanocrystal samples: CeO_2, CeO_2:Yb, Er (20%, 5%) and $AuCeO_2$ were purified and filtered to prevent contamination and homogenised at the same concentration of CeO_2. Later they were conjugated with Bovine Serum Albumin

(BSA) in 10 mM Phosphate Buffer (PB) to prevent alterations to their aggregation state due to exposure to cell culture media, which contains high concentrations of salt.[57] The experiments were carried out using a HEK-293 cell culture, and viability was measured through the PrestoBlue assay.

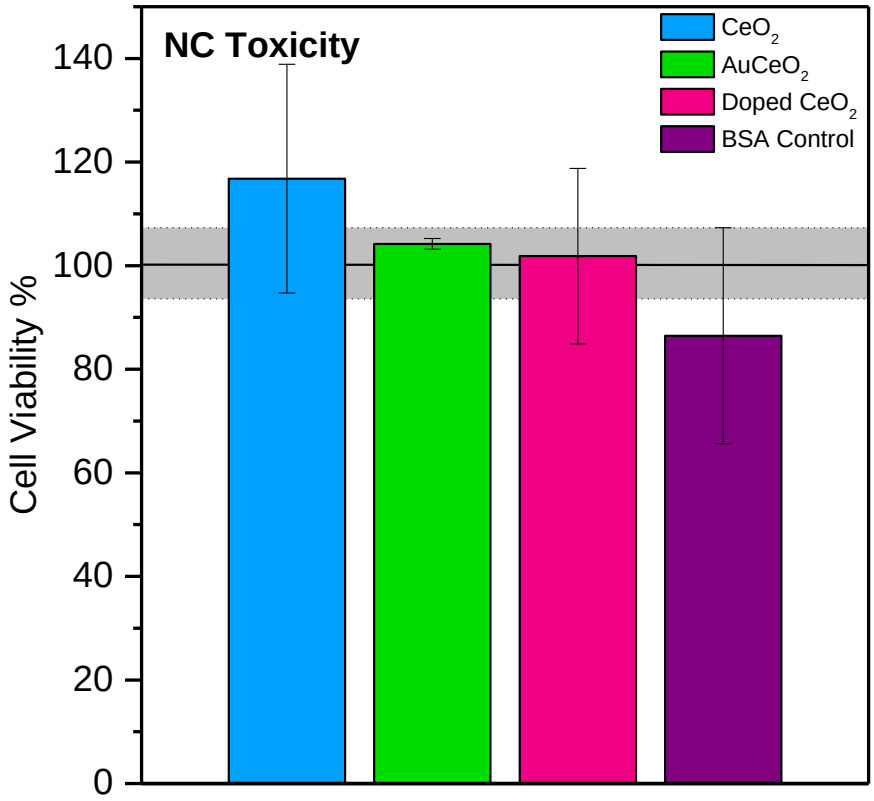

***Figure 5.8**: Viability in terms of % of a HEK-293 culture exposed to 100 μg/mL of the three CeO_2-based NCs studied and the BSA control.*

For a first assessment of the toxicity of the nanomaterials, the chosen cell line is exposed to 100 μg/mL of BSA-conjugated CeO_2-based NCs (**Figure 5.8**). After 24h, it is observed that exposed cells show notably high viability values, around 100-120% when normalised to the non-exposed control cells, more notable for the case of pure CeO_2 NCs. It would indicate that CeO_2-based nanomaterials tested did not cause any cytotoxicity. These are, however, sligthly higher viability values than expected, specially after the BSA control evidenced a small percentage of citotoxycity (viability of 86.5%), most probably caused by the partial substitution of DMEM by the BSA solution in the cell culture. The principle of the Prestoblue viability assay is based on the reduction of resazurin into a fluorescent salt by living cells. Microbial contamination or optical interference of the NCs could explain high values, but both causes were discarded with the respective controls. Thus, it could be explained by changes in the metabolism rate of the cells upon exposure to the NCs

as CeO_2. Yet, since the origin of this effect falls out of the scope of this work, no further experiment has been proposed to understand it, and the tested NCs were regarded as safe. Nonetheless, to avoid misleading readings on the second part of the experiment, regarding the prophylactic effect of the nanocrystals against H_2O_2 exposure, the normalisation for the second part was performed considering the Nanocrystal-exposed cells for the 100% value rather than the cells alone suspended in DMEM.

In order to assess the prophylactic effect of the NCs as antioxidant agents, the calibration of the ideal H_2O_2 concentration for the experiment was performed by testing the toxic effect of different peroxide concentrations on the cells. The objective was to find a concentration range in which the survival rate is as low as possible without reaching 0% to allow space for regeneration but maximising the effect of the CeO_2. For this, different concentrations of H_2O_2, ranging from 0.05 mM to 0.5 mM, were tested in the HEK-293 line, measuring the viability at 24h through the Prestoblue assay. Results are summarised in **Table 5.2**. The highest concentration tested proved to be too much excess of peroxide, and even the Prestoblue reagent was affected by it 24h after, leading to negative values of calculated viability. The middle and lower amounts (0.2 mM and 0.05 mM) proved to be more adequate, inducing high levels of oxidative stress on the cells that led to the death of most of them but allowing for the surviving ones to keep growing.

[H_2O_2]	**Viability**	**SD**
0,05 mM	2.84 %	1.35%
0,2 mM	0.27 %	0.75%
0,5 mM	<0.1 %	2.1%

***Table 5.2**: Viability results for the exposure of increasing concentrations of H_2O_2 to a HEK-293 cell line.*

The radical scavenging properties of the synthesised NCs were tested on HEK-293 cells. For this, cells were first preincubated for 24h with different doses of BSA-conjugated NCs (from 0 to 100 μg/mL of CeO_2) and then exposed to the chosen concentrations of H_2O_2 (0.05 and 0.2 mM). Since the presence of the nanocrystals on the culture wells has proved to alter positively culture growth in the previous experiment, cells exposed to the highest dose of NCs were used as reference control

for viability, as previously stated. In this way, the apparent alterations that this effect may have risen in the final determination of cell viability would be minimised. Cell viability was measured through the Prestoblue assay at 24h after peroxide exposition.

ROS scavenging properties of CeO_2-based nanomaterials in biological environments are confirmed by the *in vitro* assay. **Figure 5.9.a** shows the response of the maximum dose of each nanocrystal sample to the exposure to two different H_2O_2 concentrations previously tested: 0.2 mM and 0.05 mM. As expected, for a lower amount of peroxide, the prophylactic effect of CeO_2 is more notable. Still, in both cases, the viability increased in the presence of the nanocrystals in comparison to their absence. Furthermore, the effect of increasing doses of CeO_2 for the different nanocrystals was tested and plotted in **Figure 5.9.b-d**. Increased protection against the effect of oxidative stress is observed as the dose of CeO_2 increases, as expected based on the previous results presented, even if minor deviations appear. The tendency among the different materials is the same as in the previous tests: $AuCeO_2$ (**Figure 5.9.c**) performs slightly better than pure CeO_2 (**Figure 5.9.b**), and, while lanthanide-doped CeO_2 NCs (**Figure 5.9.d**) do not show toxicity themselves, the catalytic properties are not comparable to the other two materials. Another feature to take into account is whether the particles have been internalised inside the cells or remain free on the culture media, in order to determine if the cell is exposed to oxidative stress or not before CeO_2 acts. The degree of internalisation of de NCs in the cells as a function of preincubation time would be an interesting trial to carry out. It may lead to a better understanding of the role of the material in the evolution of free radicals. However, for the objective of this experiment, where the scavenging takes place does not affect the result.

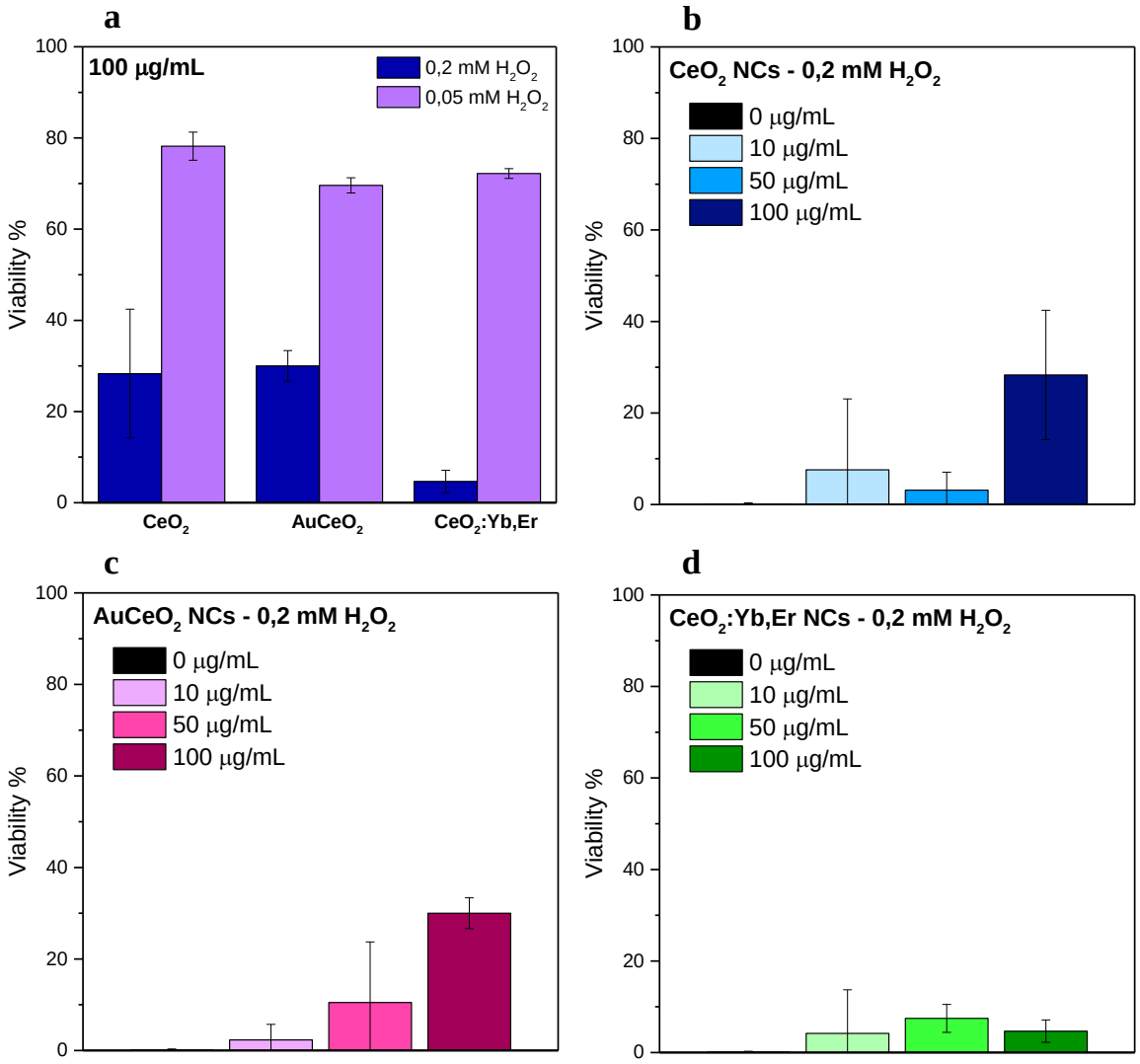

***Figure 5.9**: Viability in terms of % of a HEK-293 cell culture preincubated with CeO_2-based NCs 24h after exposition to H_2O_2. Evaluating (a) different concentrations of H_2O_2 for a given dose of the three CeO_2-based NCs studied and different doses of CeO_2 for a given H_2O_2 concentration in the case of (b) CeO_2 NCs, (c) $AuCeO_2$ NCs and (d) CeO_2:Yb, Er NCs.*

5.3 PERSPECTIVES

Regarding the CO_2 reduction reaction, as previously mentioned, there is room for improvement. The results of the performed tests as they fail to reach the requeriments to consider the materials as suitable catalysts. First, the formulation of NCs as a dry powder provokes the loss of both active surface and nanoscale traits of CeO_2 through aggregation and sintering of the nanocrystals. The strategy to avoid it is to ensure that the NCs remain dispersed after the drying through the encapsulation of these into the UiO-66 MOF structure, as mentioned before. While it entails a small loss of active surface of CeO_2 to the MOF, it is expected to be significantly lower than the uncontrolled aggregation of the NCs. If this approach does not result fruitful, and yields, selectivities and other aspects not considered (such as reusability or conversion) are not improved, the target product should be reevaluated, and a more suited reaction should be tested. While this exercise is proof of activity for reduction reactions, CeO_2 is typically employed for oxidation reactions due to its OSC.

In the case of the radical scavenging activity, the results are very promising. A deeper look at the catalytic capacity of $AuCeO_2$ hybrids as a function of shape, size, Au/Ce ratio, and other parameters controlled in the correspondent synthesis chapter could provide the necessary data for establishing the structure-activity relationships on this hybrid material. Besides this possibility, it would be interesting to go beyond the scope of the assay presented here by arranging a proper experiment to determine the amount of NCs internalised by the cells in the *in vitro* assays. The effect of the particles on metabolism should also be studied, and also cell viability should be evaluated using different methods for its determination, such as the LDH test, based on membrane integrity or cellular count, by colourimetric methods or flow cytometry. Also, tracking the subcellular localisation of the NCs would provide the necessary insights to describe the mechanism of action the NCs take on the organism. In this way, a proper description of the enzyme-mimicking catalytic activity of the nanocrystals could be provided.

Finally, two different fields of application have been tested, but there is still a wide range of potential applications worth examining. As was observed in the catalytic tests, Yb- and Er-doped CeO_2 samples do not perform adequately for reactions involving the OSC properties of the material. It can be interesting to find a field

where the catalytic activity of the material is enhanced by lanthanide doping in order to ensure the functionality of these materials. It has been mentioned several times within this thesis work how CeO_2, being a semiconductor, may perform photocatalytic reactions such as water splitting or pollutant degradations. While the characteristic electronic structure of pure CeO_2 may not be the most suitable for an efficient photocatalytic process, the case of lanthanide-doped CeO_2 NCs may overcome this problem.

5.4 REFERENCES

1. Hao, X. *et al.* Atomic-Scale Valence State Distribution inside Ultrafine CeO_2 Nanocubes and Its Size Dependence. *Small* **14**, 1802915 (2018).

2. Zhang, Y. *et al.* Unraveling the physical chemistry and materials science of CeO_2-based nanostructures. *Chem* **7**, 2022–2059 (2021).

3. Ganduglia-Pirovano, M. V., da Silva, J. L. F. & Sauer, J. Density-functional calculations of the structure of near-surface oxygen vacancies and electron localization on CeO_2(111). *Phys Rev Lett* **102**, 026101 (2009).

4. Jerratsch, J. F. *et al.* Electron localization in defective ceria films: A study with scanning-tunneling microscopy and density-functional theory. *Phys Rev Lett* **106**, 246801 (2011).

5. Trovarelli, A. Catalytic properties of ceria and CeO_2-Containing materials. *Catal Rev Sci Eng* **38**, 439–520 (1996).

6. Montini, T., Melchionna, M., Monai, M. & Fornasiero, P. Fundamentals and Catalytic Applications of CeO_2-Based Materials. *Chem Rev* **116**, 5987–6041 (2016).

7. Kašpar, J., Fornasiero, P. & Graziani, M. Use of CeO_2-based oxides in the three-way catalysis. *Catal Today* **50**, 285–298 (1999).

8. Liu, S., Wu, X., Weng, D. & Ran, R. Ceria-based catalysts for soot oxidation: a review. *Journal of Rare Earths* **33**, 567–590 (2015).

9. Sá, S., Silva, H., Brandão, L., Sousa, J. M. & Mendes, A. Catalysts for methanol steam reforming—A review. *Appl Catal B* **99**, 43–57 (2010).

10. Seo, Y. S., Shirley, A. & Kolaczkowski, S. T. Evaluation of thermodynamically favourable operating conditions for production of hydrogen in three different reforming technologies. *J Power Sources* **108**, 213–225 (2002).

11. Yi, N., Si, R., Saltsburg, H. & Flytzani-Stephanopoulos, M. Steam reforming of methanol over ceria and gold-ceria nanoshapes. *Appl Catal B* **95**, 87–92 (2010).

12. Jacobs, G., Keogh, R. A. & Davis, B. H. Steam reforming of ethanol over Pt/ceria with co-fed hydrogen. *J Catal* **245**, 326–337 (2007).

13. Ratnasamy, C. & Wagner, J. Water Gas Shift Catalysis. *http://dx.doi.org/10.1080/01614940903048661* **51**, 325–440 (2009).

14. Mansoob Khan, M. *et al.* Defect-Induced Band Gap Narrowed CeO_2 Nanostructures for Visible Light Activities. *Industrial & Engineering Chemistry Research* **53**, 9754–9763 (2014).

15. Chueh, W. C. *et al.* High-flux solar-driven thermochemical dissociation of CO_2 and H_2O using nonstoichiometric ceria. *Science (1979)* **330**, 1797–1801 (2010).

16. Yue, L. & Zhang, X. M. Structural characterization and photocatalytic behaviors of doped CeO_2 nanoparticles. *J Alloys Compd* **475**, 702–705 (2009).

17. Babu, S. *et al.* Multicolored redox active upconverter cerium oxide nanoparticle for bio-imaging and therapeutics. *Chemical Communications* **46**, 6915–6917 (2010).

18. Zhang, C., Zhang, Y. & Xie, W. Plasmonic metal/semiconductor hybrid nanomaterials for solar to chemical energy conversion. *Journal of Energy Chemistry* **63**, 40–53 (2021).

19. Kim, K. H. & Ihm, S. K. Heterogeneous catalytic wet air oxidation of refractory organic pollutants in industrial wastewaters: A review. *J Hazard Mater* **186**, 16–34 (2011).

20. Amrute, A. P. *et al.* Performance, structure, and mechanism of CeO_2 in HCl oxidation to Cl_2. *J Catal* **286**, 287–297 (2012).

21. Vivier, L. & Duprez, D. Ceria-Based Solid Catalysts for Organic Chemistry. *ChemSusChem* **3**, 654–678 (2010).

22. Carrasco, J. *et al.* Molecular-Level Understanding of CeO_2 as a Catalyst for Partial Alkyne Hydrogenation. *The Journal of Physical Chemistry C* **118**, 5352–5360 (2014).

23. Matés, J. M., Pérez-Gómez, C. & de Castro, I. N. Antioxidant enzymes and human diseases. *Clin Biochem* **32**, 595–603 (1999).

24. Banavar, S., Deshpande, A., Sur, S. & Andreescu, S. Ceria nanoparticle theranostics: harnessing antioxidant properties in biomedicine and beyond. *Journal of Physics: Materials* **4**, 042003 (2021).

25. Ma, Y., Tian, Z., Zhai, W. & Qu, Y. Insights on catalytic mechanism of CeO_2 as multiple nanozymes. *Nano Research 2022* 1–15 (2022) doi:10.1007/S12274-022-4666-Y.

26. Ernst, L. M. & Puntes, V. How Does Immunomodulatory Nanoceria Work? ROS and Immunometabolism. *Front Immunol* **13**, 974 (2022).

27. Zhao, S. *et al.* An Orally Administered CeO_2@Montmorillonite Nanozyme Targets Inflammation for Inflammatory Bowel Disease Therapy. *Adv Funct Mater* **30**, 2004692 (2020).

28. Zhao, Y., Yang, Y., Wen, Y., Zhao, M. & Dong, Y. Effect of Cerium Oxide Nanoparticles on Myocardial Cell Apoptosis Induced by Myocardial Ischemia-Reperfusion Injury. *Cell Mol Biol* **68**, 43–50 (2022).

29. D'Angelo, B. *et al.* Cerium Oxide Nanoparticles Trigger Neuronal Survival in a Human Alzheimer Disease Model By Modulating BDNF Pathway. *Curr Nanosci* **5**, 167–176 (2009).

30. Maritim, A. C., Sanders, R. A. & Watkins, J. B. Diabetes, oxidative stress, and antioxidants: A review. *J Biochem Mol Toxicol* **17**, 24–38 (2003).

31. Gao, Y., Chen, K., Ma, J. L. & Gao, F. Cerium oxide nanoparticles in cancer. *Onco Targets Ther* **7**, 835–840 (2014).

32. Chen, X., Qian, Y. & Wu, S. The Warburg effect: Evolving interpretations of an established concept. *Free Radic Biol Med* **79**, 253–263 (2015).

33. Rather, H. A. *et al.* Antioxidative study of Cerium Oxide nanoparticle functionalised PCL-Gelatin electrospun fibers for wound healing application. *Bioact Mater* **3**, 201–211 (2018).

34. Yokel, R. A. *et al.* The yin: an adverse health perspective of nanoceria: uptake, distribution, accumulation, and mechanisms of its toxicity. *Environ Sci Nano* **1**, 406–428 (2014).

35. Rogers, N. J. *et al.* Physico-chemical behaviour and algal toxicity of nanoparticulate CeO_2 in freshwater. *Environmental Chemistry* **7**, 50–60 (2010).

36. Carlander, U., Moto, T. P., Desalegn, A. A., Yokel, R. A. & Johanson, G. Physiologically based pharmacokinetic modeling of nanoceria systemic distribution in rats suggests dose- and route-dependent biokinetics. *Int J Nanomedicine* **13**, 2631–2646 (2018).

37. Rzigalinski, B. A., Carfagna, C. S. & Ehrich, M. Cerium oxide nanoparticles in neuroprotection and considerations for efficacy and safety. *Wiley Interdiscip Rev Nanomed Nanobiotechnol* **9**, 1444 (2017).

38. Asati, A., Santra, S., Kaittanis, C., Nath, S. & Perez, J. M. Oxidase-Like Activity of Polymer-Coated Cerium Oxide Nanoparticles. *Angewandte Chemie International Edition* **48**, 2308–2312 (2009).

39. Perez, J. M., Asati, A., Nath, S. & Kaittanis, C. Synthesis of Biocompatible Dextran-Coated Nanoceria with pH-Dependent Antioxidant Properties. *Small* **4**, 552–556 (2008).

40. Kaittanis, C., Santra, S., Asati, A. & Perez, J. M. A cerium oxide nanoparticle-based device for the detection of chronic inflammation via optical and magnetic resonance imaging. *Nanoscale* **4**, 2117–2123 (2012).

41. Xiao, G. *et al.* Nanoceria-Based Artificial Nanozymes: Review of Materials and Applications. *ACS Appl Nano Mater* **5**, 14147–14170 (2022).

42. Sancar, A. Structure and Function of DNA Photolyase and Cryptochrome Blue-Light Photoreceptors. *Chem Rev* **103**, 2203–2238 (2003).

43. Tian, Z. *et al.* Photolyase-Like Catalytic Behavior of CeO_2. *Nano Lett* **19**, 8270–8277 (2019).

44. Guil-López, R. *et al.* Methanol Synthesis from CO_2: A Review of the Latest Developments in Heterogeneous Catalysis. *Materials 2019* **12**, 3902 (2019).

45. García, A. C., Moral-Vico, J., Markeb, A. A. & Sánchez, A. Conversion of Carbon Dioxide into Methanol Using Cu-Zn Nanostructured Materials as Catalysts. *Nanomaterials 2022*, **12**, 999 (2022).

46. A. Rodriguez, J. *et al.* Hydrogenation of CO_2 to Methanol: Importance of Metal–Oxide and Metal–Carbide Interfaces in the Activation of CO_2. *ACS Catal* **5**, 6696–6706 (2015).

47. Arena, F. *et al.* Synthesis, characterization and activity pattern of Cu–ZnO/ZrO_2 catalysts in the hydrogenation of carbon dioxide to methanol. *J Catal* **249**, 185–194 (2007).

48. Yazdi, A. *et al.* Core–shell Au/CeO_2 nanoparticles supported in UiO-66 beads exhibiting full CO conversion at 100 °C. *J Mater Chem A Mater* **5**, 13966–13970 (2017).

49. Celardo, I., Pedersen, J. Z., Traversa, E. & Ghibelli, L. Pharmacological potential of cerium oxide nanoparticles. *Nanoscale* **3**, 1411–1420 (2011).

50. Mishin, V., Gray, J. P., Heck, D. E., Laskin, D. L. & Laskin, J. D. Application of the Amplex red/horseradish peroxidase assay to measure hydrogen peroxide generation by recombinant microsomal enzymes. *Free Radic Biol Med* **48**, 1485–1491 (2010).

51. Charbouillot, T. *et al.* Performance and selectivity of the terephthalic acid probe for OH as a function of temperature, pH and composition of atmospherically relevant aqueous media. *J Photochem Photobiol A Chem* **222**, 70–76 (2011).

52. Josephy, P. D., Eling, T. & Mason, R. P. The horseradish peroxidase-catalyzed oxidation of 3,5,3’,5’-tetramethylbenzidine. Free radical and charge-transfer complex intermediates. *Journal of Biological Chemistry* **257**, 3669–3675 (1982).

53. Burns, J. M. *et al.* Methods for reactive oxygen species (ROS) detection in aqueous environments. *Aquat Sci* **74**, 683–734 (2012).

54. Piella, J., Bastús, N. G., Casals, E. & Puntes, V. Characterizing Nanoparticles Reactivity: Structure-Photocatalytic Activity Relationship. *J Phys Conf Ser* **429**, 012040 (2013).

55. Wu, J. *et al.* Nanomaterials with enzyme-like characteristics (nanozymes): next-generation artificial enzymes (II). *Chem Soc Rev* **48**, 1004–1076 (2019).

56. Jiang, B. *et al.* Standardized assays for determining the catalytic activity and kinetics of peroxidase-like nanozymes. *Nature Protocols 2018 13:7* **13**, 1506–1520 (2018).

57. Barbero, F. *et al.* Formation of the Protein Corona: The Interface between Nanoparticles and the Immune System. *Semin Immunol* **34**, 52–60 (2017).

CHAPTER VI

ELECTRONIC STRUCTURE OF NANOSTRUCTURED CeO_2: ORIGIN OF THE CATALYTIC PROPERTIES OF THE MATERIAL

CHAPTER VI

ELECTRONIC STRUCTURE OF NANOSTRUCTURED CeO_2: ORIGIN OF THE CATALYTIC PROPERTIES OF THE MATERIAL

6.1 INTRODUCTION

Regarding CeO_2 NCs and derived nanomaterials applicability, the conversation always revolves around the catalytic properties of the material. While a specific review of this topic is due in Chapter V, it is important to note that the characteristic that makes CeO_2 interesting is what the literature describes as the ability to switch between 3+/4+ oxidation states. This ability, also known as "electron sponge" properties, turns the material into an oxygen buffer for redox properties. This "switch" balances charge excess from the loss of superficial oxygen during the catalytic cycle avoiding any change in the crystal structure. This feature finds its origin in the singular electronic structure of the material and will be further described within this chapter.

In order to understand the mechanistic aspects of the catalytic processes from the catalyst perspective; determine the differences between nano-sized and bulk CeO_2, correlating the catalytic properties to size and defect density; identify the features of the synthesised CeO_2 NCs and derived, as well as be able to predict the nature of their catalytic properties, the characterisation of the Ce 3*d* orbital by XPS and the L_3 ($2p \rightarrow 5d$) spectral line by XANES (X-Ray Absorption Near-Edge Structure) has been performed. Even if the difference between Ce^{3+}/Ce^{4+} states occurs within the 4*f* orbital, its occupancy affects the rest of the electronic structure, so both techniques should be able to discern between the different configurations of Ce atoms within the solid.

Since the analysis and interpretation of the recorded data pertain a higher degree of complexity than other characterisation techniques, these measurements are grouped together in a single chapter rather than atomised within the several characterisation sections of this work. Also, the comparison between measurements is key for understanding the system's properties. A brief description of each technique and state-of-the-art in the matter of CeO_2 is provided as introduction.

6.1.1 X-Ray Photoelectron Spectroscopy (XPS) of Ce 3*d*

XPS is a technique employed for surface chemical analysis. It is based on the photoelectric effect, which involves the emission of electrons from internal shells upon illumination under soft X-ray photons (1-2 keV) at ultrahigh vacuum conditions. Measuring the kinetic energy of emitted electrons allows to the calculation of the binding energy for their specific core level, thus identifying the chemical species. Binding energies are very sensitive to the chemical environment, making XPS one of the most interesting tools for structural characterization of nanomaterials and bulk materials' outer layers (5-10 nm). The ultrahigh vacuum conditions, x-ray bombing and charging effects, however, cause surface transformations that lead to variations within the fine structure of the recorded spectra, and must be considered for their correct interpretation. The topic of Ce ([Xe] $4f^1\ 5d^1\ 6s^2$) is a complex case for XPS to resolve. The electronic structure of the stable compounds it forms is subjected to heavy discussion and pertains to such a level of specialisation on the field that one would not expect to resolve it in a work which only approaches the topic tangentially. In order to be able to understand and compare spectra from the different materials, however, a brief explanation of the appearance of the Ce 3*d* line in XPS is due.

The resolution of the Ce spectra involves a series of discussions that can be grouped into two main issues. It was already mentioned that the two stable oxidation states for this atom are Ce^{4+} ([Xe] $4f^0$), in the oxide form CeO_2, and Ce^{3+} ([Xe] $4f^1$) in the sesquioxide form Ce_2O_3 (or as salt species of any of the two cations). The first issue is the complex structure of the Ce 3*d* spectra, showing an unusually high number of bands due to the partial *f* character of O 2*p* Valence Band orbitals. This interaction is a consequence of the partial hybridization of the mentioned O 2*p* molecular orbitals with empty Ce 4*f* orbitals. This effect is maximised under X-ray illumination,

as core holes in 3*d* orbitals rearrange the valence electrons, pulling 4*f* orbitals below the Fermi level and decreasing the energy barrier for hybridization. As a consequence, a mixture of possible ground states gives rise to the appearance of multiple transitions (see **Table 6.1**); three for the case of the 4+ oxidation state, and two for the case of the 3+ oxidation state (as the $4f^0$ configuration is not possible for the 3+ valence). The hole in the valence band left behind by the O 2*p*-Ce 4*f* hybridization is denoted in literature as either V^{n-z} (*n* being the number of electrons in the valence band and *z* the number of electrons in hybridised *f* orbitals) or L^n (being L a "ligand hole" or the extra e^- left behind by an oxygen vacancy). [1,2]

Species	Initial state	Final state	Notation
Ce^{3+}	$3d^{10}4f^1$	$3d^9 4f^2(V^{n-1})$	v^0 / u^0
		$3d^9 4f^1(V^n)$	v' / u'
Ce^{4+}	$3d^{10}4f^0$	$3d^9 4f^2(V^{n-2})$	v / u
		$3d^9 4f^1(V^{n-1})$	v'' / u''
		$3d^9 4f^0(V^n)$	v''' / u'''

***Table 6.1**: Possible XPS transitions of the Ce 3d band for the 3+ and 4+ valences due to O 2p-Ce 4f hybridization. Valence band denoted as V^n.*

In addition to said transitions, it is necessary to take into account spin-orbit splitting for the complete construction of the spectra. For all electrons except for the ones populating *s* levels (l = 0), the quantum number *j* (*j* = *l* + *s*, *l* being the angular momentum takes the value from the orbital, *s* = 0, *p* = 1, *d*= 2, etc. and s the orbital spin ±½) splits the orbital into two energy levels populated by 2*j* + 1 degenerate electrons. This effect is also referred to as *j-j* coupling. For the Ce 3*d* case, spin-orbit splitting leads to the $3d_{5/2}$ and $3d_{3/2}$ doublet, containing 6 and 4 e^-, respectively, from the total 10 e^- populating the *d* orbital. Consequently, each of the transitions from **Table 6.1** will appear as two peaks: one reflecting the transition from *j* = 5/2 (herein described as *v*) and the other reflecting the transition from *j* = 3/2 (herein described as *u*) separated by a difference of ~18.5 eV, the energy difference between the two levels. Due to the difference in population, each of the *v* ($3d_{5/2}$) peaks and the summation of all of them should match a 6/4 intensity ratio to the respective *u* ($3d_{3/2}$) and the summation of all of them. In total, the Ce^{4+} spectrum is composed of six peaks, and the Ce^{3+} spectrum consists in four peaks located at different energies.[3] **Figure 6.1** contains the indexed Ce 3*d* XPS spectrum for a commercial CeO_2 powder sample, taken in this work as a model for bulk CeO_2.

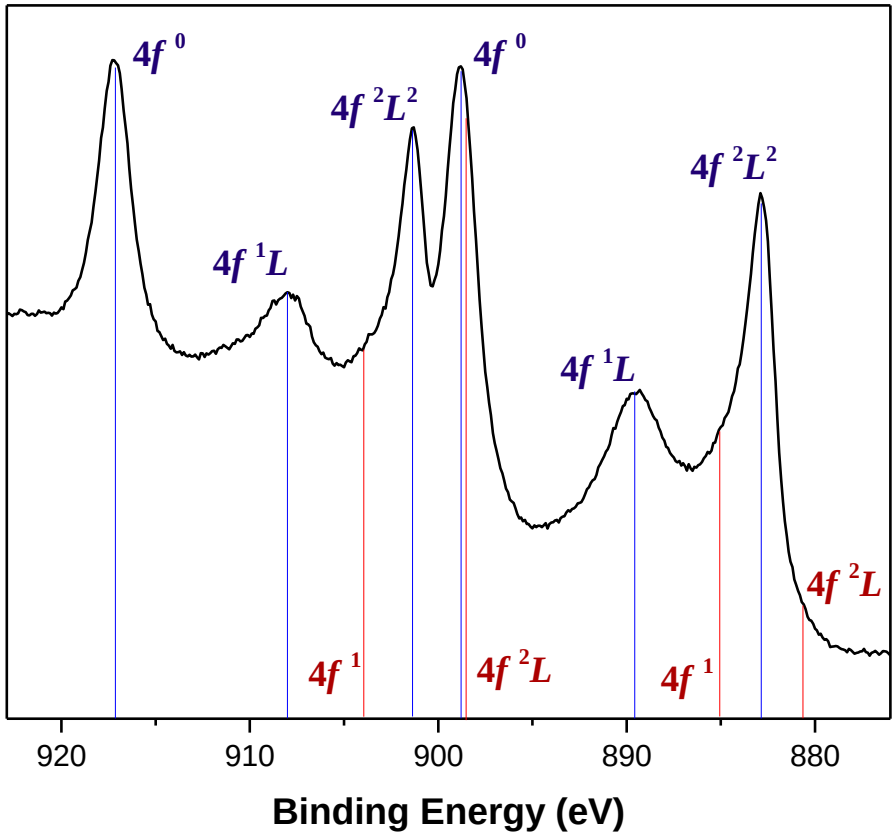

***Figure 6.1**: Ce 3d spectrum of a model bulk CeO_2 sample indexed with the transitions indicated in **Table 6.1**. Marked in blue the peaks corresponding to transitions associated to a +4 oxidation state. In red, the theoretical positions of peaks for the +3 oxidation state (which are not present in the spectrum).*

The second issue on the matter of the deconvolution of the Ce 3*d* spectra is related to the generation of oxygen vacancies in nanostructured CeO_2. Several authors associate oxygen with a "mixed valence" state between +3/+4 on the *fcc* crystalline structure.[4,5] As a consequence, their presence may lead to the coexistence of both Ce^{3+} (v^0, v', u^0, u') and Ce^{4+} (v, v'', v''', u, u'', u''') bands in the spectra, the ratio between their intensities proportional to the number of oxygen vacancies supported by the structure. The result is a spectrum containing ten peaks of different intensities.[6] Other authors, in contrast to the previous explanation for the unusually high number of peaks in Ce 3*d* XPS spectra, associate its complex structure to multiple final states, involving previously mentioned valence band hybridization to unoccupied 4*f* orbitals [$3d^9 4f^0(V^n)$, $3d^9 4f^1(V^{n-1})$ and $3d^9 4f^2(V^{n-2})$] and internal $3d^9 5p^5$ np^1 configurations, suggesting that CeO_2 contains only Ce^{4+} under a complex electronic structure.[7,8] Studies on the spectral structure of valence electrons on CeO_2 corroborate the participation of Ce 4*f* orbitals in the chemical bond between Ce-O and also, surprisingly, the involvement of 5*p* and 5*s* atomic orbitals in the formation of valence molecular orbitals, reinforcing this last hypothesis.[9]

Solving the matter of the effect of oxygen vacancies on the spectra involves not only a theoretical dimension but also a technical one. It has been previously mentioned that the concentration of oxygen vacancies is a function of the surface-to-volume ratio of the material (size of the nanocrystals), temperature and P_{O_2}. Working under ultra-high vacuum conditions provokes a perturbation of the original state of the material. Moreover, it has been pointed out that x-ray irradiation induces chemical reduction of the CeO_2 surface ($2\ CeO_2 \rightarrow Ce_2O_3 + O_2$). In consequence, spectral measurements prove to be time-dependent, and the intensity of Ce^{3+} peaks increases with exposure time, while, for Ce^{4+} peaks, it decreases.[10] Hybridization between Ce 4*f* and O 2*p*, however, affects the linearity of these changes, as explained by Romeo *et al.*: The reduction of Ce^{3+} structures results in the decrease of $4f^0$ features, as they do not participate of the Ce^{3+} spectra. At the same time, due to the position of the Fermi level, the degree of hybridization is lower in Ce^{3+} structures than in Ce^{4+} ones.[4] Since valence electrons partially populate the 4*f* orbital upon hybridization, the contribution of $4f^0$ is higher when hybridization is minimised. Both these tendencies, acting in opposite directions, are in competition during the progressive reduction of CeO_2, and it has been suggested that the intensity decrease of $4f^0$ structures is not noticeable below ~30% concentration of reduced Ce atoms. Over this amount, the crystalline structure finally collapses.[2] For the same reason, the calculation of the number of electrons populating 4*f* orbitals at the ground state is not simple, and relations between peak intensities and areas of the different transitions (v^0, *v*, *v*', etc. for the $3d_{5/2}$ and their $3d_{3/2}$ pairs u^0, *u*, *u*'…) require a complex process of deconvolution which may require different approaches for bulk and nanomaterials.[11]

Using XPS to quantify the presence of Ce atoms bearing the $4f^1$ configuration (3+ oxidation state) through the Ce 3*d* spectrum may require a higher level of expertise and not provide conclusive answers under our current tools and capacities. Therefore, as a complementary technique, X-Ray Absorption Spectroscopy studies have also been carried out in order to provide a different perspective on the matter. However, for the sake of making the most of the means employed for the CeO_2 characterisation, a model sample for bulk CeO_2 has been used to extract information about the features of the spectra of the CeO_2 NCs and CeO_2-based hybrid nanomaterials synthesised in comparison to bulk.

6.1.2 X-Ray Absorption Spectroscopy (XAS)

XAS is a set of analytic techniques based on the excitation of core electrons of matter using high energy photons belonging to the X-ray range (0.1-100 keV) to chraracterize its electronic structure. XAS is performed at synchrotron facilities due to the photon beam energy requirements. In our case, it is an alternative to the ultrahigh vacuum conditions employed in XPS, as measurement conditions allow for samples at either solid or liquid phases without any vacuum requiriments.

Upon X-ray excitation of an electron, a sharp increase of the absorption is recorded in the spectra. This notation for absorption edges (K, L or M) corresponds to the quantum number *n* of the excited electron's shell (*s* = 1, *p* = 2, *d* = 3…). According to the region of the edge studied, two techniques are differentiated. The lower energy interval of the spectrum, corresponding to discrete transitions of the excitation of electrons to higher unoccupied electronic states, is known as X-Ray Absorption Near-Edge Structure (XANES). It provides information about electronic structure and symmetry of the metal atoms' core. The higher energy range of the absorption spectra, corresponding to an excitation of the electrons to the continuum (photoelectric effect), is known as Extended X-Ray Absorption Fine Structure (EXAFS), and provides information about the number, distances, and nature of ligands, and other features from the metallic atom environment are known through EXAFS. [12,13]

The L_3 line of Ce atoms, corresponding to the excitation of 2*p* electrons, was the chosen for the characterization of the Ce-O bonds, which hold a complex structure that ultimately leads to the "*electron sponge*" properties of nanostructured CeO_2. For quadrupole transitions into 4*f* orbitals, corresponding to the weak pre-edge band, the spin-orbit term (^{2S+1}L) determines symmetry and, therefore, the shape of the spectral line, according to the selection rules. Ce^{4+} species with [Xe] $4f^0$ configurations (S = 0, L = 0) are assigned a ^{1}S symmetry term. Ce^{3+} species with [Xe] $4f^1$ configurations (S = 1/2, L = 3), are assigned a ^{2}F symmetry term. Consequently, $4f^0$ and $4f^1$ configurations will result in clearly distinct pre-edge band shapes. The final XANES spectrum is composed of the sum of all observable transitions. A system consisting of a $4f^0$ and $4f^1$ mixture will result in a spectrum containing the weighted sum of ^{1}S and ^{2}F states.[14,15]

$$\Psi_g = a|4f^0\rangle + b|4f^1L\rangle \quad (6.1)$$

In similar fashion as the three transitions contained in the Ce^{4+} 3*d* XPS band previously described, the quadrivalent CeO_2 L_3 edge band, correspondent to $2p \rightarrow 5d$ dipole transitions, shows two broad peaks. It can seem inconsistent, as both 2*p* and 3*d* holes are localized and could be expected to cause similar effects over the 4*f* states in terms of the system's multiconfiguration.[16] On the matter of the many-body final states in the XANES spectra, it arises certain discussions within the scientific community, as it is typically addressed as a mixed valence system, while in the spectroscopy field it is referred to as an interatomic intermediate valence system.[17] It was previously mentioned that the origin of the 4*f* multiconfiguration is the hybridization between localised 4*f* levels from Ce atoms and delocalised 2*p* levels from oxygen atoms, denoted as $4f^{n+1}L$, where *L* represents a ligand hole (see previous section 6.1.1). The ground state for this configuration is given by the wavefunction expressed by equation 6.1, where *a* and *b* describe the mixing ratio of the two possible configurations separated by ΔE before hybridization. Values of *a* and *b* depend on the hybridization energy (referred to typically as *V*) between localised Ce 4*f* and delocalised O 2*p* atomic orbitals, that needs to fulfil the condition $V \geq \Delta E$. This ground state is the same for both photoabsorption and photoemission spectroscopies.

For the final state, the energy difference between $4f^0$ and $4f^1L$ configurations depends not only on ΔE but also on the Coulombic interactions Q_{hd} and Q_{hf} between the hole and the *d*/*f* orbitals, which pulls them down, and the Coulombic repulsion U_{df} between 5*d* and 4*f* electrons, which pushes the *f* levels up. The value of U_{df} term is 0 in XPS, as 5*d* states remain unoccupied. Therefore, the final states are different than those of XANES spectroscopy, involving different energy separation and degree of hybridization of the electronic configurations of the final states. Authors Jo and Kotani also explained the two-peak structure of the L_3 edge band as the consequence of the effect of an intraatomic coulombic interaction between 4*f* and 5*d* states. According to them, the edge peak associated to transitions to unoccupied 5*d* states splits into two structures: the higher energy one corresponds mainly to the interaction between $4f^0$ configurations and well-localized (unscreened) 5*d* states. In comparison, the lower energy one would correspond to mainly $4f^1L$ configurations interacting with extended (screened) 5*d* states.[1,18]

6.2 RESULTS

6.2.1 XPS characterization

6.2.1.1 Ce 3d peak

The general spectra (0-1380 eV) for a total of seven samples was recorded (see experimental section for details): CeO_2 NCs both before and after the ageing process, lanthanide-doped CeO_2 NCs (10% Yb^{3+}, 10% Yb^{3+} 5% Er^{3+}, and 20% Yb^{3+} 5% Er^{3+}) and $AuCeO_2$ hybrid NCs of two different shell thicknesses (5 nm and 11 nm). In order to define a bulk model to compare the samples to, recordings of the spectra of commercial powders of CeO_2 and $Ce(OH)_4$ of ~200 nm size. A deconvolution attempt of the Ce 3*d* section of the spectra was carried out for all the samples using Origin 2018 peak fitting tool, a Shirley background, and peak position values from the literature.[2]

The accuracy of the deconvolution, however, is not as precise as expected. A number of the deconvolution parameters obtained show incongruent values, especially for nanosized samples: peak position and area values break the area conditions given by spin-orbit splitting (constant difference of ~18.5 eV and 3:2 area ratio). For that reason, upon further revision, these results are not ready to quantitatively describe the differences between bulk and nanostructured CeO_2. Obtained fittings including peak position and area values can be consulted in section 9.5.1 (Annex F, **Figure 9.13:** Ce 3d peak deconvolution of CeO_2 NCs (left) after ageing and (right) before ageing.**Figure 9.14**). A summary of literature and measurement values of peak position in each of the samples can be found in **Table 6.2**. As expected, v^0 and u^0 transitions (corresponding to the $4f^2L$ final state for the 3+ valence) are of very little importance since they correspond to a hybridised state only permitted under X-ray illumination on the (allegedly) minoritarian species within the sample (Ce^{3+}). Also some important general displacements can be observed in the peaks position (after calibration of the spectrum using the C 1*s* peak) for certain samples such as CeO_2 NCs before ageing (around -4 eV for each peak compared to literature values), that can be assumed to be artefactual. Apart from those, a dispersion of ±1 eV in all peak values in comparison to the literature values is found.

	3+	4+	3+	4+	4+		3+	4+	3+	4+	4+
Peak Index	v^0	v	v'	v''	v'''		u^0	u	u'	u''	u'''
Literature	880,6	882,6	885,4	888,8	898,4		898,9	901,0	904,0	907,4	916,7
Commercial CeO_2	-	882,8	883,9	889,4	898,8		-	901,3	902,1	908,5	917,2
Commercial $Ce(OH)_4$	-	882,8	885,6	888,5	898,7		-	901,3	902,8	907,7	917,0
CeO_2 NCs	881,7	881,7	885,2	888,2	897,5		894,7	899,9	903,3	905,1	915,8
Not aged CeO_2 NCs	876,9	878,7	881,1	884,4	894,8		893,4	897,0	899,9	903,0	913,3
CeO_2:Yb (10%)	-	882,6	886,3	888,7	898,6		-	899,2	901,2	906,4	916,8
CeO_2:Yb, Er (10%, 5%)	-	881,5	885,4	888,2	895,8		-	897,6	900,3	905,0	915,2
CeO_2:Yb,Er (20%, 5%)	-	881,8	885,5	887,9	897,7		-	900,6	902,4	905,9	915,5
$AuCeO_2$ (thin)	880,8	882,5	885,6	889,9	898,6		889,9	901,0	904,0	908,2	916,8
$AuCeO_2$ (thick)	881,5	882,9	884,6	888,6	899,0		898,6	901,3	903,6	908,0	917,3

***Table 6.2**: Literature (ref.2) and recorded values of peak position for Ce 3d transitions in each of the samples. Grey: Peaks associated with Ce^{3+} species.*

While the attempt to quantitatively characterize the presence of oxygen vacancies or valence switch within the nanosized CeO_2 found itself to be a task beyond our abilities, plenty of information about the structural traits of the set of samples studied can be extracted from the measurements. To further deepen into it, peak position was corrected for the displaced sample (CeO_2 NCs before ageing), and all the spectra were normalized by the area between the 874-923 eV interval and finally plotted together to stablish structural relations by comparison (**Figure 6.2.a**). A detailed comparison between the different samples and the synthesized CeO_2 NCs can be found in **Figure 6.2.b-e**.

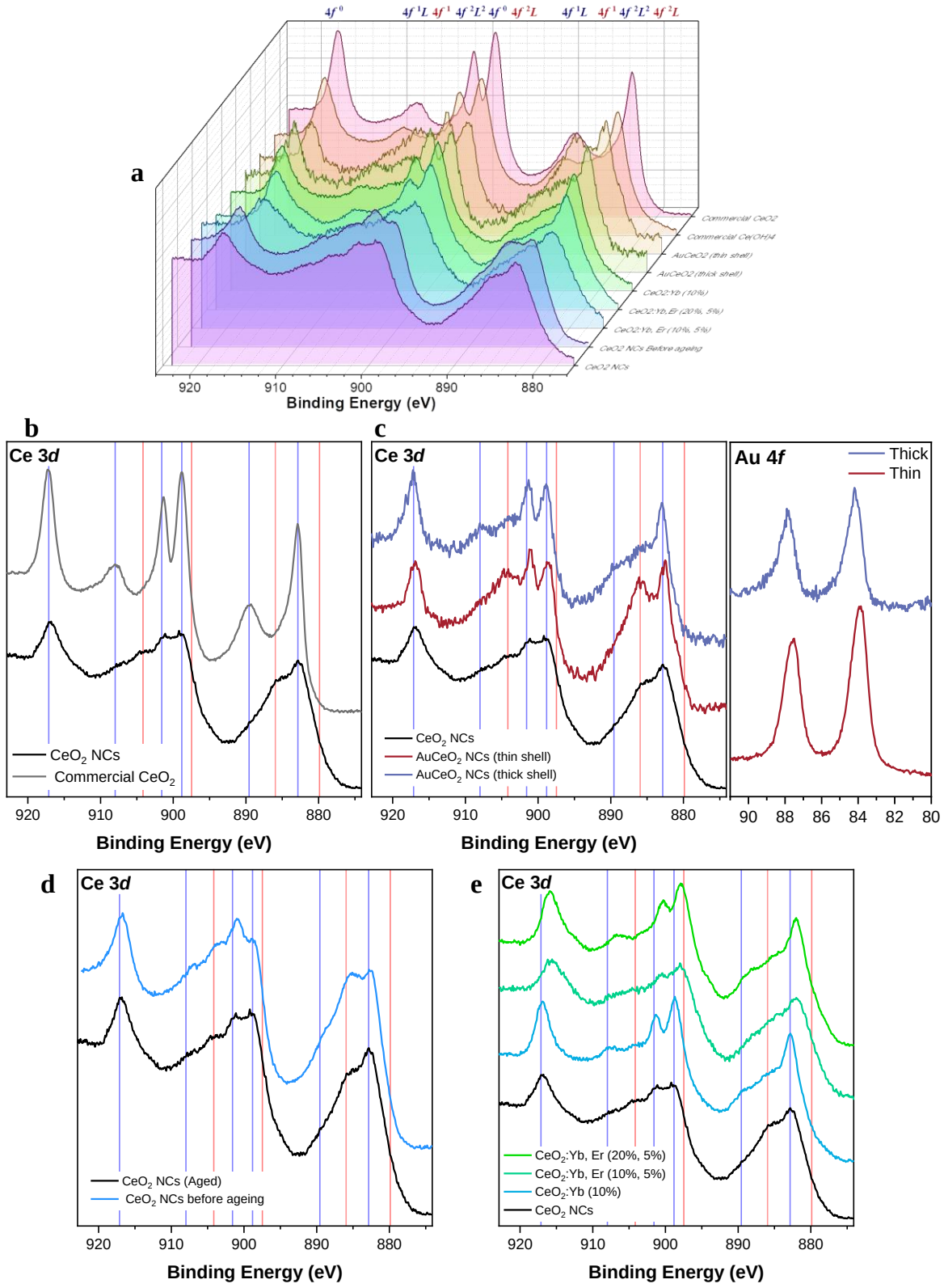

***Figure 6.2**: (a) Normalized Ce 3d XPS spectra of all measured samples. From back to front: Commercial CeO_2 (pink), Commercial $Ce(OH)_4$ (reddish orange), $AuCeO_2$ NCs of thin shell (orange), $AuCeO_2$ of thick shell (yellow), $CeO_2:Yb^{3+}$ (10%) (green), $CeO_2:Yb^{3+}$, Er^{3+} (20%, 5%) (greenish blue), $CeO_2:Yb^{3+}$, Er^{3+} (10%, 5%) (light blue), CeO_2 NCs before ageing (dark blue) and CeO_2 NCs (violet). Below: Comparison between CeO_2 NCs and (b) commercial CeO_2, (c) $AuCeO_2$ NCs (Right: Au 4f spectra), (d) CeO_2 NCs before ageing, (e) doped CeO_2 NCs. Peaks associated to Ce^{3+} transitions are marked in red, peaks associated to Ce^{4+} transitions in blue.*

The first thing to consider is that commercial samples of CeO_2 and $Ce(OH)_4$ present very similar spectra, so we assume it is the signature spectral structure of bulk Ce^{4+} compounds. Now, several structural features can be described. First, the CeO_2 NCs spectra widely diverges from the model bulk structure, showing more peaks of lower definition (**Figure 6.2.b**). Interestingly, Ce^{3+} associated transitions appear to have higher significance in smaller systems. Specifically, Ce^{3+} associated transitions are more evident for the 2.5 nm CeO_2 NC (both before and after the ageing process) (**Figure 6.2.d**) and thin-shelled $AuCeO_2$ hybrid NC samples, in opposition to the same $AuCeO_2$ hybrid NCs of thicker shell and trivalent lanthanide-doped CeO_2 NCs samples (**Figure 6.2.c** and **Figure 6.2.e**, respectively), that are more similar to the bulk sample spectrum. The yet unanswered question is whether these Ce^{3+} transitions are intrinsic to the nanomaterial or if the higher surface-to-volume ratio may increase the kinetics of reduction under X-ray illumination, making the Ce^{3+} peaks artefactual.

For the case of $AuCeO_2$ hybrid NCs, shell growth occurs through an aggregation process, and, consequently, as shell thickness increases its structure resembles more the one from the bulk material. Due to the low depth capacity of the XPS technique, signal-to-noise ratio on Au 4*f* spectra (**Figure 6.2.c**, right) of $AuCeO_2$ samples is a reflection of the thickness of the shell. A higher signal implies higher amount of Au electrons participating in the photoelectric effect, implying a thinner CeO_2 layer. In the case of doped CeO_2 NC samples, which have not been proven to hold any bulk-like features to be related to in terms of size, the portion of Ce^{4+} transitions of $4f^0$ ground states is surprisingly high. This appearance of their spectra can be associated to the loss of the "electron sponge" properties upon the dopant loading, as the correspondent catalytic tests of Chapter V demonstrate. While the position of the dopant atoms has not been mapped, they are clearly affecting the generation of oxygen vacancies, probably by blocking the 2*p*-4*f* hybridization and, therefore, the characteristic properties of nanostructured CeO_2 do not manifest.

Another feature to carefully detail while describing the plotted spectra is the ratio between *v*/*u* peaks ($4f^2L^2$ transitions) and *v'''*/*u'''* peaks ($4f^0$ transitions), meaning, the degree of hybridization on the ground state. Higher weight of *v*/*u* peak than *v'''*/*u'''* implies more density of hybridised states ($4f^2L^2$) than non-hybridised ones ($4f^0$). This feature is easy to assess qualitatively by comparing the intensity of peaks at 898 eV ($4f^0$) and 901 eV, respectively $4f^0$ and $4f^2L^2$ states, in the spectra. For the

bulk and doped CeO_2 samples, the ratio between said peaks is constant: the weight of transitions from non-hybridised final states is bigger than hybridised ones. For pure nanosized CeO_2 NCs and $AuCeO_2$ hybrid NCs, the tendency is not so clear. The intensity ratio between *v'''* and *u* peaks changes for these samples, as previously mentioned peaks show similar intensities. Especially, in the case of non-aged CeO_2 NCs and $AuCeO_2$ NCs of thinner shell, peaks corresponding to hybridised states hold more weight than peaks corresponding to non-hybridised ones. It evidences a heavier density of transitions from hybridised states.

The two main features observed from the *Ce 3d* line of the different measured samples are the presence of Ce^{3+} associated transitions at smaller sizes and the presence, in different proportions, of multiple lines belonging to both hybridized and non-hybridized states both at bulk and nanoscale. It has been described several times in this text how catalytic properties of CeO_2 are related to a valence switch between Ce^{3+}/Ce^{4+} and, specifically in the introduction of this section, how XPS is one of the strongest techniques to quantify the amount of each within the solid. Nonetheless, it is not possible to find enough correlation to suggest that the previous affirmation is correct from the results presented.

While Ce^{3+} transitions appear only at the nanoscale, it was not possible to discern whether their origin is intrinsic or artifactual. On the other hand, hybridization appears independently of the size range, but not in a constant proportion. Also, strictly speaking, size is not the cause of the singular catalytic properties of the material but the circumstance when they are most notable. Hybridization of atomic orbitals O 2*p* and Ce 4*f* within the solid is the consequence of the formation of a chemical bond. Having different proportions of hybridized and non-hybridized configurations in the bulk (or semi-bulk) material and nanosized one implies a different ground state configuration is emerging for the material when reaching the nanoscale. It could explain the origin of the catalytic behaviour of nanostructured CeO_2 and its "electron sponge" properties. The repercussions this would have are mainly a divergence on the reactivity properties of free Ce^{3+} and Ce^{4+} ions and the catalytic applications of the material, as the latter would stem from the complex structure of the Ce-O bond.

6.2.1.2 O 1s peak

Finally, the deconvolution of the O 1*s* signal also provides information about the surface composition of the sample. The chemical environment of oxygen atoms alters the binding energy of 1*s* electrons, giving rise to peak shape and position deviations. According to the work of Biesinger et al, the lattice oxygen in metallic oxides peaks at 529-530 eV depending on the metal species.[19,20] It is also reported that binding energies of surface functional groups such as hydroxyls (-OH) or peroxide groups (O^-), that originate due to defects below the surface, and adsorbed molecules containing O^{2-} (H_2O, organic molecules containing C-O or C=O bonds) are slightly higher (between 531-534 eV).[21] Specifically for the case of oxide nanomaterials of rare-earth and transition metals, the structure of the O 1*s* peak is typically associated with a density of surface defects, associating the hydration of the structure to the surface hydroxyls peak and oxygen vacancies to the H_2O/O^- one. However, for a precise quantification of these features, the absence of any O-containing species besides the material to characterize within the sample to measure is required. Organic species such as the sodium citrate employed as stabilizer can alter O 1*s* shape due to C-O and C-OH functional groups. Even if sample preparation involves a deep purification process to remove salts and other soluble species in the colloid, traces of organic molecules may remain adsorbed to the surface. Checking C 1*s* signal for each sample (Annex F, **Figure 9.17**) is a necessary step to correctly interpretate O 1*s* peak structure. So far, all the samples show the 285 eV C-C peak, and a small shoulder belonging to the C-OH groups. However, the area ratio between C 1*s* and O 1*s* peaks is not high enough to consider its contribution significant in any case except for the thin-shell $AuCeO_2$ sample. The deconvoluted O 1*s* peak for all the measured samples is shown in **Figure 6.3**. Position, relative area and all deconvolution parameters can be found in **Table 9.7** of Annex F.

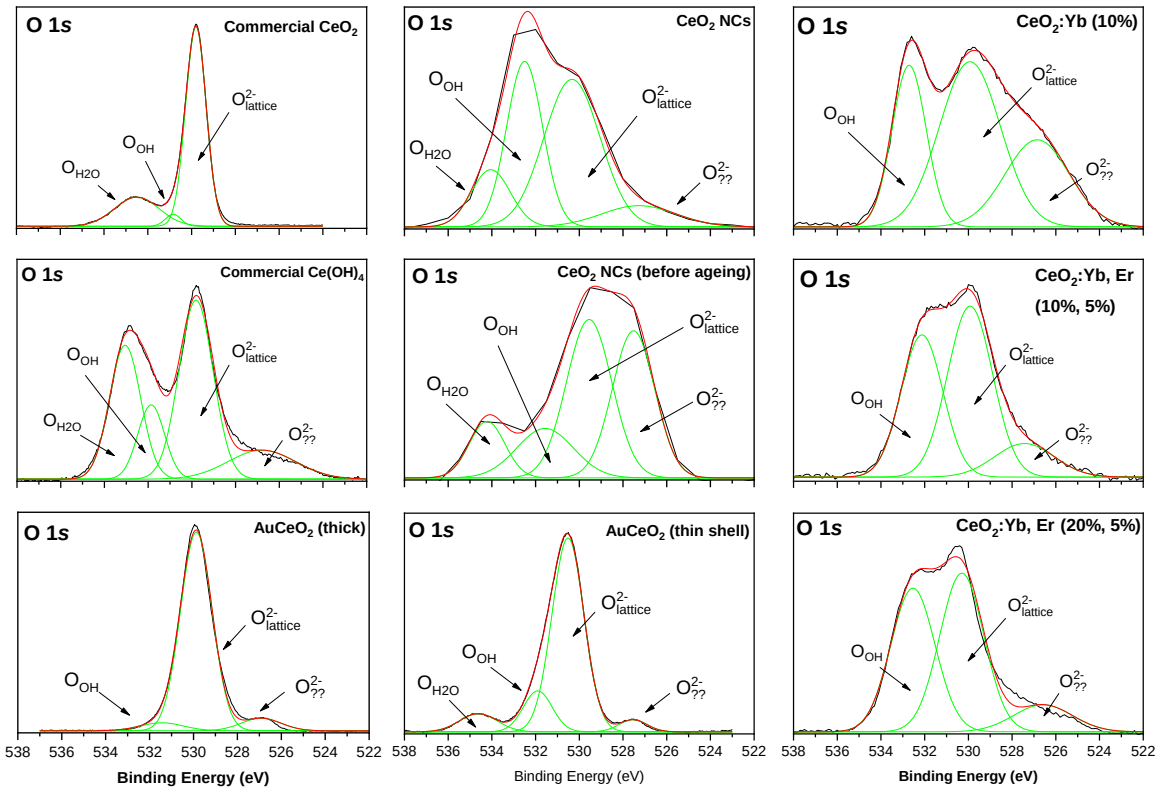

Figure 6.3: *Deconvolution of O 1s XPS peak for all of the measured spectra.*

It can be observed that the weight of the lattice oxygen peak is maximized in bulk (Commercial CeO_2 and $Ce(OH)_4$) and bulk-resembling samples ($AuCeO_2$), which matches the tendency of a lower surface-to-volume ratio. As expected, $Ce(OH)_4$ sample also presents a high contribution of -OH and H-O-H groups. Following the example of the literature, the latter ones are interpreted as adsorbed water molecules in the place of oxygen vacancies. Nanosized CeO_2 and doped CeO_2 samples are the ones containing the biggest contributions of -OH and H-O-H peaks, as expected, also, by the surface-to-volume ratio increase.

Surprisingly, an unexpected peak around 526-527 eV (out of range for lattice O^{2-} of any reported oxide) can be seen in all spectra but bulk commercial CeO_2. Since literature search did not provide with a concrete answer to its origin, no explanation can be categorically affirmed. Nevertheless, since binding energy of 1*s* electrons in oxygen follows a tendency according to the atomic environment (H-O-H > -OH /O^- > M-O^{2-}) it can be deduced that the peak corresponds either to a charging effect or to a lattice O^{2-} bonded to a different metal atom. From a qualitative point of view, the lower binding energy could be related to a lower electron density around the oxygen atom in the M-O environment, which could be a be consequence of an elongated M-O bond. Ionic radius of the different metal species present in the samples, in

increasing order, are 0.097 nm for Ce^{4+}, 0.099 nm for Yb^{3+}, 0.101 nm for Er^{3+} and 0.114 nm for Ce^{3+}.[22,23] If the 526 eV peak were to correspond to bigger interatomic distances between M-O, for the doped samples, were multiple cations of larger radius than Ce^{4+} are present, it would explain the widening of the O 1*s* peak. Also, for samples of CeO_2 NCs before and after ageing, the area of this 526 eV peak in the O 1*s* spectra would relate to Ce^{3+} peaks intensities in the correspondent Ce 3*d* spectra, since no other metal cation is present in those samples and the Ce^{3+} peaks were only notable in these two spectra. However, if this peak is a feature of the sample or an artifact product of the exposure time to incident X-rays under ultra-high vacuum conditions, cannot be asserted without further proof.

6.2.2 CeO_2 XANES Spectroscopy

The electronic structure of CeO_2 has been proven to be very dependent on the environment, to such a high degree that certain aspects of XPS measurements may be questioned. Taking advantage of the versatility of XAS, an experimental setup that allows measurement of the XANES spectra of the samples dispersed in liquid media, mimicking *in operando* conditions for the CeO_2 NCs, is prepared for the characterization of several different samples. The L_3 edge line of Ce was observed by high-energy resolution fluorescence-detected hard X-ray absorption spectroscopy (HERFD-XAS), which provides a highly selective probe for the electronic state of each element present and a high spectral resolution that allows the observation of the L_3 edge fine structure. The experiment was carried out at beamline ID26 of the European Synchrotron Radiation Facilities (ESRF)[24] in Grenoble under the guidance of Prof. Pieter Glatzel. Schematized setup for the measurements, reproduced from the published work of a previous collaboration,[25] is shown in **Figure 6.4**. For a detailed experimental description, see Chapter VII section 7.5.2.2.

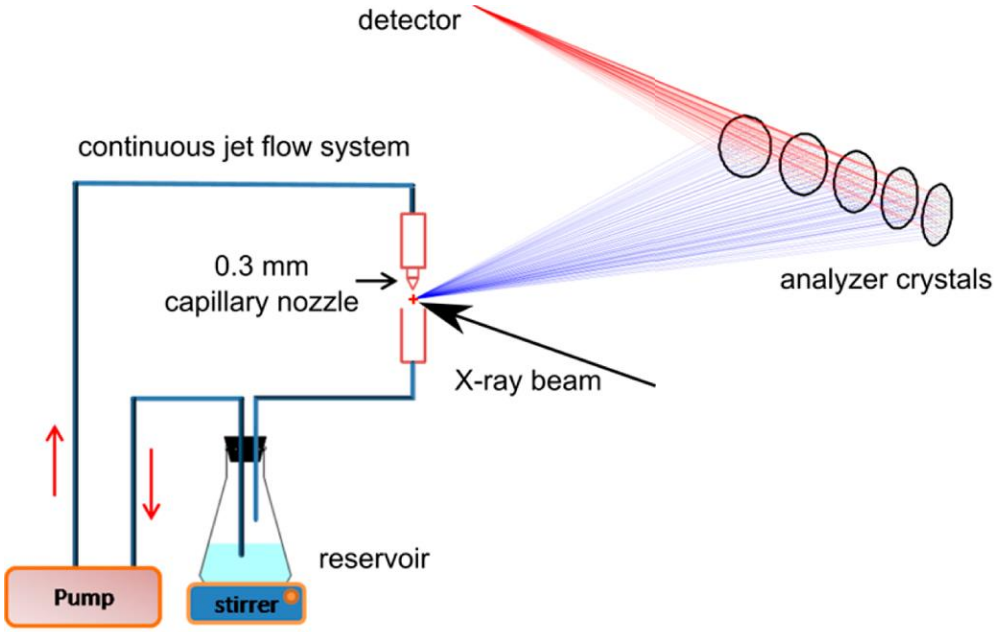

***Figure 6.4**: Scheme of experimental setup employed for XAS measurements. Reproduced from [25].*

Two distinct measurement modes were performed on a set of different CeO_2 samples. The first mode consisted in the spectrum recording of the unperturbed solvent-dispersed sample as prepared. The second one consisted in the time evolution recording of the spectra of the sample *in operando* conditions, meaning after suffering a perturbation. Specifically, the evolution of the spectra during the NC synthesis and during its catalytic activity. For the in-situ measurement of the synthesis reaction, a $[Ce(Cit)_2]^{3-}$ solution was exposed to the correspondent amount of TMAOH. The catalytic test monitored the catalase-mimetic activity of the particles during the degradation of H_2O_2. Different amounts of a H_2O_2 stock solution were added to the particle dispersion, mimicking the experiences of Chapter V section 5.2.2.1, and the time evolution of pH and XANES spectra was recorded.

Spectra were recorded on a CeO_2 NCs set of samples of different ageing stage: Non-aged CeO_2 NCs and temperature-aged CeO_2 NCs synthesized three days and three years before measurement. Chosen control for Ce^{3+} is a solution of $CeCl_3$ precursor salt. Chosen controls for bulk CeO_2 were the Commercial CeO_2 powder (50-200 nm) dispersed in milli-Q water and a sample of CeO_2 NCs synthesized in the absence of citrate (herein referred to as CeO_2 TMAOH) wich resulted in aggregates bigger than 0.2 μm in size, in order to avoid effects from possible drying treatments the commercial sample must have undergone. Finally another sample synthesized and dispersed in EtOH (herein refered to as CeO_2 EtOH), in order to reproduce the work of Cafun et al[25], was included.

While this technique requires exposure of the sample to high energy photons during long intervals, it is not expected for the X-rays to have such an aggressive effect on the sample in comparison to XPS, as the solvent and citrate present can dissipate the incident photons through alternative pathways, and the continuous movement of the jet flow prevents over-exposure of the sample to the beam. However, state of the samples after long measurement times was assessed in order to determine how the beam may affect them.

6.2.2.1 XANES characterization of CeO_2 NCs

X-ray absorption spectra of Ce L_3 Edge and pre-edge for the Ce^{3+} ($CeCl_3$ solution) and Ce^{4+} (bulk CeO_2, from a dispersion of CeO_2 commercial powder) controls is shown in **Figure 6.5.I**. The pre-edge peak (inset), correspondent to transitions from 2*p* to 4*f* orbitals, evidences the differences in the spectral shape of configurations belonging to different symmetry terms: two peaks can be distinguished for the ^2F symmetry of Ce^{3+} ions and a single peak for the ^1S of Ce^{4+}, which we assume pure since no residue of Ce^{3+} peaks is present on the spectrum. These spectra will be taken as reference to assign the symmetry of the synthesized samples. The edge peak (2*p* to 5*d* transitions) shows different spectral features for the two species: while the Ce^{3+} control contains a single peak for the transitions into unoccupied 5*d* orbitals, the bulk CeO_2 control contains a quadruplet peak, read as the two-peak spectral shape described in above section 6.1.2, correspondent to screened and unscreened states, and the fine structure of each peak family. The shoulder on the lower energy peak family (red line on **Figure 6.5.I**), corresponded to "screened" $4f^1$ states, matches the same position as the Ce^{3+} edge peak. This could be interpreted as a small fraction of Ce^{3+} atoms within the sample modifying the appearance of the Ce^{4+} peak; however, the absence of the characteristic structure of the Ce^{3+} peak in the pre-edge region invalidates this assumption. Moreover, it cannot explain the same feature for the higher energy peak family (belonging to unscreened states). The effect of crystalline structure over the spectra of metal ions d orbitals has been thoroughly detailed in the literature.[26] The characteristic splitting of the five degenerated *d* orbitals into e_g and t_{2g} levels of 3:2 area ratio upon the ligand field of the oxygen atoms in the coordination shell surrounding the metal core is an effect known as crystal field splitting. For the case of CeO_2, the splitting between the 5*d* orbitals proves to be wider than the 5*d* peak width, making it possible to observe under high-resolution

conditions such as the provided by this technique.[18,27,28] **Figure 6.5.II** compares the XAS spectra of the Ce^{3+} from the salt precursor solution before and after citrate complexation. No difference in shape in the XANES spectra is observed, apart from a small loss of intensity of both pre-edge and edge peaks compared to the EXAFS interval. Since citrate complexation does not involve any redox process, only a ligand exchange in the coordination shell, said small changes were to be expected.

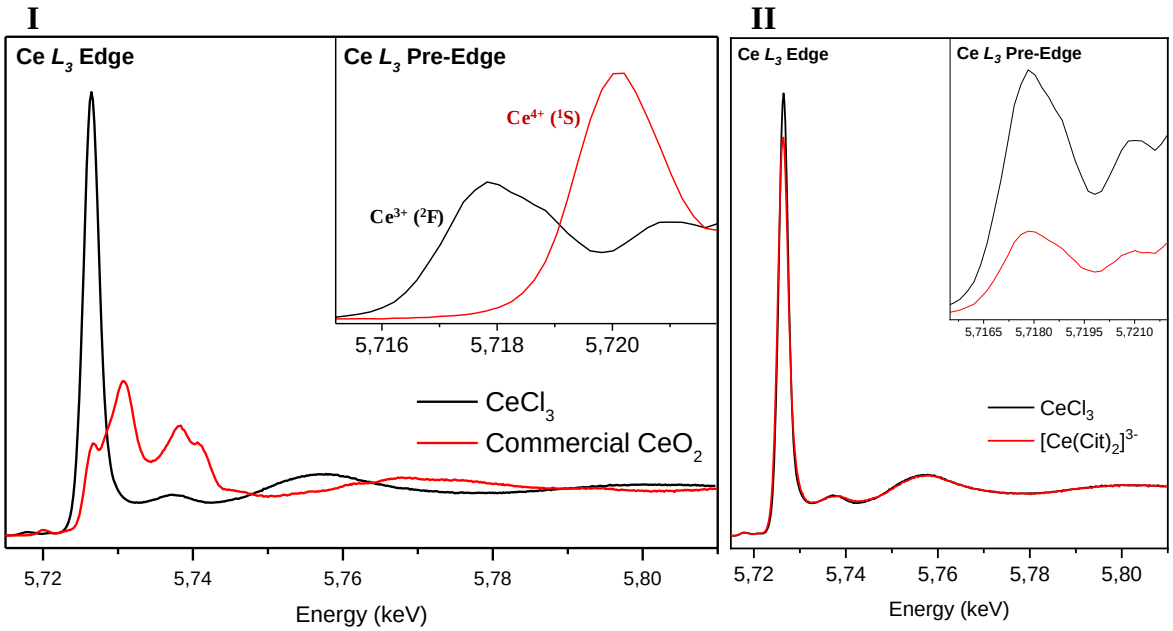

***Figure 6.5**: XAS normalized by area of (I) Ce L_3 Edge and (inset) pre-edge for $CeCl_3$ and dispersed CeO_2 commercial powder solutions used as control and (II) Ce L_3 Edge and (inset) pre-edge for $CeCl_3$ and $[Ce(Cit)_2]^{3-}$.*

Aggregated CeO_2 NCs, synthesized both in water and in ethanol, by mixing two solutions of $CeCl_3$ and TMAOH in a 1:2,7 molar ratio, are compared to the CeO_2 Commercial powder in **Figure 6.6**. The shape of XANES spectra (**Figure 6.6.I**) is the same for the aqueous aggregated sample (CeO_2 TMAOH) and the commercial one. Ethanolic one (CeO_2 EtOH) shows a higher intensity of the e_g shoulder at the expense of the t_{2g} on the screened peak. When determining the size of the dispersed particles by DLS, both Commercial CeO_2 and CeO_2 TMAOH samples generate signals at sizes bigger than 1 μm. However,the ethanolic solution, peaked both in the micron range and at 250 nm. No signal below 100 nm was obtained for any of the samples and all of them sediment if left unstirred for enough time. Size differences within the aggregate samples may be the origin of the intensity difference between e_g and t_{2g} signals. Both samples share the exact shape and position for the pre-edge peak (**Figure 6.6.II**), indicating that they are composed entirely of configurations holding a ^1S symmetry term, formally $4f^0$.

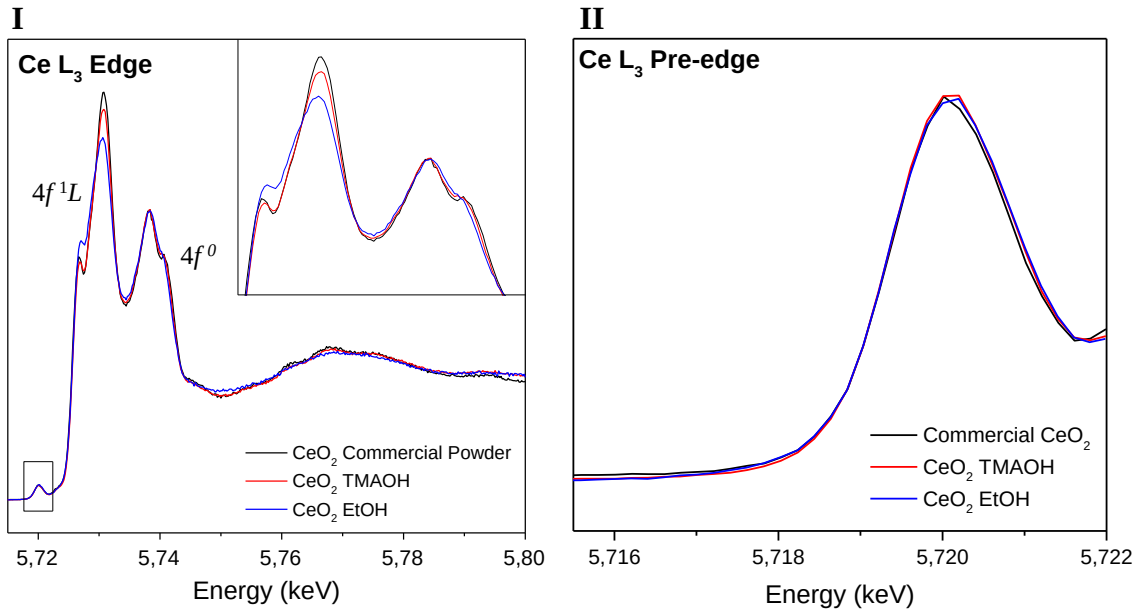

Figure 6.6: *XAS normalized by area of (I) Ce L3 Edge and (II) pre-edge for bulk CeO_2 models: Commercial CeO_2 powder (black), aqueous CeO_2 synthesized without citrate stabilization (red) and CeO_2 synthesized in ethanol (blue).*

During the *in situ* synthesis of CeO_2 NCs (**Figure 6.7**), the first of the recorded spectra, correspondent to a $[Ce(Cit)_2]^{3-}$ solution, matches the reference from **Figure 6.5.II**. Changes in the pre-edge region of the spectra during the time-lapse indicate a change from a ^2F configuration to a ^1S one exclusively within the 12h interval of the reaction, in agreement with the expected Ce^{3+} to Ce^{4+} oxidation. As time passes, the progressive oxidation causes the Ce^{3+} edge peak to decrease while Ce^{4+} spectral structure appears, including also the shoulder caused by the crystal field splitting. It indicates the precipitation of the solids along with the oxidation. The effect of the crystal field, however, is not as evident as in the bulk reference, consequence of the finite size of the nanocrystals.

The effect of age on the particles was tested by comparing previously described bulk CeO_2 spectrum to the spectra of synthesized 2.5 nm CeO_2 NCs before and after the ageing process of NCs both a few days age (Fresh CeO_2) and 3-year-old ones (**Figure 6.8**). The pre-edge spectra of the three samples (**Figure 6.8.III**) is identical to that of the CeO_2 commercial powder, containing the characteristic single peak of a ^1S symmetry. It can be assumed that size does not affect formal oxidation state of the cerium atoms, as the abrupt decrease from bulk to 2.5 nm does not produce impaired electrons at 4*f* orbitals changing the symmetry term. It, however, causes affectations to the edge band (**Figure 6.8.I**): The intensity differences between e_g and t_{2g} levels

at the screened peak also observed when comparing the ethanolic sample to the other bulk ones (**Figure 6.6.I**) and the partial loss of the fine structure at the unscreened peak, where the shoulder is less evident than the bulk case. As the name indicates, crystal field splitting is a phenomenon pertaining to.the crystalline structure. The degeneracy breaking on atomic *d* orbitals is caused by the loss of spherical symmetry when ligands alter electron density around the atom due to their position around it. In addition, local defects such as oxygen vacancies on the crystalline structure bring back orbital degeneracy. For that reason, an increase in surface atoms contribution to the spectra, where the density of defects is higher, limits the resolution of the peak and diminishes the definition of the split peaks. Synthesized 2.5 nm CeO_2 NC samples, in which the surface-to-volume ratio is maximized, exhibit spectra of less definition than their bulk counterpart.

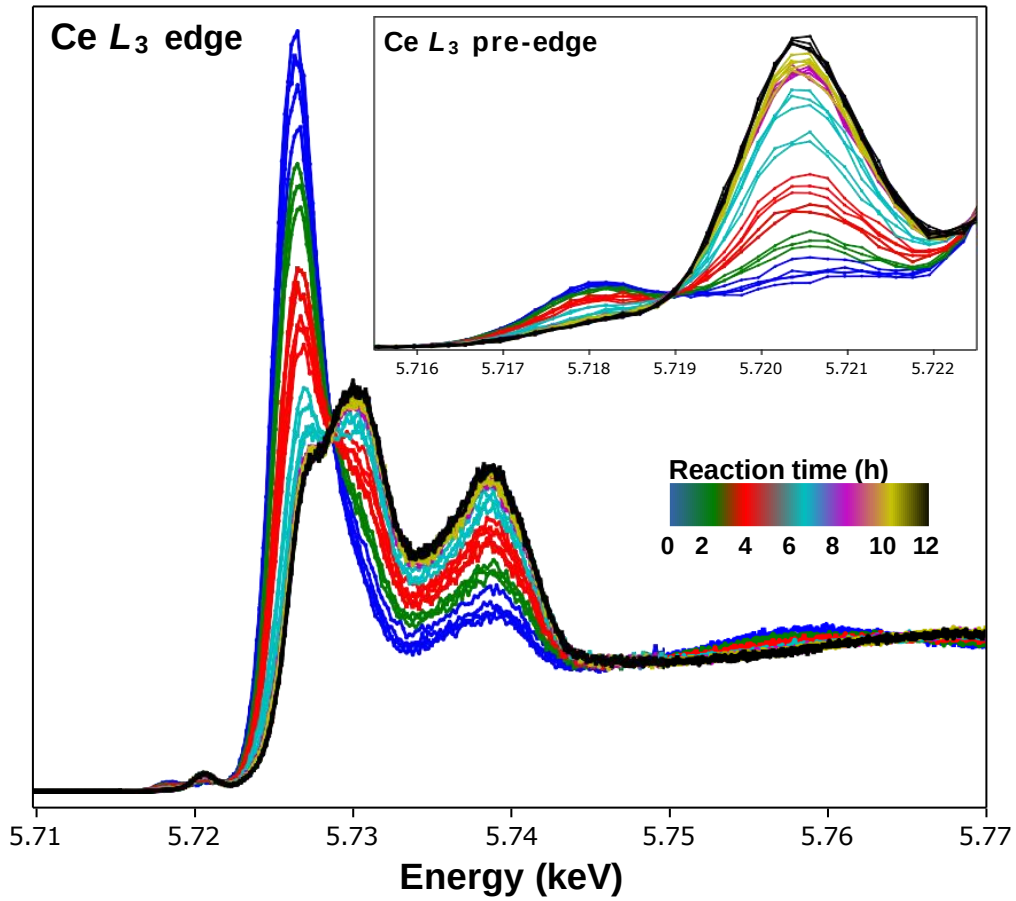

***Figure 6.7**: Time evolution of the XANES spectra of Ce L_3 Edge and (inset) pre-Edge for the room temperature synthesis of CeO_2 NCs, reproduced in situ by mixing a $[Ce(Cit)_2]^{3-}$ and a TMAOH solution in a 1:2.7 molar ratio.*

To compare the edge spectra of NC samples of different age, they have been plotted separately in **Figure 6.8.II**. The definition of the peak fine structure appears to be proportional to the sample's age. The differences between the not-aged and the freshly aged ones (green and red lines, respectively) are minimal, but apparently the ageing process lowers the number of defects on the structure, as e_g shoulder is more noticeable after the treatment. For the differences between the freshly aged and the 3-year-old one (blue line), since the composition of all samples seems to be homogeneous (as evidenced by the pre-edge spectra), it appears to be caused probably by a sharpening of the crystal structure (a decrease the amount of amorphous material of the surface) or a small degree of aggregation into 4-10 nm particle clusters, as the splitting shoulder seems to have evolved into a proper peak for the case of the screened states.

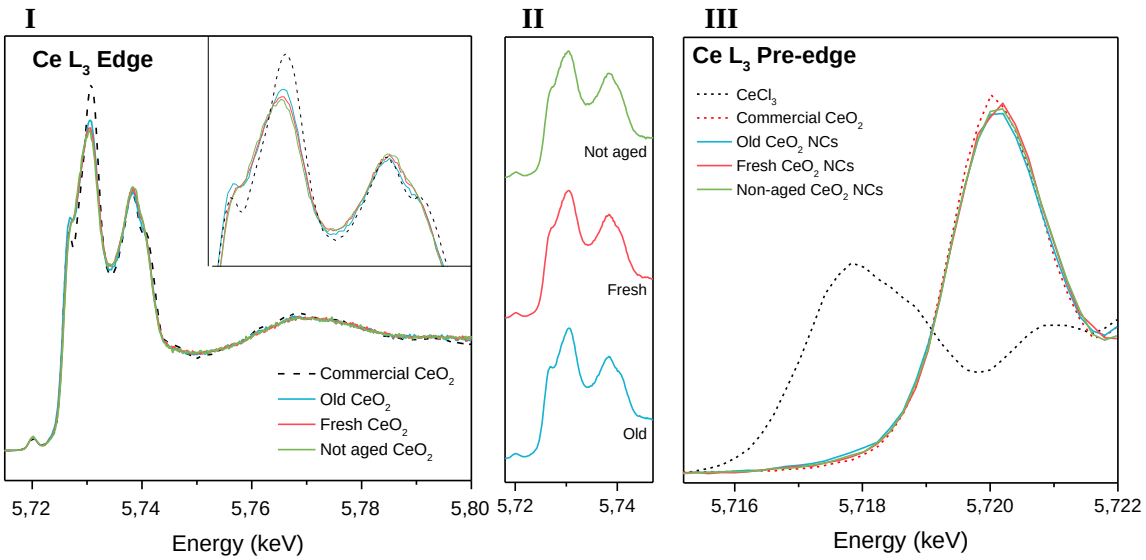

Figure 6.8: *XAS normalized by area of (I and II) Ce L_3 Edge and (III) pre-edge for synthesized CeO_2 NCs of different age: 3 years old CeO_2 NCs (blue), freshly aged (3 days old) CeO_2 NCs (red) and not aged CeO_2 NCs (green). Dotted lines: reference patterns.*

6.2.2.2 in operando XANES of CeO_2 NCs

While no Ce^{3+} configurations were found within the structure of the CeO_2 samples in the XANES characterization of the material, it is not deniable that the catalytic properties the material exhibit imply that it participates in the redox reaction, on what has been described as a 3+/4+ valence switch on the literature, that allows the structure to lose and regain structural oxygen located on (111) planes, or even substitute it with H_2O molecules. The mechanism of this catalytic electron exchange, however, has not been yet discussed in this text. Therefore, to attain some insight into this mechanism, and its dependence on hybridization between atomic Ce 4*f* and O 2*p* orbitals, changes in the XANES spectra during the catalytic activity of the material on the different samples have been monitored.

The chosen reaction is the degradation of H_2O_2 into H_2O and O_2, a vastly described reaction catalyzed by CeO_2.[29] The catalase-mimicking activity of the material has been previously studied and described in 5.2.2. It provides with a simple way to induce a catalytic process in situ on the XAS setup. To a known volume of a previously characterized sample, the required amount of H_2O_2 is injected and the continuous measurement is started.

Changes on the Ce L_3 edge band are plotted in **Figure 6.9**. Increasing CeO_2-to-H_2O_2 molar ratios were tested, increasing the difference between the spectra recorded before and after the peroxide injection. Only 1:1 and 1:5 ratios are shown, as below this amount signal variation is too small to be registered. The edge band does not show changes towards a Ce^{3+} species. Main feature observed is the temporary loss of crystal field effect after H_2O_2 injection associated to surface disorder. The e_g shoulder disappears while the peak widens and moves slightly its position. The ratio between screened ($4f^1L$) and unscreened ($4f^0$) peaks remains constant, implying no change in the degree of hybridization occurs. Changes in the pre-edge region are also very subtle, almost imperceptible, and easily mistaken for noise. This region of the spectra has been plotted in **Figure 6.9 (right)**, normalized to the peak intensity value rather than by area. Immediately after the H_2O_2 injection, a small peak displacement to lower energy is observed, however, if it occurs due to an alteration of the energy difference between 2*p* and 4*f* levels or due to a change in symmetry is not possible to discern, as spectral shape is constant during the process.

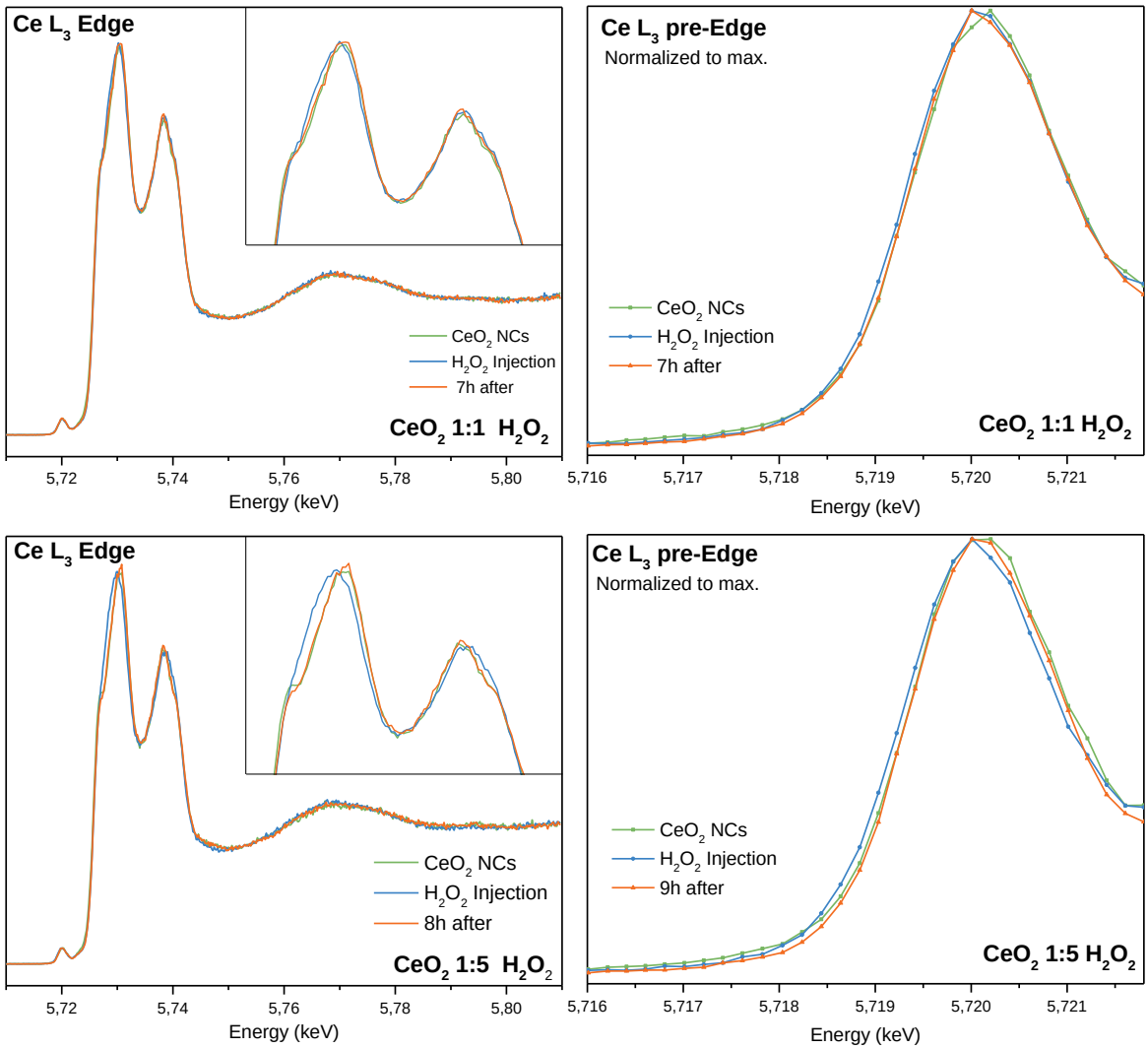

***Figure 6.9**: XAS time-dependent evolution of (left) Ce L_3 edge and (right) pre-edge band during the CeO_2 NCs catalytic degradation of H_2O_2 for a (top) 1:1 molar ratio and a (bottom) 1:5 molar ratio of CeO_2 to H_2O_2.*

After some time, the system returns to its original state. The kinetics of the process is altered in comparison to those of the same system in the absence of X-ray exposure. It does not alter in any way the objective of the experiment, however, as the objective was to achieve observation of the catalyst *in operando* conditions, not measure activity or other parameter depending on kinetics. To verify that the transformations involved are not altered, a transmittance measurement of the sample before and after XAS measurement is taken (**Annex F, Figure 9.18**), were the expected alteration in the UV-vis extinction is observed, and pH is monitored during the process to verify the equivalence to previously performed tests (**Annex F, Table 9.8**). For buffered samples, upon X-ray exposure sodium citrate is oxidized to DCA or CO_2, decreasinges its concentration in solution and lowering mixture's pH.

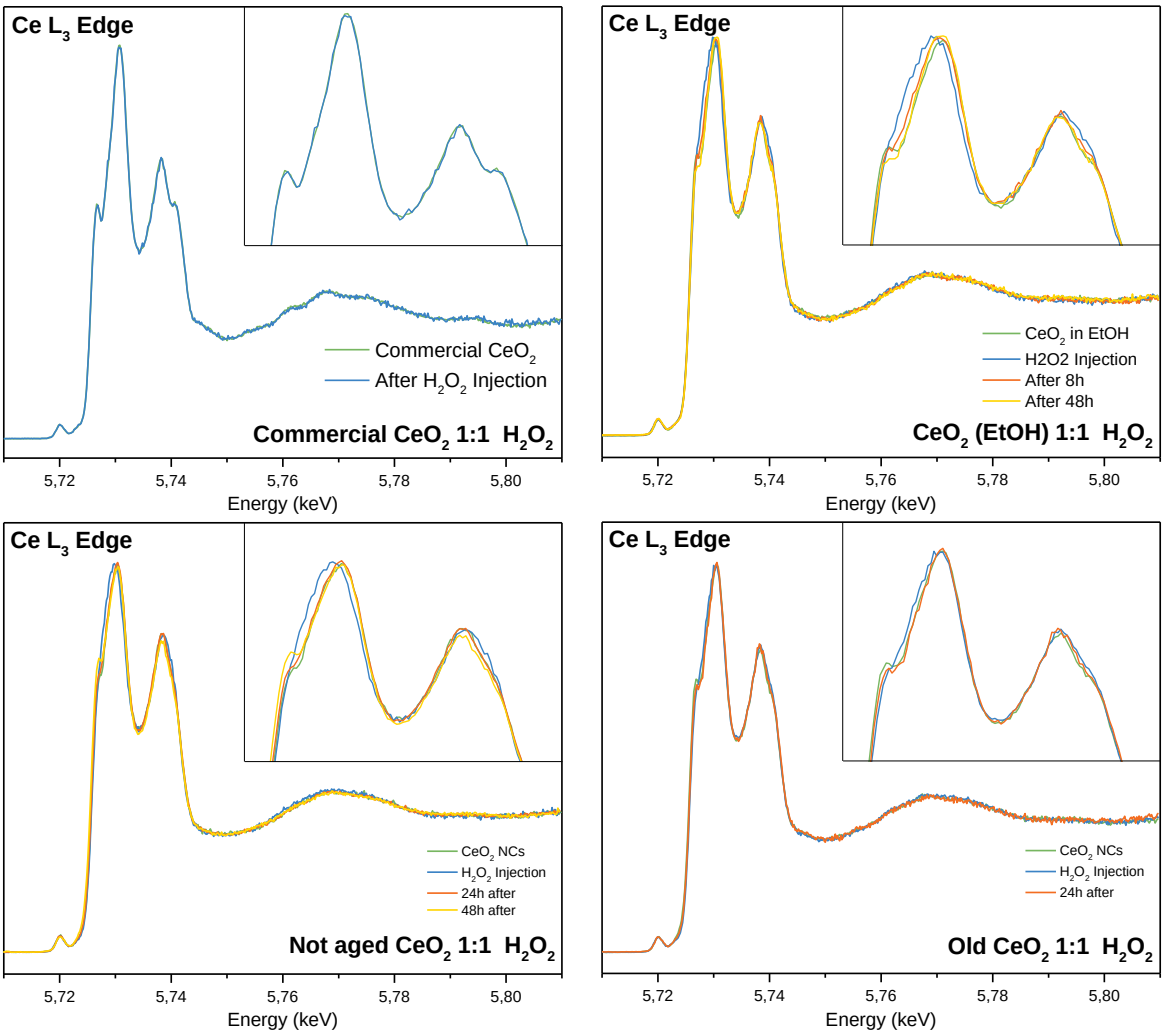

***Figure 6.10**: Ce L_3 edge band time evolution for bulk CeO_2 commercial powder (top, left), CeO_2 in EtOH (top, right), CeO_2 NCs before the ageing process (bottom, left) and 3-year-old CeO_2 NCs sample (bottom, right).*

Other CeO_2 samples previously characterized by XAS are also measured during the catalytic process. **Figure 6.10** shows the Ce L_3 edge band evolution for the bulk CeO_2 commercial powder (top, left), the ethanolic CeO_2 sample (top, right), the CeO_2 NCs before the ageing process (bottom, left) and the 3-year-old CeO_2 NCs sample (bottom, right), chosen according to size and age criteria. Bulk CeO_2 does not show any change after the peroxide injection, even if the peroxide is being degraded (as evidenced by the colour change of the suspension and presence of bubbles afterwards). For the ethanolic sample, change is more notable than the aqueous bulk counterparts. Samples of nanocrystals of same size (2.5 nm) as the CeO_2 from **Figure 6.9** behave similarly in the spectra. Degradation on aged CeO_2 is not an issue, as 3-year-old nanocrystals show the same spectral changes than freshly produced ones. The sample tested before any ageing stage takes place, however, seems to undergo a chemical ageing stage caused by the H_2O_2, so the original state is never recovered: it

evolves to the typical spectra of the aged CeO_2 NCs, were the e_g shoulder becomes more evident. Ce L_3 pre-edge band evolution for the same samples (**Figure 6.11**) follows the same tendency that the edge band: no changes for the bulk commercial CeO_2, and a subtle and temporary peak displacement just after the peroxide addition for the rest.

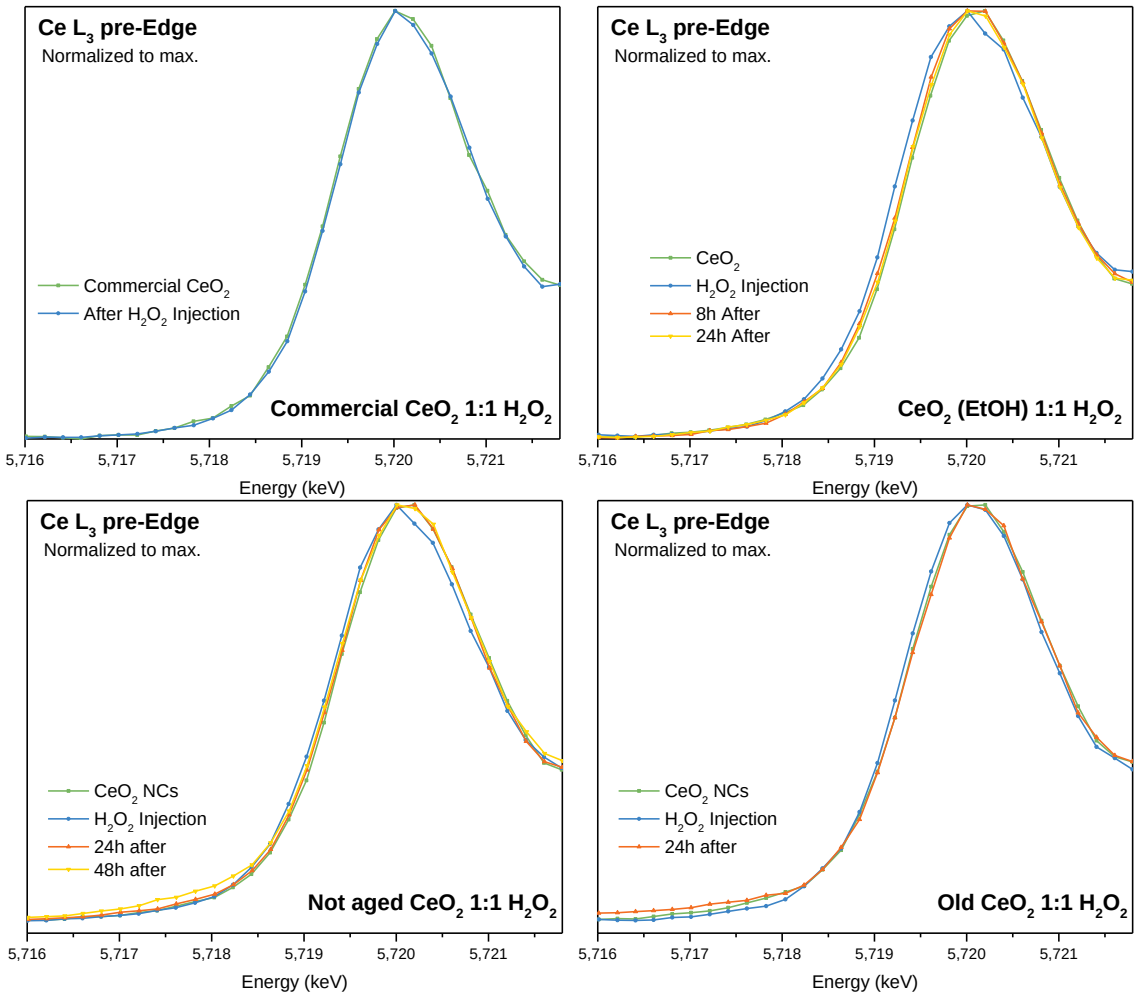

***Figure 6.11**: Ce L_3 pre-edge band time evolution for bulk CeO_2 commercial powder (top, left), CeO_2 in EtOH (top, right), CeO_2 NCs before the ageing process (bottom, left) and 3-year-old CeO_2 NCs sample (bottom, right).*

From all the changes observed, several features can be interpreted. The most notable one is the temporary loss of crystal field features during the catalytic activity, related to an increment of surface defects, such as oxygen vacancies or peroxide adsorption. The crystal fied splitting loss becomes more evident for smaller crystal sizes, where the surface contribution is most notable.. For bulk samples no changes on the XANES spectra are recorded during the experiments, the only observable perturbation being the characteristic colour change of the solution. As catalysis is a surface phenomenon, for samples with a lower surface-to-volume ratio the contribution is not significant, and therefore not distinguishable under this technique.

Both bulk and surface effects are distinguishable on a multimodal size distribution such as the ethanolic sample. However, the degree of loss of crystal field features is higher in comparison to the rest of the samples. This difference may be caused by the change in the solvent (H_2O may be occupying the oxygen vacancy sites on the surface, mitigating the impact of the defect generation, while EtOH cannot do so) but no further tests have been performed to confirm it. The behaviour of aged samples does not seem to be altered at least in a three-year interval. The small accentuation of crystal field features is probably caused by an "improved" crystal structure, accentuated by a decrease in defect density. Also, no pre-edge spectra of any of the measured samples show at any point an evident change of symmetry term indicating a reduction of surface atoms, but the origin of the small shift to lower energies is yet to be clarified.

6.2.3 Discussion

The observed changes in the Ce L_3 spectra mostly respond to changes in the material environment and do not show evident participation of 4*f* or 5*d* orbitals in the catalytic process. It raises a new formulation of the question about the role of Ce atoms in the catalytic roles of CeO_2. There is evident participation of near-surface oxygen atoms in the catalytic process, proven by the changes in the density of oxygen vacancies. Designing an experiment that allows us to look at surface oxygen, however, may cause logistic complications. Nevertheless, if the only role the CeO_2 takes in the catalytic process is as a matrix containing O atoms, the catalytic properties would be universal for any oxide of the same crystalline structure rather than a special feature of CeO_2, which is not the case. From the XPS and XANES characterization described in this chapter, it emanates that the hybridization between O 2*p* and Ce 4*f* atomic orbitals confers the chemical bond within the solid a set of properties that give rise to the catalytic activity. This is by no means an exclusive trait of CeO_2: Bianconi et al.[17] described in 1987 how, within the lanthanide oxide series, hybridization is also occurring in PrO_2 but not in UO_2, sharing the three oxides an *fcc* crystalline structure. The same work also includes $Ce(SO_4)_2$, that, containing a different ligand and different crystalline structure, presents also the Ce 4*f* – L 2*p* hybridization that appears to be the origin of such catalytic properties. If the special catalytic behaviour is not reflected in any of the participants of the bond during the catalytic process, then, it must be caused by the bond itself.

As explained at the beginning of this chapter, this work aimed to describe the origin of the catalytic properties of nanostructured CeO_2. It is common to find these catalytic properties explained within the literature as a redox cycle containing a switch between Ce^{4+}/Ce^{3+}. The explanation here provided, that the catalytic properties are the consequence of the hybridization of atomic orbitals during the formation of the chemical bond, is neither new nor does it intend to dispute or call all the literature about it into question. Both descriptions of this catalytic behaviour are complementary, not opposites: The precise and detailed description of the electronic and crystal structure of the material is required when the catalyst is the object of study; a brief, simplified description of the same is necessary when the applications, and not the material, are the primary objective. As catalytic applications research falls in a multidisciplinary area, the priority is the development of a common

language between different specialists that allows for the coordinated operation towards the final aim of any research: its application in society. This role is fulfilled by the “valence switch” explanation. The language simplification adopted, however, should not shape how this concrete reality is understood. For materials research, the scientific community should be able to discern between precise and simplified language and apply each one when required.

6.3 PERSPECTIVES

While the question motivating this chapter has been practically answered by the obtained results, a deeper understanding of the phenomena governing the catalytic properties of the material is required. From XPS, it would be interesting to determine the origin of the Ce^{3+}-associated transitions appearing on the spectra by evaluating if they are time-dependent. If they were, measurements would need to be carefully performed so that every sample is exposed to ultra-high vacuum conditions and X-ray illumination for the same amount of time. The XANES characterisation leaves more room for exploration since only pure CeO_2 samples have been characterised. It could be interesting to evaluate the effect of lanthanide doping and hybridization of plasmonic metals on the Ce L_3 line, characterising the NCs as-prepared and *in operando* conditions. In addition, since no major changes were recorded on the 4*f* or 5*d* orbitals of Ce, it could be interesting to look for the effect of the catalysis in the other atomic species present: Oxygen atoms. However, to be able to observe lattice oxygen by XAS when the measurements are performed at atmospheric conditions for water-dispersed samples is a challenge difficult to overcome.

6.4 REFERENCES

1. Jo, T. & Kotani, A. Theory of core photoabsorption spectra in CeO_2. *Solid State Commun* **54**, 451–456 (1985).

2. Romeo, M., Bak, K., el Fallah, J., le Normand, F. & Hilaire, L. XPS Study of the reduction of cerium dioxide. *Surface and Interface Analysis* **20**, 508–512 (1993).

3. Paparazzo, E. On the curve-fitting of XPS Ce(3*d*) spectra of cerium oxides. *Mater Res Bull* **46**, 323–326 (2011).

4. Kotani, A., Jo, T. & Parlebas, J. C. Many-body effects in core-level spectroscopy of rare-earth compounds. *http://dx.doi.org/10.1080/00018738800101359* **37**, 37–85 (2006).

5. Shoko, E., Smith, M. F. & McKenzie, R. H. Mixed valency in cerium oxide crystallographic phases: Valence of different cerium sites by the bond valence method. *Phys Rev B Condens Matter Mater Phys* **79**, 134108 (2009).

6. Bêche, E., Charvin, P., Perarnau, D., Abanades, S. & Flamant, G. Ce 3*d* XPS investigation of cerium oxides and mixed cerium oxide (Ce xTiyOz). in *Surface and Interface Analysis* vol. **40** (2008).

7. Thornton, G. & Dempsey, M. J. Final-state effects in the 3*d* and 4*d* X-Ray photoelectron spectra of CeO_2. *Chem Phys Lett* **77**, 409–412 (1981).

8. Teterin, Y. A., Teterin, A. Y., Lebedev, A. M. & Utkin, I. O. The XPS spectra of cerium compounds containing oxygen. *J Electron Spectros Relat Phenomena* **88–91**, 275–279 (1998).

9. Maslakov, K. I. *et al.* The electronic structure and the nature of the chemical bond in CeO_2. *Physical Chemistry Chemical Physics* **20**, 16167–16175 (2018).

10. Dauscher, A. *et al.* Characterization by XPS and XAS of supported Pt/TiO_2—CeO_2 catalysts. *Surface and Interface Analysis* **16**, 341–346 (1990).

11. Paparazzo, E. Use and mis-use of x-ray photoemission spectroscopy Ce3*d* spectra of Ce_2O_3 and CeO*2*. *Journal of Physics: Condensed Matter* **30**, 343003 (2018).

12. Yano, J. & Yachandra, V. K. X-ray absorption spectroscopy. *Photosynth Res* **102**, 241–254 (2009).

13. de Groot, F. High-Resolution X-ray Emission and X-ray Absorption Spectroscopy. *Chem Rev* **101**, 1779–1808 (2001).

14. Kotani, A. & Shin, S. Resonant inelastic x-ray scattering spectra for electrons in solids. *Rev Mod Phys* **73**, 203 (2001).

15. Cowan, R. D. *The theory of atomic structure and spectra*. (University of California Press, 1981).

16. Paidi, V. K., Brewe, D. L., Freeland, J. W., Roberts, C. A. & van Lierop, J. Role of Ce 4*f* hybridization in the origin of magnetism in nanoceria. *Phys Rev B* **99**, 180403 (2019).

17. Bianconi, A. *et al.* Specific intermediate-valence state of insulating 4f compounds detected by L_3 x-ray absorption. *Phys Rev B* **35**, 806 (1987).

18. Soldatov, A. v. *et al.* Crystal-structure effects in the Ce L_3-edge x-ray-absorption spectrum of CeO_2: Multiple-scat. *Phys Rev B* **50**, 5074 (1994).

19. Biesinger, M. C., Lau, L. W. M., Gerson, A. R. & Smart, R. S. C. Resolving surface chemical states in XPS analysis of first row transition metals, oxides and hydroxides: Sc, Ti, V, Cu and Zn. *Appl Surf Sci* **257**, (2010).

20. Biesinger, M. C. *et al.* Resolving surface chemical states in XPS analysis of first row transition metals, oxides and hydroxides: Cr, Mn, Fe, Co and Ni. *Appl Surf Sci* **257**, (2011).

21. Dupin, J. C., Gonbeau, D., Vinatier, P. & Levasseur, A. Systematic XPS studies of metal oxides, hydroxides and peroxides. *Physical Chemistry Chemical Physics* **2**, 1319–1324 (2000).

22. Shannon, R. D. Revised effective ionic radii and systematic studies of interatomic distances in halides and chalcogenides. *Acta Crystallographica Section A* **32**, (1976).

23. Behera, R. K. & Deo, C. S. Effect of Ce^{+} and Th^{4+} ion substitution in uranium dioxide. in *Materials Research Society Symposium Proceedings* vol. **1383** (2012).

24. Gauthier, C., Solé, V. A., Signorato, R., Goulon, J. & Moguiline, E. The ESRF beamline ID26: X-ray absorption on ultra dilute sample. *J Synchrotron Radiat* **6**, 164–166 (1999).

25. Cafun, J. D., Kvashnina, K. O., Casals, E., Puntes, V. F. & Glatzel, P. Absence of Ce^{3+} sites in chemically active colloidal ceria nanoparticles. *ACS Nano* **7**, 10726–10732 (2013).

26. Dorenbos, P. Crystal field splitting of lanthanide $4f^{n-1}5d$-levels in inorganic compounds. *J Alloys Compd* **341**, 156–159 (2002).

27. Soldatov, A. v., Ivanchenko, T. S., Kotani, A. & Bianconi, A. L_3 edge X-ray absorption spectrum of CeO_2: crystal structure effects. *Physica B Condens Matter* **208–209**, 53–55 (1995).

28. Prieur, D. *et al.* Size Dependence of Lattice Parameter and Electronic Structure in CeO_2 Nanoparticles. *Inorg Chem* **59**, 5760–5767 (2020).

29. Plakhova, T. v. *et al.* Towards the surface hydroxyl species in CeO_2 nanoparticles. *Nanoscale* **11**, 18142–18149 (2019).

30. Chang, F. M., Brahma, S., Huang, J. H., Wu, Z. Z. & Lo, K. Y. Strong correlation between optical properties and mechanism in deficiency of normalized self-assembly ZnO nanorods. *Scientific Reports* **9**, 1–9 (2019).

31. Wang, Y. *et al.* Nanocasted Synthesis of Mesoporous $LaCoO_3$ Perovskite with Extremely High Surface Area and Excellent Activity in Methane Combustion. *The Journal of Physical Chemistry C* **112**, 15293–15298 (2008).

32. Zhang, E., Pan, Y., Lu, T., Zhu, Y. & Dai, W. Novel synthesis of S-doped anatase TiO_2 via hydrothermal reaction of Cu–Ti amorphous alloy. *Appl Phys A Mater Sci Process* **126**, (2020).

CHAPTER VII

EXPERIMENTAL SECTION:
MATERIALS, METHODS AND TECHNIQUES

CHAPTER VII

EXPERIMENTAL SECTION: MATERIALS, METHODS AND TECHNIQUES

7.1 CHAPTER II: CeO_2 NANOCRYSTAL SYNTHESIS

7.1.1 Materials

Cerium (III) chloride heptahydrate ($CeCl_3.7H_2O$), Cerium (III) nitrate hexaydrate ($Ce(NO_3)_3.6H_2O$), Cerium (III) acetylacetonate hydrate $Ce(C_5H_7O_2)_3.xH_2O$, Trisodium Citrate dihydrate, sodium hydroxide (NaOH, ≥99%) solid reagents and TMAOH 1M solution were purchased from Sigma-Aldrich (Merck) and used as received. NH_4OH 30%wt. solution was purchased from VWR Chemicals. Milli-Q water was employed for every experiment, prepared by filtering deionised water in a type-1 Milli-Q water purification system.

7.1.2 Methods

7.1.2.1 Synthesis of 2.5 nm CeO_2 NCs

In the typical procedure, 150 mL of 10 mM CeO_2 NCs were obtained by pouring 50 mL of a 30 mM $CeCl_3$ solution onto a crystal beaker containing 50 mL of 66 mM trisodium citrate solution while stirring at room temperature. Afterwards, 50 mL of an 81 mM TMAOH solution are added, and the mixture is left closed and under stirring for at least 8h. After that time, in a three-neck round-bottom flask, the solution is boiled at reflux conditions for 4h.

This protocol was subjected to variations on $CeCl_3$, trisodium citrate and base concentrations, temperature, reaction time and other parameters for the experimental layout developed in this work.

7.1.2.2 Anisotropic CeO_2 nanostructures

Nanosheets

For the synthesis of CeO_2 nanosheets, 50 mL 5 mM of sodium citrate and 1 mM of $Ce(NO_3)_3$ were heated to 100ºC in a three-neck round-bottom flask and kept under reflux conditions for 4h.

Hollow CeO_2 spheres

48mL of a 10 mM sodium citrate solution is heated to 100ºC in a three-neck round-bottom flask. When the temperature reaches 40ºC, 2 mL of $CeCl_3$ 25 mM are injected into the mixture. When it starts boiling, 0.2 mL of TMAOH 1M are injected, and the mixture is left boiling for 3h.

7.2 CHAPTER III: LANTHANIDE-DOPED CeO_2 NANOCRYSTALS

7.2.1 Materials

Cerium (III) chloride heptahydrate ($CeCl_3 \cdot 7H_2O$, 99%), sodium citrate dihydrate ($Na_3C_6H_5O_7 \cdot 2H_2O$, ≥99%), and Tetramethylammonium hydroxide (TMAOH) 1M stock solution, were purchased from Sigma-Aldrich. $Yb(NO_3)_3.6H_2O$ and $Er(NO_3)_3.5H_2O$ were purchased from Alfa Aesar (Fisher Scientific).

All reagents were used as received. Milli-Q water was employed for every experiment, prepared by filtering deionised water in a type-1 Milli-Q water purification system.

7.2.2 Methods

7.2.2.1 Synthesis of Lanthanide-doped CeO_2 NCs

In the standard CeO_2 NCs synthetic procedure, a fraction of precursor solution volume was substituted by a solution of the same concentration of the dopant precursor. The rest of the protocol is carried out under the same conditions.

7.3 CHAPTER IV: MULTIDOMAIN Au/Ag-CeO_2 HYBRID NANOSTRUCTURES

7.3.1 Materials

Gold chloride trihydrate ($HAuCl_4 \cdot 3H_2O$, 99.9%), silver nitrate ($AgNO_3$, 99.9%) sodium citrate dihydrate ($Na_3C_6H_5O_7 \cdot 2H_2O$, ≥99%), cerium (III) chloride heptahydrate ($CeCl_3 \cdot 7H_2O$, 99%), Tetramethylammonium hydroxide (TMAOH) 1M stock solution, sodium hydroxide (NaOH, ≥99%), and 11-Mercaptoundecanoic Acid (MUA, $C_{11}H_{22}O_2S$, 95%) were purchased from Sigma-Aldrich. All reagents were used as received. Milli-Q water was employed for every experiment, prepared by filtering deionised water in a type-1 Milli-Q water purification system.

7.3.2 Methods

7.3.2.1 One-pot synthesis of Au@CeO_2 hybrid nanocrystals

In a typical procedure, 100 mL of a sodium citrate solution (10 mM) are added into a 150 mL three-necked round-bottom flask. The solution's pH is adjusted to pH 9 by the addition of a few drops of NaOH 0.1 M. The mixture is heated to reflux conditions with a heating mantle under magnetic stirring. When boiling starts, 1 mL of $HAuCl_4$ (25 mM) and 1 mL of $CeCl_3$ (25 mM) are sequentially injected. The resulting mixture is kept stirring under reflux for 2h. During the reaction, the colour of the mixture changes from black (right after precursors injection) to red (10 min), and finally purple (2h).For experimental purposes, Ce:Au ratio was varied by adding different volumes of $CeCl_3$ solution (from 0.5 mL to 5 mL), resulting in an increase in the shell thickness.

7.3.2.2 One-pot synthesis of Ag@CeO_2 hybrid nanocrystals

Similarly to the previous method, 100 mL of sodium citrate (10 mM) solution were added into a 150 mL three-necked round-bottom flask. The solution is heated to reflux conditions under magnetic stirring. When boiling starts, 1 mL of $AgNO_3$ (25 mM) and 1 mL of $CeCl_3$ (25 mM) are sequentially injected. The resulting mixture is kept stirring under reflux for 2h. During the reaction, the colour of the mixture changed from turbid white (2 min) to dark brown (10 min) and finally yellow (1h).

7.3.2.3 Size-controlled synthesis of Au NCs

Seeded growth of Au NPs up to 100 nm in diameter is performed following a protocol previously published (reference). Gold seeds (~ 10 nm, ~3.10^{12} NP/ml) were prepared by adding 1 mL $HAuCl_4$ (25 mM) into 150 ml sodium citrate 2.2 mM at 100ºC. Once the synthesis was finished, in the same vessel, the reaction was cooled down until the temperature of the solution reached 85 °C. Then, 1 mL of sodium citrate (60 mM) and 1 mL of a $HAuCl_4$ solution (25 mM) were sequentially injected (time delay ~2 min). After 30 min, the reaction was finished. This process was repeated twice. After that, the sample was diluted by extracting 50 ml of sample and adding 48 ml of MQ water and 2 ml of sodium citrate 60 mM. This solution was then used as seed solution, and the process was repeated again for up to 8 generations of gold particles of progressively larger on sizes. The concentration of each generation of particles is approximately the same as the original seed particles. Detailed synthetic scheme and characterisation of the different generations can be found at Annex D 9.3.1.

7.3.2.4 Size-controlled synthesis of Ag NCs

A 100 mL volume of aqueous sodium citrate solution (5 mM) and tannic acid (0.025 mM) was prepared and heated with a heating mantle in a three-neck round-bottomed for 15 min under vigorous stirring. A condenser was used to prevent the evaporation of the solvent. After boiling commences, 1 mL of $AgNO_3$ (25 mM) is injected into this solution and kept under reflux conditions for 15 mins. Immediately after the synthesis of the Ag seeds and in the same vessel, the seed solution was diluted by extracting 19.5 mL (stored under the name of g_0) and 16.5 mL of Milli-Q-water are added. Afterwards, the reaction is cooled until the temperature reaches 90°C and 500 μL of sodium citrate (25 mM), 1.5 mL of TA (2.5 mM), and 1 mL of $AgNO_3$ are sequentially injected (time delay ~1 min). After 20 min, the dilution process is repeated (marking, this time, the stored particles as g_1) and the rest of the solution is used as seed for another generation: 500 μL of sodium citrate (25 mM), 1.5 mL of TA (2.5 mM), and 1 mL of $AgNO_3$ is injected again. In this way, different generations of Ag NCs of progressively larger sizes were grown in a similar fashion as the Au NCs previously described. Detailed synthetic scheme and characterisation of the different generations can be found at Annex D 9.3.2.

7.3.2.5 Seeded-growth synthesis of Metal@CeO_2 core-shell hybrid NCs

Previously synthesised Au and Ag NCs of different diameters are used without further purification as seeds for the CeO_2 coating. A 50 mL aqueous solution containing sodium citrate (5 mM) and 12.5 mL of the as-synthesized Au/Ag seeds is added to a 100 mL three-necked round-bottom flask and the pH was adjusted with NaOH 0.1 M to pH 9-10. The solution is heated to reflux conditions with a heating mantle and a magnetic bar for vigorous stirring. When the temperature reaches ~70℃, a specific volume of a $CeCl_3$ solution (25 mM) is injected. Upon boiling, the colour of the reaction mixture progressively changes from red to violet as the Au seeds were coated by the CeO_2 shell. After 1h boiling, the heating mantle is switched off, and the reaction mixture is cooled down to room temperature. The resultant Metal@CeO_2 NCs are stabilised by the citrate ions in solution and stored as synthesised.

Metal@CeO_2 of different core sizes are achieved by using metal seeds of different sizes, and different CeO_2 shell thicknesses were prepared similarly by adjusting the ratio between $CeCl_3$ and metal concentration. The influence of temperature was determined by performing the same synthesis at room temperature, 80ºC and 100ºC. No relevant differences were observed for syntheses performed at a concentration of sodium citrate in the range of 2-10 mM. The use of a different base, TMAOH instead of NaOH, did not alter the overall process. Unless otherwise specified, all syntheses were performed open-air.

AuCeO_2 heterodimers and CeO_2 hollow nanocages (sacrificial Ag templating) were synthesised respectively by performing the reaction at 80ºC without any base addition using 20-30 nm Au seeds and 35 nm Ag seeds, respectively.

7.3.2.6 MUA functionalisation of Au NCs

The corresponding mass of MUA for a 1 mM stock solution is weighted and dissolved into a NaOH 15 mM solution. The ratio of MUA molecules to Au surface tested are 1, 100 and 1000 according to a 0.22 nm^2/molecule packing area, which corresponds to the addition of 0.25 mL, 2.5 mL, and 25 mL of MUA stock solution to 12.5 ml of Au NCs. The Au surface per mL was calculated according to the size and concentration of Au NCs ($6.04x10^{10}$ NP/mL, which corresponds to $7.6x10^{14}$

nm^2/mL). Ligand exchange was performed by adding the mentioned amounts of MUA stock solution to the citrate-stabilized Au NCs solution under vigorous stirring. The necessary volume of a sosium citrate 5 mM solution is slowly poured onto the mixture until reaching the final volume of 50 mL. The mixture is left under stirring for 24h, when no further peak evolution was detected by UV-vis spectroscopy.

MUA-functionalized Au NCs were used as a seeds for the growth of a CeO_2 shell without further purification following the standard procedure above described (section 7.3.2.5).

7.3.2.7 AuAuCeO_2 and Ag AuCeO_2 hybrid trimers synthesis by the combination of one-pot and seeded growth approaches.

Previously synthesised 50 nm Au NPs are diluted into a 5 mM sodium citrate solution to a total volume of 50 mL and pH is between 7.5 and 9 using a few drops of NaOH 0.1M. The mixture is heated up under vigorous stirring. Upon boiling, 0.5 mL of $HAuCl_4$ (25 mM) or $AgNO_3$ and 0.5 mL of $CeCl_3$ (25 mM) are injected, and the mixture is left to react for 1h. After that time, the reaction is left to cool down to room temperature and stored as synthesised.

Adjusting the pH of the mixture between 7.5 and 9 alters the kinetics of the process resulting in the production of different morphologies for the hybrids.

7.4 CHAPTER V: CATALYTIC APPLICATIONS OF CeO_2-BASED NANOSTRUCTURES

7.4.1 Materials

The gas bottle containing CO_2/H_2 1:3 molar ratio mixture for heterogeneous catalysis experiments was provided by Carburos Metálicos S.A. 3,3',5,5'-Tetramethylbenzidine (TMB), Dimethyl Sulfoxide DMSO. Trisodium Citrate dihydrate, H_2O_2 30%wt stock solution, Sodium Phosphate Dibasic (Na_2HPO_4), Sodium Phosphate Monobasic (NaH_2PO_4), Bovine Serum Albumin (BSA) were purchased from Sigma-Aldrich. Dulbecco's Modified Eagle Medium (DMEM), Foetal Bovine Serum (FBS), and PrestoBlue Cell Viability Reagent were purchased from Thermo Fisher.

7.4.2 Methods

7.4.2.1 CO_2 reduction

Catalytic activity for the CO_2 hydrogenation to MeOH was evaluated in a stainless-steel-packed cylindrical bed reactor of 8.9 cm in height and a diameter of 5.25 mm. Nanocrystal samples previously synthesised were dried for 48h at 80ºC. A certain mass between 10 and 50 mg of sample was added, and a small amount of glass wool was used at each reactor end to prevent possible leakage of the material. The experience was carried out both at 10 and 15 bar to evaluate pressure as a parameter. The flowrate of a stoichiometric CO_2/H_2 gas mixture was adjusted to 10 mL/min and the temperature was tested in a 180 to 300ºC range.

Samples were collected using SKC FlexFoil PLUS Sample bags, and output stream was analysed on a Shimadzu GC-2010 gas chromatograph (Inlet temperature 260ºC, flow 50 mL/min) with a Flame Ionisation Detector (FID, Temperature 280ºC, flow 35 mL/min) for methanol quantification and an Agilent 7890B GC system chromatograph (120ºC, flow 20 mL/min) coupled to a thermal conductivity detector (TCD, 150ºC and flow 50 mL/min) for CO_2 and CO quantification, using respectively Chromeleon and OpenLab software for data analysis and He as a carrier gas in both cases.

This experiment was carried out as part of a collaboration with *Compostatge de Residus Sòlids Orgànics* research group from the Department of Chemical, Biological and Environmental Engineering of Universitat Autònoma de Barcelona in their laboratory facilities, under the supervision of Dr Ahmad Abo Markeb and Dr Antonio Javier Moral Vico.

7.4.2.2 Enzymatic activity Determination

Specific activity as peroxidase enzyme-mimicking nanocrystals for the colloidal CeO_2-based nanocrystals was evaluated through a colourimetric assay based on the oxidation of a common substrate, TMB, monitored by UV-vis spectroscopy.

Samples of 2 mL of citrate buffer adjusted to pH 3.6 containing 0, 5, 10, 15 or 20 μg of nanocrystals are prepared in disposable plastic cuvettes. To the solution on the cuvette, 10 μL of 10 mg/mL of TMB solution in DMSO (a total of 0.2 mg of the substrate) and 30 μL of H_2O_2 30% stock solution (final concentration of 150 mM) are sequentially injected, and the time evolution of the UV-vis spectrum at room temperature is recorded each 10s during an interval 400 seconds for all samples except $AuCeO_2$, which was recorded every 2.5s for 70 seconds. This process is repeated for each amount of nanocrystal. Absorbance spectra (after subtraction of intrincsic nanocrystal absorbance) were plotted, and reaction-time curves were obtained by plotting ABS at 652 nm against reaction time to determine the reaction rate. The activity was determined using equation 5.10 for each nanocrystal amount, and final Specific activity value is extracted from the slope of the linear regression of the activity vs mass of nanocrystal plot.

The assay was also performed for the highest amount of nanocrystal in the absence of H_2O_2 as a control.

7.4.2.3 In vitro ROS scavenging

HEK-293 (DSMZ) cell line was maintained in a 75 cm^2 tissue culture flask using DMEM with 10% Foetal Bovine Serum (FBS) at 37ºC and humidified 5% CO_2.

Purification and Albuminisation of CeO_2-based NCs

All previously synthesised nanocrystals were purified by centrifugation using an Amicon® Ultra-15 centrifugal filter unit of regenerated cellulose membrane (3 kDa pore size) and redispersed in a 2.2 mM sodium citrate solution to a final concentration of 1.72 mg/mL of CeO_2.

Purified NCs dispersed in 2.2 mM of sodium citrate were conjugated to BSA prior to their addition to a cell culture. A stock solution of 60 mg/mL of BSA in 10 mM Phosphate Buffer (PB) was prepared. Correspondent volumes of NC dispersion and BSA stock solution were mixed so the molar ratio Ce-to-BSA is 1:15 and the final concentration of NCs is 1 mg/mL. The mixture is left stirring for 24h at 4ºC for the protein corona to form and used between the 24-48h time window to prevent denaturalisation. All the procedure was carried out in a laminar flow cabinet, and all solutions were filtered using 0.22 μm sterilised syringe filters to prevent contamination.

Cytotoxicity assessment: PrestoBlue™ assay

Viability of the HEK-293 cells in the different experiments was evaluated through the PrestoBlue™ assay, which consisted first of the exchange of the consumed DMEM by new one and, second, the addition of 10 μL of the PrestoBlue™ reagent to each well and its incubation at 37ºC for at least 30 min. After that time, fluorescence was measured (λ_{ex}=531 nm, λ_{em}=572 nm) on a Varioskan LUX (Thermo Fisher Scientific) plate reader. To act as absorbance blank, the fluorescence of the reagent at working concentration in the absence of cells was also measured. Viability of each sample was calculated as follows:

$$\%\, Viability = \frac{A_{sample} - A_-}{A_+ - A_-} \times 100 \qquad (7.1)$$

Being A_{sample} the measured intensity of the sample, A_- the negative control of cells exposed to DMSO representing 0% viability and A_+ the positive control of unexposed cells representing 100% viability. All measurements were carried out in triplicate.

Cytotoxicity of Albuminized NC samples and H_2O_2

HEK-293 cells were seeded to 10^5 cell/mL in a 96-well plate in DMEM for 24h before exposition to the albuminised particles, which amounted to a final 10% of the total well volume (200 μL), in a final concentration of 100 μg/mL of CeO_2, or the H_2O_2 in increasing concentrations (0.05 mM, 0.2 mM, and 0.5 mM). After 24h of exposition, the PrestoBlue™ assay described above was performed to determine viability. The positive control consisted of not-exposed cells in DMEM, the negative control consisted of cells exposed to 10 μL of DMSO, and an additional control consisting of the exposition to 20 μL of the BSA in PB stock solution was also performed. Each sample assay was performed by triplicate.

In-vitro radical scavenging assessment of CeO_2-based NCs

For this assay, HEK-293 cells were seeded to 10^5 cell/mL in a 96-well plate in DMEM and maintained at 37ºC and humidified 5% CO_2. After 24h, 20 μL of albuminised NCs at different concentrations were added, resulting in final doses of 10, 50 and 100 μg/mL in the corresponding wells. For those wells where particles were not injected, volume differences are compensated by adding 20 μL of DMEM to ensure same conditions for each well. The plate is maintained at 37ºC and humidified 5% CO_2 for 24h, and afterwards, the necessary amount of H_2O_2 stock solution is added to the corresponding wells to achieve final concentrations of 0.05 and 0.2 mM. Again, volume is homogenised by adding the correspondent amount of DMEM in those wells where peroxide was not injected or injected in a lower amount. After 24h, viability is determined through the PrestoBlue™ assay described above.

The experimental design consisted of the exposure to 0.2 mM of H_2O_2 of cells previously exposed to different doses of albuminised CeO_2-based NC samples (0, 10, 50 and 100 μg/mL) and, in order to test the effect of different H_2O_2 concentrations, 0.05 mM of H_2O_2 was also exposed to the maximum dose of each sample of albuminised NCs (100 μg/mL of CeO_2). The following controls were employed: Unexposed cells in DMEM (acting as 100% viability for wells not exposed to NCs), cells exposed to BSA in PB stock solution, cells exposed to 100 μg/mL of each albuminised NC sample (to act as 100% control of cells exposed to both cells and peroxide) and cells exposed to 10 μL of DMSO (representing the 0% viability). Each assay was performed by triplicate on the same plate.

7.5 CHAPTER VI: ELECTRONIC STRUCTURE OF NANOSTRUCTURED CeO_2

7.5.1 Materials

Cerium (III) chloride heptahydrate, cerium(IV) oxide powder, cerium(IV) hydroxide powder, TMAOH solution 25%wt in H_2O, ethanol ACS reagent (absolute alcohol 99.8%) without additive, hydrogen peroxide ACS reagent 30 wt% in H_2O were purchased from Sigma Aldrich.

7.5.2 Methods

7.5.2.1 XPS

X-ray Photoelectron Spectroscopy (XPS) was performed on a SPECS PHOIBOS 150 hemispherical analyser (SPECS GmbH, Berlin, Germany) monochromatic Al K-alpha radiation (1486.74 eV) as excitation source operated at 300 W. Binding energy (BE) values were referred to the C 1 s peak at 285.0 eV. The fitting of the XPS spectra was performed by OriginPro 2016 software after Shirley subtraction of the background.

Sample preparation involved the purification and concentration of the colloidal NCs via centrifugation for the deposition of a few drops of the concentrated disperison onto a 25 mm^2 Silicon wafer, which is left to dry for at least 24h before the measurements.

7.5.2.2 XAS

Synthesis of bulk CeO_2 (CeO_2-TMAOH)

The necessary mass of cerium (III) chloride heptahydrate was dissolved in 100 mL of MQW at room temperature to a final concentration of 10 mM. 1 mL of TMAOH solution 25%wt (2.74 M) is added to this solution and the mixture is left under stirring for 24h. After this time, the solution is centrifugated at 5000 rcf for 10 minutes and resuspended to the same volume in a 10 mM TMAOH solution.

Synthesis of CeO_2 in EtOH

The necessary mass of cerium (III) chloride heptahydrate was dissolved in 100 mL of absolute ethanol at room temperature to a final concentration of 10 mM. The solution was stirred for 30 min and then 1 mL of TMAOH to the 100 mL solution was added 1 mL of TMAOH solution 25%wt (2.74 M) in water. The mixture was left under stirring for 4h and stored as prepared.

High-Energy Resolution Fluorescence-Detected X-ray Absorption Spectroscopy (HERFD-XAS) Measurements

Measurements were performed at beamline ID26 of the European Synchrotron Radiation Facility (ESRF) in Grenoble. Technical aspects of the setup are taken from the work of Cafun et al. (ref. 25 of chapter VI): The incident energy was selected using the (111) reflection from a double Si crystal monochromator. Rejection of higher harmonics was achieved by three Si mirrors working under total reflection. The incident photon flux was monitored by detecting the X-rays scattered from a foil using a photodiode. Five spherically bent (R = 1 m) Ge crystal analysers in (331) reflection were chosen to be suitable for the detection of the $L\alpha_1$ emission line of Ce (4839 eV). The combined energy bandwidth was 0.9 eV. The sample, analyser crystal, and photon detector (avalanche photodiode) were arranged in a vertical Rowland geometry (See figure 6.4 chapter VI). The HERFD-XAS spectra were recorded at scattering angles covering 70 – 110º in the horizontal plane. The measuring conditions were optimised by Dr Vinod Paidi and Prof. Pieter Glatzel, carefully chosen to avoid radiation damage due to the exposure of the CeO_2 NCs to the X-ray.

7.6 CHARACTERISATION TECHNIQUES

UV-vis spectroscopy

UV-vis spectroscopy measures light extinction (comprised of the absorption and scattering contributions to the loss of light) within the visible and near ultraviolet regions of the electromagnetic spectrum of an incident beam passing through the sample. Each of the UV-vis spectra were acquired using an Agilent Cary 60 UV-Vis Spectrophotometer. 1 mL of sample is placed in a quartz cuvette, and a selected range between 180-1100 nm is recorded. Measurements are taken at room temperature.

Dynamic Light Scattering (DLS)

Dynamic Light Scattering uses Brownian motion and the Stokes-Einstein equation to characterise the size distribution profile of colloids and suspensions through fluctuations on the intensity of light scattering. Since the principle to determine particle size is the diffusion coefficient of the particle, it provides information about the particle's hydrodynamic radius, which is, by definition, bigger than the naked, dry particle.

Particle size and concentration determinations by DLS were performed in a Malvern ZetaSizer Ultra instrument at a 532 nm wavelength and fixed backscatter angle of 173º using a plastic cell of 10 mm optical path. The equipment also allows for the determination of surface charge through measurement of the ζ-potential profile.

Transmission Electron Microscopy (TEM)

Particle imaging for size and morphology analysis was performed in a 20 keV STEM (FEI Magellan 400L XHR SEM) in bright field transmission mode for low-magnification characterisation and a FEI Tecnai G2 F20 S-TWIN HR(S)TEM, operating at an acceleration voltage of 200 kV in both High-Resolution TEM, and HAADF-STEM and equipped with a FEI monochromator for high-energy-resolution EELS.

For grid preparation, samples were purified by and resuspended in Milli-Q water. Afterwards, 5 µL were deposited on an ultrathin carbon-coated 200-mesh copper grid from Ted Pella Inc and left to dry 24h before the observation.

Energy Dispersive X-Ray (EDX) Spectroscopy

Spectroscopic technique for the elemental characterisation of a sample under the electron beam of a microscope. It determines the energy of X-Rays emitted by inner electronic shells of the sample's atoms, identifying their species and quantifying their relative abundance. Spectra were recorded at an acceleration voltage of 200 keV in a FEI Tecnai G2 F20 S-TWIN HR(S)TEM during imaging sessions.

Thermogravimetric Analysis (TGA)

Structural water content of samples was determined by thermogravimetric analysis (TG)-differential scanning calorimetry/differential thermal analysis (heat flow DSC/DTA) system NETZSCH-STA 449 F1 Jupiter at the Thermal Analysis Service of ICMAB.

X-Ray Diffraction (XRD)

XRD obtains the diffraction pattern of a crystalline material through the elastic scattering of an incident X-ray beam, which is related to its crystal structure through Bragg's law. X-ray powder diffraction patterns of the NC samples were collected on an X-PERT PRO MPD analytical diffractometer (PANalytical) operating at 45 kV and 40 mA using Cu−Kα radiation (λ = 1.5418 Å).

Sample preparation included the purification and posterior drying of the material suspension. Once dried, the solid is carefully milled and deposited onto a Si holder.

X-Ray Photoelectron Spectroscopy (XPS)

XPS allows the determination of the electronic structure of the surface of the sample through the measurement of the kinetic energy of electrons ejected from it under X-Ray illumination in Ultra-high vacuum conditions. It provides information about chemical composition of the sample and its elemental quantification. Spectra were recorded on a hemispherical Phoibos 150 analyser (SPECS) with mean radius of 150 mm under dual anode X-Ray source (Al−Kα 1486.74 eV and Ag−Lα 2984.3 eV).

Inductively Coupled Plasma - Optical Emission Spectroscopy (ICP-OES)

For atomic characterisation, ICP techniques ionise elements from the sample at high temperatures and OES quantifies them by measuring radiation emission. In this work, the Agilent 5900 ICP-OES equipment from UAB Chemical Analysis Service was employed to calculate reaction yields and doping concentrations.

CHAPTER VIII

GENERAL CONCLUSIONS

CHAPTER VIII

GENERAL CONCLUSIONS

In this work, the synthesis of colloidal CeO_2 NCs has been performed, along with that of CeO_2-based nanomaterials of a higher degree of complexity: Lanthanide-doped CeO_2 NCs and hybrid Metal@CeO_2 NCs. All the synthetic procedures carried out follow the principles of "Green Chemistry", including, among other traits, performing the process in aqueous media, using mild reaction conditions, and avoiding the generation of hazardous waste to ensure the sustainability of the final products. The extensive characterisation performed for each nanomaterial has led to the detailed description of their physicochemical properties, allowing to conclude that all synthetic protocols described have been optimized.

The applicability of the synthesised nanomaterials (CeO_2 NCs, Au NCs, AuCeO_2 NCs and lanthanide-doped CeO_2 NCs) has been assessed by determining their activity for two model reactions in different research fields. In the first place, for the reaction of methanol production from CO_2 and H_2 towards their application in the field of heterogeneous catalysis and, in second place, for the degradation of ROS in the biological context. .It is concluded that potential aplicability of the produced nano.materials has been defined. Finally, the characterization of the electronic structure of the material, carried out through two complementary core-level spectroscopy techniques led to the conclusion that the origin of the catalytic properties shown by the different CeO_2-based materials lies on the chemical bond between Ce and O atoms, that leads to the partial hybridization of atomic orbitals and gives rise to a multiconfigurational ground state of the material's electronic structure.

In detail:

8.1 CHAPTER II – CeO_2 NANOCRYSTAL SYNTHESIS

Highly dispersed and colloidally stable CeO_2 NCs have been successfully synthesized. The obtained 2.5 nm diameter has been found to be the minimal stable size possible, which is undoubtedly the most practical solution for enhancing CeO_2 efficiency for its different applications.

Different synthetic parameters have been evaluated in order to optimise the synthetic protocol: Salt precursor choice, base, pH (and subsequentially, precursor-to-base ratio), Temperature and sodium citrate concentration leading to the final synthetic protocol described. The optimal conditions were found to be a room temperature oxidation and precipitation consequence of the sequential mixing of the three reagents (Salt precursor, sodium citrate and base) in a 1:2.2:2.7 molar ratio.

The posterior ageing process, in which the precipitated crystals reconstruct their crystal structure towards the elimination of surface defects, reaching the most thermodynamically stable state, was found to be spontaneous and slow in standard conditions. However, kinetics of this process could be enhanced either physically (increasing temperature) or chemically (introducing a reactive species such as H_2O_2).

Finally, the extensive physicochemical characterization performed allowed to adequately describe de material's properties and conclude that the produced NCs are indeed composed of Ce and O atoms, hold the expected *fcc* crystalline structure, hold the expected optical properties of the material and have a colloidal and chemical stability high enough to last up to three years without altering its physicochemical state when appropriately stored at RT.

8.2 CHAPTER III – LANTHANIDE DOPED CeO_2 NCS

The incorporation of other lanthanide cations (Yb^{3+}, Er^{3+}) to the synthesised CeO_2 NCs structure was successfully achieved through a simple and effective method, which consisted in partially substituting metal precursor in the reaction media with the dopant precursor in the previously described synthetic protocol.

The developed doping method is concluded to not cause alterations on size, morphology and other colloidal properties of the produced NCs through their physicochemical characterisation. Moreover, it is concluded that this method allows

for the total control of dopant concentration on the crystal structure up to 25%, as the determination of doping concentration on the prepared samples performed by both EDX and ICP-OES evidences. The versatility of the developed methodology may allow for its extension to other species, both rare earths or transition metals.

The evaluation of the emission within the visible range upon illumination of the resultant nanocrystals with a 980 nm *cw* laser of 120 mW led to the conclusion that the doped material does not hold any significant Photon Upconversion properties.

8.3 CHAPTER IV – MULTIDOMAIN Au/Ag-CeO_2 HYBRID NCS

It is concluded that the synthesis of colloidally stable $AuCeO_2$, $AgCeO_2$ and $AuAgCeO_2$ hybrid nanostructures has been successfully performed and optimized, achieving the merging of a CeO_2 domain and a plasmonic metal domain (Au and Ag) into a single hybrid nanomaterial.

Characterization of the produced materials using electron microscopy and spectroscopic techniques led to the conclusion that the exploration and of two different synthetic strategies (the one-pot approach and the seeded-growth approach) and the combination of both has allowed to control size, morphology, and complexity of the produced hybrid nanostructures through different synthetic parameters such as precursors ratio, pH, and temperature. The one-pot approach ensured the simple and quick obtention of the minimal-sized hybrid nanostructure. The seeded-growth approach allowed for total size and morphological control of the final hybrid nanostructure by sequencing the reaction into several steps. The combination of both led to achieving highly complex nanostructure achitectures for both two- and three-domained hybrids.

Lastly, the synergistic properties emerging from coupling the metal and metal oxide domains are evidenced through the enhancement of the efficiency of the LSPR extinction. It is concluded that near-field effect causes this optical enhancement in the resultant hybrid nanostructures, acting as further proof of the epitaxial contact between both crystalline domains and could be an indicator of the enhancement of other properties of each component.

8.4 CHAPTER V – CATALYTIC APPLICATIONS OF CeO_2-BASED NANOSTRUCTURES

Proof of the catalytic properties of CeO_2 beyond oxidation reactions was achieved through the test of the catalytic performance of the different CeO_2-based nanomaterials for the reductive transformation of CO_2 to methanol. The obtained STY and selectivity values at different temperatures evidenced differences in activity between CeO_2 and $AuCeO_2$ NCs, and very poor to no activity for the case of the lanthanide-doped CeO_2 NCs. Since the Au NPs used as control also did not produce any relevant STY value, it is concluded that the increase of catalytic activity in the hybrid structure is related to the synergistic effects arising from the existence of a metal-metal oxide interface, rather than the sum of the individual components' catalytic properties.

In the biomedical field, the radical scavenging properties of CeO_2-based nanomaterials have been satisfactorily proven. From the changes on the extinction profile of the NCs upon exposure to hydrogen peroxide, the molecule chosen as ROS model, it is concluded that the catalytic process takes place generating oxygen vacancy defects on the material's surface that finally reflect on its bandgap. At the same time, the constant generation of bubbles upon exposure to H_2O_2 indicates its oxidation to molecular oxygen. It allows to conclude that nanostructured CeO_2 possesses ROS scavenging properties.

The specific peroxidase-mimetic activity values obtained of each CeO_2-based nanomaterial, determined through an standarised assay, allowed to conclude that pure CeO_2 NCs hold great potential as radical scavengers, as the obtained values are higher than those of other materials reported in the literature as ROS scavengers, and that attaching the Au domain to the CeO_2 confers the nanostructure with much more efficient catalytic properties than the pure CeO_2 NCs (and Au NCs) alone, as the obtained results fall out of the upper linearity range of the performed test. On the other hand, the results for the case of lanthanide-doped CeO_2 NCs are an indication that the doping blocks the mechanism of the catalytic cycle.

The assessment of the cell toxicity of the nanomaterials suggested that none of the materials result toxic for the cell line employed. However, viability values higher than 100% indicate that they do cause alterations to some extent in cell metabolism.

The *in vitro* assessment of the catalytic properties of the materials confirmed the ROS scavenging activity in a biological environment, but since the differences between pure CeO_2 and $AuCeO_2$ NCs were not as stricking as in previous tests, it was concluded that differences on size, morphology and functionalization affect the degree on cell internalization of the NCs and the routes taken for it, which impact the final performance.

Finally, the absence of any satisfactory results in any of the catalytic tests performed on lanthanide-doped CeO_2 NCs and the absence of Photon Upconversion properties lead to the hypothesis that the material may perform well in photocatalytic or photothermal processes, as absorbed IR radiation must be dissipated in some way. However, no test was performed to confirm this hypothesis.

8.5 CHAPTER VI – ELECTRONIC STRUCTURE OF NANOSTRUCTURED CeO_2

This chapter addressed the origin of the catalytic properties of nanostructured CeO_2, which is a matter in discussion within the community. From the multiple peaks appearing in the Ce 3*d* line in XPS for all the samples and controls it is concluded that CeO_2 presents a partially hybridised ground state. This multiconfiguration due to the partial hybridisation is susceptible to changes in surface-to-volume ratio of the material.

Ce^{3+}-associated transitions appeared mainly on nanosized samples of pure CeO_2 and were not present on the doped samples or the bulk references. Furthermore, $AuCeO_2$ hybrid samples, which have previously shown the highest catalytic activity, proved to resemble either nano or bulk spectra according to the size of the CeO_2 shell. All of it allowed to conclude that catalytic performance may not be directly related to a switch on oxidation state of Ce atoms.

The ultra high vacuum conditions, the reducing effect of X-Ray illumination and the higher reactivity of smaller nanocrystals may result in a faster rise of Ce^{3+} transitions in the spectra, which would make them artefactual, but no definitive conclusion could be draw as no time-dependent measurements were taken.

From the analysis of the O 1*s* peak on the same samples, it was concluded that nanosized samples hold a higher portion of surface hydroxyl groups and oxygen vacancies than bulk and bulk-resembling samples.

XANES spectroscopy was succesfully employed to measure the Ce L_3 line on pure CeO_2 NCs and further describe the hybridized ground state of the material and its role during the catalytic activity.

The analysis of the pre-edge region of the spectra, correspondent to the $2p \rightarrow 4f$ transitions which reflect the electronic configuration (and, therefore, oxidation state) of the Ce atoms, concluded that all CeO_2 NC samples are composed of Ce^{4+}, and no Ce^{3+} is present on the crystal structure.

Small differences between bulk and nanosized samples in the signal of the edge peak of the Ce L_3 line ($2p \rightarrow 5d$ transition, which mainly reflects crystal features), in terms of definition of the peak, led to the conclusion that the number of defects is inversely proportional to size and quality of the crystal. At the same time, variations on ageing time in CeO_2 NCs evidenced how ageing is a process affecting crystalline structure rather than oxidation state of the surface Ce atoms.

It was concluded that no formal reduction of Ce^{4+} to Ce^{3+} occurs during the catalytic activity, as no notable alterations on the pre-edge peak were recorded on time-dependent XANES spectra of the CeO_2 NCs *in operando* conditions for the catalytic degradation of H_2O_2.

The temporal loss of crystalline features within the L_3 edge structure upon exposure to H_2O_2, however, indicated sudden changes on density of surface defects. Coupled to the change in color of the samples and the presence of bubbling from O_2 generation, it proved that catalytic activity was taking place. It can be then concluded that Ce^{3+} configurations are not necessarily paired to oxygen vacancies within the crystal structure or take any role in the catalytic cycle.

As a general conclussion, catalytic properties of nanostructured CeO_2 seem to be a consequence of the hybridization between O 2*p* and Ce 4*f* atomic orbitals when the chemical bond is formed, which avoids the generation of unpaired electrons associated with Ce^{3+} species upon oxygen vacancies generation. The terminology

typically found in literature to refer to these properties, variations of "valence switch" or "3+/4+ tautomery", may be consequence of over-simplification and not an alternative explanation for the same phenomenon.

To further deepen into this concept, it could be interesting to analyze changes in the degree of orbital hybridization in the material's electronic structure when introducing variations on the system: size/surface-to-volume ratio, doping or coupling with Au or Ag domains, during the catalytic activity for different processes, etc.

ANNEX

ANNEX

9.1 ANNEX B: CeO_2 NANOCRYSTAL SYNTHESIS

9.1.1 Bibliographical recompilation of synthesis methods for producing CeO_2 nanomaterials

This section contains a recompilation of synthesis methods for producing CeO_2 nanoparticles in aqueous media by the precipitation method reported on the literature, and a summary of the respective synthetic conditions employed. They are classified into different categories.

Contents:

Ceria precursor	Base	pH	T	Time	Size	Ref.
$Ce(NO_3)_3 \cdot 6H_2O$	NH_4OH	9	RT	<1h	3-5 nm	[10]
$Ce(NO_3)_3 \cdot 6H_2O$	NH_4OH	10-12	RT		4-5 nm	[11]
$Ce(NO_3)_3 \cdot 6H_2O$	NH_4OH	10	RT		3-4 nm	[12]
$Ce(NO_3)_3 \cdot 6H_2O$	NaOH	7-10	RT	24h	10-20 nm	[13]
$Ce(NO_3)_3 \cdot 6H_2O$	NH_4OH	9	RT		5-10 nm	[10]
$Ce(NO_3)_3 \cdot 6H_2O$	NH_4OH	10.6	0-90ºC	1-20h	7-25 nm	[14]
$Ce(NO_3)_3 \cdot 6H_2O$	NH_4OH	8.4	30-90ºC		7-19 nm	[15]
$Ce(NO_3)_3 \cdot 6H_2O$	NH_4OH	>10	100ºC	24h	16-17 nm	[16]
$Ce(NO_3)_3 \cdot 6H_2O$	NaOH	7-8	100-180ºC	24h	9-25 nm	[17]
$Ce(NO_3)_3 \cdot 6H_2O$	NH_3		180ºC*	8-24h	15 nm	[18]
$Ce(NO_3)_3 \cdot 6H_2O$	NH_4OH	10	180ºC*	4h	15-20 nm	[12]
$Ce(NO_3)_3 \cdot 6H_2O$	NH_4OH	10	5ºC	<1h	5-8 nm	[12]
$Ce(NO_3)_3 \cdot 6H_2O$	H_2O_2	<10	85ºC	<1h	3-4 nm	[12]

***Table 9.1**: Surfactant-free protocols for the synthesis of quasi-spherical/polyhedral CeO_2 NPs from Ce (III) salt precursors*

Ceria precursor	Base	Surfactant	T	Time	Shape	Ref.
$(NH4)_2Ce(NO_3)_6$	NaOH	Oleic acid	120-160ºC	6-24h	NPs	[19]
$Ce(NO_3)_3.9H_2O$	TMAOH	Azo-dicarbonamide	80ºC	3h	NPs	[20]
$Ce(NO_3)_3$	NaOH	Decanoic acid	400ºC*	10 min	Nanocubes	[21]
$Ce(NO_3)_3$	*Tert*-butylamine	Oleic Acid	180ºC	24h	Nanocubes	[22]
$(NH4)_2Ce(NO_3)_6$ $Ce(NO_3)_3$	NH_3	Sodium Oleate	150-200ºC	1-30h	Nanocubes	[23]
$CeCl_3.7H_2O$	NH_3	CTMABr	80ºC*	4 days	Nanorods	[24]

***Table 9.2**: Surfactant-assisted protocols for the synthesis of CeO_2 NPs*

*Thermal treatment after washing room temperature precipitate

Ceria precursor	Base	pH	T	Time	Shape	Ref.
$Ce(NO_3)_3 \cdot 6H_2O$	NaOH	14	160-180ºC	24h	cubes/100 nm	13
$Ce(NO_3)_3 \cdot 6H_2O$	NaOH	14	140-180ºC	24h	cubes/100 nm	17
$Ce(NO_3)_3 \cdot 6H_2O$	NaOH	14	140ºC	48h	cubes	25
$Ce(NO_3)_3 \cdot 6H_2O$	$NH_3 \cdot H_2O$	-	180ºC*	8-24h	cubes	18
Ce(IV)	Urea	-	120-180ºC	-	Stamps/20 nm	26
$Ce(NO_3)_3 \cdot 6H_2O$	NaOH	14	20-100ºC	24h	Nanowires	13
$Ce(NO_3)_3 \cdot 6H_2O$	NH_4OH	10.6	70-90ºC	<1h	Nanowires	15
$Ce(NO_3)_3 \cdot 6H_2O$	NaOH	14	100ºC	24h	Nanowires	17
$Ce(NO_3)_3 \cdot 6H_2O$	NaOH	-	100ºC	8 min	Nanorods	27
$Ce(NO_3)_3 \cdot 6H_2O$	NaOH	14	110ºC	24h	Nanowires	13
$CeCl_3.7H_2O$	NaOH	14	140ºC	48h	Nanorods	25
$CeCl_3.7H_2O$	NaOH	14	180ºC	24h	Nanowires	28
$CeCl_3.7H_2O$	$NH_3 \cdot H_2O$	-	180ºC*	8-24h	Nanowires	18
$CeCl_3.7H_2O$	NaOH→H_2O_2	11	40ºC	-	Nanorods	29
$Ce(NO_3)_3 \cdot 6H_2O$	$Na_3PO_4 \cdot 6H_2O$	4-7	140-220ºC	144h	Nanorods	30
$Ce(NO_3)_3 \cdot 6H_2O$	$Na_3PO_4 \cdot 6H_2O$	4-7	170ºC	120h	Nanorods	31
$CeCl_3 \cdot 7H_2O$	$Na_3PO_4 \cdot 6H_2O$ $NH_3 \cdot H_2O$	-	180ºC	8-24h	Nanorods	32

***Table 9.3**:Surfactant-free protocols for the synthesis of anisotropic CeO_2 NPs*

Ceria precursor	Base	pH	T	Time	Size	Ref.
$(NH_4)_2Ce(NO_3)_6$	NH_4OH	10	90ºC	1-20h	3-5 nm	14
$Ce(SO_4)_2 \cdot 4H_2O$	Na_4OH	>10	140-200ºC	5-40h	3-8 nm	33
$Ce(NH_4)_4(SO_4)_4 \cdot 2H_2O$	Na_4OH	>10	140-200ºC	5-40h	3-8 nm	33
$Ce(SO_4)_2 \cdot 4H_2O$	Urea	7.8	180ºC	5h	10 nm	33
$Ce(SO_4)_2 \cdot 4H_2O$	Urea	2.7	180ºC	5h	20 nm	33
$Ce(SO_4)_2 \cdot 4H_2O$	NaOH		245ºC*	1-5d		34
$Ce(NH_4)_4(SO_4)_4 \cdot 2H_2O$	NH_4OH		2-6h	300ºC	3-10 nm	35
$Ce(SO_4)_2 \cdot 4H_2O$	Na_4OH	>10	140-200ºC	5-40h	3-8 nm	16
$Ce(NH_4)_4(SO_4)_4 \cdot 2H_2O$	Na_4OH	>10	140-200ºC	5-40h	3-8 nm	16
Ce(IV)	Urea		120-180ºC		10-14 nm	26

***Table 9.4**: Surfactant-free protocols for the synthesis of quasi-spherical/polyhedral CeO_2 NPs from Ce (IV) salt precursors*

*Thermal treatment after washing room temperature precipitate

9.1.2 References

10. Zhou, X. D., Huebner, W. & Anderson, H. U. Processing of nanometer-scale CeO_2 particles. *Chemistry of Materials* **15**, 378–382 (2003).

11. Zhou, X. D., Huebner, W. & Anderson, H. U. Room-temperature homogeneous nucleation synthesis and thermal stability of nanometer single crystal CeO_2. *Appl Phys Lett* **80**, 3814 (2002).

12. Djuričić, B. & Pickering, S. Nanostructured cerium oxide: preparation and properties of weakly-agglomerated powders. *J Eur Ceram Soc* **19**, 1925–1934 (1999).

13. Pan, C., Zhang, D., Shi, L. & Fang, J. Template-Free Synthesis, Controlled Conversion, and CO Oxidation Properties of CeO_2 Nanorods, Nanotubes, Nanowires, and Nanocubes. *Eur J Inorg Chem* 2008, 2429–2436 (2008).

14. Chang, H. Y. & Chen, H. I. Morphological evolution for CeO_2 nanoparticles synthesized by precipitation technique. *J Cryst Growth* **283**, 457–468 (2005).

15. Chen, H. I. & Chang, H. Y. Synthesis of nanocrystalline cerium oxide particles by the precipitation method. *Ceram Int* **31**, 795–802 (2005).

16. Hirano, M. & Kato, E. Hydrothermal Synthesis of Cerium(IV) Oxide. *Journal of the American Ceramic Society* **79**, 777–780 (1996).

17. Mai, H. X. *et al.* Shape-selective synthesis and oxygen storage behavior of ceria nanopolyhedra, nanorods, and nanocubes. *Journal of Physical Chemistry B* **109**, 24380–24385 (2005).

18. Wang, W. *et al.* A surfactant and template-free route for synthesizing ceria nanocrystals with tunable morphologies. *J Mater Chem* **20**, 7776–7781 (2010).

19. Huo, Z. *et al.* One-pot synthesis of monodisperse CeO_2 nanocrystals and superlattices. *Chemical Communications* 3741–3743 (2008) doi:10.1039/B803215G.

20. Yin, L., Wang, Y., Pang, G., Koltypin, Y. & Gedanken, A. Sonochemical Synthesis of Cerium Oxide Nanoparticles—Effect of Additives and Quantum Size Effect. *J Colloid Interface Sci* **246**, 78–84 (2002).

21. Kaneko, K. *et al.* Structural and morphological characterization of cerium oxide nanocrystals prepared by hydrothermal synthesis. *Nano Lett* **7**, 421–425 (2007).

22. Yang, S. & Gao, L. Controlled synthesis and self-assembly of CeO_2 nanocubes. *J Am Chem Soc* **128**, 9330–9331 (2006).

23. Taniguchi, T., Katsumata, K. I., Omata, S., Okada, K. & Matsushita, N. Tuning growth modes of ceria-based nanocubes by a hydrothermal method. *Cryst Growth Des* **11**, 3754–3760 (2011).

24. Vantomme, A., Yuan, Z. Y., Du, G. & Su, B. L. Surfactant-assisted large-scale preparation of crystalline CeO2 nanorods. *Langmuir* **21**, 1132–1135 (2005).

25. Wu, Q. *et al.* Great influence of anions for controllable synthesis of CeO_2 nanostruetures: From nanorods to nanocubes. *Journal of Physical Chemistry C* **112**, 17076–17080 (2008).

26. Zhou, Y., Phillips, R. J. & Switzer, J. A. Electrochemical Synthesis and Sintering of Nanocrystalline Cerium(IV) Oxide Powders. *Journal of the American Ceramic Society* **78**, 981–985 (1995).

27. Du, N., Zhang, H., Chen, B., Ma, X. & Yang, D. Ligand-free self-assembly of ceria nanocrystals into nanorods by oriented attachment at low temperature. *Journal of Physical Chemistry C* **111**, 12677–12680 (2007).

28. Fu, X. Q., Wang, C., Yu, H. C., Wang, Y. G. & Wang, T. H. Fast humidity sensors based on CeO_2 nanowires. *Nanotechnology* **18**, 145503 (2007).

29. Yamashita, M. *et al.* Synthesis and microstructure of calcia doped ceria as UV filters. *Journal of Materials Science 2002* **37**, 683–687 (2002).

30. Yu, R., Yan, L., Zheng, P., Chen, J. & Xing, X. Controlled synthesis of CeO_2 flower-like and well-aligned nanorod hierarchical architectures by a phosphate-assisted hydrothermal Route. *Journal of Physical Chemistry C* **112**, 19896–19900 (2008).

31. Yan, L., Yu, R., Chen, J. & Xing, X. Template-free hydrothermal synthesis of CeO_2 nano-octahedrons and nanorods: Investigation of the morphology evolution. *Cryst Growth Des* **8**, 1474–1477 (2008).

32. Wang, W. *et al.* A surfactant and template-free route for synthesizing ceria nanocrystals with tunable morphologies. *J Mater Chem* **20**, 7776–7781 (2010).

33. Hirano, M. & Kato, E. Hydrothermal Synthesis of Nanocrystalline Cerium(IV) Oxide Powders. *Journal of the American Ceramic Society* **82**, 786–788 (1999).

34. Wu, N. C., Shi, E. W., Zheng, Y. Q. & Li, W. J. Effect of pH of Medium on Hydrothermal Synthesis of Nanocrystalline Cerium(IV) Oxide Powders. *Journal of the American Ceramic Society* **85**, 2462–2468 (2002).

35. Wang, Z. L. & Feng, X. Polyhedral Shapes of CeO_2 Nanoparticles. *Journal of Physical Chemistry B* **107**, 13563–13566 (2003).

9.2 ANNEX C: LANTHANIDE DOPED CeO_2 NCS:

Contents:

9.2.1 Characterization of lanthanide dopant salt precursors

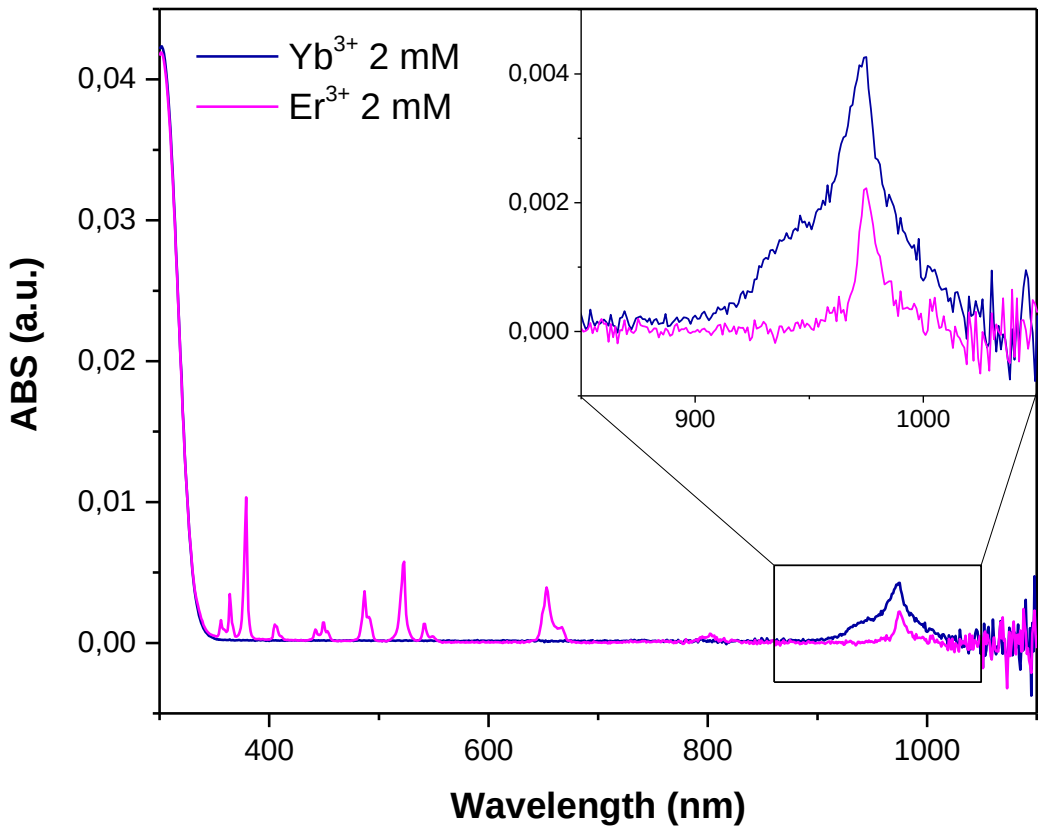

Figure 9.1: UV-vis absorbance spectra of lanthanide dopants precursors.

9.2.2 Characterization of lanthanide-doped CeO_2 NCs

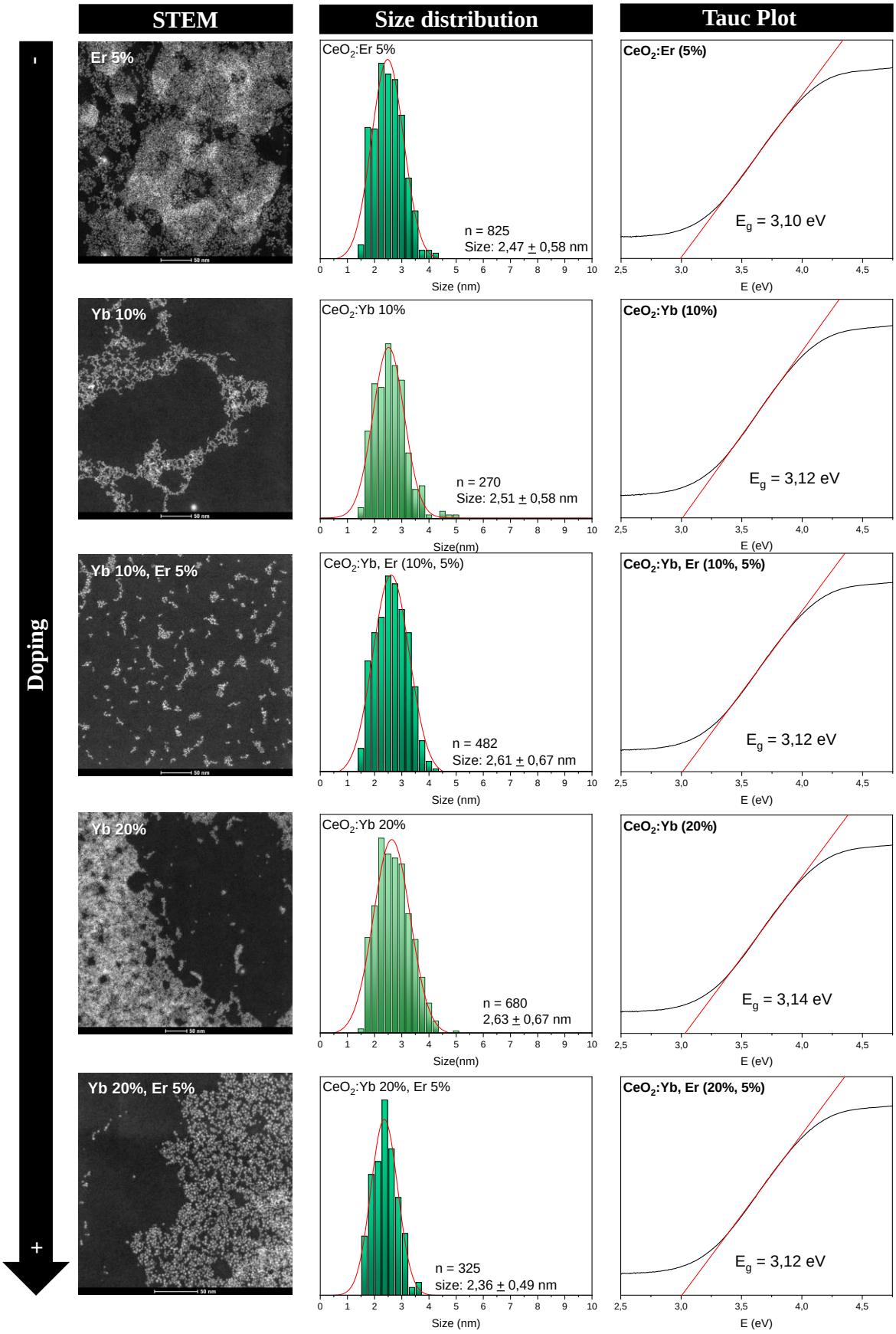

***Figure 9.2**: HRSTEM imaging (left), size distribution (center) and Tauc's plot (right) for each of the CeO_2:Yb,Er samples*

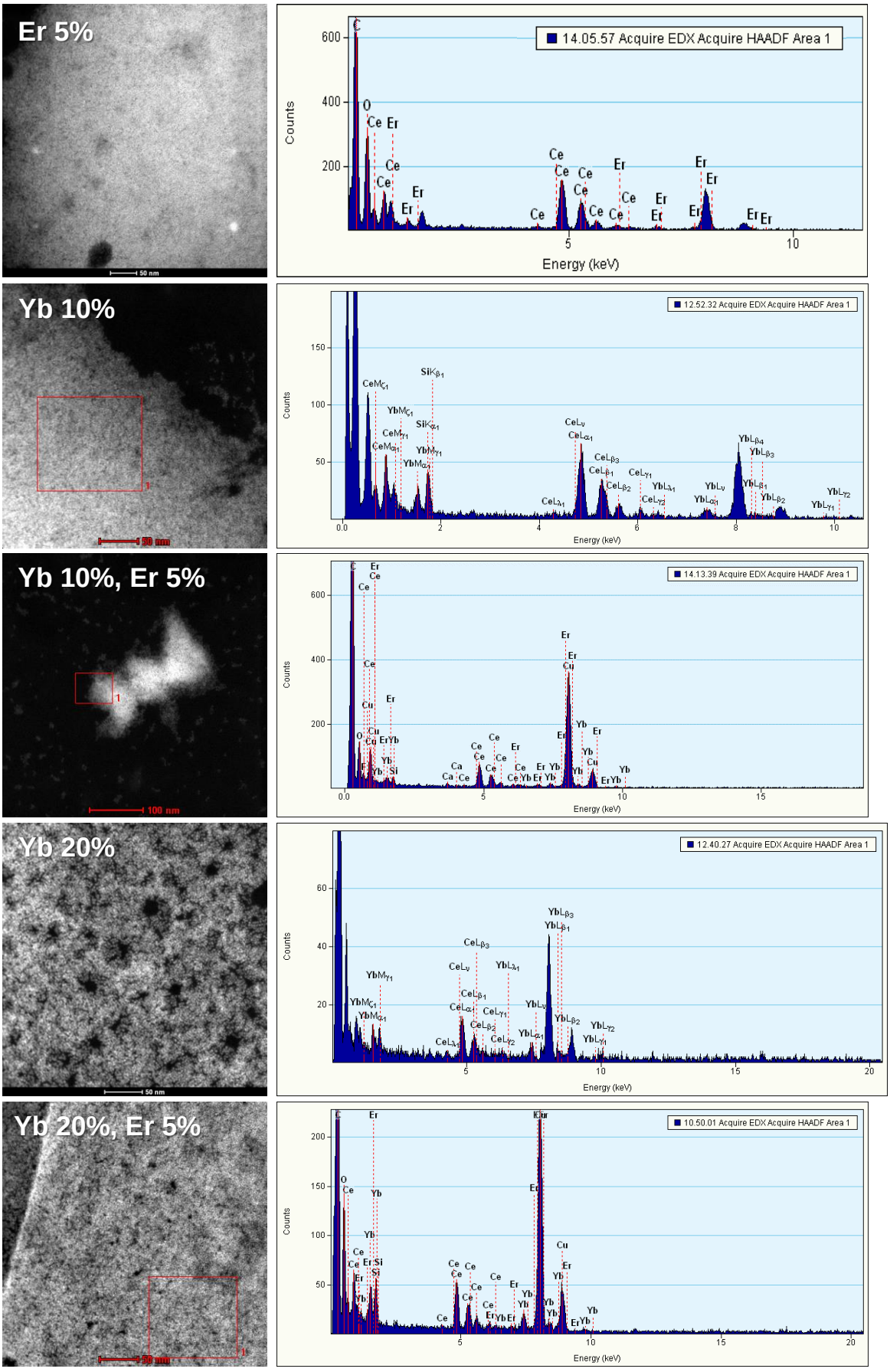

***Figure 9.3**: Recorded EDX spectra for each of the CeO_2:Yb, Er samples*

9.3 ANNEX D: MULTIDOMAIN Au/Ag-CeO_2 HYBRID NANOCSTRUCTURES

Contents:

9.3.1 Characterization of size-controlled synthesis of Au NCs

For the synthesis of size-controlled Au NCs a variation of the seeded-growth method previously developed and published by the group is employed. Experimental aspects are detailed in 7.3.2.3. **Figure 9.4** shows the schematic summary of the procedure. After the synthesis, 2 mL of each generation stored are employed for the total characterization by UV-vis spectroscopy and STEM (**Figure 9.5**). **Table 9.5** summarizes mean size, concentration and LSPR peak position of each generation.

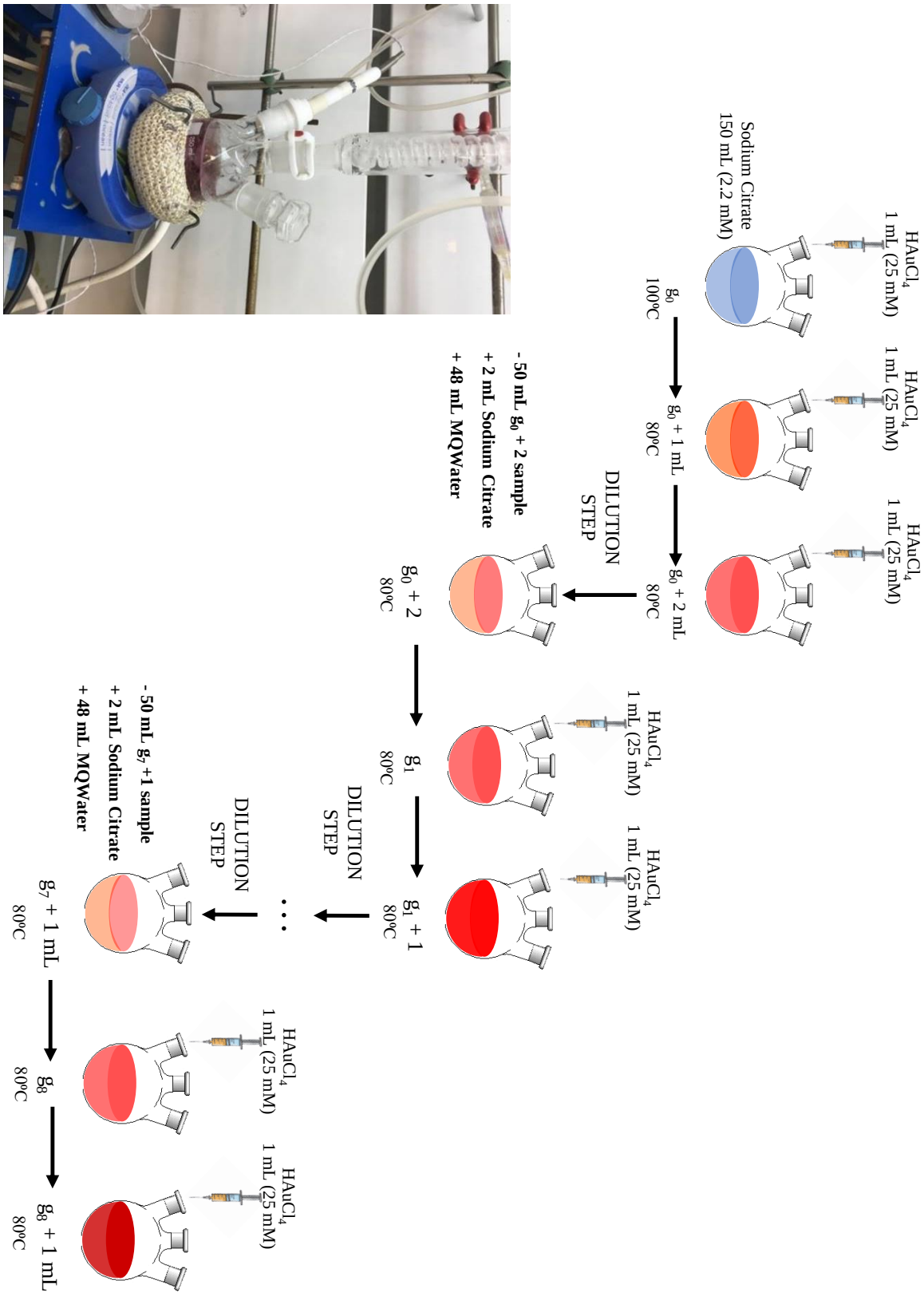

***Figure 9.4**: Scheme of the synthetic procedure for Au NCs*

Name	Concentration	TEM Size	LSPR peak
G_0	0.033 mg/mL	10.8 nm	519 nm
$G_0 + 2$	0.099 mg/mL	14.9 nm	521 nm
$G_1 + 1$	0.131 mg/mL	18.5 nm	522 nm
$G_2 + 1$	0.159 mg/mL	23.9 nm	524 nm
$G_3 + 1$	0.165 mg/mL	29.7 nm	526 nm
$G_4 + 1$	0.173 mg/mL	34.2 nm	528 nm
$G_5 + 1$	0.180 mg/mL	40.6 nm	530 nm
$G_6 + 1$	0.183 mg/mL	47.3 nm	533 nm
$G_7 + 1$	0.186 mg/mL	53.2 nm	537 nm

***Table 9.5**: Total concentration, particle size and LSPR peak position of each generation of Au NCs.*

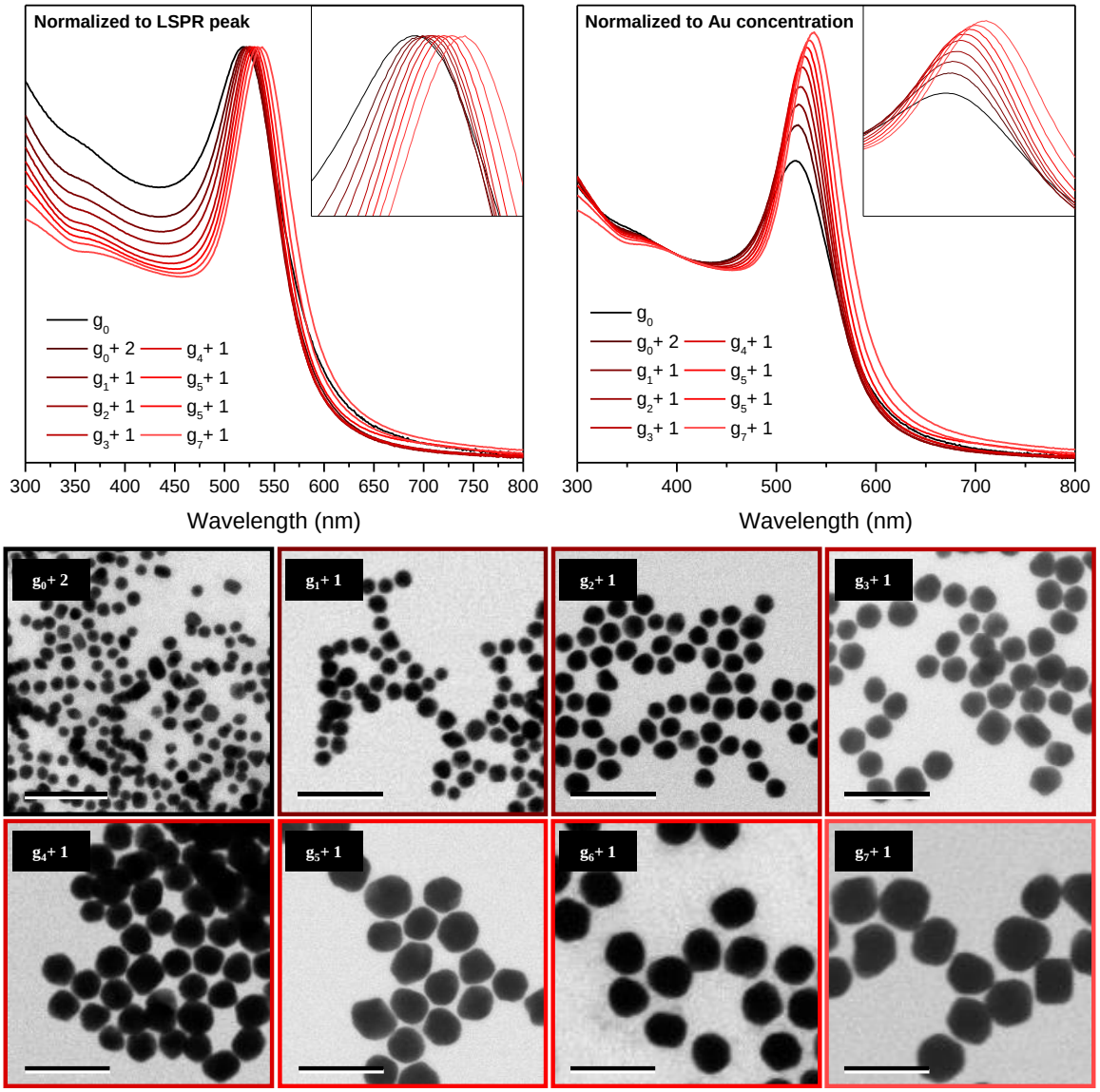

***Figure 9.5**: UV-vis spectroscopy and STEM characterization of each generation of Au NCs produced. Scale bars: 100 nm*

9.3.2 Characterization of Size-controlled synthesis of Ag NCs

For the synthesis of size-controlled Ag NCs a seeded-growth method previously developed and published by the group is employed. Experimental aspects are detailed in 7.3.2.4. **Figure 9.6** shows the schematic summary of the procedure and **Figure 9.7** the total characterization by UV-vis spectroscopy and STEM. **Table 9.6**: Total concentration, particle size and LSPR peak position of each generation of Ag NCs. summarizes mean size, concentration and LSPR peak position of each generation.

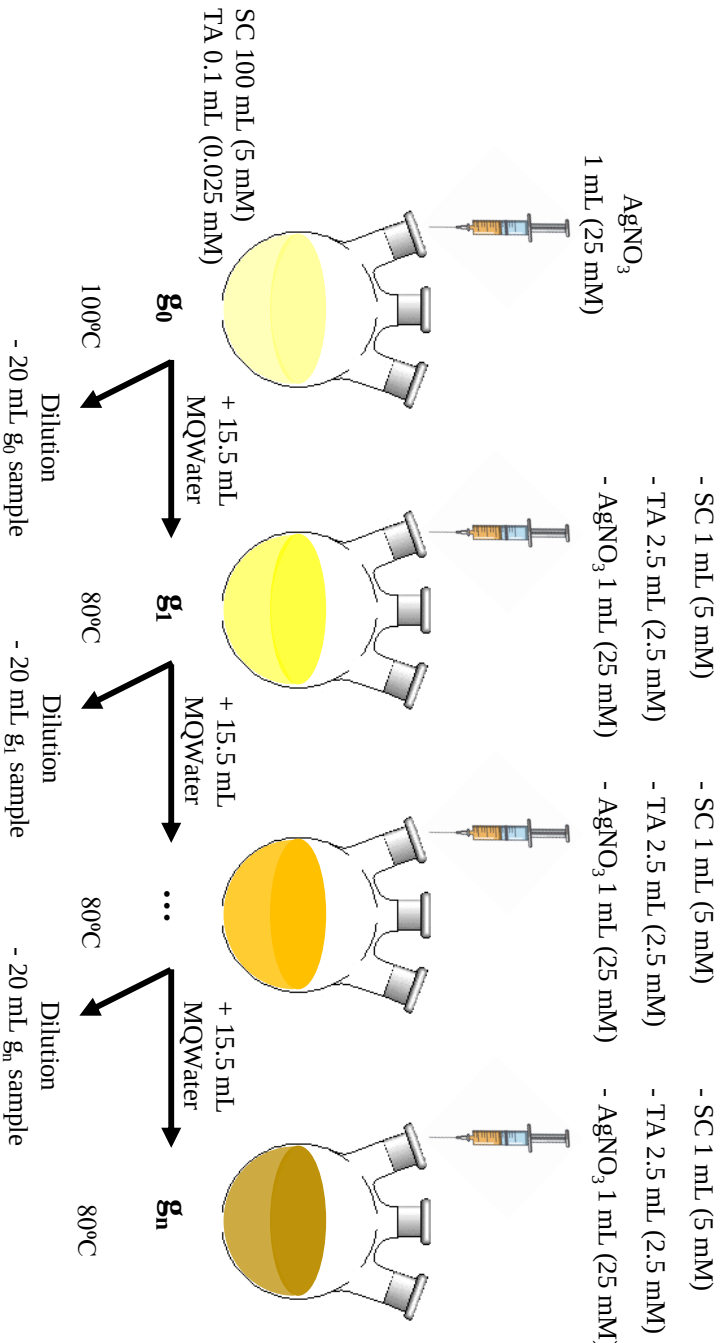

***Figure 9.6**:Scheme of the synthetic procedure for Ag NCs*

Name	Concentration	TEM Size	LSPR peak
G_0	0.25 mM	14.8 nm	401 nm
G_1	0.45 mM	19.7 nm	404 nm
G_2	0.61 mM	24.0 nm	408 nm
G_3	0.74 mM	28.0 nm	411.5 nm
G_4	0.84 mM	29.8 nm	416 nm
G_5	0.92 mM	31.6 nm	418.5 nm
G_6	0.99 mM	37.0 nm	421 nm
G_7	1.04 mM	41.2 nm	425 nm
G_8	1.08 mM	44.0 nm	427.5 nm
G_9	1.12 mM	47.9 nm	430 nm
G_{10}	1.14 mM	53.2 nm	432 nm
G_{11}	1.16 mM	55.8 nm	438 nm
G_{12}	1.18 mM	60.8 nm	442 nm
G_{13}	1.20 mM	66.6 nm	446 nm
G_{14}	1.21 mM	71.4 nm	452 nm

***Table 9.6**: Total concentration, particle size and LSPR peak position of each generation of Ag NCs.*

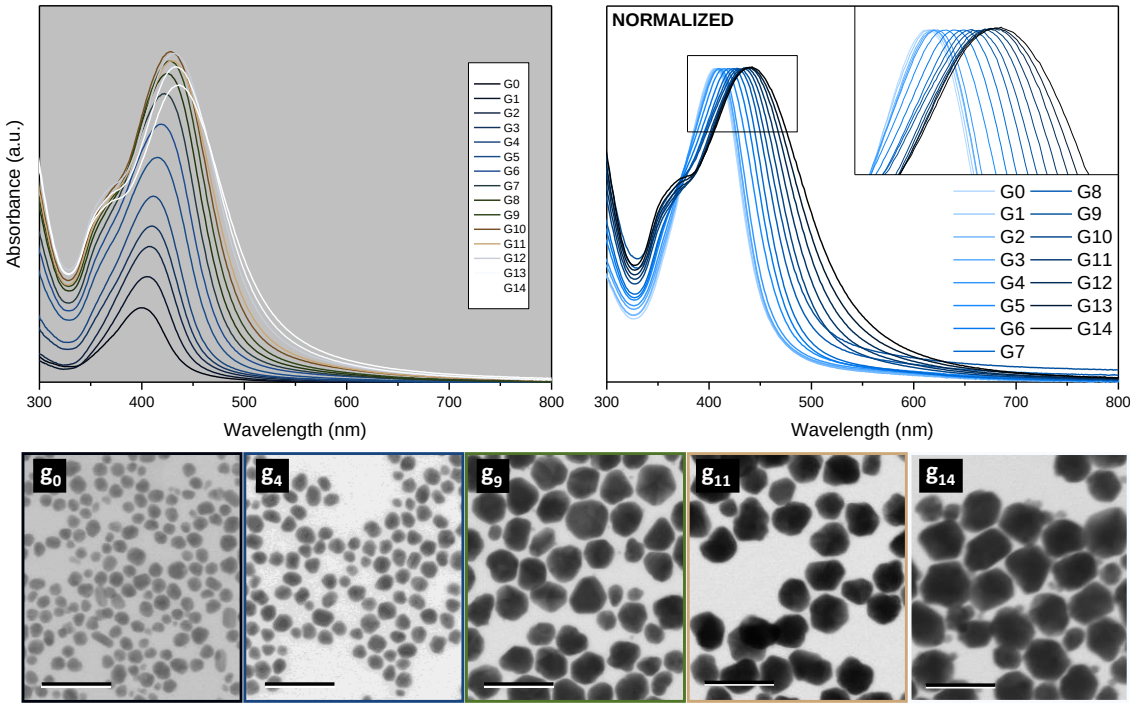

***Figure 9.7**: UV-vis spectroscopy and STEM characterization of different generations of the Ag NCs produced. Scale bars: 100 nm*

9.4 ANNEX E: CATALYTIC APPLICATIONS OF CeO_2-BASED NANOSTRUCTURES

Contents:

9.4.1 Radical Scavenging: Effect of catalytic activity on CeO_2

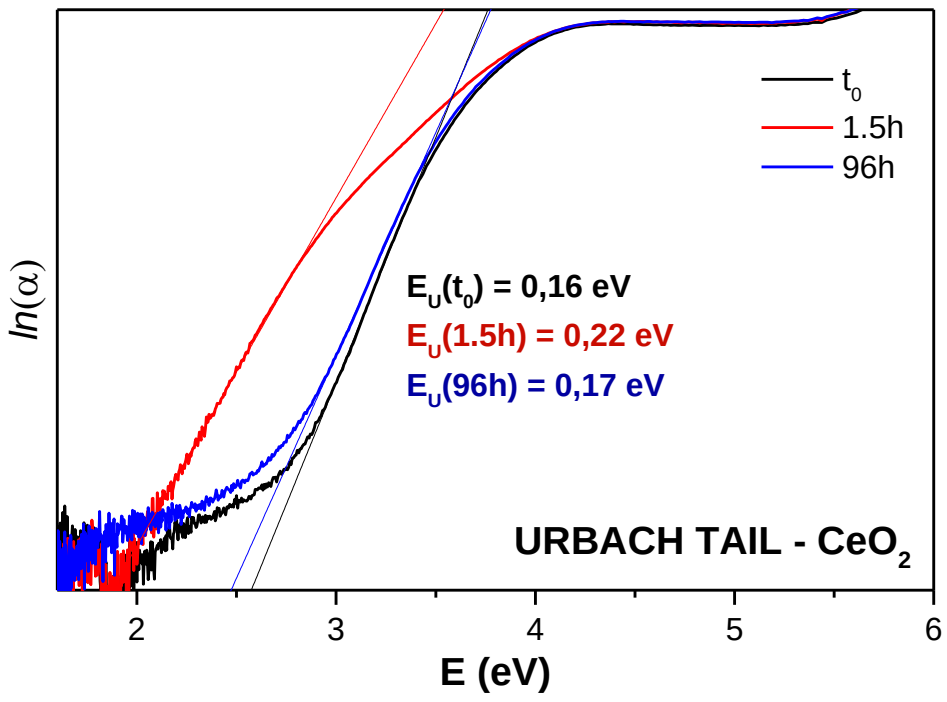

Figure 9.8: *Time evolution of Urbach plot of CeO_2 NCs after H_2O_2 exposition*
Complementary to ***Figure 5.4***

9.4.2 Enzymatic activity

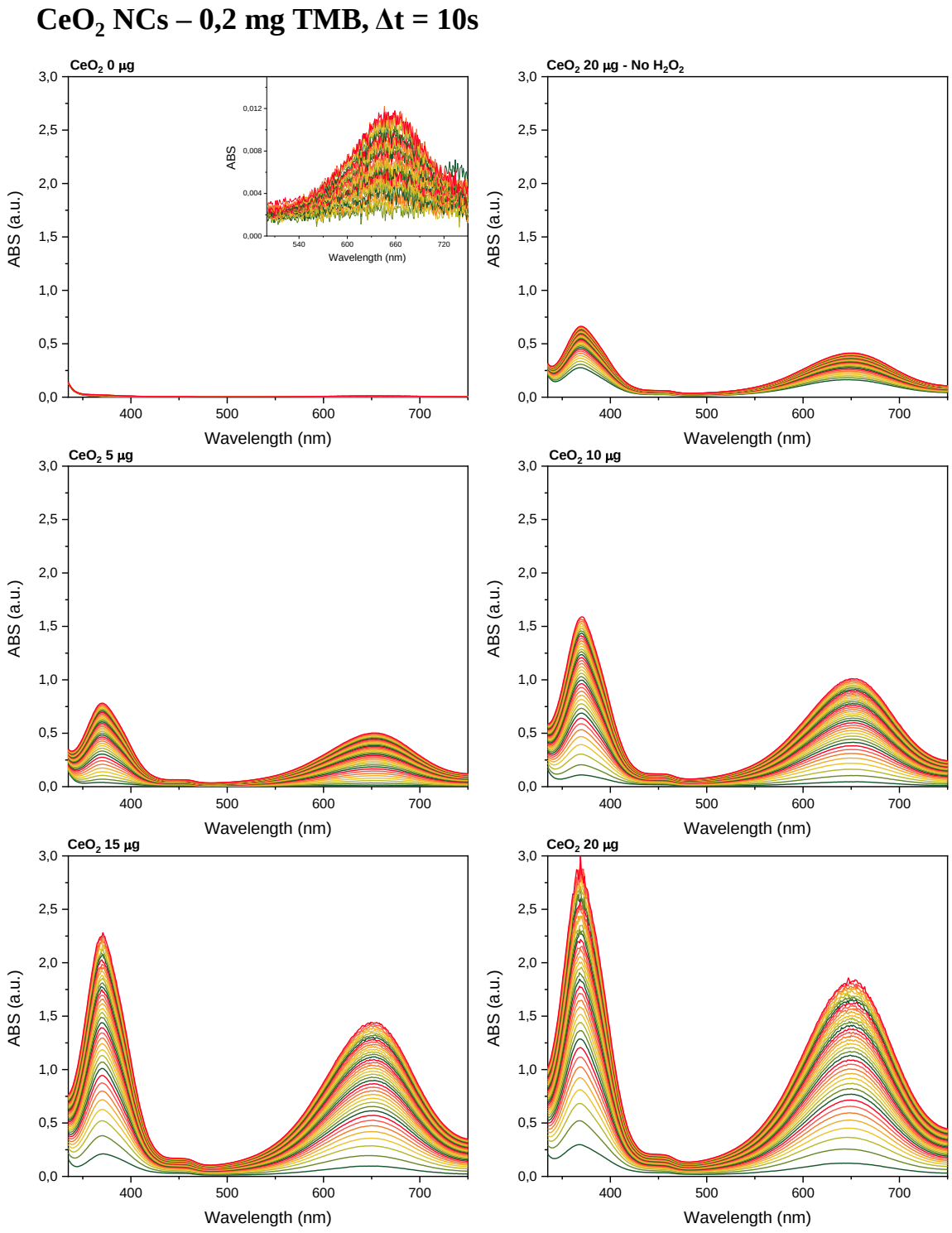

Figure 9.9: *Time evolution of the UVvis spectra for the catalytic degradation of 0.2 mg of TMB in 150 mM of H_2O_2 using increasing amounts of catalyst (CeO_2 NCs).*

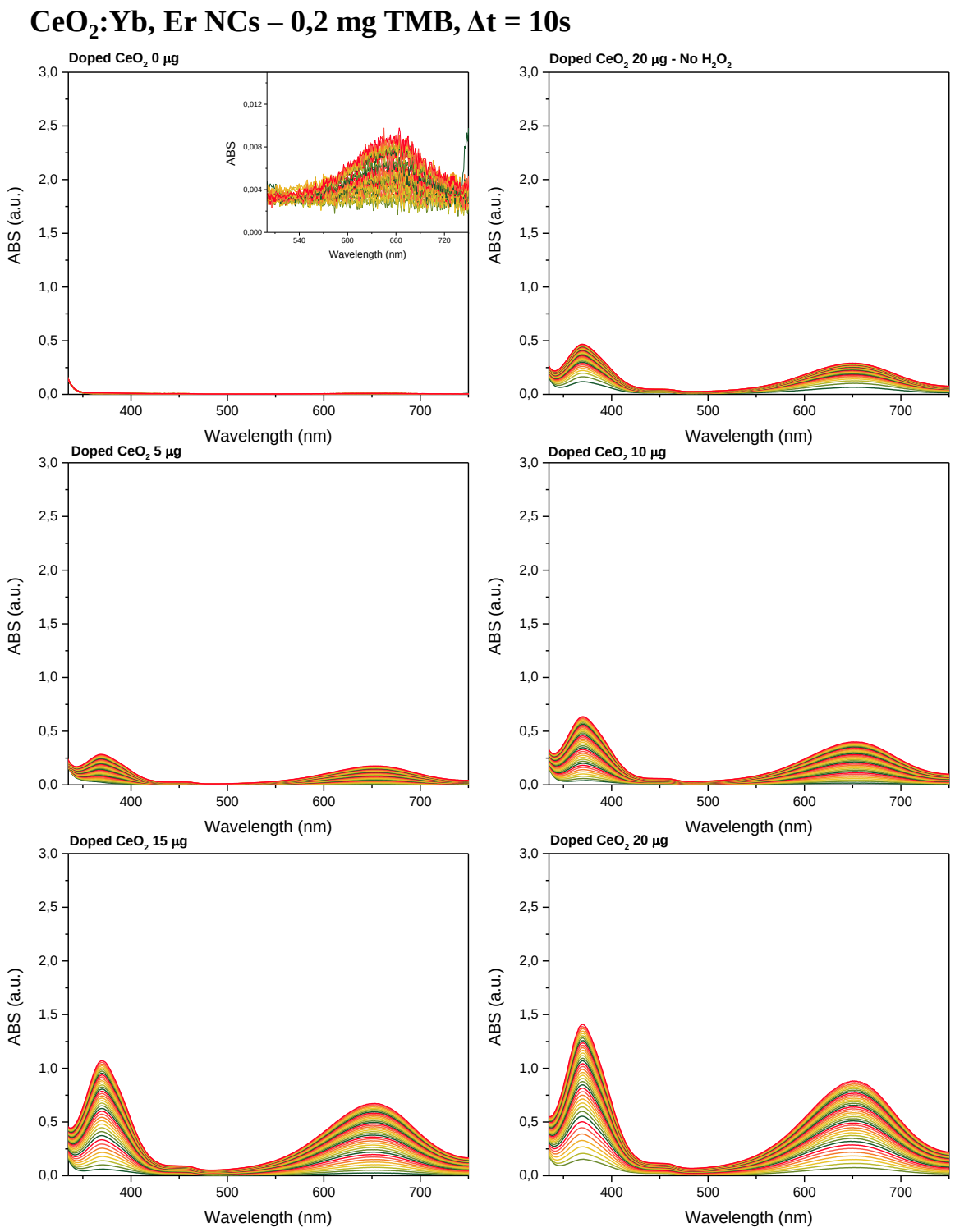

***Figure 9.10**: Time evolution of the UVvis spectra for the catalytic degradation of 0.2 mg of TMB in 150 mM of H_2O_2 using increasing amounts of catalyst (CeO_2:Yb, Er NCs).*

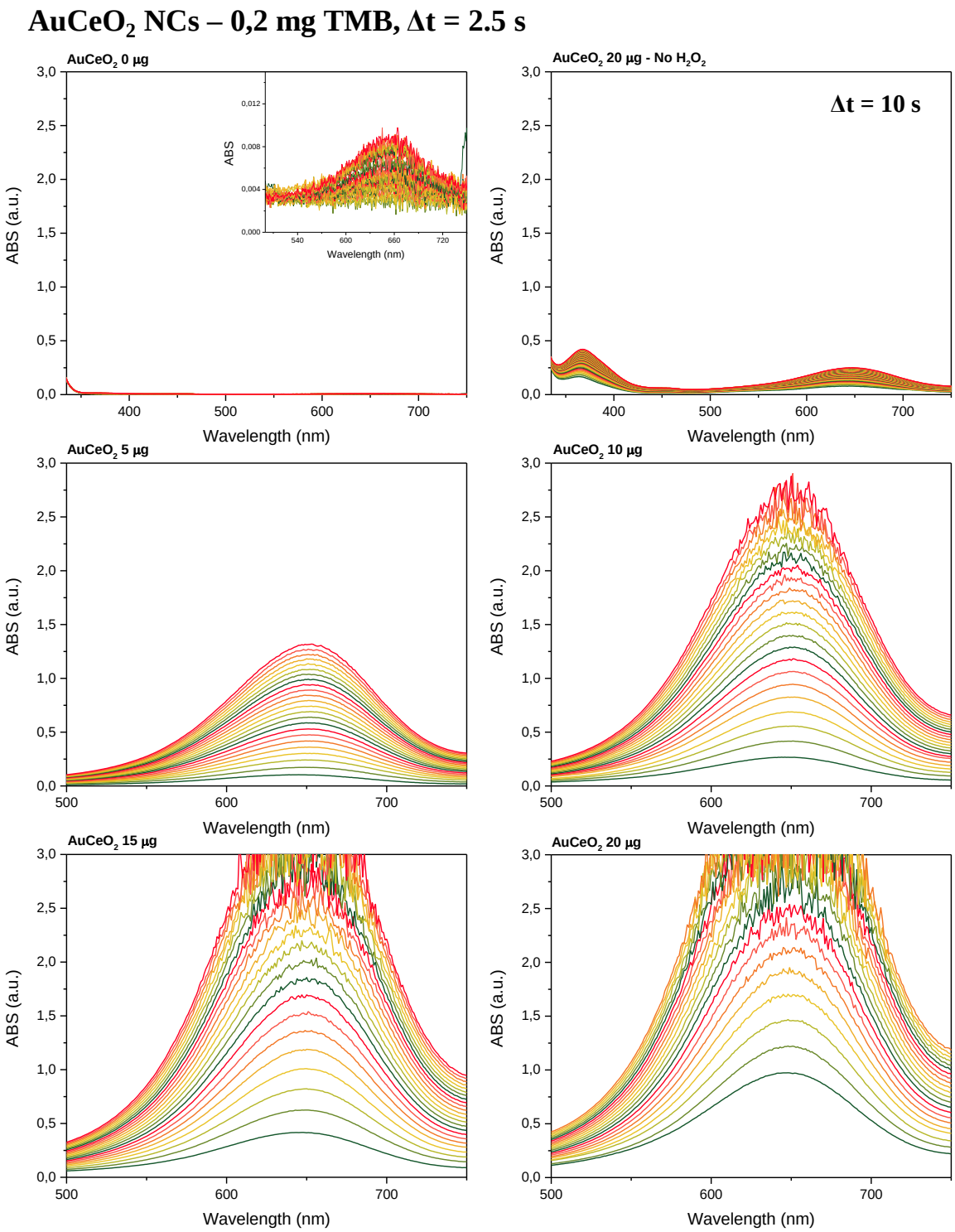

***Figure 9.11**: Time evolution of the UVvis spectra for the catalytic degradation of 0.2 mg of TMB in 150 mM of H_2O_2 using increasing amounts of catalyst ($AuCeO_2$ NCs). Time interval between spectra is 2.5 for each experience except for the one in absence of H_2O_2, in which the time interval is 10s between each spectrum recorded.*

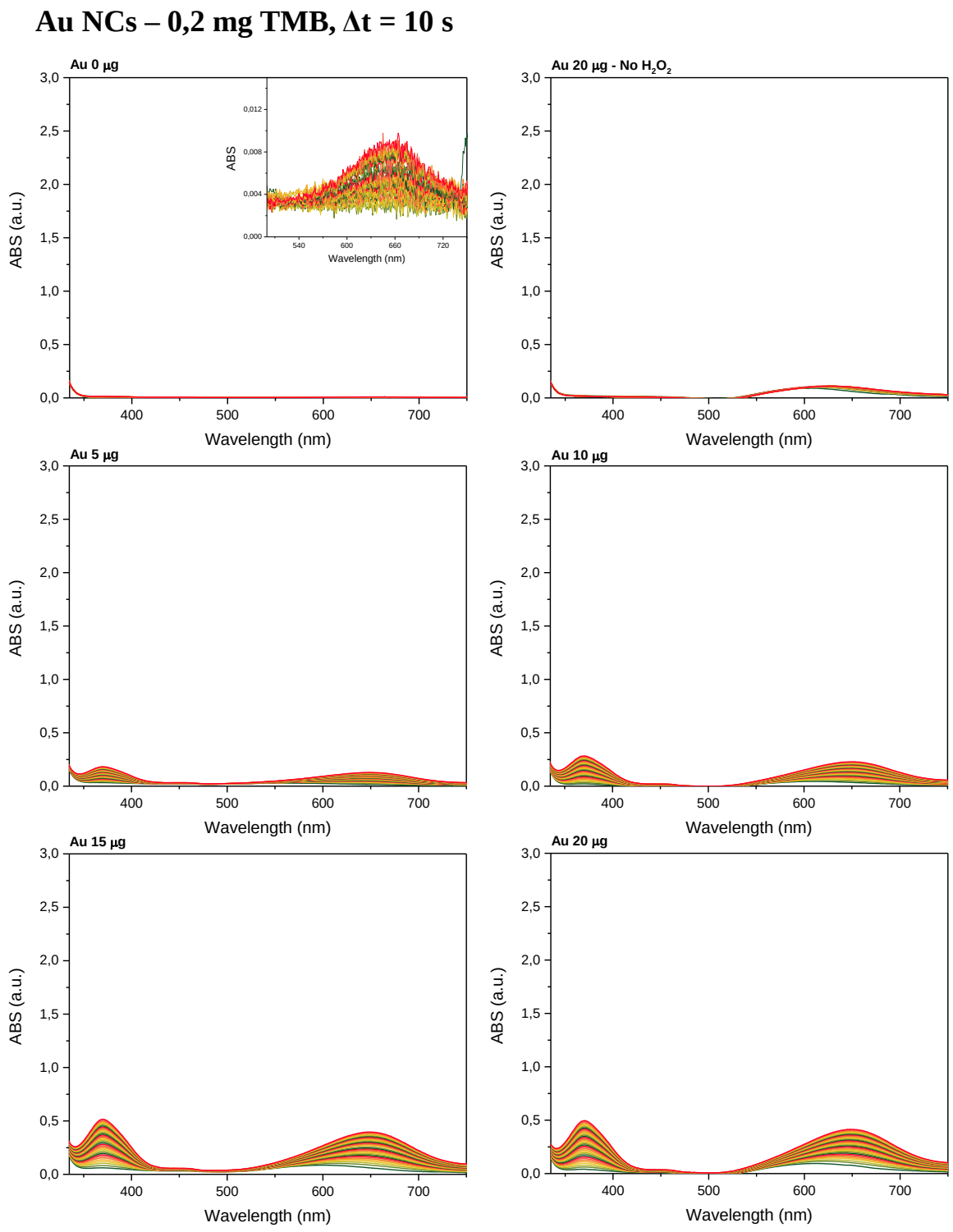

***Figure 9.12**: Time evolution of the UVvis spectra for the catalytic degradation of 0.2 mg of TMB in 150 mM of H_2O_2 using increasing amounts of catalyst (Au NCs).*

9.5 ANNEX F: ELECTRONIC STRUCTURE OF NANOSTRUCTURED CeO_2

Contents:

9.5.1 XPS Characterization

Ce 3d deconvolution

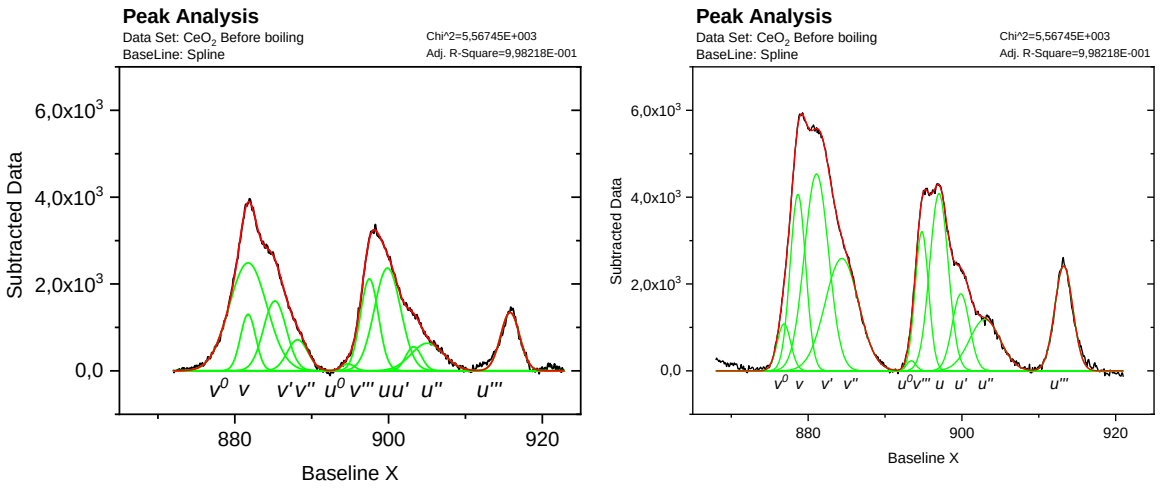

Figure 9.13: *Ce 3d peak deconvolution of CeO_2 NCs (left) after ageing and (right) before ageing.*

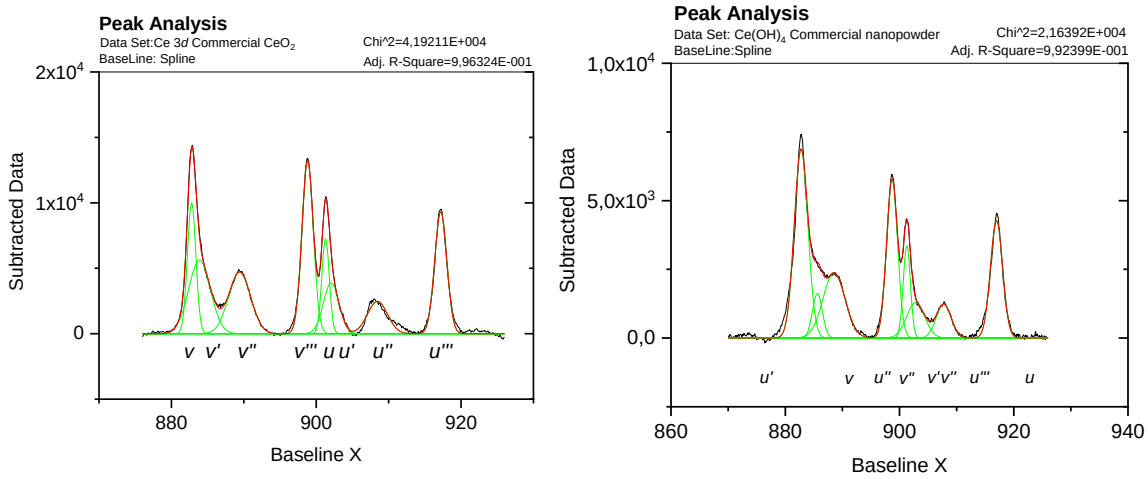

***Figure 9.14**: Ce 3d peak deconvolution of commercial (left) CeO_2 and (right) $Ce(OH)_4$ powders.*

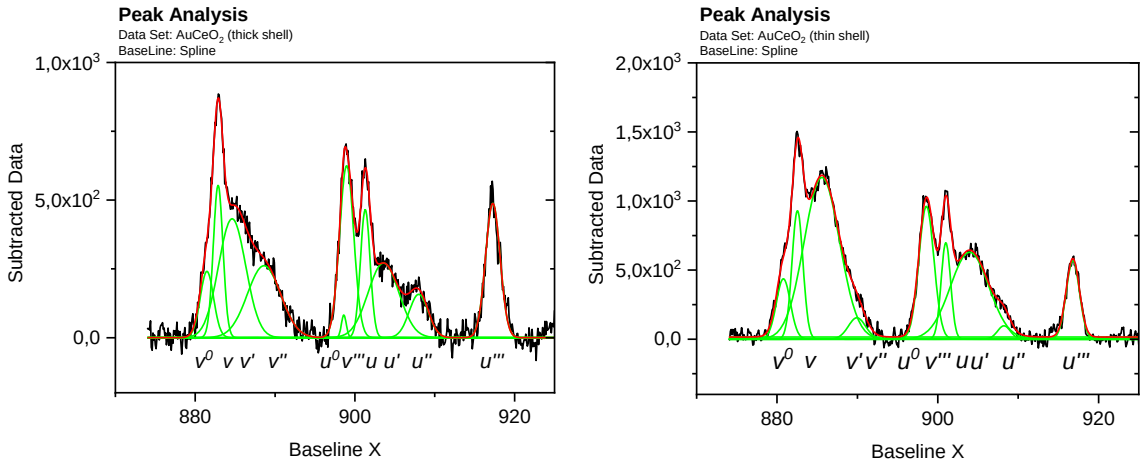

***Figure 9.15**: Ce 3d peak deconvolution of $AuCeO_2$ NCs of (left) thick and (right) thin shell.*

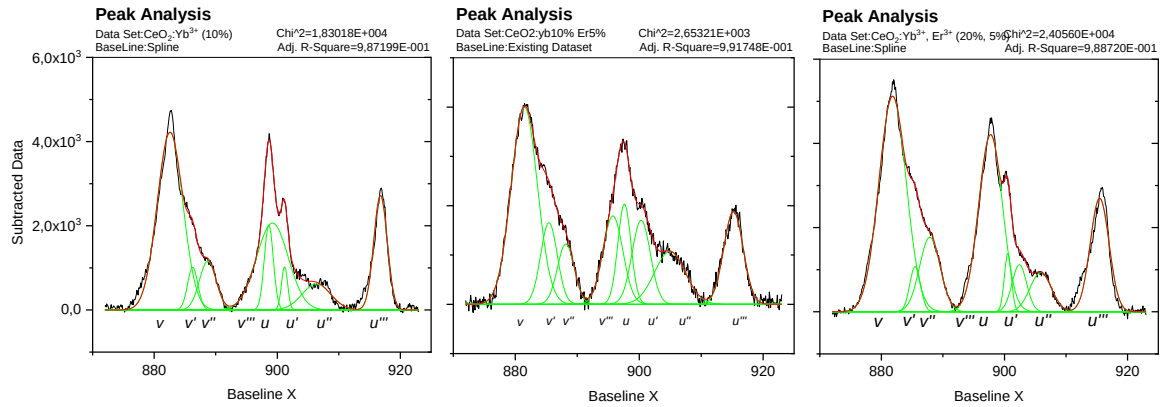

***Figure 9.16**: Ce 3d peak deconvolution of CeO_2 doped NCs: (left) 10% Yb^{3+}, (middle) 10% Yb^{3+} 5% Er^{3+}, (right) 20% Yb^{3+} 5% Er^{3+}.*

O 1s deconvolution

Sample	Peak	FWHM	Intensity	Position (eV)	Area %
Commercial	O_{lat}	1,11	95,53	529,80	73,44
	O_{OH}	2,39	13,97	532,50	23,19
	O_{H2O} (ads)	0,85	5,73	530,84	3,37
$Ce(OH)_4$	O^{2-} ?	3,64	13,84	526,80	13,76
	O_{lat}	1,84	85,51	529,81	42,97
	O_{OH}	1,44	35,47	531,86	13,96
	O_{H2O} (ads)	1,68	63,94	533,05	29,31
CeO_2 NCs	O^{2-} ?	4,02	10,13	527,28	8,76
	O_{lat}	3,03	70,43	530,33	45,90
	O_{OH}	1,94	79,00	532,50	32,96
	O_{H2O} (ads)	2,11	27,31	534,05	12,38
CeO_2 NCs (before ageing)	O^{2-} ?	2,28	70,59	527,52	34,23
	O_{lat}	2,44	76,03	529,55	39,41
	O_{OH}	1,91	27,14	534,22	11,02
	O_{H2O} (ads)	3,04	23,73	531,57	15,33
CeO_2:Yb (10%)	O^{2-} ?	3,47	41,58	526,85	26,40
	O_{lat}	3,30	78,86	529,93	47,59
	O_{OH}	1,84	77,15	532,71	26,01
CeO_2:Yb, Er (10%, 5%)	O^{2-} ?	3,22	16,01	527,44	12,81
	O_{lat}	2,42	81,64	529,92	49,19
	O_{OH}	2,25	67,92	532,12	38,00
CeO_2:Yb, Er (20%, 5%)	O^{2-} ?	3,16	13,00	526,59	10,62
	O_{lat}	2,38	76,16	530,30	46,85
	O_{OH}	2,39	68,96	532,54	42,53
$AuCeO_2$ (thin)	O^{2-} ?	1,50	5,81	527,54	4,01
	O_{lat}	1,73	93,07	530,52	73,88
	O_{OH}	1,55	19,63	531,90	14,00
	O_{H2O} (ads)	2,02	8,72	534,62	8,12
$AuCeO_2$ (thick)	O^{2-} ?	2,13	6,02	526,92	7,00
	O_{lat}	1,70	95,42	529,87	88,23
	O_{OH}	2,29	3,82	531,44	4,77

***Table 9.7**: O 1s deconvolution for all the recorded samples*

C 1s peak

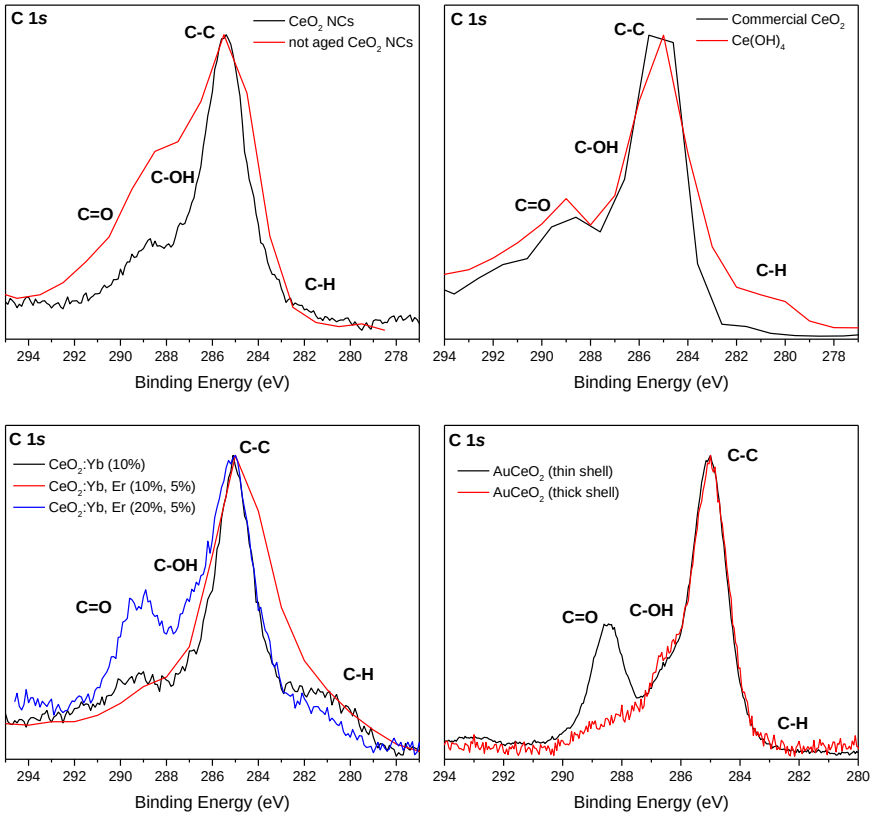

***Figure 9.17**: C 1s signal for each spectra recorded (XPS).*

9.5.2 Xanes characterization

Transmitance measurements

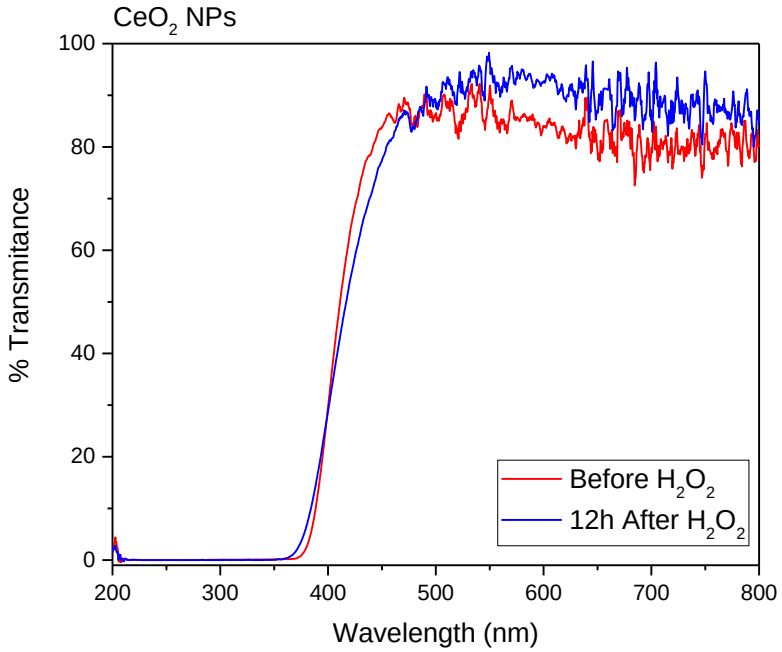

***Figure 9.18**: Transmitance measurements of the CeO_2 NCs sample exposed to the beam before and after the H_2O_2 injection.*

Sample	pH (before beam)	pH (after beam)	H_2O_2 Injection	Final pH
CeO_2 NCs (Fresh)	9,03	7,65	pH Drops	7,7
Not aged CeO_2 NCs	9,13	7,75	pH Drops	7,6
Old CeO_2 NCs	x	7,6	pH Drops	7,6
CeO_2 in EtOH	-	-	-	
$CeCl_3$	4,8	4,8		
CeO_2 Commercial	5	5		

***Table 9.8**: pH measurements before and after x-ray exposure and peroxide injection for the different samples.*